Occlusion of Nanoparticles within Inorganic Crystals

Yin Ning

Department of Chemistry

The University of Sheffield

Submitted to the University of Sheffield

In fulfilment of the requirements for the award of

Doctor of Philosophy

September 2016

Declaration

The work described in this Thesis was carried out at the University of Sheffield under the supervision of Professor Steven P. Armes FRS between October 2013 and September 2016 and has not been submitted, either wholly or in part, for this or any other degree. All the work is the original work of the author, except where acknowledged by references.

Signature: _____

Yin Ning   September 2016

Abstract

This Thesis describes the occlusion of nanoparticles (either diblock copolymer nanoparticles or polymer modified metal sols) within either $CaCO_3$ (calcite) or ZnO (wurtzite).

First, new spherical diblock copolymer nanoparticles were synthesised via reversible addition-fragmentation chain transfer (RAFT) aqueous dispersion polymerisation of 2-hydroxypropyl methacrylate at 70 °C and 20 % w/w solids using either poly(carboxybetaine methacrylate) or poly(proline methacrylate) as the steric stabiliser block. Both these stabilisers contain carboxylic acid groups, but poly(proline methacrylate) is anionic above pH 9.2, whereas poly(carboxybetaine methacrylate) has zwitterionic character at this pH. When calcite crystals are grown at an initial pH 9.5 in the presence of these two types of nanoparticles, it is found that the anionic poly(proline methacrylate)-stabilised particles are occluded uniformly throughout the crystals (up to 6.8 % by mass, 14.0 % by volume). In contrast, the zwitterionic poly(carboxybetaine methacrylate)-stabilised particles show no signs of occlusion into calcite crystals grown under identical conditions. The presence of carboxylic acid groups alone therefore does not guarantee efficient occlusion: overall anionic character is an additional prerequisite.

Second, we demonstrate for the first time that poly(ammonium 2-sulfatoethyl methacrylate)-poly(benzyl methacrylate) diblock copolymer nanoparticles can be prepared with either high or low poly(ammonium 2-sulfatoethyl methacrylate) stabiliser surface densities using either RAFT dispersion polymerisation in a 2:1 v/v ethanol/water mixture or RAFT aqueous emulsion polymerisation, respectively. We then use these model nanoparticles to gain new insight into a key topic in materials chemistry - the occlusion of organic additives into inorganic crystals. Substantial differences are observed for the extent of occlusion of these two types of anionic nanoparticles into calcite, which serves as a suitable host crystal. A low poly(ammonium 2-sulfatoethyl methacrylate) stabiliser surface density leads to uniform nanoparticle occlusion within calcite at up to 7.5 % w/w (16 % v/v), while minimal occlusion occurs when using nanoparticles with a high poly(ammonium 2-sulfatoethyl methacrylate) stabiliser surface density. This counter-intuitive observation suggests an *optimum* anionic surface density is required for efficient occlusion, which provides a hitherto unexpected design rule for the incorporation of nanoparticles within crystals.

Third, a series of new well-defined anionic diblock copolymer nanoparticles are synthesised by polymerisation-induced self-assembly (PISA) via RAFT aqueous emulsion polymerisation and then evaluated as crystal habit modifiers for the *in situ* formation of ZnO in aqueous solution. Systematic studies indicate that both the chemical nature (i.e. whether sulfate-based or carboxylate-based) and the mean degree of polymerisation (DP) of the anionic stabiliser block play vital roles in determining the crystal morphology. In particular, sulfate-functionalised nanoparticles are efficiently incorporated within the ZnO crystals whereas carboxylate-functionalised nanoparticles are excluded. Moreover, the extent of nanoparticle occlusion within the ZnO phase can be as high as 23 % by mass depending on the sulfate-based nanoparticle concentration. The optical properties, chemical composition and crystal structure of the resulting nanocomposite crystals are evaluated and an occlusion mechanism is proposed based on the observed evolution of the ZnO morphology in the presence of these sulfate-based anionic nanoparticles.

Last, we describe an efficient aqueous route that enables the direct occlusion of *non-ionic* poly(glycerol monomethacrylate)$_{70}$-stabilised gold nanoparticles (G_{70}-AuNPs) at remarkably high levels (~20 % w/w) during the *in situ* growth of ZnO crystals under relatively mild conditions. Depending on the synthesis protocol, the G_{70}-AuNPs can be (i) solely located within a central region, (ii) uniformly distributed throughout the ZnO host crystal or (iii) confined to a surface layer. The G_{70} stabiliser is essential for successful occlusion: its pendent *cis*-diol side-groups bind Zn^{2+} cations, which promotes nanoparticle interaction with the growing ZnO crystal surface. XPS studies indicate significant shifts in the Au4f and Zn2p binding energies, which suggests an intimate interaction between the G_{70}-AuNPs and the host ZnO crystals. Finally, we demonstrate that occlusion of G_{70}-AuNPs throughout the whole ZnO is beneficial for the enhanced photocatalytic decomposition of rhodamine B, which serves as a model dye.

Publications

Ning, Y.; Fielding, L. A.; Andrews, T. S.; Growney, D. J.; Armes, S. P. Sulfate-based anionic diblock copolymer nanoparticles for efficient occlusion within zinc oxide, *Nanoscale* **2015**, *7*, 6691-6702.

Ning, Y.; Fielding, L. A.; Doncom, K. E. B.; Penfold, N. J. W.; Kulak, A. N.; Matsuoka, H.; Armes, S. P. Incorporating diblock copolymer nanoparticles into calcite crystals: do anionic carboxylate groups alone ensure efficient occlusion? *ACS Macro Letters* **2016**, *5*, 311-315.

Ning, Y.; Fielding, L. A.; Ratcliffe, L. P. D.; Wang, Y-W; Meldrum, F. C.; Armes, S. P. Occlusion of sulfate-based diblock copolymer nanoparticles within calcite: effect of varying the surface density of anionic stabiliser chains, *Journal of the American Chemical Society* **2016**, *138*, 11734-11742.

Ning, Y.; Fielding, L. A.; Kulak, A. N.; Meldrum, F. C.; Armes, S. P. Efficient synthesis of metal/semiconductor nanocomposites via spatially-controlled occlusion of polymer-stabilised gold nanoparticles within ZnO, submitted manuscript.

Penfold, N. J. W.; **Ning, Y.**; Armes, S. P.; Verstraete, P.; Smets, J. Cross-linked cationic diblock copolymer worms are superflocculants for micrometer-sized silica particles, *Chemical Science*, **2016**, *7*, 6894-6904.

Akpinar, B.; Fielding, L. A.; Cunningham, V. J.; **Ning, Y.**; Mykhaylyk, O. O.; Fowler, P. W.; Armes, S. P. Determining the effective density and stabilizer layer thickness of sterically stabilized nanoparticles, *Macromolecules* **2016**, *49*, 5160-5171.

Cunningham, V. J.; **Ning, Y.**; Armes, S. P.; Musa, O. M. Poly(*N*-2-(methacryloyloxy)ethyl pyrrolidone)-poly(benzyl methacrylate) diblock copolymer nano-objects via RAFT alcoholic dispersion polymerisation in ethanol, *Polymer*, **2016**, *106*, 189-199.

Conferences

May 2015	Sheffield University GRAD School, Sheffield, UK
September 2015	Oral presentation at 29th European Colloid and Interface Society Conference, Bordeaux, France
August 2015	Poster presentation at Armes Fest 500 conference, Sheffield, UK
July 2016	Poster presentation at 4th Warwick polymer conference, Warwick, UK

Acknowledgements

First and foremost, a huge thank you goes to my supervisor Prof. Steven P. Armes FRS for giving me the opportunity to study in the Armes group. Your encouragement, advice, support and reading proof are greatly appreciated. Without you, there is no way I could complete this Thesis. I would also like to thank the Overseas Study Program of Guangzhou Elite Project for funding my PhD studies.

I have really enjoyed the past three years in the Armes group. Much of the work in this Thesis wouldn't have been possible without the help of so many people. First of all, a big thank you goes to Dr. Lee Fielding for training me to use many instruments and advising on my draft publications; Dr. Matt Derry for always helping me at anytime, anywhere, anything and under any circumstance; and of course I also want to thank other E38 members, including Dr. David Growney, Dr. Mark Williams, Dr. Andrew Morse, Amy Cockram, Erik Cornel and Bernice Akpinar. You guys make me feel that we are not only work colleagues but true friends as well. I also want to thank other Armes group members: Dr. Pengcheng Yang, Dr. Peter Madsen, Dr. Liam Ratcliffe, Dr. Kay Doncom, Dr. Renhua Deng, Dr. Nick Warren, Dr. Nan Cheng, Dr. Kate Kirkham, Dr. Greg Smith, Dr. Beulah McKenzie, Dr. Sarah Canning, Dr. Irene Canton, Dr. Lizzy Jones, Dr. Joe Lovett, Dr. Vicki Cunningham, Dr. Fiona Hatton, Charlotte Mable, Nick Penfold, Matt Rymaruk, Craig Jesson, Sarah Byard etc. Thank you all for helping me in the past three years.

I also want to thank Prof. Graham Leggett and Dr. Deborah Hammond for XPS discussions, Prof. Beverley Inkson, Dr. Svetomir Tzokov, and Dr. Ian Ross for TEM technical assistance and Dr. Christopher Hill for ultramicrotomy. Especially, Dr. Svetomir Tzokov helped me a lot to get good quality TEM images. Dr. Sharon Spey is thanked for the XRD measurements and Dr. Stephen Atkin is also appreciated for his help.

Last but not least, I want to thank my wife, Lily, who is always behind me and supports me in many ways. My parents (including my parents-in-law) and sister are also thanked for their unconditional love.

Nomenclature

DP	-	Degree of polymerisation
CMC	-	Critical micelle concentration
IEP	-	Isoelectric point
LCST	-	Lower critical solution temperature
M_n	-	Number-average molecular weight
M_w	-	Weight-average molecular weight
Đ	-	Dispersity ($Đ = M_w/M_n$)
CTA	-	Chain transfer agent
RAFT	-	Reversible addition-fragmentation chain transfer polymerisation
PISA	-	Polymerisation-induced self-assembly
DMSO	-	Dimethyl sulfoxide
THF	-	Tetrahydrofuran
DCM	-	Dichloromethane
ZnO	-	Zinc oxide
$CaCO_3$	-	Calcium carbonate
DLS	-	Dynamic light scattering
PDI	-	Polydispersity index
^{1}H NMR	-	Proton nuclear magnetic resonance spectroscopy
DCP	-	Disc centrifuge photosedimentometry
FE-SEM	-	Field emission scanning electron microscopy
TEM	-	Transmission electron microscopy
FT-IR	-	Fourier transform infra-red
GPC	-	Gel permeation chromatography
XPS	-	X-ray photoelectron spectroscopy
XRD	-	X-ray diffraction
TGA	-	Thermogravimetric analysis

ACVA   -   4,4'-azobis(4-cyanovaleric acid)
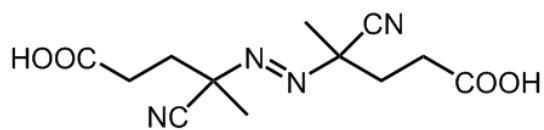
CPCP   -   4-Cyano-4-(phenylcarbonothioylthio)-pentanoic acid
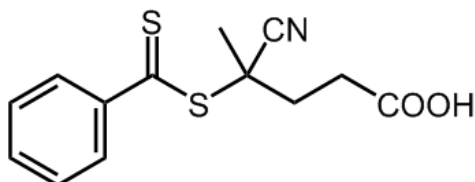
PETTC   -   4-Cyano-4-(2-phenylethane sulfanylthiocarbonyl) sulfanylpentanoic acid
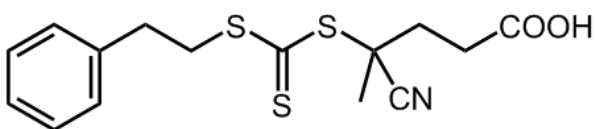
S monomer   -   Ammonium 2-sulfatoethyl methacrylate
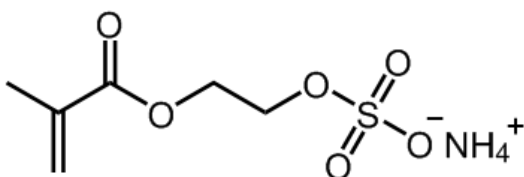
G monomer   -   Glycerol monomethacrylate
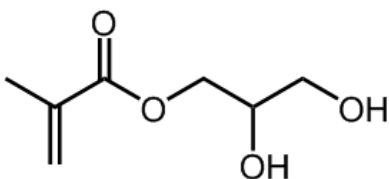
H monomer   -   2-Hydroxypropyl methacrylate
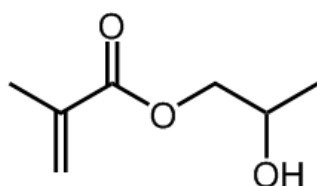
B   -   Benzyl methacrylate

monomer
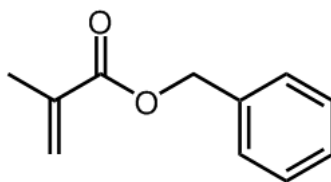
P   -   *O*-Methacryloyl-*trans*-4-hydroxy-*L*-proline

monomer

C   -   Carboxybetaine methacrylate

monomer

Contents

Contents

1. Chapter one

1. Introduction

Occlusion of nanoparticles within inorganic crystalline hosts not only provides a model for understanding the crystallisation process, but also offers a direct route for the preparation of nanocomposite materials in which nanoparticles are distributed within the crystal matrix.[1-4] The incporpation of nanoparticles into the crystals can be *in situ* monitored by atomic force microscopy (AFM) and examined by electron microscopy (EM).[5-7] Compared to single component materials, hybrid nanostructures can exhibit superior properties or new functionalities derived from synergistic interactions between the host and guest components.[8-10] It is widely recognised that metal oxide semiconductors such as ZnO or TiO_2 are promising materials for energy conversion and storage, photocatalysis, sensors, solar cells and nanodevices.[11-17] Over the past decade or so, considerable attention has focused on noble metal/semiconductor hybrid materials because combining plasmonic noble metals with metal oxide semiconductors can, in principle, extend the lifetime of electron-hole pairs and enhance light absorption efficiency, thereby improving performance.[8,9]

Crystallisation, a common phenomenon in Nature, is an important process in a wide range of scientific disciplines including chemistry, physics, biology, geology, and materials science.[18] With the recent development of the latter discipline, considerable research effort is now focused on combining synthetic materials with design concepts adapted from Nature, since this is a promising and bio-green route to achieve new materials with either unique or enhanced mechanical properties at ambient conditions. Biominerals such as bones, teeth and seashells provide an important inspiration for this approach.[19-22] A key feature of these biomaterials, which sets them apart from synthetic crystals, is their nanocomposite structure, which derives from the intimate association of organic molecules with the mineral host.[19-23] However, precisely how these organic molecules are incorporated into the mineral and the associated structure-property relationships remain poorly understood. Although considerable progress has been made in the last few years in producing artificial biominerals containing various occluded additives,[1-3,5-7,24] the synthetic routes remain largely empirical, such that targeting desired morphologies, compositions, and structures typically relies on time-consuming trial-and-error experiments. To gain a deeper understanding of biomineralisation and thus mimic its

occlusion mechanism for the synthesis of new materials with enhanced properties is highly desirable.

With the rapid development of synthetic polymer chemistry, especially reversible-addition fragmentation chain transfer (RAFT) polymerisation, a wide range of functional polymers, such as homopolymers, block copolymers and star polymers can be readily prepared. These copolymers can be hydrophilic, hydrophobic or amphiphilic depending on the nature of the monomers utilised. Recently, polymerisation-induced self-assembly (PISA) based on RAFT polymerisation has proven to be a versatile and efficient route for the synthesis of various types of diblock copolymer spheres, worms or vesicles.[25-30] More importantly, the surface chemistry of such nano-objects can be readily controlled by using non-ionic,[31-34] anionic,[35,36] cationic[37,38] or zwitterionic[39-41] blocks as the steric stabiliser for the PISA formulation. Therefore, in principle, we are able to prepare copolymers with desired functionalities and systematically evaluate their interaction with inorganic crystals.

In this Thesis, we seek to synthesise bespoke block copolymer nanoparticles or polymer stabilised-inorganic nanoparticles with appropriate surface functionality and then incorporate these nanoparticles into inorganic crystals in order to probe the occlusion mechanism as well as producing novel nanocomposite materials.

1.1 Fundamentals of Polymer Science

A polymer, or macromolecule, is a long-chain molecule whose structure is composed of multiple repeating units with a characteristically high relative molecular mass. The average number of repeat units is defined by the mean degree of polymerisation (DP). There are several parameters used to describe the molecular weight of a polymer. Two common terms will be discussed herein: the number-average molecular weight (M_n) and weight-average molecular weight (M_w). They are defined by the following equations.

$$M_n = \frac{\sum n_i M_i}{\sum n_i} \qquad (1.1)$$

where n_i is the number of chains containing i repeat units, and M_i is the molecular weight of these chains.

$$M_w = \frac{\sum w_i M_i}{\sum w_i} = \frac{\sum n_i M_i^2}{\sum n_i M_i} \qquad (1.2)$$

where w_i is the weight fraction of chains with i repeat units, which is equal to the product of $n_i M_i$.

Polymer chains rarely possess a unique DP, hence there is always a distribution around an average value, which differs from pure small molecules. Thus the molecular weight distribution (MWD) is used to describe the relationship between the number of moles of each polymer species (n_i) and the molar mass (M_i) of that species. The width of the MWD can be crudely characterised by the dispersity ($Đ$), as indicated in equation 1.3.[42]

$$Đ = \frac{M_w}{M_n} \qquad (1.3)$$

M_w tends to give a skewed view of the molecular weight distribution of chains, representing the higher molecular weight species to a greater extent than the M_n. As a result, the $Đ$ is always greater than unity (since $M_w > M_n$).

1.2 Polymer Architectures

Given that a single polymer chain can be composed of several different monomer residues, many polymer architectures can be accessed. **Figure 1.1** shows a range of polymers with different architectures. A homopolymer, which is only composed of a single type of repeat unit, is the simplest architecture. The development of synthetic polymer chemistry has enabled the synthesis of a wide range of copolymers with unique architectures (i.e. block, random(statistical), graft, alternating, star-like,

comb-like, brush-like etc.). In particular, block copolymers will be the focus of this Thesis and will be discussed in more detail in the following text.
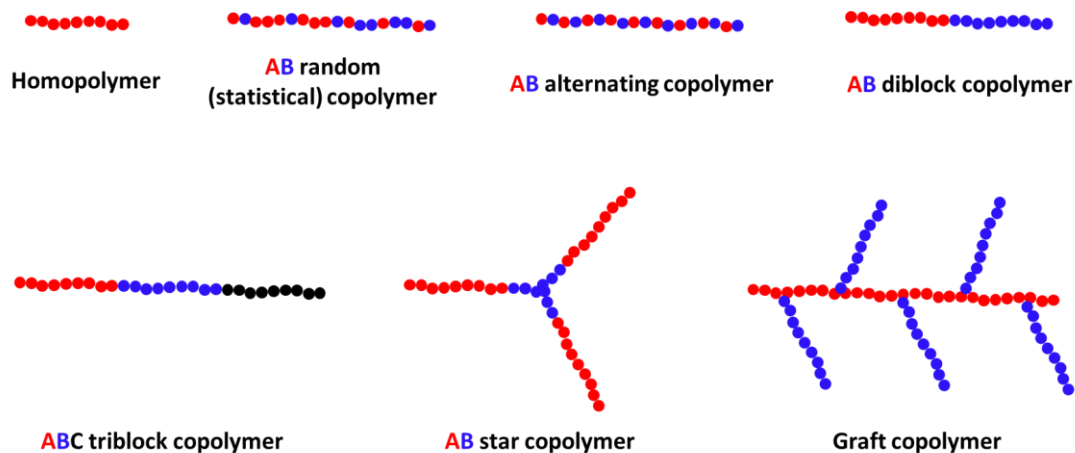
Figure 1.1. Several examples of polymer architectures.

1.3 Polymer Synthesis

1.3.1 Free Radical Polymerisation (FRP)

FRP involves the formation of polymer chains by the successive addition of monomer units via free radical active centres.[43] It is a key synthetic route for obtaining a wide range of different copolymers. The highly reactive nature of free radicals makes this one of the most versatile forms of polymerisation available and allows facile polymerisation of many functional monomers. The mechanism of FRP is summarised in **Figure 1.2**.

FRP mainly involves initiation, propagation, chain transfer and termination (see **Figure 1.2**). In the initiation stage, the initiating free radicals ($I^\cdot$) are created by thermal or UV homolytic cleavage of an initiator (I_2, see **Figure 1.2**). These reactive radicals will immediately react with monomer (M), forming a new active centre (I-$M^\cdot$ or $P_1^\cdot$). Further addition of monomer to these new active radical centres is termed propagation and proceeds with a rate constant k_p; the rate of propagation is much faster than the rate of initiator decomposition (k_d). Chain termination can proceed via two termination mechanisms (see termination step (4) in **Figure 1.2**).

Initiation:

(1) $\quad I_2 \xrightarrow{k_d} 2I^{\bullet}$
$\qquad\qquad R_d \;=\; -\dfrac{d[I]}{dt} \;=\; k_d[I]$

(2) $\quad I^{\bullet} + M \xrightarrow{k_i} I\text{-}M^{\bullet}\;(P_1)$
$\qquad\qquad R_i \;=\; \dfrac{d[I\text{-}M^{\bullet}]}{dt} \;=\; 2fR_d \;=\; 2fk_d[I]$

Propagation:

(3) $\quad P_n^{\bullet} + M \xrightarrow{k_p} P_{n+1}^{\bullet}$
$\qquad\qquad R_p \;=\; -\dfrac{d[M]}{dt} \;=\; k_p[M][P_n^{\bullet}]$

Termination:

(4) $\quad P_n^{\bullet} + P_m^{\bullet}$

$\xrightarrow{k_{tc}} P_{n+m}$
$\qquad\qquad R_{tc} \;=\; k_{tc}[P^{\bullet}]^2$

$\xrightarrow{k_{td}} P_n= \;+\; P_m\text{-}H$
$\qquad\qquad R_{td} \;=\; k_{td}[P^{\bullet}]^2$

Transfer:

(5) $\quad P_n^{\bullet} + I\text{-}I \xrightarrow{k_{trI}} P_n\text{-}I \;+\; I^{\bullet}$
$\qquad\qquad R_{trI} \;=\; k_{trI}[P_n^{\bullet}][I]$

(6) $\quad P_n^{\bullet} + M \xrightarrow{k_{trM}} P_n \;+\; M^{\bullet}$
$\qquad\qquad R_{trM} \;=\; k_{trM}[P_n^{\bullet}][M]$

(7) $\quad P_n^{\bullet} + P_x \xrightarrow{k_{trP}} P_n \;+\; P_x^{\bullet}$
$\qquad\qquad R_{trP} \;=\; k_{trP}[P_n^{\bullet}][P_x]$

(8) $\quad P_n^{\bullet} + S \xrightarrow{k_{trS}} P_n \;+\; S^{\bullet}$
$\qquad\qquad R_{trS} \;=\; k_{trS}[P_n^{\bullet}][S]$
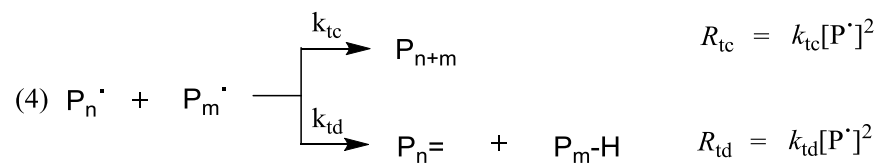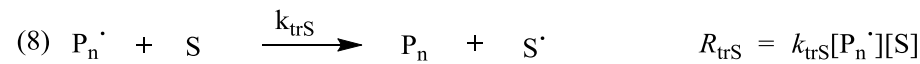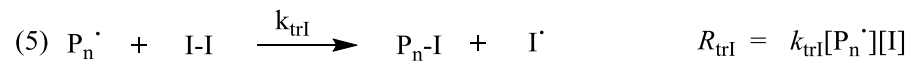
Figure 1.2. Fundamental steps including initiation, propagation and termination for free radical polymerisation (FRP) and the corresponding rate equations of each step.[44,45] I_2 represents the initiator, M means the monomer, $P^{\bullet}$ stands for the polymer radical, R and k are the rate of reaction and rate constant, respectively.

One mechanism is combination, in which two polymer radicals couple together to form a "dead" polymer. The other mechanism is disproportionation, in which one chain radical supplies a hydrogen atom to a second polymer radical, resulting in one chain with an unsaturated terminus ($P_n=$) and a second "dead" chain bearing a saturated terminus ($P_m\text{-}H$). The effective overall rate constant for termination (k_t) can be described as the sum of k_{tc} and k_{td}. In addition, chain transfer can also occur, but such side reactions do not result in the net loss of radicals. Chain transfer can

proceed via various pathways, such as transfer to initiator, monomer, polymer or solvent, as shown in **Figure 1.2.** The relevant rate equation for each chain transfer reaction is also summarised in **Figure 1.2.**

Assuming these chain transfer side reactions are negligible, the rate of initiation is equal to the rate of termination ($R_i = R_t$, the so-called 'steady state' approximation), and the number of monomer units consumed during initiation is negligible compared to those consumed during propagation, the overall rate of polymerisation (R_{polym}) is given by the following equation:

$$R_{polym} = k_p[M]\sqrt{\frac{fk_d[I]}{k_t}} \tag{1.4}$$

where k_p is the rate of propagation, $[M]$ is the monomer concentration, f, is the initiator efficiency, k_d is the rate of decomposition, $[I]$ is the initiator concentration and k_t is the rate of termination.

Based on equation (1.4), the rate of polymerisation follows first-order kinetics with respect to the monomer concentration, $[M]$, and depends on the square root of the initiator concentration, $[I]$. Given that the rate of initiation is much slower than that of propagation ($R_i \ll R_p$, because the active radicals interact with monomer molecules much faster than the rate of initiator decomposition)[46] and the two termination mechanisms discussed above, polymers prepared via FRP usually exhibit characteristically broad MWDs ($M_w/M_n \geq 2.0$).

The kinetic chain length (D_k) is defined as the mean number of monomer molecules consumed per active radical centre and equates to R_p/R_i. (N.B. $R_i = R_t$, hence $[P\cdot] = (fk_d[I]/k_t)^{0.5}$).

$$D_k = \frac{k_p[M]}{2(fk_tk_d[I])^{0.5}} \tag{1.5}$$

Termination leads to a relatively short lifetime for the propagating polymer radicals during FRP. Thus it is not possible to synthesise well-defined block copolymer architectures by this technique.[46]

1.3.2 Living Anionic Polymerisation (LAP)

Unlike FRP, LAP utilises an anionic active centre. A typical mechanism for anionic polymerisation is shown in **Figure 1.3**. Mutual electrostatic repulsion between the growing polymer chain-ends occurs, hence no intrinsic termination is possible.[47] This results in a so-called 'living' polymerisation under ideal conditions, i.e. when conducted using a suitable monomer in a dry, inert solvent. Initiation is essentially complete before any propagation occurs, because the rate of initiation (R_i) is much faster than the rate of propagation (R_p). Therefore, the molecular weight increases linearly with monomer conversion and polymers with narrow MWDs can be achieved ($M_w/M_n \lesssim 1.10$). Meanwhile, the rate of propagation (R_p) can be simply given by the following equation.

$$R_P = k_p[M^-][M] \tag{1.6}$$

where k_p is the propagation rate constant, $[M^-]$ is the total concentration of all of the types of living anionic propagating centres (including free ions and ion pairs) in the system and $[M]$ is the monomer concentration.[48]

LAP can be used to prepare well-defined block copolymers with narrow MWDs via sequential monomer addition. Unfortunately, LAP is very sensitive to protic impurities (rigorous purification of the monomer, solvent, initiator and reaction vessel is required) and the range of vinyl monomers that are suitable for LAP is rather limited. All these drawbacks restrict the wide application of LAP for the industrial manufacture of polymers.
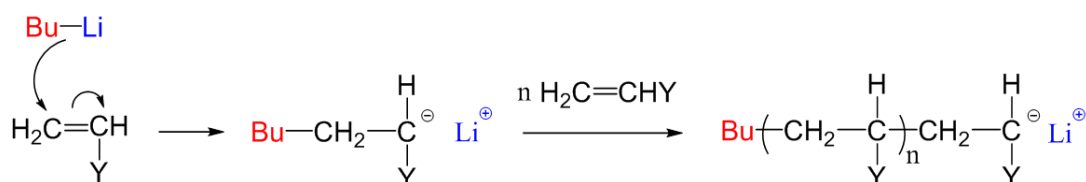
Figure 1.3. Typical mechanism for a living anionic polymerisation (LAP), where *n*-butyl lithium is the initiator. Y represents the pendant functionality of the polymer chains, e.g. phenyl or $CH=CH_2$ in the case of styrene or butadiene, respectively.[43]

1.3.3 Reversible Deactivation Radical Polymerisation (RDRP)

RDRP refers to polymerisations that have controlled "living" character.[49] It bridges FRP and LAP, maintaining most of their advantages while eliminating some of their inherent disadvantages. For example, FRP can be used to polymerise many vinyl monomers and is highly tolerant of functionality in both monomer and solvent. It can also be conducted under various conditions (e.g., bulk, solution, dispersion, emulsion, mini-emulsion, precipitation and suspension) in either water or organic solvents.[46] However, FRP cannot be used to precisely target molecular weight, achieve narrow MWDs, or prepare well-defined block copolymers. Conversely, LAP allows the synthesis of polymers with narrow MWDs and well-defined block copolymers. However, it requires stringent reaction conditions (LAP cannot tolerate even traces of H_2O or other protic impurities) and is confined to the use of relatively few vinyl monomers in inert, non-protic solvents.[43] In contrast, RDRP enables good control to be achieved over the target molecular weight, the MWD and the copolymer architecture for many functional monomers.[49]

Although there are a number of RDRP techniques,[46] the most commonly used are Nitroxide-Mediated Polymerisation (NMP),[50] Atom Transfer Radical Polymerisation (ATRP)[51,52] and Reversible Addition-Fragmentation chain Transfer (RAFT)[53] polymerisation. The common feature of such RDRP processes is the existence of a dynamic (and rapid) equilibrium between the propagating radicals and a 'dormant' or deactivated species during the polymerisation,[54] which reduces the instantaneous concentration of propagating polymer radicals. In turn, the termination rate is suppressed relative to that of propagation because the former is proportional to the square of the radical concentration, while the latter is proportional to the radical concentration.

1.3.3.1 Nitroxide-Mediated Polymerisation (NMP)

NMP was first reported by Solomon and Rizzardo in 1986[55] and involves the reversible reaction of a stable free radical (a nitroxide) with the growing polymer radical.[56] As shown in **Figure 1.4**, the equilibrium favours the capped dormant chains and leads to a relatively low concentration of propagating polymer radicals

(P˙), thus reducing the probability of the bimolecular termination reactions that are so prevalent in conventional FRP.
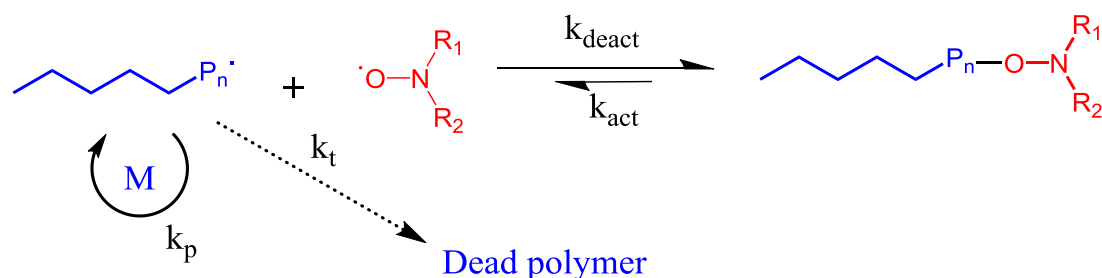
Figure 1.4. Reversible deactivation/activation equilibrium for NMP.[56]

However, NMP is probably still the least versatile technique for the synthesis of block copolymers. The controlled homopolymerisation of methacrylates via NMP has yet to be achieved, although statistical copolymerisation with relatively small amounts of styrene has been reported.[57,58] In addition, NMP is also quite sensitive to the order of polymerisation for two or more monomer classes.[58]

1.3.3.2 Atom Transfer Radical Polymerisation (ATRP)

ATRP was developed in 1995 and has attracted tremendous attention due to its controlled synthesis of well-defined polymeric materials and broad scope for polymerising a wide range of functional monomers.[51,52,59] In ATRP, the dormant species in the deactivation/activation dynamic equilibrium is usually a halide-capped polymer chain (P_n-X, see **Figure 1.5**).[52] This dormant species is activated via reaction with a transition metal complex in its lower oxidation state (e.g. Cu^I/Ligand), resulting in the formation of active propagating polymer radicals ($P_n^\bullet$) and a transition metal complex in a higher oxidation state (e.g. X-Cu^{II}/Ligand).[60] The polymer radicals propagate by addition of multiple monomer units prior to reversible deactivation. The equilibrium for this process lies in favour of the deactivated halogen-capped polymer chains. Thus rapid reversible chain capping ensures that only a relatively low concentration of polymer radicals exists at any given time, giving rise to "living character".
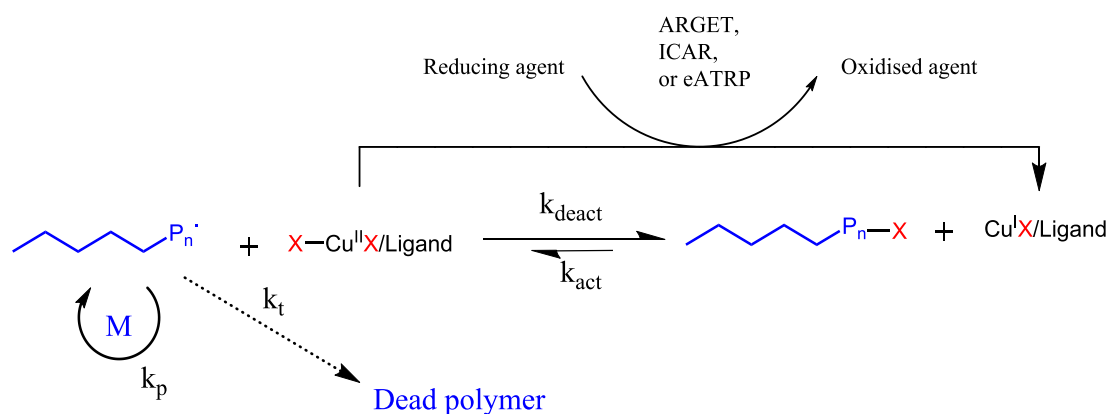
Figure 1.5. Reversible deactivation/activation equilibrium for Cu-mediated ATRP together with recent advances for Cu(I) regeneration, including activator (re)generated by electron transfer (ARGET), initiators for continuous activator regeneration (ICAR) or electrochemically-mediated ATRP (eATRP).[61] X represents a halide atom.

Subsequent ATRP research has led to *in situ* regeneration of the metal catalyst, which can be achieved in several ways, including 'Activator Regenerated by Electron Transfer' (ARGET) ATRP,[62,63] 'Initiators for Continuous Activator Regeneration (ICAR) ATRP,[64] and electrochemically-mediated ATRP (eATRP).[65] These developments essentially reduce the concentration of copper catalyst required for the polymerisation, which consequently has greater tolerance to the presence of trace oxygen. Unfortunately, the synthesis of block copolymers is still subject to some limitations and cost-effective removal of the catalyst is potentially problematic for applications where even trace amounts of copper are unacceptable. The latter drawback is particularly problematic when contemplating block copolymer nanoparticle syntheses.

1.3.3.3 Reversible Addition-Fragmentation Chain Transfer (RAFT)

RAFT was first described by Moad and co-workers in 1998.[53] Since then, several review papers concerning RAFT polymerisation have appeared in the literature.[66-68] RAFT polymerisation has received considerable attention. It has revolutionised the field of polymer synthesis because it provides a versatile tool for the production of complex polymeric architectures, which is a decisive advantage compared to

conventional free radical polymerisation.[68] RAFT polymerisation enables the synthesis of functional copolymers with desired compositions or architectures, such as gradient copolymers,[69] diblock copolymers,[70] triblock copolymers,[71, 72] star copolymers,[73] microgels,[74] polymer brushes or graft copolymers.[75]
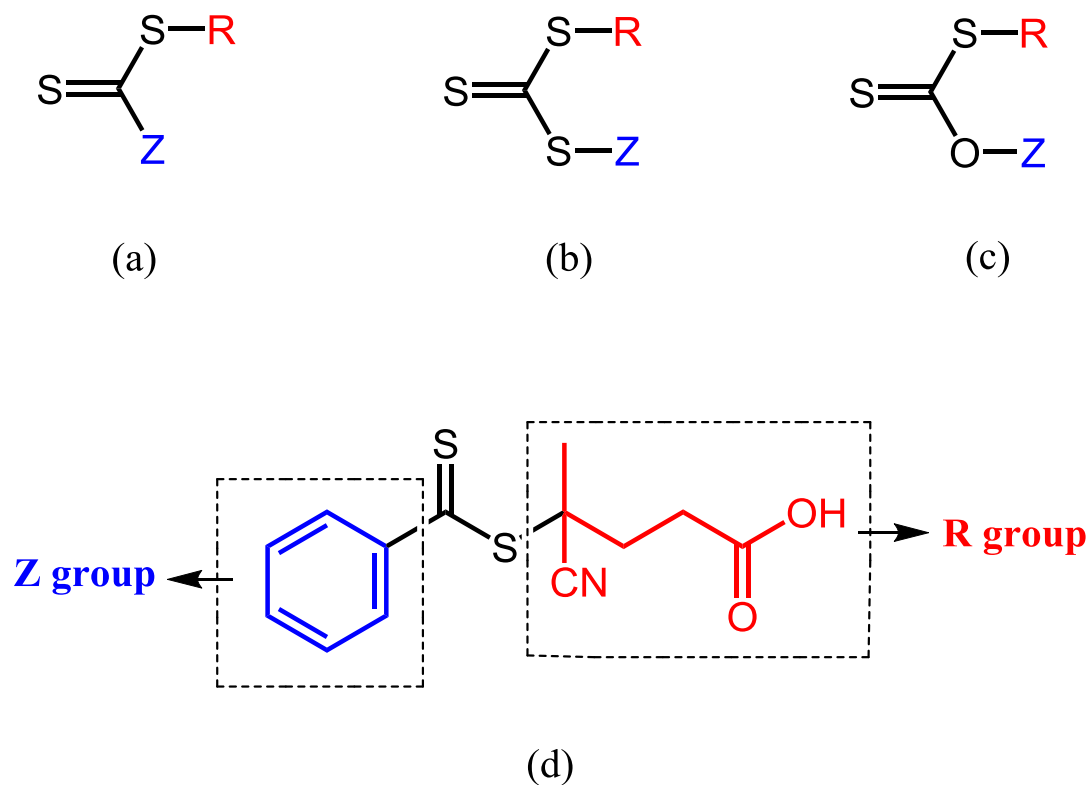
Figure 1.6 General chemical structures of RAFT chain transfer agents: (a) dithiobenzoates, (b) trithiocarbonates and (c) xanthates. (d) Chemical structure of 4-cyano-4-(phenylcarbonothioylthio)pentanoic acid (CPCP), which is a type of the CTAs used in this Thesis.

All the polymers described in this Thesis are synthesised via RAFT polymerisation, so its mechanism will be discussed in detail. The main difference between RAFT polymerisation and conventional free radical polymerisation is the presence of the RAFT chain transfer agent (CTA). These CTAs are organic compounds possessing a thiocarbonylthio moiety (see **Figure 1.6,** which describes the three main types of chain transfer agent). The nature of the R and Z groups are of critical importance for a successful RAFT polymerisation. The role of the Z group is to activate the thiocarbonyl bond towards radical addition and stabilise the resulting radical adduct, while the R group should be able to not only efficiently reinitiate the monomer in its

radical form, but it also should be a better leaving group than the propagating radical. This is important during the pre-equilibrium stage of the polymerisation. Although some details of the precise mechanism of RAFT polymerisation remain controversial, the basic mechanism shown in **Figure 1.7** is widely accepted.

Initiation:
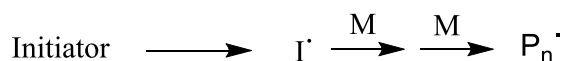
Reversible chain transfer/propagation:
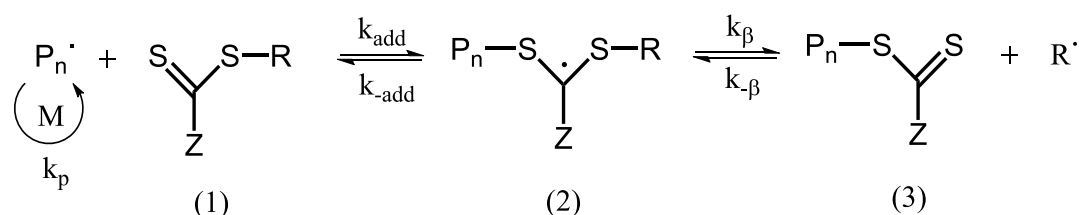
Reinitiation:
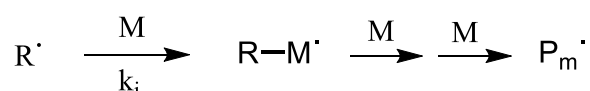
Chain equilibration/propagation:
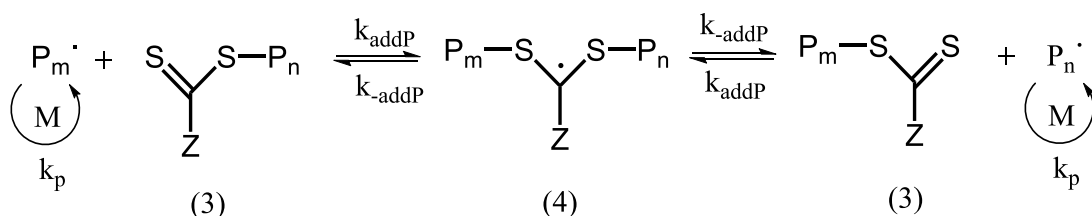
Termination:
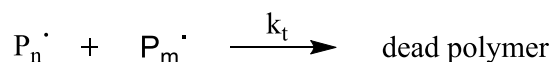
Figure 1.7. Mechanism of reversible addition-fragmentation chain transfer (RAFT) polymerisation according to Rizzardo and co-workers.[66-68]

RAFT polymerisation also involves initiation, propagation, transfer and termination steps as in conventional radical polymerisation. The first step is initiation, in which radicals are created by thermal decomposition of initiator. These radicals then react with monomer to form oligomeric radicals, which are reversibly capped by the

RAFT chain transfer agent. It is worth noting that the RAFT agent should be fully consumed before any propagation commences.[76] This is because its C=S bond is highly reactive, which means that radical addition is favoured over addition to vinyl monomer.

The propagating radical ($P_n^\bullet$) reacts with the thiocarbonylthio compound [RSC(Z)=S (1), see **Figure 1.7**], followed by fragmentation of the intermediate radical to provide a polymeric thiocarbonylthio compound [$P_nS(Z)C=S$ (3), **Figure 1.7**] and a new radical ($R^\bullet$). This new radical can reinitiate polymerisation by reaction with further monomer to form another propagating polymer radical $P_m^\bullet$. Rapid equilibrium between these active propagating radicals ($P_n^\bullet$ and $P_m^\bullet$) and the dormant polymeric thiocarbonylthio compounds (3) ensures that all chains grow with equal probability and suppresses termination. This unique mechanism explains why polymers with narrow MWDs can be obtained via RAFT polymerisation. Although termination is limited, it still occurs via combination or disproportionation, as shown in **Figure 1.7**. Based on this mechanism, most of the polymer chains retain their RAFT end-groups after the polymerisation is complete (or quenched at intermediate conversion).
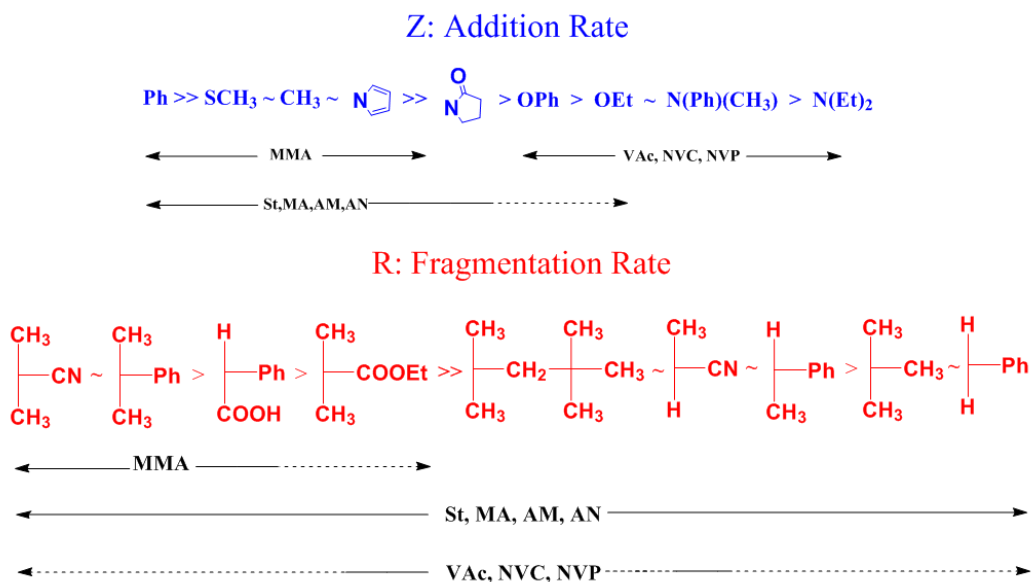
Figure 1.8. Guidelines for selection of an appropriate RAFT CTA for various monomer types. Solid lines indicate that good control can be achieved, whereas dashed lines indicate that only partial control (e.g. broad MWD or substantial retardation) can be achieved. For Z groups, addition rates decrease and fragmentation rates increases from left to right. For R groups, fragmentation rates decrease from left to right.[66]

RAFT polymerisation typically avoids the use of protecting group chemistry and tolerates both polar and non-polar solvents. It can be used to polymerise a wide range of vinyl monomers such as styrene, acrylates and acrylamides, methacrylates and methacrylamides, and vinyl esters. This opens up the design of well-defined copolymers with a wide range of functionality and with various copolymer architectures. The precise nature of the Z and R groups on the CTA plays a vital role in controlling RAFT polymerisations. Moad et al.[66] reported an extensive set of guidelines for selection of an appropriate RAFT CTA for a particular monomer class (**Figure 1.8**).

1.4 Emulsion Polymerisation

Emulsion polymerisation was developed[77] in the 1920s and has been widely used in industry to produce a wide range of latex copolymers due to its inherent advantages (i.e. low viscosity, high heat capacity, efficient heat dissipation, and use of a non-toxic solvent, water) over other polymerisation techniques.[78] Notably, emulsion polymerisation allows high molecular weight polymers to be generated at fast polymerisation rates and very high monomer conversions can be achieved.

The mechanism of emulsion polymerisation can be depicted as follows. At the beginning of emulsion polymerisation, surfactant-stabilised monomer droplets are dispersed in aqueous solution (see **Figure 1.9**). Although the monomer is largely water-insoluble, a very small amount is nevertheless present in the aqueous phase, which reacts with the water-soluble radials derived from the initiator to generate oligoradicals. Such oligomers are initially soluble in water until a critical chain length is attained. Thereafter, these insoluble oligoradicals can either transfer into pre-existing micelles (heterogeneous nucleation) or aggregate and adsorb free surfactant to produce new micelles (homogeneous nucleation).[79] The precise nucleation mechanism depends on the surfactant concentration and the aqueous solubility of the monomer. In either case, the polymerisation proceeds rapidly because the monomer concentration inside the micelles is much higher than that in the bulk solution and the polymerisation rate, as well as particle number, increases during the polymerisation. When particle nucleation is complete, polymerisation

continues inside the monomer-swollen latex particles with further monomer diffusing from the monomer droplets. Ideally, the polymerisation continues until all the monomer has been consumed.[80,81]
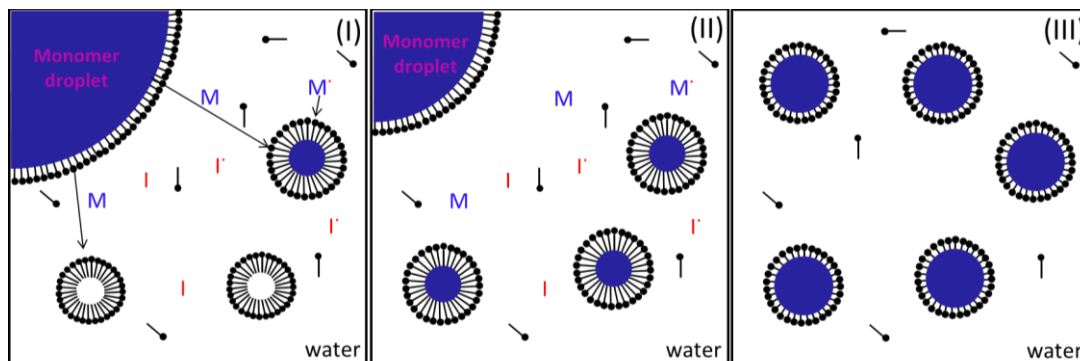
Figure 1.9. Schematic representation of the three main intervals in emulsion polymerisation. Stage I: Monomer droplets stabilised by surfactant are dispersed in water and the free radicals generated in the aqueous phase react with trace monomer dissolved in water, forming oligomers. These oligomers then migrate into the surfactant-stabilised monomer droplets; Stage II: Monomer continually transports from the monomer droplets into the swollen latex particles; Stage III: Polymerisation continues inside the monomer-swollen particles until the monomer is depleted.[80,81]

Disadvantages of emulsion polymerisation include: (i) surfactants and other polymerisation adjuvants either remain in the formulation or are difficult to remove; (ii) for dry (isolated) polymers, water removal is an energy-intensive process; (iii) emulsion polymerisations are usually designed to operate at high monomer conversion. This can result in significant chain transfer to polymer.

1.5 Dispersion Polymerisation

Depending on the nature of the solvent, dispersion polymerisation can be simply categorised as aqueous dispersion polymerisation, non-aqueous dispersion polymerisation or mixed aqueous dispersion polymerisation. However, in all cases, the common feature is that the monomer is dissolved in the initial reaction solution while the resulting polymer is not. The first description of dispersion polymerisation was reported in 1962,[82] whereby sterically-stabilised latexes were synthesised in

non-polar solvents. This technique has since been extended to include polar solvents, such as water,[83,84] alcohols[85,86] and water/alcohol solvent mixtures.[87-89]

I = Initiator; M = monomer; I˙ = radical; ∿˙ = polymeric oligomer; ∿∿ = polymeric stabiliser
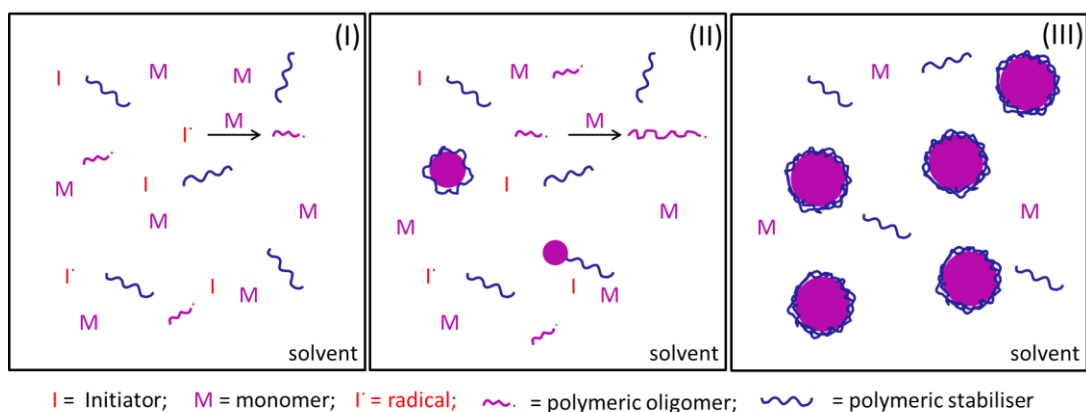
Figure 1.10. Schematic representation of a typical dispersion polymerisation. Stage I: The monomer, initiator and stabiliser are dissolved in solvent. Stage II: Homopolymerisation occurs with phase separation from solution to form primary particles at some critical chain length; Stage III: Polymerisation continues within these monomer-swollen primary particles, eventually resulting in sterically-stabilised polymer latexes.[90]

The generally accepted mechanism of latex formation via dispersion polymerisation can be briefly summarised as follows (see **Figure 1.10**). All components, including initiator, monomer and polymeric stabiliser, are dissolved in the solvent (continuous phase) prior to polymerisation. Free radicals are generated by thermal decomposition of the initiator and interact with monomers to form oligomeric radicals. The solubility of these oligomers decreases with increasing molecular weight and precipitation occurs at a critical chain length to form primary particles. The stabiliser physically adsorbs or chemically grafts (by transfer reactions) onto the colloidally unstable nascent particles. When all particles have acquired sufficient stabiliser to confer colloidal stability, the monomer-swollen particles grow by diffusive capture of oligomers and very small polymeric nuclei precursors, as well as further monomer. Ideally, the polymerisation continues until all monomer is consumed. It is worth noting that a suitable stabiliser for dispersion polymerisation must meet two conflicting requirements: it must have some affinity for the surface of the polymer particles and also be soluble in the chosen solvent.[90] However, dispersion polymerisation is important because it can produce nearly monodisperse polymer

particles of 0.1~15 µm, which fills the gap between particle size generated by conventional emulsion polymerisation (0.006~0.7 µm) in batch process and that of suspension polymerisation (50~1000 µm).[90]

Packing parameter (p)

$$p = \frac{v}{a_o l_c}$$

p < 1/3 : Spherical micelles;
1/3 < p < 1/2 : Cylindrical micelles;
1/2 < p < 1 : Vesicles or bilayers;
p = 1 : Lamellae
p > 1 : Inverted structures
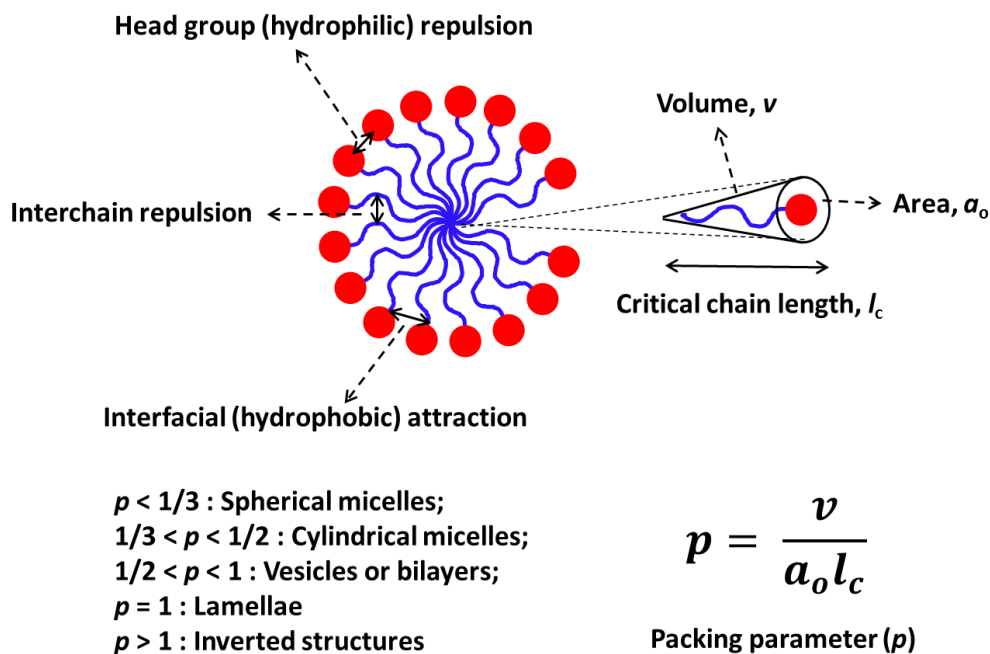
Figure 1.11. Schematic representation of the geometric packing of surfactant molecules inside a colloidal aggregate. The packing parameter (p), as defined by the equation, determines the aggregate morphology.[91]

1.6 Self-Assembly

Self-assembly is a process in which a disordered system of components forms an organised structure or pattern. It is a ubiquitous phenomenon in Nature, such as the formation of membranes in living cells by the self-assembly of amphiphilic phospholipids. Such microcompartmentalisation is essential for life itself. In the present Thesis, surfactant self-assembly, block copolymer self-assembly and polymerisation-induced self-assembly (PISA) will be discussed.

1.6.1 Surfactant Self-Assembly

Surfactant molecules are composed of a polar (or hydrophilic) head that is compatible with water and a non-polar (or hydrophobic) tail that is compatible with

oil. This amphiphilic character enables surfactants to undergo self-assembly to reduce the interfacial tension between two phases.[92] Depending on the type of surfactant and the solution conditions, various self-assembled architectures can be achieved, including spherical, globular, rod-like or spherical bilayers.[91,93] The closed aggregates with hydrophobic interiors are known as micelles while the spherical bilayers containing an encapsulated aqueous phase are called vesicles.[94]

It is primarily the packing parameter (p, see equation in **Figure 1.11**), that determines the morphology of the colloidal aggregates, where v is the volume of the hydrophobic segment, a_o is the contact area of the head group, and l_c is the length of the hydrophobic segment.[91] When $p < 1/3$, spheres are formed; when $1/3 < p < 1/2$, cylinders are obtained; when $1/2 < p < 1$, vesicles or bilayers are produced; when $p = 1$, planar lamellae are obtained finally, if $p > 1$, inverted structures can be observed.

1.6.2 Block Copolymer Self-Assembly

The ability of amphiphilic block copolymers to self-assemble in selective solvents has been intensively studied for decades.[95-98] Amphiphilic diblock copolymers comprise a hydrophilic and a hydrophobic block, which enables the formation of various copolymer morphologies by self-assembly (either in the bulk or in solution)[99-105] based on similar principles to those for the self-assembly of small-molecule amphiphiles. Compared to small-molecule aggregates, copolymer aggregates exhibit higher stability and greater durability, which suggests potential industrial applications.[96]

Although block copolymer self-assembly is known in the bulk, the present Thesis will focus on block copolymer self-assembly in solution. Block copolymer self-assembly can lead to a wide range of morphologies, including spherical micelles, rods, bicontinuous structures, lamellae, vesicles, hexagonally-packed hollow hoops (HHHs), large compound micelles (LCMs), etc.[97] As shown in **Figure 1.12**, Eisenberg and co-workers have shown that a wide range of morphologies can be achieved via the self-assembly of polystyrene-poly(acrylic acid) diblock copolymers. The morphology is mainly dependent on the copolymer composition,[98] copolymer

concentration,[106] water content,[107,108] nature of the common solvent[109,110] and presence of certain additives (such as ions,[105] or homopolymer[98]).
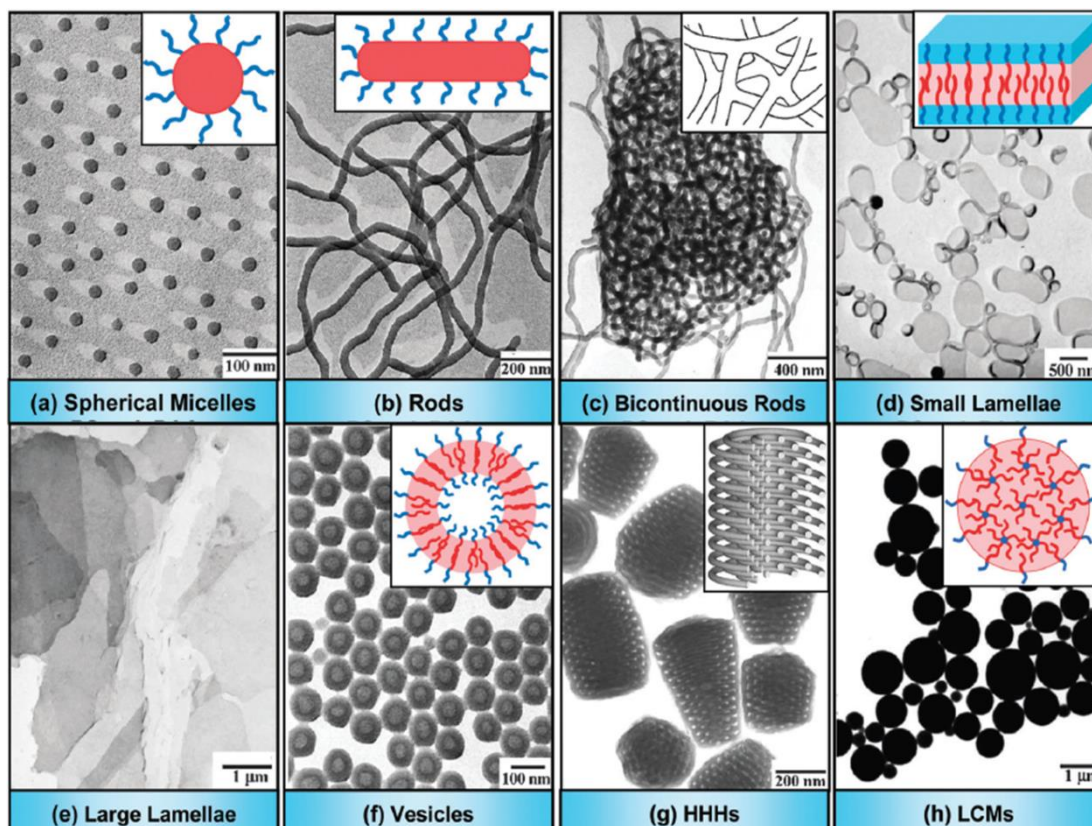
Figure 1.12. Transmission electron microscopy (TEM) images and corresponding cartoons for a range of copolymer morphologies formed by the self-assembly of asymmetric amphiphilic polystyrene-poly(acrylic acid) diblock copolymers in selective solvents (x and y represent the DPs of the PS and PAA blocks, respectively). In the cartoons, red denotes the hydrophobic PS block, while blue represents the hydrophilic PAA block.[97]

Block copolymer self-assembly can be thermodynamically induced or kinetically controlled.[96] During self-assembly of amphiphilic block copolymers, progressive addition of the precipitant induces aggregation of the insoluble block, while the soluble block acts as a stabiliser. During self-assembly, the relatively high entropy of single chains is sacrificed. However, a larger enthalpic penalty caused by energetically unfavourable hydrophobe-water interactions is avoided. Hence, self-assembly lowers the total free energy of the system ($\Delta G < 0$).[96] Under thermodynamic control, the block copolymer composition and/or temperature of the system are the main factors that dictate the copolymer morphology.[98,111] When self-assembly occurs under kinetic control,[106,108] the rate of formation of kinetically-

controlled aggregates depends on the hydrodynamic interactions between the aggregates and/or copolymer chains, as well as the chain dynamics within the hydrophobic domains of the aggregates.

In addition to the phase separation discussed above, self-assembly can also be driven by a pH switch,[112] thin film rehydration[113] or crystallisation processes.[114,115] Unfortunately, well-defined morphologies can usually only be achieved in *dilute* solution using such methods, which significantly limits their practical applications.

1.6.3 Polymerisation-Induced Self-Assembly (PISA)

In the past several years, PISA has received intensive attention and become widely recognised as a robust and efficient method to prepare block copolymer nano-objects of controlled size, morphology, and surface chemistry.[26-28] PISA possesses several advantages: (i) it enables the formation of nano-objects at *high* copolymer concentrations, which is an important advantage over conventional block copolymer self-assembly routes; (ii) block copolymer nano-objects can be readily prepared with a wide range of morphologies, including spheres, worms or vesicles, simply by tuning the DP of the core-forming and stabiliser blocks; (iii) the surface chemistry of the nano-objects can be readily tuned by varying the chemical nature of the stabiliser chains. As a result, PISA offers an unprecedented opportunity to investigate the relationship between the surface chemistry of block copolymer nanoparticles and their occlusion within inorganic crystals. This is the main topic of this Thesis.

Figure 1.13 shows a schematic representation of the synthesis of diblock copolymer spheres, worms, and vesicles. PISA involves a soluble macro-CTA, which is chain-extended using the monomer that forms the insoluble core-forming insoluble block. Micellar nucleation occurs when the core-forming block reaches a critical DP. Because the core-forming block DP increases with monomer conversion, the packing parameter for the diblock copolymer chains also increases during the polymerisation. Generally, the morphology of the diblock copolymer nanoparticles evolves from spheres to worms to vesicles during PISA, as described by Blanazs and co-workers.[33,34]

$P \leq 1/3$

$1/3 < P \leq 1/2$

$1/2 < P \leq 1$

Soluble macro-CTA

Monomer

chain-extending with an insoluble block

RAFT mediated PISA
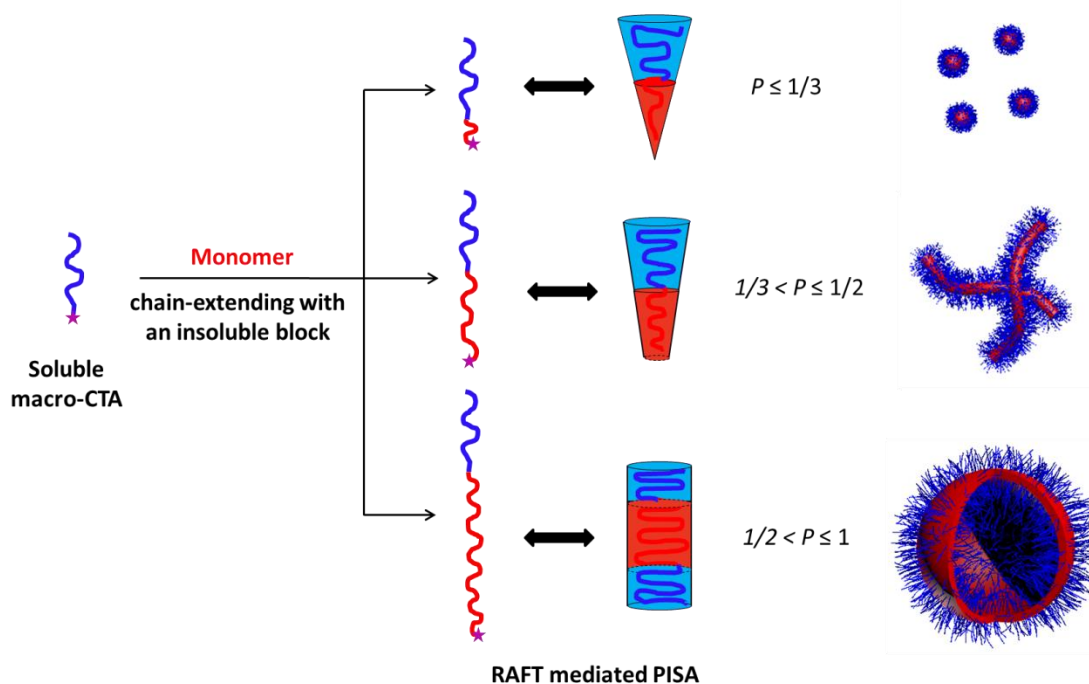
Figure 1.13. Schematic representation of the synthesis of diblock copolymer nano-objects via PISA. The macro-CTA is soluble in the continuous phase, which can be polar solvents (such as water, ethanol) or non-polar solvents (such as *n*-alkanes).[27]

In principle, the surface chemistry (e.g. non-ionic,[31,33,116-120] anionic,[35,121] cationic[37,122] or zwitterionic[39,40,123]) of the block copolymer nanoparticles can be controlled by using appropriate macro-CTAs. Based on the initial core-forming monomer solubility, there are two main PISA formulations: RAFT dispersion polymerisation and RAFT emulsion polymerisation.

1.7 PISA via RAFT Dispersion Polymerisation

RAFT dispersion polymerisation refers to those polymerisations that are conducted in a solvent which can dissolve the macro-CTA, initiator and core-forming monomers, but cannot dissolve the core-forming block once it reaches a critical DP. In this formulation, a RAFT macro-CTA is used as the stabiliser block, which remains soluble in the continuous phase both before and after polymerisation. The second block is generated via polymerisation of the soluble monomer which forms

an insoluble block *in situ*.[26-28] Such RAFT mediated PISA syntheses can be conducted in either polar or non-polar solvents.[28,31,36,124-126]
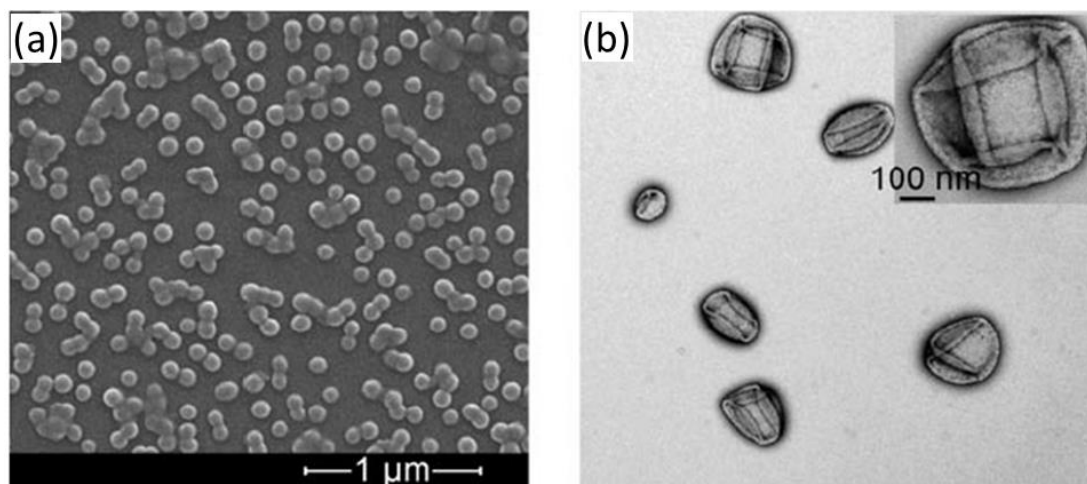
Figure 1.14. (a) Scanning electron microscopy (SEM) image of poly(glycerol monomethacrylate)$_{65}$-poly(2-hydroxypropyl methacrylate)$_{300}$ (G$_{65}$-H$_{300}$) spheres prepared at 10 % solids. (b) TEM image of G$_{65}$-H$_{300}$ vesicles prepared at 20 % solids.[31]

1.7.1 PISA via RAFT Dispersion Polymerisation in Aqueous Solution

Li et al. reported the preparation of a range of sterically-stabilised nanoparticles or vesicles (see **Figure 1.14**) by RAFT aqueous dispersion polymerisation of 2-hydroxypropyl methacrylate under surfactant-free conditions using a poly(glycerol monomethacrylate) macro-CTA (G macro-CTA) as a steric stabiliser.[31] The mean size of the spherical nano-objects could be precisely controlled in the range of 20 ~ 105 nm diameter simply by varying the target DP of the hydrophobic poly(2-hydroxypropyl methacrylate) block.[31] In this formulation, the G macro-CTA and azo initiator are fully dissolved, but 2-hydroxypropyl methacrylate monomer (H monomer) is not necessarily fully dissolved because the solubility of H monomer in water is around 13 % w/w at room temperature. However, the reaction solution gradually turns transparent at the reaction temperature of 70 °C because of the gradual consumption of H monomer.
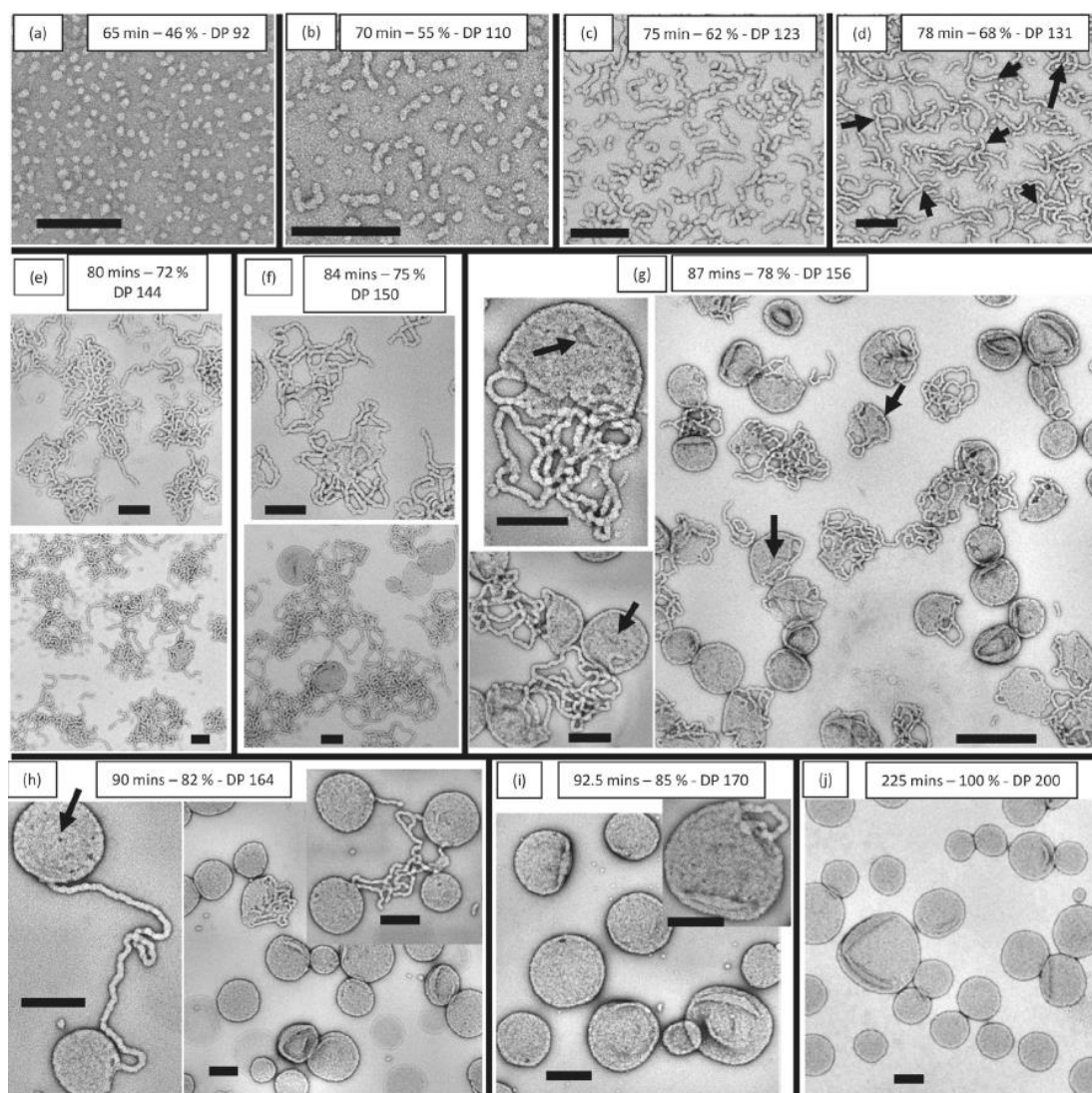
Figure 1.15. Nanoparticle morphology evolution as the DP of the poly(2-hydroxypropyl methacrylate) core-forming block is systematically increased when targeting G_{47}-H_{200} diblock copolymer nano-objects via RAFT aqueous dispersion polymerisation of 2-hydroxypropyl methacrylate at 70 °C and 10 w/v % solids.[34] TEM images of (a) spheres, (b) short worms, (c) long worms, (d) branched worms, (e, f) partially coalesced worms, (g) jellyfish, and (h~j) vesicles. Scale bars = 200 nm.

In a later study of this particular G-H diblock copolymer system, the full range of copolymer morphologies (spheres, worms and vesicles) were obtained.[11,12] To gain a deeper understanding of PISA, the gradual evolution of the nano-object morphology (from spheres to worms to vesicles) was examined by carefully monitoring the whole 2-hydroxypropyl methacrylate polymerisation (see **Figure 1.15**). Micellar nucleation of nascent spheres occurred at a poly(2-hydroxypropyl methacrylate) DP of ~92. As the poly(2-hydroxypropyl methacrylate) block DP increases, a mixture of spheres

and linear worms are observed. Intermediate nanostructures such as linear or branched worms are formed, and the number of branch points and extent of worm clustering increases when the DP of the poly(2-hydroxypropyl methacrylate) block increases up to 150. So-called "jellyfish" and finally pure vesicles were obtained at high poly(2-hydroxypropyl methacrylate) DPs (~200).

It is worth noting that this morphology evolution is particularly well-established for G_{47}-H_{200} prepared by RAFT aqueous dispersion polymerisation at 70 °C and 10 w/v % solids. Although the nano-object morphology is governed by the packing parameter, it is also dependent on the copolymer concentration, as well as the DP of the stabiliser block.[33,36,124,126] More interestingly, G-H diblock copolymer nanoparticles exhibit thermo-responsive behaviour,[32,127] with pH-responsive behaviour being observed when using a pH-responsive macro-CTA.[128,129] This suggests potential applications in drug release, cell storage, etc.[130]

1.7.2 PISA via RAFT Dispersion Polymerisation in Alcoholic Solution

Pan and co-workers have reported that PISA can be conducted via RAFT dispersion polymerisation of styrene in alcoholic solution.[131-134] However, in all cases the rate of polymerisation was relatively slow and the final monomer conversion was rather low (only 30 – 70 %) within 48 h at 80 °C. These disadvantages unfortunately limit the industrial application of such formulations due to the high cost of removing the excess styrene monomer. This slow rate of polymerisation is related to the relatively low propagation rate constant for styrene.[135-137] However, Semsarilar et al. have shown that high monomer conversions can be achieved for the RAFT dispersion polymerisation of benzyl methacrylate (B) in alcoholic media within 24 h at 70 °C.[36] Moreover, the MWD of these diblock copolymers can be relatively narrow ($M_w/M_n \leq$ 1.30) and the steric stabiliser block utilised can be either non-ionic poly(glycerol monomethacrylate), anionic poly(methacrylic acid), cationic poly(2-(dimethylamino)ethyl methacrylate), and zwitterionic poly(2-(methacryloyloxy)ethyl phosphorylcholine) .

As shown in **Figure 1.16**, a detailed phase diagram can be achieved by fixing the DP of the poly(methacrylic acid) stabiliser, while varying the total solids concentration

and the DP of the core-forming poly(benzyl methacrylate) block. Based on this phase diagram, pure phases of either spheres, or worms, or vesicles can be reproducibly targeted by choosing appropriate conditions.
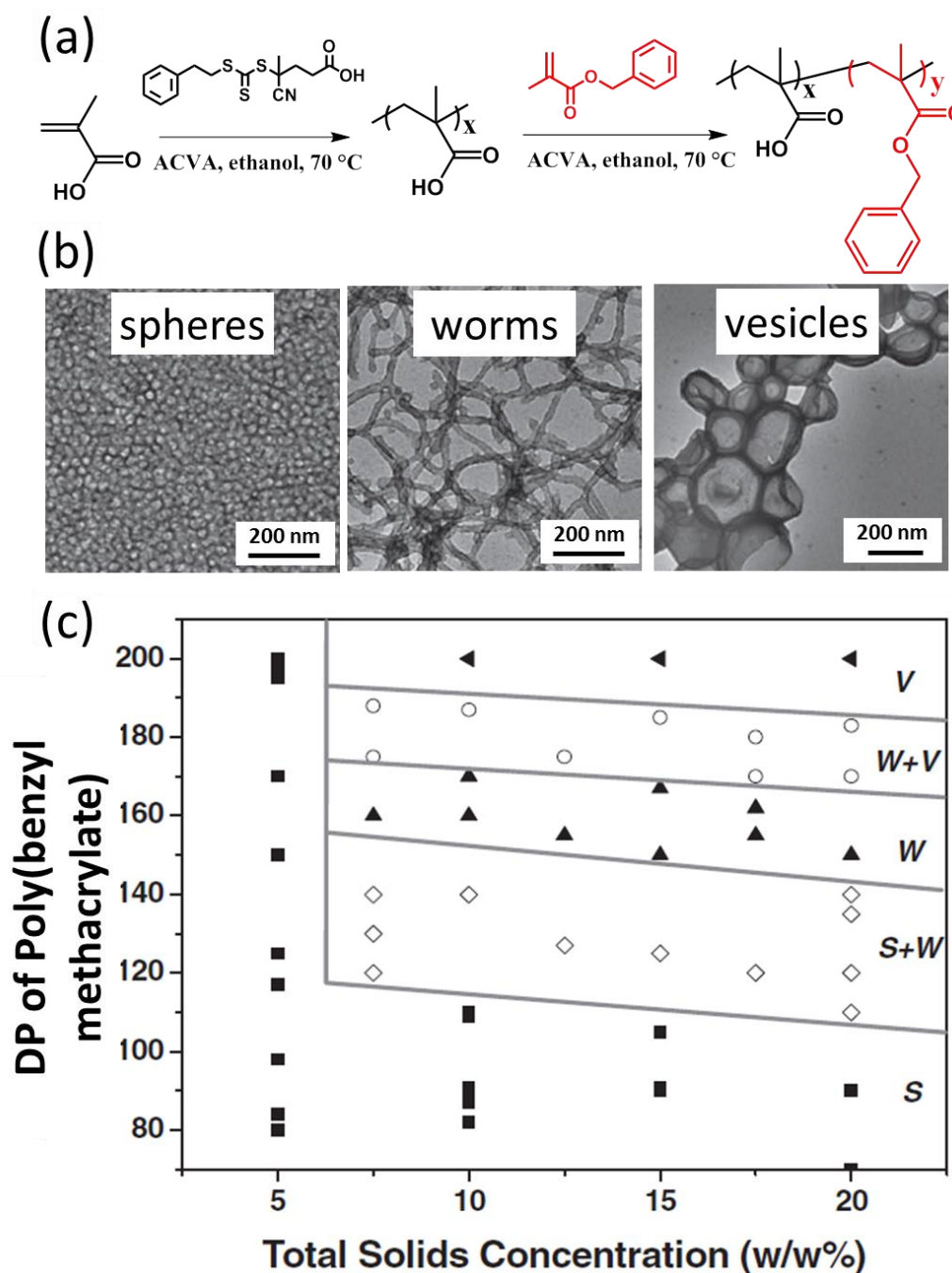
Figure 1.16. (a) Synthesis of poly(methacrylic acid)$_x$-poly(benzyl methacrylate)$_y$ (M_x-B_y) diblock copolymer nanoparticles via RAFT alcoholic dispersion polymerisation; (b) TEM images of spheres, worms or vesicles of M_x-B_y diblock copolymer nanoparticles; (c) Phase diagram for the M_{71}-B_y diblock copolymer nano-objects prepared by RAFT dispersion polymerisation of BzMA in ethanol. (Note: S represents spheres; W represents worms; V represents vesicles).[36] ACVA is the initiator.

1.7.3 PISA via RAFT Dispersion Polymerisation in Aqueous Alcoholic Solution

RAFT dispersion polymerisation can also be conducted in aqueous alcoholic solution.[88,138-141] It has been shown that the solvent composition not only influences the polymerisation kinetics, but also the final copolymer morphology. Increasing the proportion of water content significantly accelerates the rate of benzyl methacrylate polymerisation but inhibits the formation of so-called higher order morphologies.[138] Jones et al. investigated the effect of water content on the diblock copolymer morphology.[141] More specifically, poly(2-(dimethylamino)ethyl methacrylate)$_{43}$-poly(benzyl methacrylate)$_y$ (D_{43}-B_y) diblock copolymer nanoparticles were prepared via RAFT-mediated PISA in various water/ethanol mixtures. Higher order morphologies such as vesicles and worms could only be obtained when using relatively low water contents (see **Figure 1.17**) for a given target D-B block composition.[141] The copolymer morphology was restricted to spheres due to the build-up of cationic charge in the poly(2-(dimethylamino)ethyl methacrylate) stabiliser chains on addition of water. In related work, it was shown that diblock copolymer nanoparticles prepared by PISA in aqueous media are typically limited to spheres when using polyelectrolytic stabilisers.[35,37]
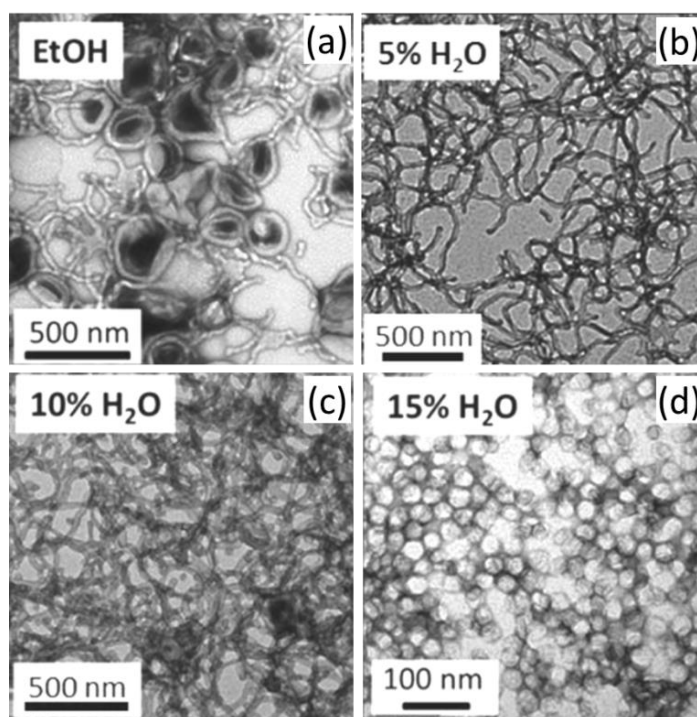
Figure 1.17. TEM images of poly(2-(dimethylamino)ethyl methacrylate)$_{43}$-poly(benzyl methacrylate)$_{120}$ (D_{43}-B_{120}) nano-objects prepared via RAFT dispersion polymerisation at 15 % w/w solids at 70 °C in (a) 100 % ethanol; (b) 95:5 v/v ethanol/water; (c) 90:10 v/v ethanol/water; (d) 85:15 v/v ethanol/water.[141]
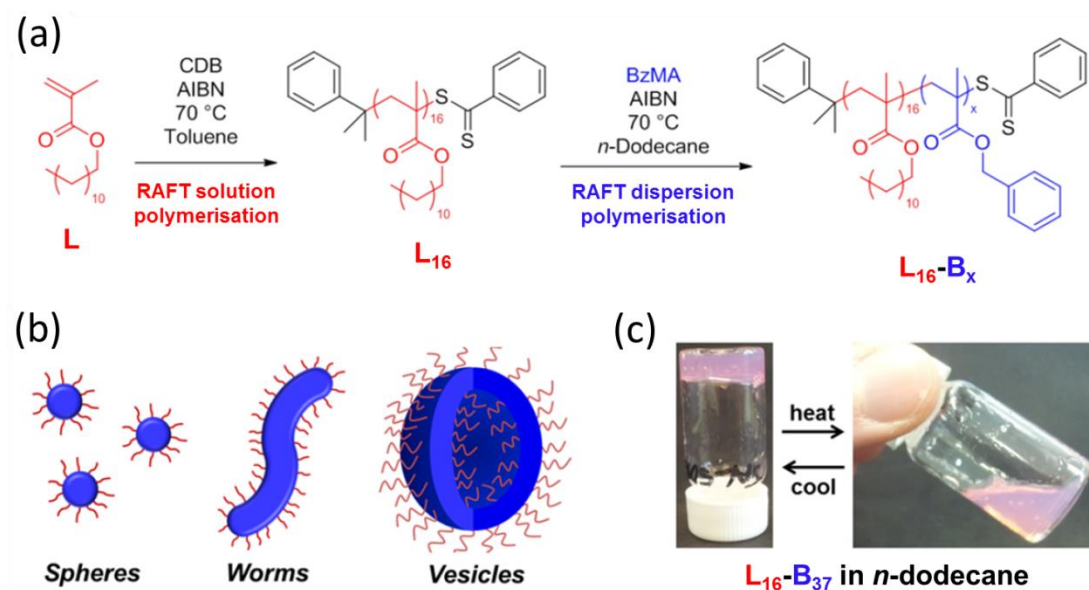
Figure 1.18. (a) RAFT dispersion polymerisation synthesis of poly(lauryl methacrylate)$_{16}$-poly(benzyl methacrylate)$_x$ (L$_{16}$-B$_x$) diblock copolymer nano-objects; (b) Cartoons depicting spheres, worms or vesicles; (c) thermo-responsive behavior of a 20% w/w dispersion of L$_{16}$-B$_{37}$ diblock copolymer nanoparticles from a free-standing worm gel at 20 °C to a dispersion of spheres on heating to 70 °C in *n*-dodecane.[126]

1.7.4 PISA via RAFT Dispersion Polymerisation in Non-polar Solvents

Fielding et al. [124,126] reported the first example of an efficient all-methacrylic RAFT dispersion polymerisation formulation conducted in non-polar solvents (*n*-heptane [124] or *n*-dodecane[126]). It was demonstrated that the stabiliser DP strongly influenced the copolymer morphology. In these formulations, a poly(lauryl methacrylate) macro-CTA was chain-extended with benzyl methacrylate in *n*-heptane at 90 °C or in *n*-dodecane at 70 °C (see **Figure 1.18**). Again, such worm dispersions proved to be thermo-responsive: a worm-to-sphere transition was observed when heating from 20 °C to 90 °C as a result of surface plasticisation of the worms leading to a reduction in the effective packing parameter.

The poly(lauryl methacrylate) macro-CTA is soluble in *n*-heptane (and *n*-dodecane) during the benzyl methacrylate polymerisation, whereas the growing poly(benzyl methacrylate) block becomes insoluble at a critical DP, thus leading to PISA. It was found that only kinetically-trapped spherical nanoparticles could be prepared when utilising a relatively long poly(lauryl methacrylate) macro-CTA. The nanoparticle

sphere diameter was systematically increased as longer core-forming block DPs were targeted. Nevertheless, higher order morphologies such as worms and vesicles can be produced by using a sufficiently short poly(lauryl methacrylate) macro-CTA. A detailed phase diagram constructed for poly(lauryl methacrylate)$_x$-poly(benzyl methacrylate)$_y$ nanoparticles in *n*-dodecane is shown in **Figure 1.19**.
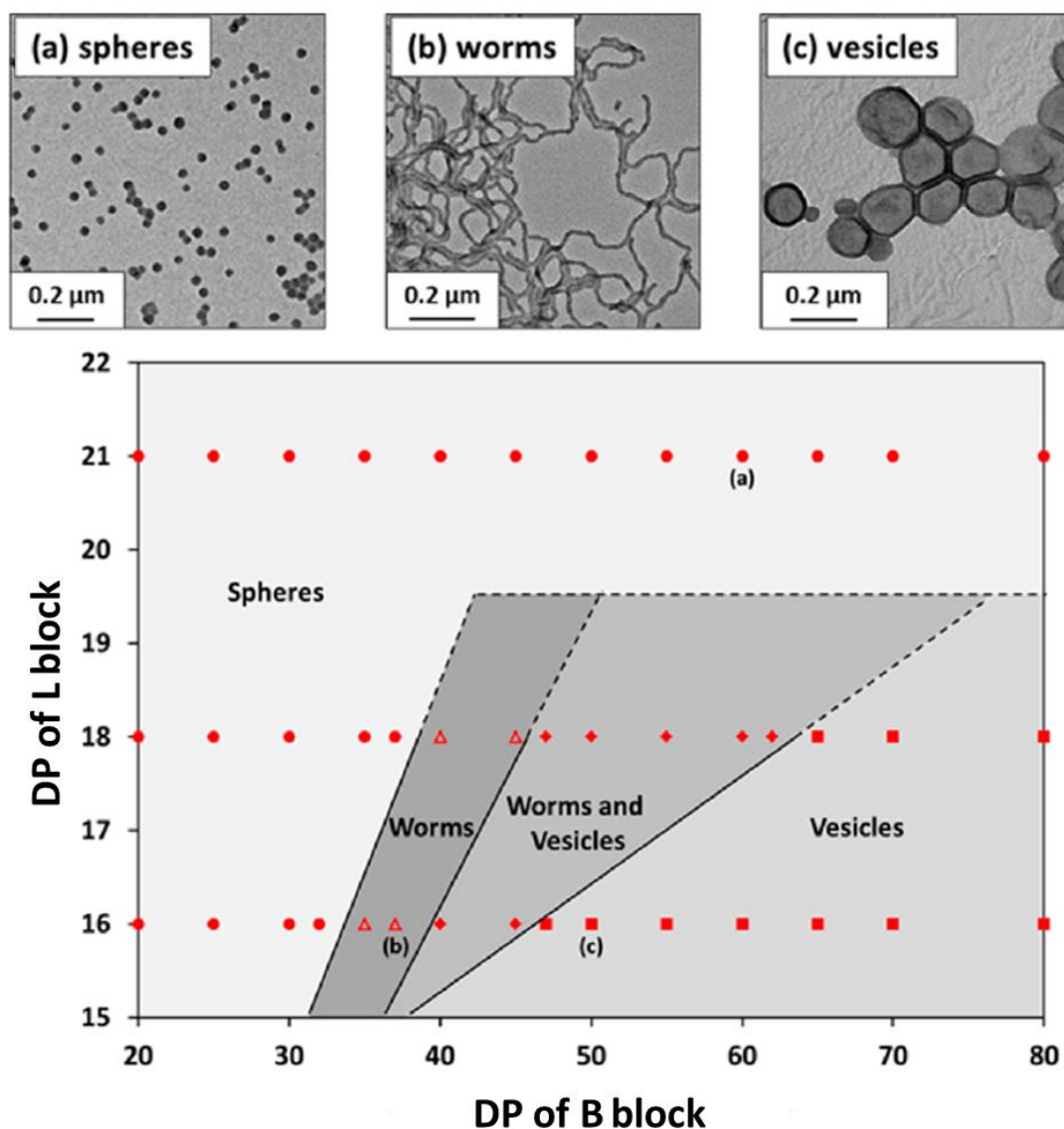
Figure 1.19. A detailed phase diagram constructed for poly(lauryl methacrylate)$_x$-poly(benzyl methacrylate)$_y$ (L$_x$-B$_y$) diblock copolymer nanoparticles prepared by RAFT dispersion polymerisation of benzyl methacrylate using AIBN initiator at 70 °C in *n*-dodecane at a total solids concentration of 20 % w/w. TEM images of the three pure morphologies (spheres, worms or vesicles) are indicated as (a), (b), and (c), respectively.[126] Note: dash line means predicted phase boundary.

PISA formulations conducted in non-polar solvents were further investigated by Derry et al[125,142] and Lopez-Oliva et al.[143] Notably, a range of poly(stearyl methacrylate)-poly(benzyl methacrylate) diblock copolymer nano-objects were prepared at 90 °C in mineral oil and the evolution of nanoparticle morphology was monitored using *in situ* small-angle X-ray scattering (SAXS).[125] This sophisticated technique confirmed the evolution of copolymer morphology from spheres to worms to vesicles during PISA.

1.8 PISA via RAFT Aqueous Emulsion Polymerisation

As discussed previously, traditional aqueous emulsion polymerisations via FRP involve a water-immiscible monomer, a water-soluble initiator, surfactant and water. Conversely, RAFT aqueous emulsion polymerisation utilise a water-soluble macro-CTA rather than surfactants, eliminating any requirement for the post-polymerisation removal of excess surfactant. This is potentially advantageous for industrial applications. However, RAFT emulsion polymerisation may suffer from side reactions[144] (e.g. undesired homogeneous nucleation when the reactivity of the macro-CTA or the concentration of the macro-CTA is too low). Under such conditions, the primary radicals rapidly react with hydrophobic monomer and the nascent polymer chains precipitate to form nuclei, leading to poor control over the RAFT polymerisation.[144]

Hawkett et al. pioneered the first *ab initio* RAFT emulsion polymerisation of *n*-butyl acrylate.[145-148] A hydrophilic poly(acrylic acid) was first prepared using a trithiocarbonate CTA. Then this PAA macro-CTA was chain-extended with *n*-butyl acrylate, resulting in self-assembly of poly(acrylic acid)-poly(*n*-butyl acrylate) chains to form micelles when the hydrophobic poly(*n*-butyl acrylate) block reaches its critical DP. Good living character (e.g. narrow MWDs) is maintained and the final latexes exhibited good colloidal stability due to the covalently-bonded hydrophilic poly(acrylic acid) stabiliser blocks. This protocol was also utilised to prepare ABC triblock copolymers by chain-extending with a second hydrophobic monomer (styrene), which forms the third block.[148]

More recently, Charleux and co-workers showed that RAFT emulsion polymerisation can be performed using a wide range of hydrophilic stabiliser blocks based on methacrylic acid,[149] PEO,[150,151] or acrylamide[152] and hydrophobic core-forming blocks based on methyl methacrylate[153] or benzyl methacrylate[154]. The first example of preparing higher order morphologies via RAFT aqueous emulsion polymerisation was also reported by the same research group.[155] A series of poly(acrylic acid-co-poly(ethylene oxide) methyl ether acrylate) macro-CTAs with varying acrylic acid/poly(ethylene oxide) methyl ether acrylate molar ratios were synthesised and subsequently chain-extended with hydrophobic monomer (styrene) under various conditions, including differing solution pH and salt concentration. Spheres, fibres and vesicles were successfully prepared under appropriate conditions.
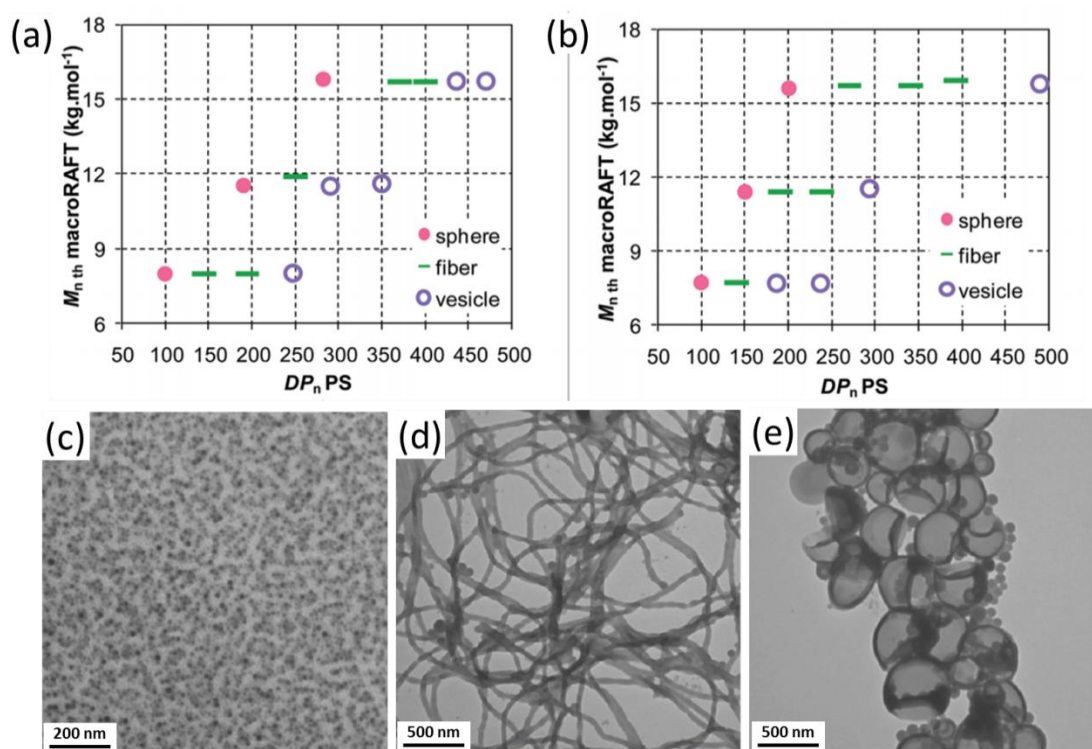
Figure 1.20. Phase diagrams constructed for poly(methacrylic acid-co-poly(ethylene oxide) methyl ether acrylate)-polystyrene block copolymer nano-objects prepared using two poly(methacrylic acid-co-poly(ethylene oxide) methyl ether acrylate) macro-CTAs (methacrylic acid/poly(ethylene oxide) methyl ether acrylate = 50/50 (a) and 67/33 (b) at pH 5). TEM images of block copolymer nano-objects, (c) spherical micelles, (d) nanofibers, (e) vesicles.[156]

More specifically, only spherical micelles of 20 to 80 nm diameter can be obtained when chain-extending pure poly(acrylic acid) macro-CTA or pure poly(methacrylic

acid) macro-CTA with styrene monomer. Nevertheless, higher order morphologies can be achieved by using a 50/50 poly(acrylic acid-co-poly(ethylene oxide) methyl ether acrylate) RAFT agent at acidic pH or in the presence of added salt (NaHCO$_3$).[155] Similarly, pure spheres, worms or vesicles can be targeted using all-methacrylic PISA formulation, as shown in **Figure 1.20**.[156] Spherical micelles, nanofibers or vesicles can be accessed for either 50/50 or 67/33 methacrylic acid/poly(ethylene oxide) methyl ether acrylate compositions, depending on the molar masses of the hydrophilic and hydrophobic blocks. It was found empirically that pH 5 enabled the formation of higher order morphologies while maintaining good control over the chain growth.[156]
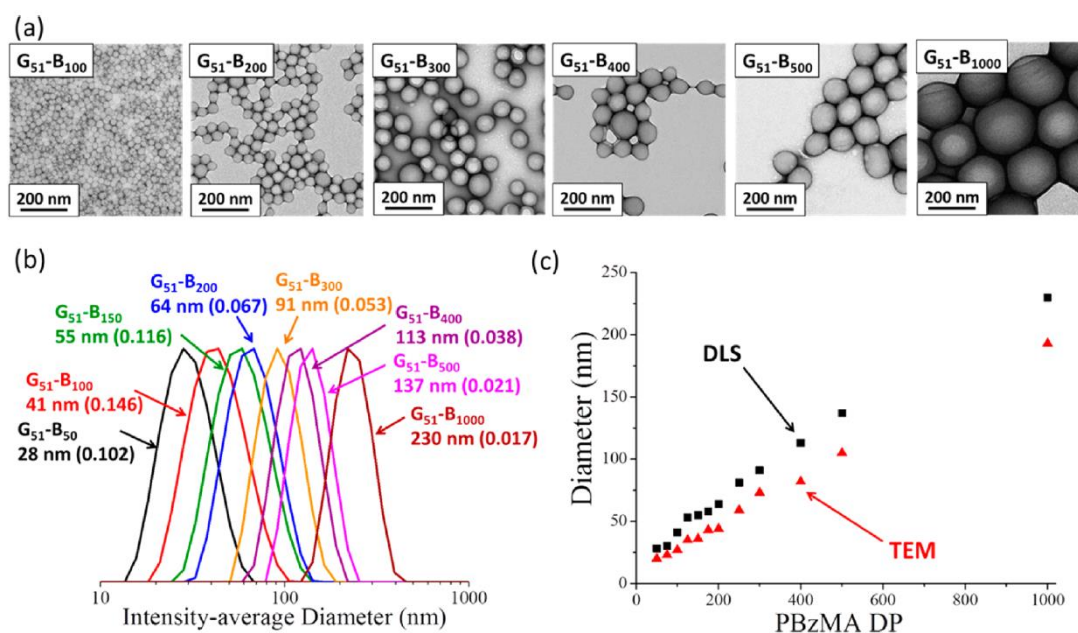
Figure 1.21. Poly(glycerol monomethacrylate)$_{51}$-poly(benzyl methacrylate)$_x$ (G$_{51}$-B$_x$) diblock copolymer nanoparticles prepared via RAFT aqueous emulsion polymerisation at 10% w/w solids (70 °C): (a) TEM images showing the increasing size of spherical nanoparticles with higher DP of the core-forming block; (b) corresponding DLS intensity-average size distributions; (c) comparison of mean particle diameters reported by DLS and TEM.[154]

Armes and co-workers reported the RAFT emulsion polymerisation of benzyl methacrylate using a non-ionic poly(glycerol monomethacrylate)$_{51}$ macro-CTA.[154] A series of G-B diblock copolymer spheres with diameters ranging from 20 to 200 nm were readily prepared in aqueous media (see **Figure 1.21**). Purely spherical nanoparticles were obtained even when targeting a very high DP for the poly(benzyl

methacrylate) block. Such diblock copolymer nanoparticles could be efficiently produced at high solids (up to 50% w/w) without sacrificing control over the RAFT polymerisation. Because of the *cis*-diol functionality on the poly(glycerol monomethacrylate)$_{51}$ stabiliser chains, these copolymer nanoparticles can bind reversibly with phenylboronic acid derivatives. Indeed, it was demonstrated that G_{51}-B_{100} nanoparticles are selectively adsorbed onto a micro-patterned planar surface functionalised with phenylboronic acid units by forming a cyclic boronate ester at pH 10.[154]

1.9 Occlusion of Nanoparticles within Inorganic Crystals

Block copolymer self-assembly can lead to nano-objects with various morphologies, as discussed above. Similarly, in inorganic chemistry, the self-assembly of atoms, ions or molecules results in crystals with well-defined polymorphs and morphologies. Moreover, the size of these crystals can be generated by controlling the relative rates of nucleation and growth. As a major stage of a crystallization process, crystal growth involves the addition of new atoms, ions, or polymer strings into the characteristic arrangement of a crystalline Bravais lattice. The growth typically follows an initial stage of either homogeneous or heterogeneous nucleation, unless a "seed" crystal was purposely added to start the growth. Although crystallisation is traditionally used as a means of purification,[24] certain "impurities" can be occluded within a crystal lattice under appropriate conditions, thus creating bicomponent hybrid materials.[24] Biominerals such as bones, teeth and seashells are naturally-occurring materials that are composed of brittle inorganic components and flexible macromolecules.[19-22] It is worth to point out that the organic macromolecule content within those biominerals is quite low. It is a challenge to locate their location within the crystal and systematically evaluate their occlusion mechanisms.[19-22]

1.9.1 Double-hydrophilic Block Copolymers as Crystal Modifiers

As one of the most abundant minerals on Earth, calcium carbonate ($CaCO_3$) exists in various polymorphs, including calcite, aragonite and vaterite. Calcite has a

rhombohedral crystal structure with space group $R\bar{3}c$, aragonite has an orthorhombic crystal structure with space group *Pmcn*, and vaterite is hexagonal with space group *P63*. Vaterite is a metastable form of calcium carbonate and believed to be a precursor for calcite and aragonite.[18,157-159]
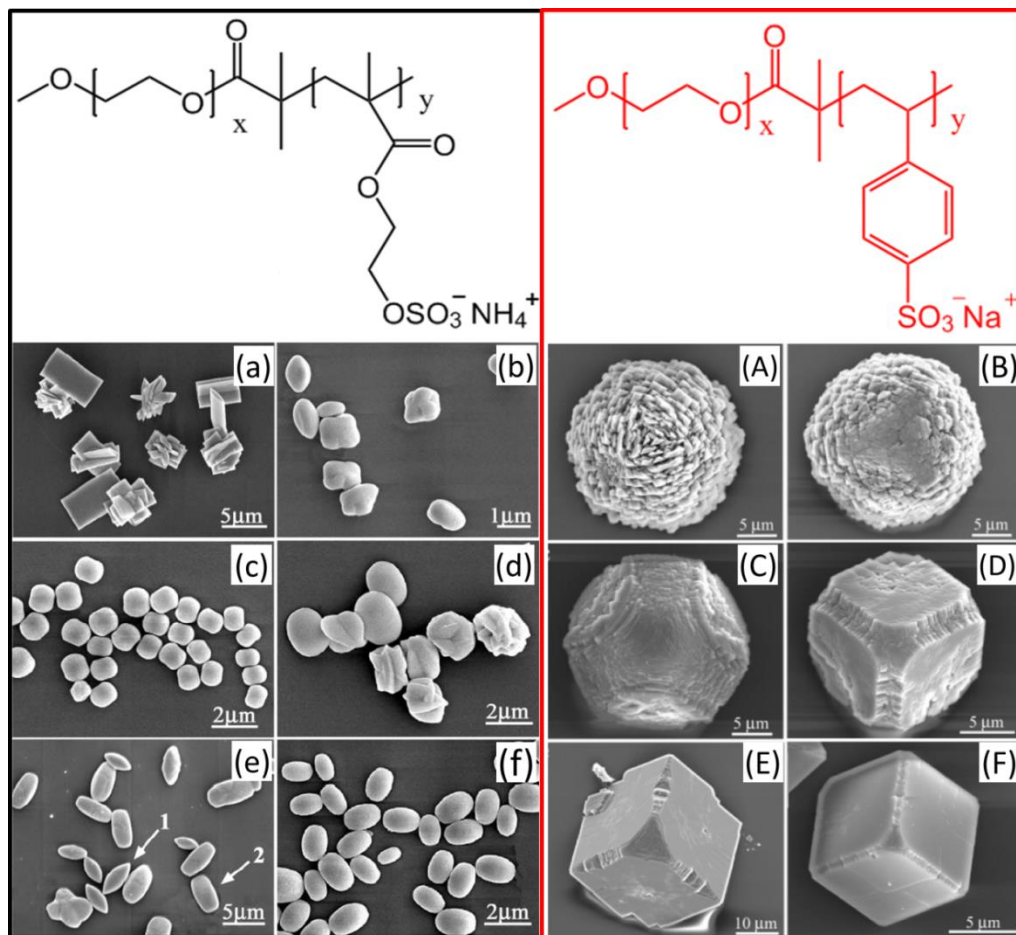
Figure 1.22. Chemical structure of poly(ethylene oxide)$_x$-poly(ammonium 2-sulfatoethyl methacrylate)$_y$ and poly(ethylene oxide)$_x$-poly(sodium 4-styrenesulfonate)$_y$. The left-hand black column shows SEM images of $BaSO_4$ particles precipitated under various conditions: (a) without any additive; (b) poly(ammonium 2-sulfatoethyl methacrylate) homopolymer at $[SO_4^{2+}]_{polymer}$: $[Ba^{2+}]$ = 1 : 1; (c) poly(ammonium 2-sulfatoethyl methacrylate) homopolymer at 2 : 1; (d) poly(ethylene oxide)$_{45}$-poly(ammonium 2-sulfatoethyl methacrylate)$_{11}$ at 1 : 10; (e) poly(ethylene oxide)$_{45}$-poly(ammonium 2-sulfatoethyl methacrylate)$_{42}$ at 2 : 1 and (f) poly(ethylene oxide)$_{113}$-poly(ammonium 2-sulfatoethyl methacrylate)$_{40}$ at 2 : 1. The angular and rounded particles are indicated as 1 and 2 respectively in (e). The right-hand red column depicts SEM images of $CaCO_3$ precipitated from a solution containing Ca^{2+} and poly(ethylene oxide)$_{22}$-poly(sodium 4-styrenesulfonate)$_{49}$ at a fixed $[Ca^{2+}]:[SO_3^-]_{polymer}$ molar ratio of 1.25:1 and Ca^{2+} concentrations of (A) 10, (B) 5, (C) 2.5, (D) 1, (E) 0.5, and (F) 0.1 mM. $[SO_4^{2+}]_{polymer}$ and $[SO_3^-]_{polymer}$ stand for the molar concentrations of polymerised sulfate and sulfonate groups, respectively.[2,160]

Crystallisation is generally sensitive to additives, especially those that can strongly interact with the growing crystal.[18] The groups of Cölfen and Qi have utilised poly(ethylene oxide)-based block copolymers as crystallisation modifiers to investigate their effect on the crystallisation behaviour of calcium carbonate,[161-163] barium sulfate,[164] barium tungstate[165] and calcium oxalate dehydrate.[166]

An effective additive can modify the crystallisation behaviour, crystal morphology, and crystal size, etc. For example, Robinson and co-workers reported that poly(ethylene oxide)-poly(ammonium 2-sulfatoethyl methacrylate) diblock copolymers can effectively change the crystallisation habit for the *in situ* precipitation of $BaSO_4$ particles (see **Figure 1.22**).[160] Depending on the relative block DPs, near-monodisperse $BaSO_4$ particles with a "lozenge" morphology could be prepared in aqueous solution. Systematic studies suggested that only the highly anionic poly(ammonium 2-sulfatoethyl methacrylate) block, which contains multiple sulfate groups, can directly interact with the growing $BaSO_4$ crystals. However, the poly(ethylene oxide) block also plays a vital role in controlling the crystal growth by acting as a steric stabiliser, as evidenced by independent variation of the poly(ethylene oxide) and poly(ammonium 2-sulfatoethyl methacrylate) block DPs. The morphology, particle size distribution and crystalline structure of the inorganic phase are all sensitive to these two parameters.

In 2007 Kulak and co-workers examined double-hydrophilic diblock copolymers, poly(ethylene oxide)$_x$-poly(sodium 4-styrenesulfonate)$_y$, as additives during the in situ crystallisation of calcium carbonate particles.[2] The formation of single crystals, mesocrystals, and polycrystalline aggregates were observed in the presence of this diblock copolymer (see **Figure 1.22**). This work strongly suggests a unifying model of copolymer-directed crystallisation, demonstrating experimentally for the first time that a continuous transition in particle structures and crystallisation mechanisms occurs between polycrystalline aggregates, mesocrystals and single crystals.[2]

1.9.2 Occlusion of 3D Hydrogels within Crystals

Given the small size and radiation sensitivity of occluded organic molecules and the lack of well-developed methods for preparing electron-transparent samples from

micron-sized specimens that are required for high resolution imaging, it is a formidable technical challenge to study the internal structure of these organic/inorganic hybrid materials at atomic resolution and in 3 dimensions using traditional electron microscopy and X-ray diffraction.[167] Taking advantage of advances in focused ion beam (FIB), annular dark-field scanning TEM (ADF-STEM) and annular dark-field electron tomography for three-dimensional imaging, Estroff and co-workers have visualised the internal structure of calcite crystals incorporated with agarose hydrogel, which is a linear polysaccharide consisting of alternating 1,3-linked *β-D*-galactopyranose and 1,4-linked 3,6-anhydro-*α-L*-galactopyranose (see **Figure 1.23**).[168] An inter-connected network of darker fibres (average diameter of 13 ± 5 nm) within a brighter matrix can be observed by low-angle ADF-STEM (LAADF-STEM) images of a thin section of gel-grown calcite (**Figure 1.23c**).

These fibrous structures are assigned to be the agarose fibers owing to the difference in the elastic scattering cross-section of the two materials. The lower mean atomic number (Z) of the organic polymer compared with that of the calcite results in the observed difference in electron-contrast between the two materials. Meanwhile, tomographic reconstruction generated from a tilt series of high-angle ADF-STEM images indicates that the incorporated polymer formed a 3D random network throughout the section of the calcite crystal (see **Figures 1.23e and 1.23f**).

This protocol was further extended to incorporate gold nanoparticles (AuNPs) and Fe_3O_4 nanoparticles into calcite crystal.[169] Briefly, the pre-made AuNPs and/or Fe_3O_4 nanoparticles were dispersed in agarose hydrogel, followed by crystallisation of calcite via ammonium carbonate diffusion method. These nanoparticles were successfully incorporated into (rather than expelled from) the calcite because they were physically trapped within the gel. Notably, the resulting composite crystals were infused with colour (ascribed to the AuNPs) and/or superparamagnetism (due to the magnetic Fe_3O_4 nanoparticles) and the crystalline lattice of the host calcite was not substantially disrupted.[169]
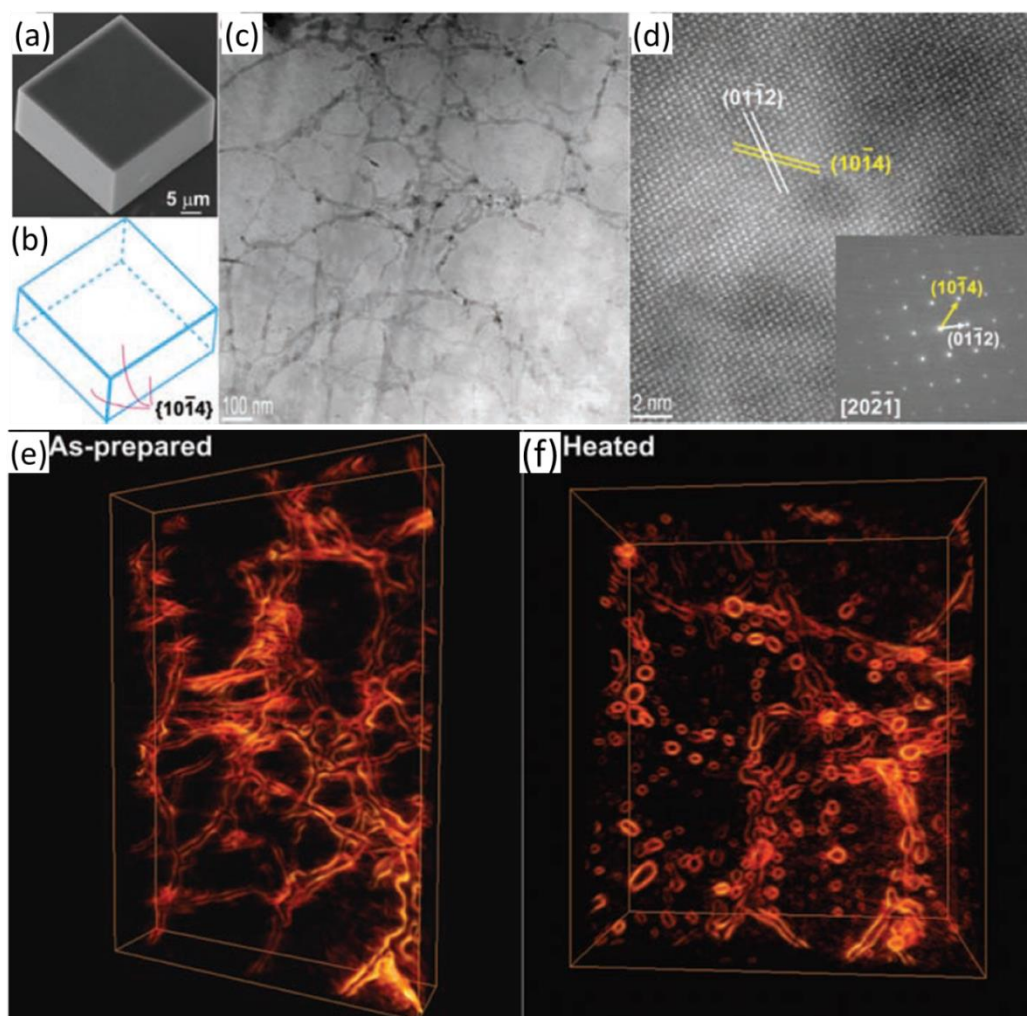
Figure 1.23. (a) An SEM image of a gel-grown calcite crystal. (b) A model of a calcite crystal expressed by six $\{10\bar{1}4\}$ faces. (c) A low-angle annular dark field-scanning transmission electron microscopy (LAADF-STEM) image of a thin section cut from a gel-grown calcite crystal by means of FIB. (d) A LAADF-STEM lattice image viewed down the $[20\bar{2}\bar{1}]$ zone axis of calcite. (Inset) a selected area electron diffraction (SAED) pattern of the cut section. The examined area (diameter of 800 nm) contains both crystal and fibers. Tomographic reconstructions of (e) an agarose network inside a section of as-prepared crystal and (f) cavities inside a section of annealed crystal.[168]

1.9.3 Occlusion of Polymeric Nanoparticle within Crystals

Compared to the occlusion of water-soluble block copolymers, occluding a 3D hydrogel[168] (as well as nanoparticles entrapped within a 3D hydrogel[169]) within crystals represents significant scientific progress. However, direct incorporation of polymeric nanoparticles into crystals is challenging. It is an interesting research topic,

because polymeric nanoparticles differ from the above-mentioned water-soluble block copolymers in their mode of interaction with growing crystals. Water-soluble polymers can either bind or physically interact with the growing crystals. However, sterically-stabilised copolymer nanoparticles have far fewer degrees of freedom. Nevertheless, it is much easier to examine the localisation of occluded nanoparticles within crystals because they are large enough to be readily detected using electron microscopy.

In 2005 Qi and co-workers used monodisperse polystyrene latex particles with carboxylate surface functionality prepared by traditional radical polymerisation as effective colloidal templates for the controlled crystallisation of calcium carbonate (or Cu_2O) in aqueous solution.[170] Unfortunately, such particles are only occluded within the surface layer of the crystal, as shown **Figures 1.24a~1.24c**. This surface occlusion was also observed by Hanisch et al.,[121] who demonstrated that not only block copolymer spheres, but also worms and vesicles decorated with surface phosphate groups can be incorporated into the surface layer of calcite crystals.

Meldrum and co-workers have used commercially available polystyrene nanoparticles with a high surface density of carboxylate groups as crystallisation additives and successfully incorporated these latexes into calcite single crystals.[1] This was the first example of polymeric nanoparticles are homogeneously incorporated into calcite single crystals. As shown in **Figures 1.24d** and **1.24e**, the internal structure of the composite crystals confirmed that quite efficient occlusion of these latex particles could be achieved. Cross-sections prepared using FIB enabled clear visualisation of the location of individual particles, revealing a uniform distribution throughout the crystal. Image analysis suggested that the particles were incorporated at up to approximately 20 % v/v, while thermogravimetric analysis (TGA) indicated a loading of ~9 % w/w. However, only polystyrene latexes with a high content of surface carboxylic acid groups can be uniformly occluded within calcite. As it is very difficult to precisely control the surface chemistry via conventional polymerisation, correlation of the surface density of such acid groups with occlusion efficiency is rather problematic.
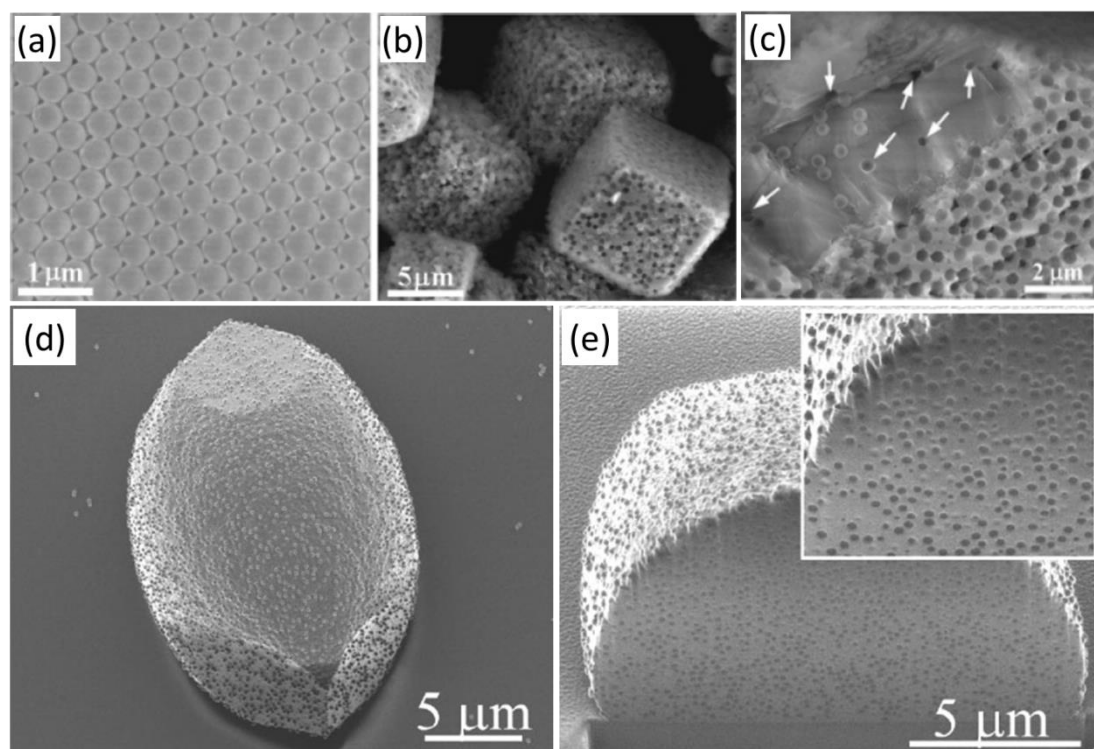
Figure 1.24. SEM images of polystyrene latex particles and corresponding latex particle-CaCO$_3$ composites. (a) latex particles with a particle size of approximately 380 nm; (b) as-prepared latex particle-CaCO$_3$ composite; (c) internal structure of latex particle-CaCO$_3$ composite, showing that latex particles were only occluded within the surface layer of CaCO$_3$;[170] (d) calcite incorporated with polystyrene particles functionalised with surface carboxylate groups (with mean latex diameters of 220-250 nm); (e) a cross-section created by FIB, showing a high density of particles uniformly distributed throughout the crystal.[1] The arrows in (c) indicate inner pores templated by the latex particles incorporated inside the composite particles.

To more precisely control the surface functionality, ATRP was utilised to design a precursor diblock copolymer: poly(2-hydroxypropyl methacrylate)-poly(2-(diisopropylamino)ethyl methacrylate) (H-P). This copolymer was then reacted with succinic anhydride, converting the 2-hydroxypropyl methacrylate residues into carboxylic acid groups via esterification (see chemical structure shown in **Figure 1.25a**). As a zwitterionic diblock copolymer, it forms a poly(2-(diisopropylamino)ethyl methacrylate)-core micelles with coronal chains containing carboxylate group in basic aqueous solution.[7] These anionic copolymer micelles were therefore co-precipitated with calcium carbonate. Using X-ray diffraction and infrared spectroscopy, these occluded micelles led to an increase in the level of

atomic disorder at the inorganic-organic interface and a compressive-strain gradient within the calcite lattice. Examination of cross-sections of crystals revealed occlusion of the copolymer micelles via both FE-SEM and TEM. The micelles undergo a change in shape during their incorporation within the crystal lattice (**Figure 1.25d**). The mechanism for this change in morphology was further studied in detail by Cho et al.,[5] who used *in situ* atomic force microscopy (AFM) to monitor the nanoparticle occlusion process.
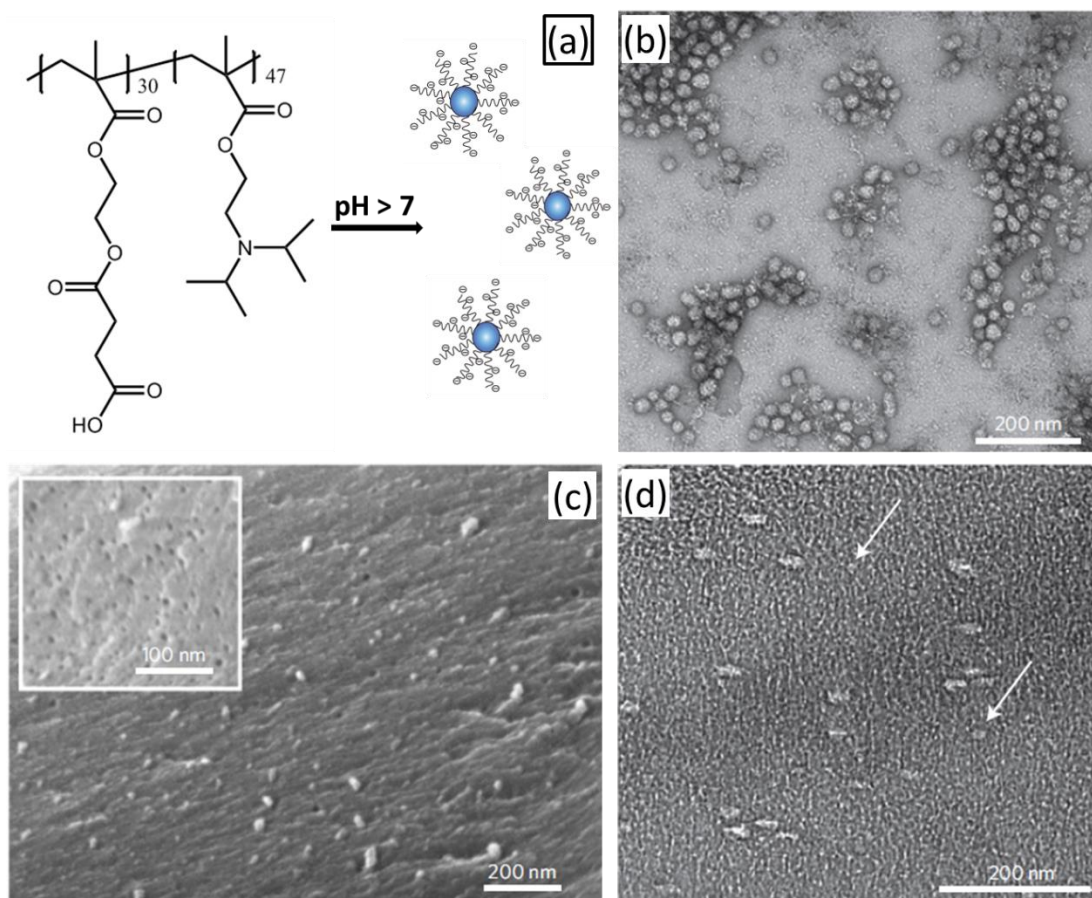
Figure 1.25. (a) Chemical structure and schematic cartoon of the block copolymer; (b) TEM image of the micelles at pH > 7; (c) cross-section through a fractured crystal revealing occluded copolymer micelles as voids and elongated particles; (d) a thin section cut through the nanocomposite crystal, showing the occluded copolymer micelles. This low-magnification image shows that the copolymer particles undergo a change in shape during occlusion, and examples of particles cut to give a smaller cross-section are arrowed.[7]

ATRP is a versatile method to prepare well-defined block copolymers. However, it is not as convenient as RAFT polymerisation particularly in the context of PISA.

Semsarilar et al has shown that poly(methyl methacrylate)-poly(benzyl methacrylate) nanoparticles can be readily synthesised in ethanol by RAFT dispersion polymerisation.[6,36] A range of morphologies, including spheres, worms, and vesicles, can be achieved by simply varying the DP of the core-forming block. These nano-objects are highly anionic above pH 7 after transferring from ethanol to water via dialysis, because the ionised steric stabiliser.[36] Remarkably, the vesicle nano-objects can be uniformly occluded within calcite at loading of up to ~20 % w/w.[6]

Occlusion of such a high level of organic nanoparticles within calcite single crystals provides a unique opportunity for conducting a comprehensive, multiscale investigation of the structure and properties of the resulting nanocomposite materials. The mechanical properties of the nanocomposite crystals were investigated using nanoindentation, which revealed that this artificial biomineral exhibited analogous texture and defect structures to biogenic calcite crystals and was harder than pure calcite of geological origin (see **Figure 1.26**).[1,6,7]
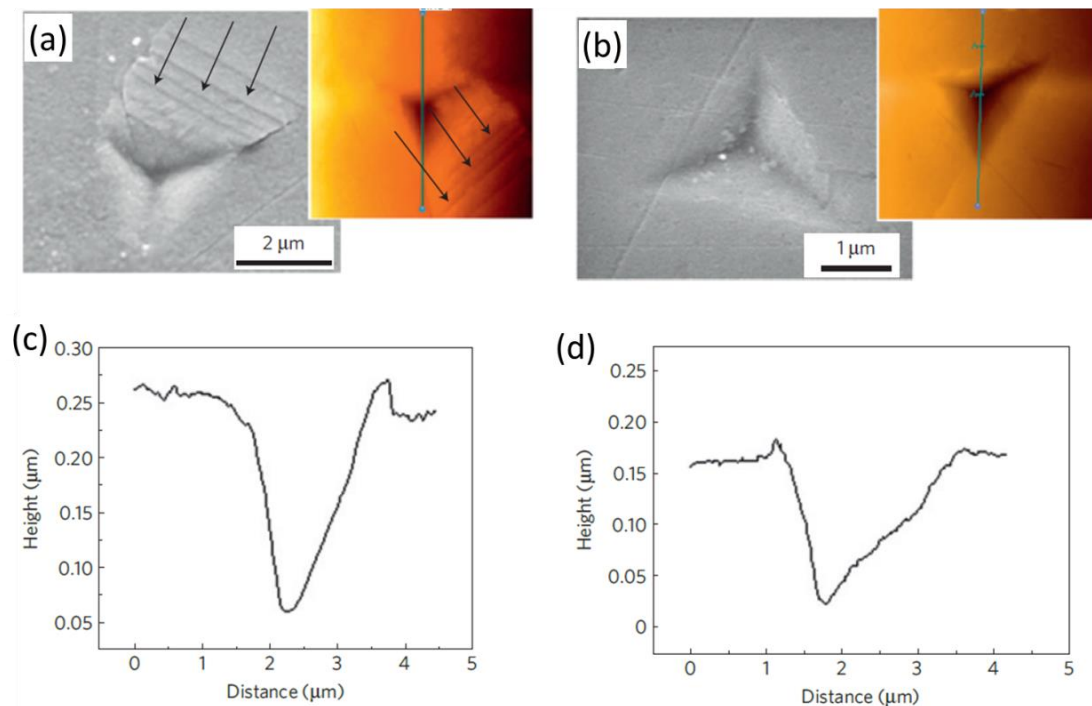
Figure 1.26. SEM and AFM images obtained for pure calcite (a) and nanocomposite crystals (b); AFM profiles of nano-indentation marks on a calcite control crystal (c) and a nanocomposite crystal after nanoindentation (d). Step formation around the indent in pure calcite was observed, as indicated by the arrows. However, this was not observed for the nanocomposite crystal.[7]

As a well-known II–VI compound semiconductor, ZnO has three common crystal structures: rocksalt, zinc blende and wurtzite.[13] Wurtzite ZnO is thermodynamically stable under ambient conditions while zinc blende ZnO is less stable unless grown on cubic substrates.[13] The rocksalt form of ZnO has been reported to be metastable at atmospheric pressure and can be obtained via transformation from wurtzite under high pressure.[15] In wurtzite ZnO structure, each O^{2-} anion is surrounded by four Zn^{2+} cations at the corners of a tetrahedron, and vice versa. ZnO is a promising material for semiconductor device application because it has a direct and wide band gap and a large free-exciton binding energy hence excitonic emission processes persists at or even above room temperature.[171,172]

Wegner and co-workers systematically investigated surface-functionalised latex particles as occlusion additives for the mineralisation of ZnO in aqueous solution.[173-175] Polystyrene latexes with varying hydrophilic functional groups, including acrylic acid, maleic acid, and ethylene glycol methacrylate phosphate, were prepared by miniemulsion polymerisation. Latex with acrylic acid surface functionality was studied in particular detail. The effect of the chemical nature of the surface functionalisation and the latex concentration on the crystal growth, morphology, and crystalline structure of the resulting zinc oxide particles were analysed.

Using zinc nitrate hexahydrate as a soluble precursor and hexamethylenetetramine as a pH buffer, control ZnO particles with a hexagonal prismatic rod morphology were typically obtained. It was further shown that acrylic acid functionalised polystyrene latexes were incorporated into ZnO, giving a rod-like but hollow surface structure based on electron microscopy analysis (**Figure1.27b**). ZnO is sensitive to latexes functionalised with maleic acid or ethylene glycol methacrylate phosphate, as can be seen from **Figures 1.27c** and **1.27d**. The extent of occlusion of acrylic acid-functionalised polystyrene latex within the ZnO host crystals could be up to ~10 % w/w when using a relatively high initial latex concentration (such as 9 g L^{-1}).
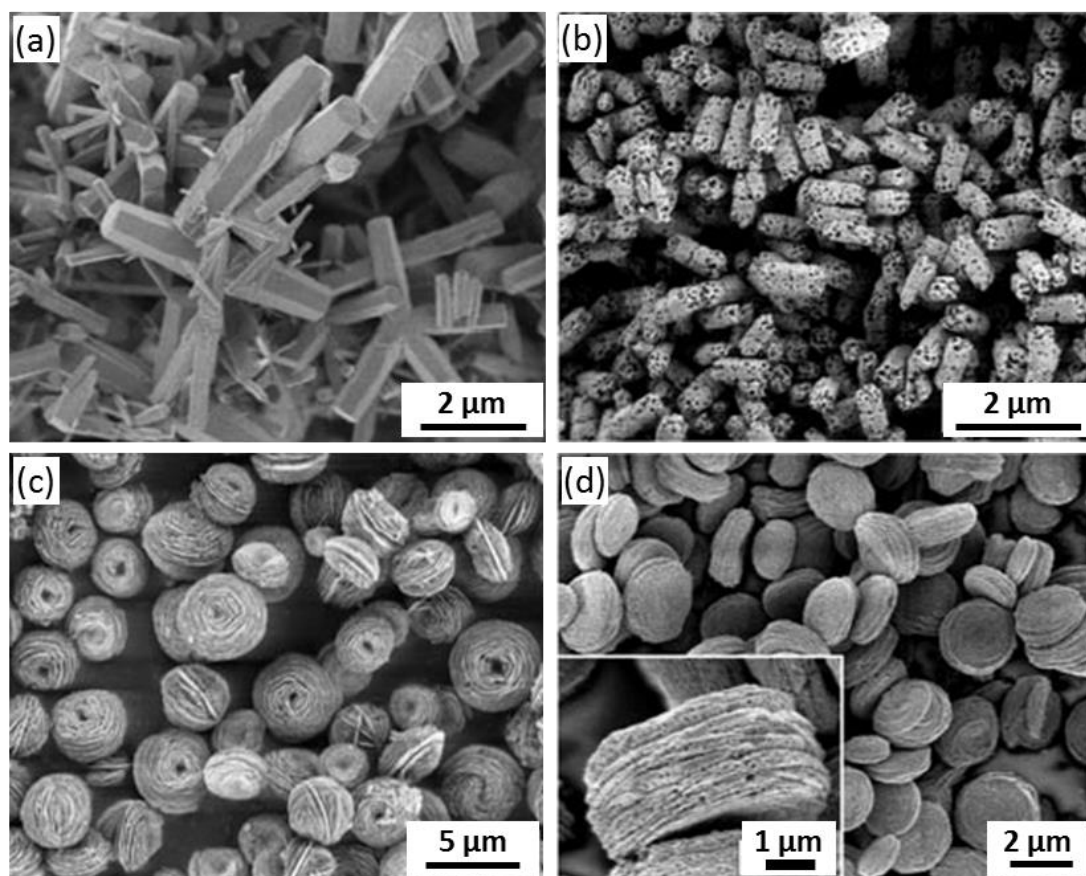
Figure 1.27. Zinc oxide samples crystallised (a) without additive; (b) 6 g L^{-1} polystyrene latex surface-functionalised with acrylic acid; (c) 6 g L^{-1} polystyrene latex surface-functionalised with maleic acid; (d) 6 g L^{-1} polystyrene latex surface-functionalised with ethylene glycol methacrylate phosphate.[173]

1.9.4 Occlusion of Copolymer-Modified Inorganic Nanoparticles within Crystals

Obviously, it is the nanoparticle surface functionality that promotes interaction with the growing crystal and hence dictates the extent of occlusion. Thus, in principle any nanoparticles with appropriate surface functionality should be incorporated into crystals under appropriate conditions.

As presented in **Figure 1.28**, a novel double-hydrophilic diblock copolymer, poly(methacrylic acid)-poly(sodium 4-styrenesulfonate), was synthesised using RAFT solution polymerisation and thereafter magnetite nanoparticles (MNP) were precipitated in the presence of this anionic copolymer. The weakly acidic poly(methacrylic acid) is believed to adsorb onto the surface of the MNPs as an

anchor block, while the poly(sodium 4-styrenesulfonate) block acts as the anionic stabiliser block.
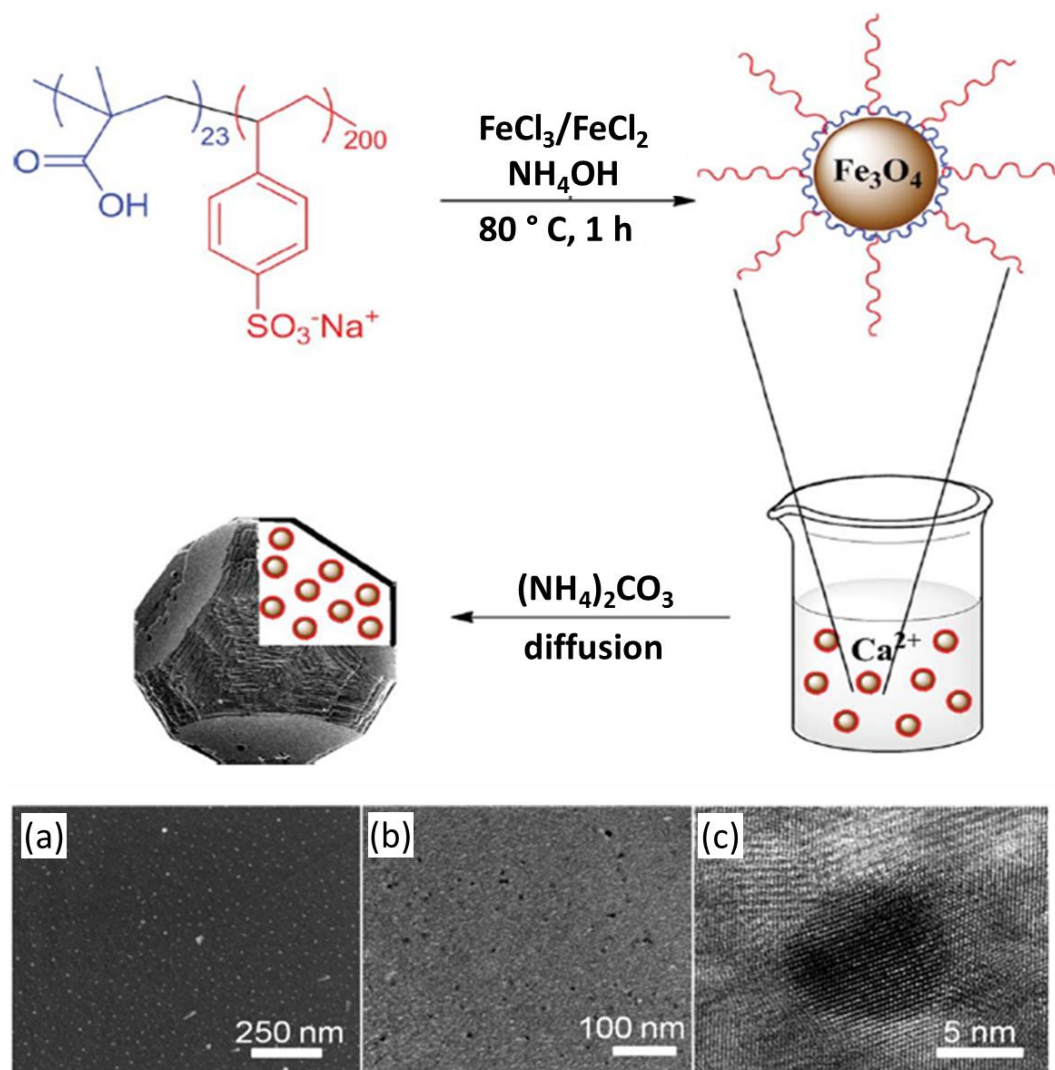
Figure 1.28. Schematic representation of the synthesis of magnetite nanoparticles surface-modified using a poly(methacrylic acid)-poly(sodium 4-styrenesulfonate) diblock copolymer, and their occlusion within calcite single crystals. (a) SEM image of the cross-section through a calcite single crystal prepared in the presence of copolymer-modified MNPs. (b) TEM image of a thin section through the nanocomposite crystal, and (c) a high resolution TEM image showing the continuity of the crystal lattice around an isolated occluded magnetite particle.[2]

Spatial distribution of the MNPs throughout the calcite crystals was confirmed by electron microscopy analysis. In **Figure 1.28a**, the FE-SEM image shows a cross-section of a fractured crystal, indicating a uniform distribution of copolymer-modified MNPs throughout the host matrix. Moreover, this uniform distribution was

further evidenced by TEM images shown in **Figures 1.28b** and **1.28c**. Similarly, AuNPs stabilised using suitable copolymer can also be occluded within calcite. However, in this latter case the Au loading is relatively low (about 3 % w/w).[3]

Compared to the incorporation of biomacromolecules into crystals, efficient occlusion of nanoparticles within crystal produces a unique 'artificial biomineral', in which nanoparticles act as "pseudo-proteins".[1,2,5-7] High level of occlusion facilitates comprehensive studies of the influence of additives on the structure and properties of the resulting nanocomposite crystals. However, the occlusion mechanism is clearly complex and depends on many factors, including the wetting of the crystal face by the nanoparticles, the mean size of the nanoparticles, and the rate of crystallisation.[1] Thus, progress in incorporating nanoparticles into inorganic cyrtals to date has mainly relied on empirical trial-and-error experiments and a robust set of design rules for efficient occlusion has not yet been established.

1.10 Project Motivation

RAFT polymerisation is now a well-established method for the synthesis of a range of functional block copolymers.[66-68] Moreover, RAFT-mediated PISA enables the facile synthesis of a wide range of bespoke organic diblock copolymer nano-objects of controllable size, morphology and surface functionality.[26-28] Although the incorporation of *soluble* (macro)molecules within inorganic crystals has been intensively studied, the occlusion of polymeric *nanoparticles* within such host matrices is still an emerging research area.[1-3,5-7]

We aim to test a number of hypotheses regarding nanoparticle occlusion within inorganic crystals in the present Thesis.

(1) According to the literature, carboxylic acid functionality seems to be crucial for efficient nanoparticle occlusion within calcite. In this context, we will examine whether there is any difference between anionic carboxylate groups and carboxylate groups that are present in the form of zwitterionic carboxybetaines.

(2) We wish to harness the advantages of RAFT polymerisation to precisely tailor copolymer structures and/or compositions, and hence identify the key parameters that dictate nanoparticle occlusion within host crystals. In particular, the effect of varying the surface stabiliser density on nanoparticle occlusion will be studied for the first time.

(3) One intriguing question is whether the selection of appropriate anionic stabiliser chains can promote greater nanoparticle occlusion within certain host crystals. For example, a relatively modest level of occlusion has been previously reported for carboxylated latexes within ZnO. Are there more effective anionic stabilisers that are more colloidally stable under the *in situ* crystallisation conditions that could promote higher levels of occlusion?

(4) In principle, any inorganic nanoparticles with the appropriate surface chemistry can be occluded into any given crystal. We seek to extend the concept of nanoparticle occlusion to include other functional materials, such as plasmonic gold nanoparticles as guests and semiconductor ZnO crystals as a host. This should open up a generic route to a diverse range of inorganic-inorganic nanocomposite materials.

1.11 Thesis Outline

In Chapter 2, two types of diblock copolymer nanoparticles are synthesised via RAFT aqueous dispersion polymerisation of 2-hydroxypropyl methacrylate using either poly(carboxybetaine methacrylate) or poly(proline methacrylate) as the steric stabiliser block. Both these stabilisers contain carboxylic acid groups, but poly(proline methacrylate) is anionic above pH 9.2, whereas poly(carboxybetaine methacrylate) has zwitterionic character at this pH. The following occlusion experiments indicate that apparently minor structural differences can lead to profoundly different occlusion outcomes.

Chapter 3 describes the synthesis of poly(ammonium 2-sulfatoethyl methacrylate)-poly(benzyl methacrylate) diblock copolymer nanoparticles with either high or low stabiliser surface densities using either RAFT dispersion polymerisation in a 2:1 v/v ethanol/water mixture or RAFT aqueous emulsion polymerisation, respectively. These model nanoparticles are then used to gain new insight into a key topic in materials chemistry - the occlusion of organic additives into inorganic crystals. Substantial differences are observed for the extent of occlusion of these two types of anionic nanoparticles into calcite ($CaCO_3$). This is rationalised in terms of differing stabiliser surface densities.

Chapter 4 presents the synthesis of poly(ammonium 2-sulfatoethyl methacrylate)-poly(benzyl methacrylate) diblock copolymer nanoparticles via RAFT emulsion polymerisation and the as-prepared nanoparticles were directly used as nanoparticle additives for the growth of wurtzite ZnO crystals.

Finally, instead of incorporating copolymer nanoparticles into inorganic crystals, Chapter 5 shows that the occlusion of surface-modified AuNPs within ZnO crystals using poly(glycerol monomethacrylate) as a steric stabiliser. Evidence is presented for the complexation of Zn^{2+} by the *cis*-diol groups on this non-ionic water-soluble polymer. Depending on the synthesis protocol, the G_{70}-AuNPs can be uniformly distributed throughout the ZnO host crystal, solely located within a central region, or confined to a surface layer. XPS studies indicate an intimate interaction between the G_{70}-AuNPs and the host ZnO crystals, which leads to enhanced photocatalytic performance.

1.12 References

(1) Kim, Y.-Y.; Ribeiro, L.; Maillot, F.; Ward, O.; Eichhorn, S. J.; Meldrum, F. C. Bio-Inspired Synthesis and Mechanical Properties of Calcite-Polymer Particle Composites. *Advanced Materials* **2010**, *22*, 2082-2086.

(2) Kulak, A. N.; Semsarilar, M.; Kim, Y.-Y.; Ihli, J.; Fielding, L. A.; Cespedes, O.; Armes, S. P.; Meldrum, F. C. One-pot synthesis of an inorganic heterostructure: uniform occlusion of magnetite nanoparticles within calcite single crystals. *Chemical Science* **2014**, *5*, 738-743.

(3) Kulak, A. N.; Yang, P.; Kim, Y.-Y.; Armes, S. P.; Meldrum, F. C. Colouring crystals with inorganic nanoparticles. *Chemical Communications* **2014**, *50*, 67-69.

(4) Kulak, A. N.; Grimes, R.; Kim, Y.-Y.; Semsarilar, M.; Anduix-Canto, C.; Cespedes, O.; Armes, S. P.; Meldrum, F. C. Polymer-Directed Assembly of Single Crystal Zinc Oxide/Magnetite Nanocomposites under Atmospheric and Hydrothermal Conditions. *Chemistry of Materials* **2016**, *28*, 7528-7536.

(5) Cho, K.-R. K., Y.-Y.; Yang, P.; Cai, W.; Pan, H.; Kulak, A. N.; Lau, J. L.; Kulshreshtha, P.; Armes, S. P.; Meldrum, F. C.; De Yoreo, J. J. Direct observation of mineral-organic composite formation reveals occlusion mechanism. *Nature Communications* **2016**, *7*, 10187.

(6) Kim, Y.-Y.; Semsarilar, M.; Carloni, J. D.; Cho, K. R.; Kulak, A. N.; Polishchuk, I.; Hendley, C. T.; Smeets, P. J. M.; Fielding, L. A.; Pokroy, B.; Tang, C. C.; Estroff, L. A.; Baker, S. P.; Armes, S. P.; Meldrum, F. C. Structure and Properties of Nanocomposites Formed by the Occlusion of Block Copolymer Worms and Vesicles Within Calcite Crystals. *Advanced Functional Materials* **2016**, *26*, 1382-1392.

(7) Kim, Y.-Y.; Ganesan, K.; Yang, P.; Kulak, A. N.; Borukhin, S.; Pechook, S.; Ribeiro, L.; Kroeger, R.; Eichhorn, S. J.; Armes, S. P.; Pokroy, B.; Meldrum, F. C. An artificial biomineral formed by incorporation of copolymer micelles in calcite crystals. *Nature Materials* **2011**, *10*, 890-896.

(8) Jiang, R.; Li, B.; Fang, C.; Wang, J. Metal/Semiconductor Hybrid Nanostructures for Plasmon-Enhanced Applications. *Advanced Materials* **2014**, *26*, 5274-5309.

(9) Kochuveedu, S. T.; Jang, Y. H.; Kim, D. H. A study on the mechanism for the interaction of light with noble metal-metal oxide semiconductor nanostructures for various photophysical applications. *Chemical Society Reviews* **2013**, *42*, 8467-8493.

(10) Tjong, S. C. Novel nanoparticle-reinforced metal matrix composites with enhanced mechanical properties. *Advanced Engineering Materials* **2007**, *9*, 639-652.

(11) Wang, Z. L. Zinc oxide nanostructures: growth, properties and applications. *Journal of Physics: Condensed Matter* **2004**, *16*, 829-858.

(12) Liu, D.; Kelly, T. L. Perovskite solar cells with a planar heterojunction structure prepared using room-temperature solution processing techniques. *Nature Photonics* **2014**, *8*, 133-138.

(13) Guo, Y. G.; Hu, J. S.; Wan, L. J. Nanostructured materials for electrochemical energy conversion and storage devices. *Advanced Materials* **2008**, *20*, 2878-2887.

(14) Janotti, A.; Van de Walle, C. G. Fundamentals of zinc oxide as a semiconductor. *Reports on Progress in Physics* **2009**, *72*, 126501.

(15) Hochbaum, A. I.; Yang, P. Semiconductor nanowires for energy conversion. *Chemical Reviews* **2009**, *110*, 527-546.

(16) Hoffmann, M. R.; Martin, S. T.; Choi, W.; Bahnemann, D. W. Environmental applications of semiconductor photocatalysis. *Chemical Reviews* **1995**, *95*, 69-96.

(17) Fine, G. F.; Cavanagh, L. M.; Afonja, A.; Binions, R. Metal oxide semi-conductor gas sensors in environmental monitoring. *Sensors* **2010**, *10*, 5469-5502.

(18) Meldrum, F. C.; Cölfen, H. Controlling Mineral Morphologies and Structures in Biological and Synthetic Systems. *Chemical Reviews* **2008**, *108*, 4332-4432.

(19) Belcher, A. M.; Wu, X. H.; Christensen, R. J.; Hansma, P. K.; Stucky, G. D.; Morse, D. E. Control of crystal phase switching and orientation by soluble mollusc-shell proteins. *Nature* **1996**, *381*, 56-58.

(20) Berman, A.; Hanson, J.; Leiserowitz, L.; Koetzle, T. F.; Weiner, S.; Addadi, L. Biological control of crystal texture: a widespread strategy for adapting crystal properties to function. *Science* **1993**, *259*, 776-779.

(21) Mann, S. *Biomineralization, Principles and Concepts in Bioinorganic Materials Chemistry;* Oxford University Press: Oxford, **2001**.

(22) Lowenstam, H. A.; Weiner, S. *On biomineralization*; Oxford University Press: New York, **1989**.

(23) Kim, Y.-Y.; Carloni, J. D.; Demarchi, B.; Sparks, D.; Reid, D. G.; Kunitake, M. E.; Tang, C. C.; Duer, M. J.; Freeman, C. L.; Pokroy, B. Tuning hardness in calcite by incorporation of amino acids. *Nature Materials* **2016**, *15*, 903-910.

(24) Kahr, B.; Gurney, R. W. Dyeing crystals. *Chemical Reviews* **2001**, *101*, 893-951.

(25) Blanazs, A.; Armes, S. P.; Ryan, A. J. Self-Assembled Block Copolymer Aggregates: From Micelles to Vesicles and their Biological Applications. *Macromolecular Rapid Communications* **2009**, *30*, 267-277.

(26) Warren, N. J.; Armes, S. P. Polymerization-Induced Self-Assembly of Block Copolymer Nano-objects via RAFT Aqueous Dispersion Polymerization. *Journal of the American Chemical Society* **2014**, *136*, 10174-10185.

(27) Canning, S. L.; Smith, G. N.; Armes, S. P. A Critical Appraisal of RAFT-Mediated Polymerization-Induced Self-Assembly. *Macromolecules* **2016**, *49*, 1985-2001.

(28) Derry, M. J.; Fielding, L. A.; Armes, S. P. Polymerization-induced self-assembly of block copolymer nanoparticles via RAFT non-aqueous dispersion polymerization. *Progress in Polymer Science* **2016**, *52*, 1-18.

(29) Sun, J.-T.; Hong, C.-Y.; Pan, C.-Y. Recent advances in RAFT dispersion polymerization for preparation of block copolymer aggregates. *Polymer Chemistry* **2013**, *4*, 873-881.

(30) Cunningham, M. F. Controlled/living radical polymerization in aqueous dispersed systems. *Progress in Polymer Science* **2008**, *33*, 365-398.

(31) Li, Y.; Armes, S. P. RAFT Synthesis of Sterically Stabilized Methacrylic Nanolatexes and Vesicles by Aqueous Dispersion Polymerization. *Angewandte Chemie-International Edition* **2010**, *49*, 4042-4046.

(32) Blanazs, A.; Verber, R.; Mykhaylyk, O. O.; Ryan, A. J.; Heath, J. Z.; Douglas, C. W. I.; Armes, S. P. Sterilizable Gels from Thermoresponsive Block Copolymer Worms. *Journal of the American Chemical Society* **2012**, *134*, 9741-9748.

(33) Blanazs, A.; Ryan, A. J.; Armes, S. P. Predictive Phase Diagrams for RAFT Aqueous Dispersion Polymerization: Effect of Block Copolymer Composition, Molecular Weight, and Copolymer Concentration. *Macromolecules* **2012**, *45*, 5099-5107.

(34) Blanazs, A.; Madsen, J.; Battaglia, G.; Ryan, A. J.; Armes, S. P. Mechanistic Insights for Block Copolymer Morphologies: How Do Worms Form Vesicles? *J Am Chem Soc* **2011**, *133*, 16581-16587.

(35) Semsarilar, M.; Ladmiral, V.; Blanazs, A.; Armes, S. P. Anionic Polyelectrolyte-Stabilized Nanoparticles via RAFT Aqueous Dispersion Polymerization. *Langmuir* **2012**, *28*, 914-922.

(36) Semsarilar, M.; Jones, E. R.; Blanazs, A.; Armes, S. P. Efficient Synthesis of Sterically-Stabilized Nano-Objects via RAFT Dispersion Polymerization of Benzyl Methacrylate in Alcoholic Media. *Advanced Materials* **2012**, *24*, 3378-3382.

(37) Semsarilar, M.; Ladmiral, V.; Blanazs, A.; Armes, S. P. Cationic Polyelectrolyte-Stabilized Nanoparticles via RAFT Aqueous Dispersion Polymerization. *Langmuir* **2013**, *29*, 7416-7424.

(38) Smith, A. E.; Xu, X.; Kirkland-York, S. E.; Savin, D. A.; McCormick, C. L. "Schizophrenic" Self-Assembly of Block Copolymers Synthesized via Aqueous RAFT Polymerization: From Micelles to Vesicles. *Macromolecules* **2010**, *43*, 1210-1217.

(39) Doncom, K. E. B.; Warren, N. J.; Armes, S. P. Polysulfobetaine-based diblock copolymer nano-objects via polymerization-induced self-assembly. *Polymer Chemistry* **2015**, *6*, 7264-7273.

(40) Sugihara, S.; Blanazs, A.; Armes, S. P.; Ryan, A. J.; Lewis, A. L. Aqueous Dispersion Polymerization: A New Paradigm for in Situ Block Copolymer Self-Assembly in Concentrated Solution. *Journal of the American Chemical Society* **2011**, *133*, 15707-15713.

(41) Sun, J.-T.; Yu, Z.-Q.; Hong, C.-Y.; Pan, C.-Y. Biocompatible Zwitterionic Sulfobetaine Copolymer-Coated Mesoporous Silica Nanoparticles for Temperature-Responsive Drug Release. *Macromolecular Rapid Communications* **2012**, *33*, 811-818.

(42) Stepto, R. F. T. Dispersity in polymer science. *Pure and Applied Chemistry* **2009**, *81*, 351-353.

(43) Odian, G. *Principles of Polymerization, 4th ed.*, John Wiley & Sons, Inc.: New York, **2004**.

(44) Hiemenz, P. C.; Lodge, T. P. *Polymer Chemistry, second edition,* CRC Press, Bosa Roca, **2007**.

(45) Matyjaszewski, K. G., Y.; Leibler, L. *Macromolecular Engineering: Precise Synthesis, Materials Properties, Applications*. Wiley-VCH Verlag GmbH & Co. KGaA, Weinheim, **2007**.

(46) Braunecker, W. A.; Matyjaszewski, K. Controlled/living radical polymerization: features, developments, and perspectives. *Progress in Polymer Science* **2007**, *32*, 93-146.

(47) Szwarc, M. 'Living' polymers. *Nature* **1956**, *178*, 1168-1169.

(48) Odian, G. *Principles of Polymerization,* McGraw-Hill, New York, **1970**.

(49) Jenkins, A. D. J., R. G.; Moad, G. Terminology for reversible-deactivation radical polymerization previously called "controlled" radical or "living" radical polymerization (IUPAC Recommendations 2010). *Pure and Applied Chemistry* **2010**, *82*, 483.

(50) Hawker, C. J.; Bosman, A. W.; Harth, E. New polymer synthesis by nitroxide mediated living radical polymerizations. *Chemical Reviews* **2001**, *101*, 3661-3688.

(51) Kato, M.; Kamigaito, M.; Sawamoto, M.; Higashimura, T. Polymerization of methyl methacrylate with the carbon tetrachloride/dichlorotris-(triphenylphosphine) ruthenium (II)/methylaluminum bis (2, 6-di-tert-butylphenoxide) initiating system: possibility of living radical polymerization. *Macromolecules* **1995**, *28*, 1721-1723.

(52) Wang, J.-S.; Matyjaszewski, K. Controlled/"living" radical polymerization. Atom transfer radical polymerization in the presence of transition-metal complexes. *Journal of the American Chemical Society* **1995**, *117*, 5614-5615.

(53) Chiefari, J.; Chong, Y.; Ercole, F.; Krstina, J.; Jeffery, J.; Le, T. P.; Mayadunne, R. T.; Meijs, G. F.; Moad, C. L.; Moad, G. Living free-radical polymerization by reversible addition-fragmentation chain transfer: the RAFT process. *Macromolecules* **1998**, *31*, 5559-5562.

(54) Goto, A.; Fukuda, T. Kinetics of living radical polymerization. *Progress in Polymer Science* **2004**, *29*, 329-385.

(55) Solomon, D. H.; Rizzardo, E.; Cacioli, P. 1986; Vol. US Patent 4,581,429,.

(56) Georges, M. K.; Veregin, R. P.; Kazmaier, P. M.; Hamer, G. K. Narrow molecular weight resins by a free-radical polymerization process. *Macromolecules* **1993**, *26*, 2987-2988.

(57) Nicolas, J.; Mueller, L.; Dire, C.; Matyjaszewski, K.; Charleux, B. Comprehensive modeling study of nitroxide-mediated controlled/living radical copolymerization of methyl methacrylate with a small amount of styrene. *Macromolecules* **2009**, *42*, 4470-4478.

(58) Nicolas, J.; Guillaneuf, Y.; Lefay, C.; Bertin, D.; Gigmes, D.; Charleux, B. Nitroxide-mediated polymerization. *Progress in Polymer Science* **2013**, *38*, 63-235.

(59) Matyjaszewski, K.; Xia, J. Atom transfer radical polymerization. *Chemical Reviews* **2001**, *101*, 2921-2990.

(60) di Lena, F.; Matyjaszewski, K. Transition metal catalysts for controlled radical polymerization. *Progress in Polymer Science* **2010**, *35*, 959-1021.

(61) Matyjaszewski, K. Atom transfer radical polymerization (ATRP): current status and future perspectives. *Macromolecules* **2012**, *45*, 4015-4039.

(62) Jakubowski, W.; Matyjaszewski, K. Activator generated by electron transfer for atom transfer radical polymerization. *Macromolecules* **2005**, *38*, 4139-4146.

(63) Jakubowski, W.; Min, K.; Matyjaszewski, K. Activators regenerated by electron transfer for atom transfer radical polymerization of styrene. *Macromolecules* **2006**, *39*, 39-45.

(64) Pintauer, T.; Matyjaszewski, K. Atom transfer radical addition and polymerization reactions catalyzed by ppm amounts of copper complexes. *Chemical Society Reviews* **2008**, *37*, 1087-1097.

(65) Magenau, A. J.; Strandwitz, N. C.; Gennaro, A.; Matyjaszewski, K. Electrochemically mediated atom transfer radical polymerization. *Science* **2011**, *332*, 81-84.

(66) Moad, G.; Rizzardo, E.; Thang, S. H. Living Radical Polymerization by the RAFT Process - A Second Update. *Australian Journal of Chemistry* **2009**, *62*, 1402-1472.

(67) Moad, G.; Rizzardo, E.; Thang, S. H. Living radical polymerization by the RAFT process - A first update. *Australian Journal of Chemistry* **2006**, *59*, 669-692.

(68) Moad, G.; Rizzardo, E.; Thang, S. H. Living radical polymerization by the RAFT process. *Australian Journal of Chemistry* **2005**, *58*, 379-410.

(69) Mayadunne, R. T. A.; Rizzardo, E.; Chiefari, J.; Chong, Y. K.; Moad, G.; Thang, S. H. Living radical polymerization with reversible addition-fragmentation chain transfer (RAFT polymerization) using dithiocarbamates as chain transfer agents. *Macromolecules* **1999**, *32*, 6977-6980.

(70) Chong, Y. K.; Le, T. P. T.; Moad, G.; Rizzardo, E.; Thang, S. H. A more versatile route to block copolymers and other polymers of complex architecture by living radical polymerization: The RAFT process. *Macromolecules* **1999**, *32*, 2071-2074.

(71) Mayadunne, R. T. A.; Rizzardo, E.; Chiefari, J.; Krstina, J.; Moad, G.; Postma, A.; Thang, S. H. Living polymers by the use of trithiocarbonates as reversible addition-fragmentation chain transfer (RAFT) agents: ABA triblock copolymers by radical polymerization in two steps. *Macromolecules* **2000**, *33*, 243-245.

(72) Chambon, P.; Blanazs, A.; Battaglia, G.; Armes, S. P. Facile Synthesis of Methacrylic ABC Triblock Copolymer Vesicles by RAFT Aqueous Dispersion Polymerization. *Macromolecules* **2012**, *45*, 5081-5090.

(73) Moad, G.; Mayadunne, R. T. A.; Rizzardo, E.; Skidmore, M.; Thang, S. H. Synthesis of novel architectures by radical polymerization with reversible addition fragmentation chain transfer (RAFT polymerization). *Macromolecular Symposia* **2003**, *192*, 1-12.

(74) Lord, H. T.; Quinn, J. F.; Angus, S. D.; Whittaker, M. R.; Stenzel, M. H.; Davis, T. P. Microgel stars via Reversible Addition Fragmentation Chain Transfer (RAFT) polymerisation - a facile route to macroporous membranes, honeycomb patterned thin films and inverse opal substrates. *Journal of Materials Chemistry* **2003**, *13*, 2819-2824.

(75) Edmondson, S.; Osborne, V. L.; Huck, W. T. S. Polymer brushes via surface-initiated polymerizations. *Chemical Society Reviews* **2004**, *33*, 14-22.

(76) McLeary, J. B.; Calitz, F. M.; McKenzie, J. M.; Tonge, M. P.; Sanderson, R. D.; Klumperman, B. A H-1 NMR investigation of reversible addition-fragmentation

chain transfer polymerization kinetics and mechanisms. Initialization with different initiating and leaving groups. *Macromolecules* **2005**, *38*, 3151-3161.

(77) Stevens, M. P. *Polymer Chemistry: An Introduction. 3rd edition.; Oxford University Press: Oxford,* **1999**, 175.

(78) Hunter, R. J. *Introduction to Modern Colloid Science.* Oxford University Press: Oxford**, 1993**.

(79) Morse, A. J.; Dupin, D.; Thompson, K. L.; Armes, S.; Ouzineb, K.; Mills, P.; Swart, R. Novel Pickering emulsifiers based on pH-responsive poly (tert-butylaminoethyl methacrylate) latexes. *Langmuir* **2012**, *28*, 11733-11744.

(80) Gilbert, R. G. *Emulsion Polymerisation - A Mechanistic approach.* Academic Press: London, **1995**.

(81) Lovell, P. A. E.-A., M. S., *Emulsion Polymerisation and Emulsion Polymers.* John Wiley and Sons, Chichester UK, **1997**.

(82) Osmond, D. W. J. T., H. H. *GB893429(A)* **1962**.

(83) Qiu, J.; Charleux, B.; Matyjaszewski, K. Controlled/living radical polymerization in aqueous media: homogeneous and heterogeneous systems. *Progress in Polymer Science* **2001**, *26*, 2083-2134.

(84) Ali, A. I.; Pareek, P.; Sewell, L.; Schmid, A.; Fujii, S.; Armes, S. P.; Shirley, I. Synthesis of poly (2-hydroxypropyl methacrylate) latex particles via aqueous dispersion polymerization. *Soft Matter* **2007**, *3*, 1003-1013.

(85) Almog, Y.; Reich, S.; Levy, M. Monodisperse polymeric spheres in the micron size range by a single step process. *British Polymer Journal* **1982**, *14*, 131-136.

(86) Baines, F. L. D., S.; Billingham, N. C.; Armes, S. P. Use of block copolymer stabilizers for the dispersion polymerization of styrene in alcoholic media. *Macromolecules* **1996**, *29*, 3096-3102.

(87) Ahmad, H.; Dupin, D.; Armes, S. P.; Lewis, A. L. Synthesis of Biocompatible Sterically-Stabilized Poly(2-(methacryloyloxy) ethyl phosphorylcholine) Latexes via Dispersion Polymerization in Alcohol/Water Mixtures. *Langmuir* **2009**, *25*, 11442-11449.

(88) Xiao, X.; He, S.; Dan, M.; Su, Y.; Huo, F.; Zhang, W. Brush macro-RAFT agent mediated dispersion polymerization of styrene in the alcohol/water mixture. *Journal of Polymer Science Part A: Polymer Chemistry* **2013**, *51*, 3177-3190.

(89) Sugihara, S.; Sugihara, K.; Armes, S. P.; Ahmad, H.; Lewis, A. L. Synthesis of Biomimetic Poly(2-(methacryloyloxy)ethyl phosphorylcholine) Nanolatexes via Atom Transfer Radical Dispersion Polymerization in Alcohol/Water Mixtures. *Macromolecules* **2010**, *43*, 6321-6329.

(90) Kawaguchi, S.; Ito, K. In *Polymer Particles*; Springer, **2005**.

(91) Israelachvili, J. N. *Intermolecular and surface forces: revised third edition*; Academic press: New York, **2011**.

(92) Tanford, C. *The Hydrophobic Effect*, Wiley: New York. **1973**.

(93) Fong, C.; Le, T.; Drummond, C. J. Lyotropic liquid crystal engineering–ordered nanostructured small molecule amphiphile self-assembly materials by design. *Chemical Society Reviews* **2012**, *41*, 1297-1322.

(94) Nagarajan, R.; Ruckenstein, E. Theory of surfactant self-assembly: a predictive molecular thermodynamic approach. *Langmuir* **1991**, *7*, 2934-2969.

(95) Zhang, L.; Eisenberg, A. Multiple morphologies of "crew-cut" aggregates of polystyrene-b-poly (acrylic acid) block copolymers. *Science* **1995**, *268*, 1728-1731.

(96) Mai, Y.; Eisenberg, A. Self-assembly of block copolymers. *Chemical Society Reviews* **2012**, *41*, 5969-5985.

(97) Cameron, N. S.; Corbierre, M. K.; Eisenberg, A. 1998 EWR Steacie Award Lecture Asymmetric amphiphilic block copolymers in solution: a morphological wonderland. *Canadian Journal of Chemistry* **1999**, *77*, 1311-1326.

(98) Zhang, L.; Eisenberg, A. Multiple morphologies and characteristics of "crew-cut" micelle-like aggregates of polystyrene-b-poly(acrylic acid) diblock copolymers in aqueous solutions. *Journal of the American Chemical Society* **1996**, *118*, 3168-3181.

(99) Alexandridis, P.; Lindman, B. *Amphiphilic block copolymers: self-assembly and applications*; Elsevier, Amsterdam. **2000**.

(100) Thomas, E. L.; Anderson, D. M.; Henkee, C. S.; Hoffman, D. Periodic area-minimizing surfaces in block copolymers. *Nature* **1988**, *334*, 598-601.

(101) Bates, F. S. Polymer-polymer phase behavior. *Science* **1991**, *251*, 898-905.

(102) Bates, F. S.; Fredrickson, G. Block copolymers-designer soft materials. *Physics Today* **1999**, *52*, 32-38.

(103) Van Hest, J.; Delnoye, D.; Baars, M.; Van Genderen, M.; Meijer, E. Polystyrene-dendrimer amphiphilic block copolymers with a generation-dependent aggregation. *Science* **1995**, *268*, 1592-1595.

(104) Zhang, L. F.; Eisenberg, A. Multiple morphologies of "crew-cut" aggregates of polystyrene-b-poly (acrylic acid) block copolymers. *Science* **1995**, *268*, 1728-1731.

(105) Zhang, L.; Yu, K.; Eisenberg, A. Ion-induced morphological changes in" crew-cut" aggregates of amphiphilic block copolymers. *Science* **1996**, *272*, 1777.

(106) Zhang, L.; Eisenberg, A. Thermodynamic vs kinetic aspects in the formation and morphological transitions of crew-cut aggregates produced by self-assembly of polystyrene-b-poly (acrylic acid) block copolymers in dilute solution. *Macromolecules* **1999**, *32*, 2239-2249.

(107) Discher, D. E.; Eisenberg, A. Polymer vesicles. *Science* **2002**, *297*, 967-973.

(108) Zhang, L.; Shen, H.; Eisenberg, A. Phase separation behavior and crew-cut micelle formation of polystyrene-b-poly (acrylic acid) copolymers in solutions. *Macromolecules* **1997**, *30*, 1001-1011.

(109) Yu, Y.; Zhang, L.; Eisenberg, A. Morphogenic effect of solvent on crew-cut aggregates of apmphiphilic diblock copolymers. *Macromolecules* **1998**, *31*, 1144-1154.

(110) Bhargava, P.; Zheng, J. X.; Li, P.; Quirk, R. P.; Harris, F. W.; Cheng, S. Z. Self-Assembled Polystyrene-b lock-poly (ethylene oxide) Micelle Morphologies in Solution. *Macromolecules* **2006**, *39*, 4880-4888.

(111) Jain, S.; Bates, F. S. On the origins of morphological complexity in block copolymer surfactants. *Science* **2003**, *300*, 460-464.

(112) Bütün, V.; Armes, S. P.; Billingham, N. C. Synthesis and aqueous solution properties of near-monodisperse tertiary amine methacrylate homopolymers and diblock copolymers. *Polymer* **2001**, *42*, 5993-6008.

(113) Howse, J. R.; Jones, R. A.; Battaglia, G.; Ducker, R. E.; Leggett, G. J.; Ryan, A. J. Templated formation of giant polymer vesicles with controlled size distributions. *Nature materials* **2009**, *8*, 507-511.

(114) Qiu, H.; Gao, Y.; Boott, C. E.; Gould, O. E.; Harniman, R. L.; Miles, M. J.; Webb, S. E.; Winnik, M. A.; Manners, I. Uniform patchy and hollow rectangular platelet micelles from crystallizable polymer blends. *Science* **2016**, *352*, 697-701.

(115) Qiu, H.; Hudson, Z. M.; Winnik, M. A.; Manners, I. Multidimensional hierarchical self-assembly of amphiphilic cylindrical block comicelles. *Science* **2015**, *347*, 1329-1332.

(116) Warren, N. J.; Mykhaylyk, O. O.; Mahmood, D.; Ryan, A. J.; Armes, S. P. RAFT Aqueous Dispersion Polymerization Yields Poly(ethylene glycol)-Based Diblock Copolymer Nano-Objects with Predictable Single Phase Morphologies. *Journal of the American Chemical Society* **2014**, *136*, 1023-1033.

(117) Zhou, W.; Qu, Q.; Xu, Y.; An, Z. Aqueous Polymerization-Induced Self-Assembly for the Synthesis of Ketone-Functionalized Nano-Objects with Low Polydispersity. *ACS Macro Letters* **2015**, *4*, 495-499.

(118) Shen, W.; Chang, Y.; Liu, G.; Wang, H.; Cao, A.; An, Z. Biocompatible, antifouling, and thermosensitive core− shell nanogels synthesized by RAFT aqueous dispersion polymerization. *Macromolecules* **2011**, *44*, 2524-2530.

(119) Ladmiral, V.; Semsarilar, M.; Canton, I.; Armes, S. P. Polymerization-Induced Self-Assembly of Galactose-Functionalized Biocompatible Diblock Copolymers for Intracellular Delivery. *Journal of the American Chemical Society* **2013**, *135*, 13574-13581.

(120) Jiang, Y.; Xu, N.; Han, J.; Yu, Q.; Guo, L.; Gao, P.; Lu, X.; Cai, Y. The direct synthesis of interface-decorated reactive block copolymer nanoparticles via polymerisation-induced self-assembly. *Polymer Chemistry* **2015**, *6*, 4955-4965.

(121) Hanisch, A.; Yang, P.; Kulak, A. N.; Fielding, L. A.; Meldrum, F. C.; Armes, S. P. Phosphonic Acid-Functionalized Diblock Copolymer Nano-Objects via Polymerization-Induced Self-Assembly: Synthesis, Characterization, and Occlusion into Calcite Crystals. *Macromolecules* **2016**, *49*, 192-204.

(122) Williams, M.; Penfold, N. J. W.; Armes, S. P. Cationic and reactive primary amine-stabilised nanoparticles via RAFT aqueous dispersion polymerisation. *Polymer Chemistry* **2016**, *7*, 384-393.

(123) Ladmiral, V.; Charlot, A.; Semsarilar, M.; Armes, S. P. Synthesis and characterization of poly(amino acid methacrylate)-stabilized diblock copolymer nano-objects. *Polymer Chemistry* **2015**, *6*, 1805-1816.

(124) Fielding, L. A.; Derry, M. J.; Ladmiral, V.; Rosselgong, J.; Rodrigues, A. M.; Ratcliffe, L. P. D.; Sugihara, S.; Armes, S. P. RAFT dispersion polymerization in non-polar solvents: facile production of block copolymer spheres, worms and vesicles in n-alkanes. *Chemical Science* **2013**, *4*, 2081-2087.

(125) Derry, M. J.; Fielding, L. A.; Warren, N. J.; Mable, C. J.; Smith, A. J.; Mykhaylyk, O. O.; Armes, S. P. In situ small-angle X-ray scattering studies of sterically-stabilized diblock copolymer nanoparticles formed during polymerization-induced self-assembly in non-polar media. *Chemical Science* **2016**, *7*, 5078-5090.

(126) Fielding, L. A.; Lane, J. A.; Derry, M. J.; Mykhaylyk, O. O.; Armes, S. P. Thermo-responsive Diblock Copolymer Worm Gels in Non-polar Solvents. *Journal of the American Chemical Society* **2014**, *136*, 5790-5798.

(127) Mable, C. J.; Gibson, R. R.; Prévost, S.; McKenzie, B. E.; Mykhaylyk, O. O.; Armes, S. P. Loading of silica nanoparticles in block copolymer vesicles during polymerization-induced self-assembly: encapsulation efficiency and thermally-triggered release. *Journal of the American Chemical Society* **2015**, *137*, 16098-16108.

(128) Penfold, N. J. W.; Lovett, J. R.; Warren, N. J.; Verstraete, P.; Smets, J.; Armes, S. P. pH-Responsive non-ionic diblock copolymers: protonation of a morpholine end-group induces an order-order transition. *Polymer Chemistry* **2016**, *7*, 79-88.

(129) Lovett, J. R.; Warren, N. J.; Ratcliffe, L. P. D.; Kocik, M. K.; Armes, S. P. pH-Responsive Non-Ionic Diblock Copolymers: Ionization of Carboxylic Acid End-Groups Induces an Order-Order Morphological Transition. *Angewandte Chemie-International Edition* **2015**, *54*, 1279-1283.

(130) Canton, I.; Warren, N. J.; Chahal, A.; Amps, K.; Wood, A.; Weightman, R.; Wang, E.; Moore, H.; Armes, S. P. Mucin-Inspired Thermoresponsive Synthetic Hydrogels Induce Stasis in Human Pluripotent Stem Cells and Human Embryos. *ACS Central Science* **2016**, *2*, 65-74.

(131) Cai, W.; Wan, W.; Hong, C.; Huang, C.; Pan, C. Morphology transitions in RAFT polymerization. *Soft Matter* **2010**, *6*, 5554-5561.

(132) He, W.-D.; Sun, X.-L.; Wan, W.-M.; Pan, C.-Y. Multiple morphologies of PAA-b-PSt assemblies throughout RAFT dispersion polymerization of styrene with PAA Macro-CTA. *Macromolecules* **2011**, *44*, 3358-3365.

(133) Huang, C.-Q.; Pan, C.-Y. Direct preparation of vesicles from one-pot RAFT dispersion polymerization. *Polymer* **2010**, *51*, 5115-5121.

(134) Wan, W.-M.; Pan, C.-Y. One-pot synthesis of polymeric nanomaterials via RAFT dispersion polymerization induced self-assembly and re-organization. *Polymer Chemistry* **2010**, *1*, 1475-1484.

(135) Mahabadi, H. K.; O'driscoll, K. Absolute rate constants in free-radical polymerization. III. Determination of propagation and termination rate constants for styrene and methyl methacrylate. *Journal of Macromolecular Science-Chemistry* **1977**, *11*, 967-976.

(136) Buback, M.; Gilbert, R. G.; Hutchinson, R. A.; Klumperman, B.; Kuchta, F. D.; Manders, B. G.; O'Driscoll, K. F.; Russell, G. T.; Schweer, J. Critically evaluated rate coefficients for free-radical polymerization, 1. Propagation rate coefficient for styrene. *Macromolecular Chemistry and Physics* **1995**, *196*, 3267-3280.

(137) Matheson, M. S.; Auer, E.; Bevilacqua, E. B.; Hart, E. Rate Constants in Free Radical Polymerization. III. Styrene1. *Journal of the American Chemical Society* **1951**, *73*, 1700-1706.

(138) Zhang, X.; Rieger, J.; Charleux, B. Effect of the solvent composition on the morphology of nano-objects synthesized via RAFT polymerization of benzyl methacrylate in dispersed systems. *Polymer Chemistry* **2012**, *3*, 1502-1509.

(139) Wang, X.; Xu, J.; Zhang, Y.; Zhang, W. Polymerization of styrene in alcohol/water mediated by a macro-RAFT agent of poly (N-isopropylacrylamide) trithiocarbonate: From homogeneous to heterogeneous RAFT polymerization. *Journal of Polymer Science Part A: Polymer Chemistry* **2012**, *50*, 2452-2462.

(140) Huo, F.; Wang, X.; Zhang, Y.; Zhang, X.; Xu, J.; Zhang, W. RAFT dispersion polymerization of styrene in water/alcohol: the solvent effect on polymer particle growth during polymer chain propagation. *Macromolecular Chemistry and Physics* **2013**, *214*, 902-911.

(141) Jones, E.; Semsarilar, M.; Wyman, P.; Boerakker, M.; Armes, S. Addition of water to an alcoholic RAFT PISA formulation leads to faster kinetics but limits the evolution of copolymer morphology. *Polymer Chemistry* **2016**, *7*, 851-859.

(142) Derry, M. J.; Fielding, L. A.; Armes, S. P. Industrially-relevant polymerization-induced self-assembly formulations in non-polar solvents: RAFT dispersion polymerization of benzyl methacrylate. *Polymer Chemistry* **2015**, *6*, 3054-3062.

(143) Lopez-Oliva, A. P.; Warren, N. J.; Rajkumar, A.; Mykhaylyk, O. O.; Derry, M. J.; Doncom, K. E.; Rymaruk, M. J.; Armes, S. P. Polydimethylsiloxane-Based Diblock Copolymer Nano-objects Prepared in Nonpolar Media via RAFT-Mediated Polymerization-Induced Self-Assembly. *Macromolecules* **2015**, *48*, 3547-3555.

(144) Charleux, B.; Delaittre, G.; Rieger, J.; D'Agosto, F. Polymerization-induced self-assembly: from soluble macromolecules to block copolymer nano-objects in one step. *Macromolecules* **2012**, *45*, 6753-6765.

(145) Ferguson, C. J.; Hughes, R. J.; Pham, B. T.; Hawkett, B. S.; Gilbert, R. G.; Serelis, A. K.; Such, C. H. Effective ab initio emulsion polymerization under RAFT control. *Macromolecules* **2002**, *35*, 9243-9245.

(146) Ferguson, C. J.; Hughes, R. J.; Nguyen, D.; Pham, B. T. T.; Gilbert, R. G.; Serelis, A. K.; Such, C. H.; Hawkett, B. S. Ab Initio Emulsion Polymerization by RAFT-Controlled Self-Assembly. *Macromolecules* **2005**, *38*, 2191-2204.

(147) Sprong, E.; Leswin, J. S.; Lamb, D. J.; Ferguson, C. J.; Hawkett, B. S.; Pham, B. T.; Nguyen, D.; Such, C. H.; Serelis, A. K.; Gilbert, R. G. Molecular Watchmaking: ab initio Emulsion Polymerization by RAFT-controlled Self-assembly. *Macromolecular Symposia* **2005**, *231*, 84-93.

(148) Ganeva, D. E.; Sprong, E.; De Bruyn, H.; Warr, G. G.; Such, C. H.; Hawkett, B. S. Particle formation in ab initio RAFT mediated emulsion polymerization systems. *Macromolecules* **2007**, *40*, 6181-6189.

(149) Chaduc, I.; Zhang, W.; Rieger, J.; Lansalot, M.; D'Agosto, F.; Charleux, B. Amphiphilic Block Copolymers from a Direct and One-pot RAFT Synthesis in Water. *Macromolecular Rapid Communications* **2011**, *32*, 1270-1276.

(150) Rieger, J.; Osterwinter, G.; Bui, C.; Stoffelbach, F.; Charleux, B. Surfactant-free controlled/living radical emulsion (co) polymerization of n-butyl acrylate and

methyl methacrylate via RAFT using amphiphilic poly (ethylene oxide)-based trithiocarbonate chain transfer agents. *Macromolecules* **2009**, *42*, 5518-5525.

(151) Rieger, J.; Stoffelbach, F.; Bui, C.; Alaimo, D.; Jérôme, C.; Charleux, B. Amphiphilic poly (ethylene oxide) macromolecular RAFT agent as a stabilizer and control agent in ab initio batch emulsion polymerization. *Macromolecules* **2008**, *41*, 4065-4068.

(152) Rieger, J.; Zhang, W.; Stoffelbach, F.; Charleux, B. Surfactant-free RAFT emulsion polymerization using poly (N, N-dimethylacrylamide) trithiocarbonate macromolecular chain transfer agents. *Macromolecules* **2010**, *43*, 6302-6310.

(153) Zhang, W.; D'Agosto, F.; Dugas, P.-Y.; Rieger, J.; Charleux, B. RAFT-mediated one-pot aqueous emulsion polymerization of methyl methacrylate in presence of poly (methacrylic acid-co-poly (ethylene oxide) methacrylate) trithiocarbonate macromolecular chain transfer agent. *Polymer* **2013**, *54*, 2011-2019.

(154) Cunningham, V. J.; Alswieleh, A. M.; Thompson, K. L.; Williams, M.; Leggett, G. J.; Armes, S. P.; Musa, O. M. Poly(glycerol monomethacrylate)-Poly(benzyl methacrylate) Diblock Copolymer Nanoparticles via RAFT Emulsion Polymerization: Synthesis, Characterization, and Interfacial Activity. *Macromolecules* **2014**, *47*, 5613-5623.

(155) Boisse, S.; Rieger, J.; Belal, K.; Di-Cicco, A.; Beaunier, P.; Li, M.-H.; Charleux, B. Amphiphilic block copolymer nano-fibers via RAFT-mediated polymerization in aqueous dispersed system. *Chemical Communications* **2010**, *46*, 1950-1952.

(156) Zhang, W.; D'Agosto, F.; Boyron, O.; Rieger, J.; Charleux, B. Toward a better understanding of the parameters that lead to the formation of nonspherical polystyrene particles via RAFT-mediated one-pot aqueous emulsion polymerization. *Macromolecules* **2012**, *45*, 4075-4084.

(157) Leeuw, N. H.; Parker, S. C. Surface structure and morphology of calcium carbonate polymorphs calcite, aragonite, and vaterite: an atomistic approach. *The Journal of Physical Chemistry B* **1998**, *102*, 2914-2922.

(158) Meldrum, F. C.; Ludwigs, S. Template-directed control of crystal morphologies. *Macromolecular Bioscience* **2007**, *7*, 152-162.

(159) Mann, S.; Archibald, D. D.; Didymus, J. M.; Douglas, T.; Heywood, B. R.; Meldrum, F. C.; Reeves, N. J. Crystallzation at inorganic-organic interfaces - biominerals and biomimetic synthesis. *Science* **1993**, *261*, 1286-1292.

(160) Robinson, K. L.; Weaver, J. V. M.; Armes, S. P.; Marti, E. D.; Meldrum, F. C. Synthesis of controlled-structure sulfate-based copolymers via atom transfer radical polymerisation and their use as crystal habit modifiers for $BaSO_4$. *Journal of Materials Chemistry* **2002**, *12*, 890-896.

(161) Cölfen, H.; Antonietti, M. Crystal design of calcium carbonate microparticles using double-hydrophilic block copolymers. *Langmuir* **1998**, *14*, 582-589.

(162) Sedlák, M.; Cölfen, H. Synthesis of double-hydrophilic block copolymers with hydrophobic moieties for the controlled crystallization of minerals. *Macromolecular Chemistry and Physics* **2001**, *202*, 587-597.

(163) Cölfen, H.; Qi, L. A Systematic Examination of the Morphogenesis of Calcium Carbonate in the Presence of a Double-Hydrophilic Block Copolymer. *Chemistry–A European Journal* **2001**, *7*, 106-116.

(164) Qi, L.; Cölfen, H.; Antonietti, M. Control of barite morphology by double-hydrophilic block copolymers. *Chemistry of Materials* **2000**, *12*, 2392-2403.

(165) Shi, H.; Qi, L.; Ma, J.; Cheng, H. Polymer-directed synthesis of penniform BaWO4 nanostructures in reverse micelles. *Journal of the American Chemical Society* **2003**, *125*, 3450-3451.

(166) Zhang, D.; Qi, L.; Ma, J.; Cheng, H. Morphological control of calcium oxalate dihydrate by a double-hydrophilic block copolymer. *Chemistry of Materials* **2002**, *14*, 2450-2457.

(167) Li, H.; Xin, H. L.; Kunitake, M. E.; Keene, E. C.; Muller, D. A.; Estroff, L. A. Calcite Prisms from Mollusk Shells (Atrina Rigida): Swiss-cheese-like Organic-Inorganic Single-crystal Composites. *Advanced Functional Materials* **2011**, *21*, 2028-2034.

(168) Li, H.; Xin, H. L.; Muller, D. A.; Estroff, L. A. Visualizing the 3D Internal Structure of Calcite Single Crystals Grown in Agarose Hydrogels. *Science* **2009**, *326*, 1244-1247.

(169) Liu, Y.; Yuan, W.; Shi, Y.; Chen, X.; Wang, Y.; Chen, H.; Li, H. Functionalizing Single Crystals: Incorporation of Nanoparticles Inside Gel-Grown Calcite Crystals. *Angewandte Chemie-International Edition* **2014**, *53*, 4127-4131.

(170) Lu, C. H.; Qi, L. M.; Cong, H. L.; Wang, X. Y.; Yang, J. H.; Yang, L. L.; Zhang, D. Y.; Ma, J. M.; Cao, W. X. Synthesis of calcite single crystals with porous surface by templating of polymer latex particles. *Chemistry of Materials* **2005**, *17*, 5218-5224.

(171) Ozgur, U.; Alivov, Y. I.; Liu, C.; Teke, A.; Reshchikov, M. A.; Dogan, S.; Avrutin, V.; Cho, S. J.; Morkoc, H. A comprehensive review of ZnO materials and devices. *Journal of Applied Physics* **2005**, *98,* 041301.

(172) Janotti, A.; Van de Walle, C. G. Fundamentals of zinc oxide as a semiconductor. *Reports on Progress in Physics* **2009**, *72,* 126501.

(173) Muñoz-Espí, R.; Qi, Y.; Lieberwirth, I.; Gómez, C. M.; Wegner, G. Surface-functionalized latex particles as controlling agents for the mineralization of zinc oxide in aqueous medium. *Chemistry-A European Journal* **2006**, *12*, 118-129.

(174) Muñoz-Espí, R.; Chandra, A.; Wegner, G. Crystal perfection in zinc oxide with occluded carboxyl-functionalized latex particles. *Crystal Growth & Design* **2007**, *7*, 1584-1589.

(175) Muñoz-Espí, R.; Jeschke, G.; Lieberwirth, I.; Gomez, C. M.; Wegner, G. ZnO-latex hybrids obtained by polymer-controlled crystallization: A spectroscopic investigation. *The Journal of Physical Chemistry B* **2007**, *111*, 697-707.

2. Chapter Two

2. Expermental and Characterisation

2.1 Experimental

2.1.1 Materials

Carboxybetaine methacrylate (C) was kindly donated by Dr. Saruwatari of the Osaka Organic Chemical Company, Japan. *O*-Methacryloyl-*trans*-4-hydroxy-*L*-proline (P) was synthesised as previously reported by Kristensen et al.[1] 4-(2-Aminoethyl)morpholine (99%) was purchased from Sigma Aldrich (UK) and distilled under vacuum before use. Ammonium 2-sulfatoethyl methacrylate (S, Bisomer SEM® solution, supplied as a 25.0 % w/v aqueous solution) and glycerol monomethacrylate (G; 99.8%) were supplied by GEO Specialty Chemicals (Hythe, UK) and used without further purification. Methacrylic acid (M) and benzyl methacrylate (B) were purchased from Alfa Aesar and passed through a basic aluminum oxide column to remove inhibitor prior to use. 4,4′-Azobis(4-cyanovaleric acid) (ACVA, 99 %) and 2-hydroxypropyl methacrylate (H, 98 %) were obtained from Alfa Aesar (UK). *N*-hydroxyl succinimide (98%), *N,N'*-dicyclohexylcarbodiimide (99%), 4-cyano-4-(phenylcarbonothioylthio)pentanoic acid (CPCP), ammonium carbonate, calcium chloride hexahydrate, zinc nitrate hexahydrate, hexamethylenetetramine, rhodamine B (RhB), sodium citrate tribasic dihydrate, sodium borohydride and $HAuCl_4 \cdot 3H_2O$ were all purchased from Sigma-Aldrich (UK) and used as received. Deuterium oxide (D_2O), deuterated methanol (CD_3OD) and dichloromethane (CD_2Cl_2) were obtained from Cambridge Isotope laboratories (UK). Dialysis tubing was received from SpectraPor. Deionised water was used in all cases and was obtained from an Elgastat Option 3A water purification unit.

2.1.2 Synthesis of Monomers, macro-CTAs, Diblock Copolymer Nanoparticles and Inorganic Nanoparticles

2.1.2.1 Synthesis of Morpholine-Functional Trithiocarbonate-based RAFT Chain Transfer Agent (MPETTC)

Step one:

4-Cyano-4-(2-phenylethanesulfanyl-thiocarbonyl)sulfanylpentanoic acid (PETTC) was synthesised in-house according to a previous protocol.[2] All glassware was dried in a 150 °C oven overnight, then flame-dried under vacuum before use to remove trace water. To synthesise 4-cyano-4-(2-phenylethanesulfanylthiocarbonyl)sulfanyl pentanoic succinimide ester (SPETTC), a 50 mL one-neck round-bottom flask was charged with PETTC (1.60 g, 4.71 mmol) and *N*-hydroxyl succinimide (0.54 g, 4.71 mmol), which were then dissolved in anhydrous dichloromethane (20.0 g, 15.0 mL). *N,N'*-Dicyclohexylcarbodiimide (0.97 g, 4.71 mmol) was added and then stirred in the dark for 16 h. The insoluble *N,N'*-dicyclohexylurea was removed by filtration. The organic solution was washed with water (four 10 ml portions), dried with $MgSO_4$, concentrated under vacuum and purified by recrystallisation from a 4:1 (v/v) ethyl acetate/*n*-hexane mixture to yield 4-cyano-4-(2-phenylethanesulfanylthiocarbonyl)sulfanyl pentanoic succinimide ester (SPETTC, 1.90 g, 92% yield). ^{1}H NMR (400 MHz, CD_2Cl_2, 25 °C): δ 1.89 (s, 3H, -(CN)C***H₃***), 2.51 − 2.68 (m, 2H, -(CH₃)(CN)C***H₂***CH₂C(=O)O), 2.81 (s, 4H, -(C=O)(C***H₂***)₂(C=O), 2.90 − 2.96 (t, 2H, -(CH₃)(CN)CH₂C***H₂***C(=O)), 2.97 − 3.03 (t, 2H, PhC***H₂***CH₂S(C=S)S), 3.56 − 3.64 (t, 2H, PhCH₂C***H₂***S(C=S)S), 7.20 - 7.36 (m, 5H, ***Ph***CH₂CH₂S(C=S)S). ^{13}C NMR (400 MHz, $CDCl_3$, 25 °C): δ 24.8 (***C***H₃), 25.7 (-C(=O)(***C***H₂)₂C(=O)), 26.9 (-CH₂***C***H₂C(=O)ON), 33.2 (Ph***C***H₂CH₂S), 34.1 (-***C***H₂CH₂C(=O)O), 38.1 (PhCH₂***C***H₂S), 46.2 (-S***C***(CH₃)(CN)CH₂), 118.7 -SC(CH₃)(***C***N)CH₂), 126.9, 128.6, 128.8, 139.2 (***Ph***CH₂), 167.2 (***C***=O), 168.9 (-***C***(=O)(CH₂)₂***C***(=O)), 216.4 (***C***=S). HRMS (ES$^+$) *m/z* calcd: 437.0658 Found: 437.0658 Microanalyses: calculated for $C_{19}H_{20}N_2O_4S_3$: C, 52.27; H, 4.62; N, 6.42; S, 22.03; found C, 52.65; H, 4.72; N, 6.39; S, 21.93.

Step two:

A 500 ml one-neck round-bottom flask containing a magnetic stirrer bar was charged with SPETTC (5.35 g, 12.3 mmol), which was dissolved in anhydrous chloroform (250 mL). In a separate 50 ml one-neck round-bottom flask, freshly distilled 4-(2-aminoethyl)morpholine (1.52 g, 1.53 mL, 11.7 mmol) was dissolved in anhydrous chloroform (25 mL), then added in one portion to the solution of SPETTC. The yellow reaction mixture was heated at 30 °C for 90 min, filtered and washed with saturated $NaHCO_3$ solution (3 x 400 mL) to remove residual *N*-hydroxysuccinimide, before being dried with $MgSO_4$. After solvent removal, the yellow oil was purified to remove any residual SPETTC via column chromatography using silica gel 60 (Merck) as the stationary phase and a 95:5: v/v dichloromethane/methanol mixed eluent, followed by drying in a vacuum oven overnight to isolate a viscous yellow oil (MPETTC, 4.75 g, 86%). ^{1}H NMR (400 MHz, CD_2Cl_2, 25 °C): δ 1.89 (s, 3H, -(CN)C**H$_3$**), 2.31 – 2.56 (m, 10H, -S(C(CH$_3$)(CN))C**H$_2$**C**H$_2$**C(=O), -CH$_2$NC**H$_2$**(C**H$_2$**)), 2.96 – 3.03 (t, 2H, PhC**H$_2$**CH$_2$S(C=S)S), 3.27 – 3.34 (q, 2H, -C(=O)NHC**H$_2$**CH$_2$), 3.56 – 3.62 (t, 2H, PhCH$_2$C**H$_2$**S(C=S)S), 3.64 – 3.71 (t, 4H, -CH$_2$NCH$_2$C**H$_2$**O) 5.98 – 6.13 (s, 1H, CON**H**), 7.20 - 7.36 (m, 5H, **Ph**CH$_2$CH$_2$S(C=S)S). ^{13}C NMR (400 MHz, $CDCl_3$, 25 °C): δ 25.1 (-**CH$_3$**), 31.8 (-CH$_2$**CH$_2$**CONH), 34.6 (Ph**CH$_2$**CH$_2$S), 34.5 (-**CH$_2$**CH$_2$CONH), 35.7 (-CONH**CH$_2$**CH$_2$N), 37.9 (PhCH$_2$**CH$_2$**S), 46.8 (-S**C**(CH$_3$)(CN)CH$_2$), 53.3 (-N**CH$_2$**CH$_2$O), 56.9 (-CONHCH$_2$**CH$_2$**N), 66.9 (-NCH$_2$**CH$_2$**O), 119.2 (-SC(CH$_3$)(**CN**)CH$_2$), 126.8, 128.5, 128.7, 139.1 (**Ph**CH$_2$), 170.1 (**C=O**), 216.8 (**C=S**). HRMS (ES$^+$) *m/z* calcd: 452.1495 Found: 452.1495. Microanalyses: calculated for $C_{21}H_{29}N_3O_2S_3$: C, 55.85; H, 6.47; N, 9.30; S, 21.29; found C, 55.47; H, 6.48; N, 9.08; S, 21.09.

2.1.2.2 Synthesis of Poly(carboxybetaine methacrylate)$_{52}$ macro-CTA (C_{52} macro-CTA)

MPETTC RAFT agent (0.97 g, 2.3 mmol), C monomer (30.0 g, 140 mmol) and ACVA (130 mg, 0.46 mmol, CTA/ACVA molar ratio = 5.0) were weighed into a 500 ml round-bottomed flask containing a stir bar. Deionised water (120 g) was added and the pH slowly adjusted to *ca.* pH 3.5 using a dilute aqueous solution of HCl. The solution was purged with nitrogen for 45 min and sealed with a rubber

septum under a positive nitrogen pressure. The flask was then immersed in a pre-heated oil bath set at 70 °C. The polymerisation was quenched after 40 min by rapid cooling in liquid nitrogen (final monomer conversion = 83 %). The crude **macro-CTA** was purified by exhaustive dialysis (SpectraPor membrane, MWCO = 3.5 kDa) against water, followed by lyophilisation with an 80 % yield; $M_{n\ NMR}$ = 11,600 g mol^{-1}, $M_{n\ SEC}$ = 9,500 g mol^{-1}, M_w/M_n = 1.17.

2.1.2.3 Synthesis of Poly(carboxybetaine methacrylate)$_{52}$-Poly(2-hydroxypropyl methacrylate)$_{250}$ (C$_{52}$-H$_{250}$) via RAFT Aqueous Dispersion Polymerisation of HPMA

C$_{52}$ macro-CTA (0.22 g, 0.019 mmol), **2-hydroxypropyl methacrylate** (H monomer, 0.68 g, 4.7 mmol), ACVA (1.0 mg, 0.004 mmol, CTA/ACVA molar ratio = 5.0) and water (5.1 g) were weighed into a glass vial containing a stir bar. The solution was purged with nitrogen for 30 min and sealed with a rubber septum under a positive nitrogen pressure, prior to immersion in a pre-heated oil bath at 70 °C for 6 h. The reaction was quenched by exposure to air and rapid cooling at 20 °C. For kinetic studies, aliquots were periodically removed for analysis by ^{1}H NMR spectroscopy.

2.1.2.4 Synthesis of *O*-Methacryloyl-trans-4-hydroxy-*L*-proline (P monomer)

P monomer was synthesised as previously reported by Kristensen et al.[1] A brief description of the synthesis is as follows: a 500 mL round-bottomed flask was charged with CF$_3$CO$_2$H (120 mL) and immersed in an ice bath. *Trans*-4-hydroxy-*L*-proline (34 g, 0.26 mol) was added in small portions with vigorous stirring. After 5 minutes stirring, the ice bath was removed and CF$_3$SO$_3$H (4.5 mL) was added. After a further 5 min, methacryloyl chloride (50 mL, 0.51 mol) was added in a single portion. A loose glass stopper was fitted and the reaction allowed to proceed at room temperature for 3 h. The reaction vessel was then cooled by immersion in an ice bath and diethyl ether (360 mL) was added slowly, over a period of 15 min with vigorous stirring. After stirring for a further 15 min in the ice bath, the white precipitate was separated by filtration, washed with diethyl ether and dried overnight under vacuum to yield P monomer in 62% yield. A small amount of the starting material, *trans*-4-

hydroxy-*L*-proline, was detected by ^{1}H NMR spectroscopy. However, the monomer was used in the synthesis of the P macro-CTA with no further purification. ^{1}H NMR spectroscopy (400 MHz, CD$_3$OD, 298 K): δ = 1.92 (s, 3H, -C*H$_3$*), 2.48 (m, 1H, -OCHC*H*HCH), 2.72 (m, 1H, -OCHCH*H*CH), 3.65 (m, 1H, -OCHC*H*HNH), 3.75 (m, 1H, -OCHCH*H*NH), 4.65 (m, 1H, -OCHCH$_2$C*H*), 5.56 (t, 1H, -OC*H*CH$_2$CH), 5.77 (s, 1H, -CH$_3$CH=C*H*H), 6.17 (s, 1H, -CH$_3$CH=CH*H*).

2.1.2.5 Synthesis of Poly(O-Methacryloyl-trans-4-hydroxy-L-proline)$_{50}$ macro-CTA (P$_{50}$ macro-CTA)

MPETTC RAFT agent (0.81 g, 1.9 mmol), P monomer (20.0 g, 96 mmol) and ACVA (100 mg, 0.36 mmol, CTA/ACVA molar ratio = 5.0) were weighed into a 500 ml round-bottomed flask containing a stir bar and deionised water (60 g) was added. The solution was purged with nitrogen for 45 min and sealed with a rubber septum under a positive nitrogen pressure. The flask was then immersed in a pre-heated oil bath set at 70 °C. The polymerisation was quenched after 2 h by rapid cooling in liquid nitrogen (final monomer conversion = 92 %). The crude macro-CTA was purified by precipitation into first *iso*-propanol and then diethyl ether with an overall recovered yield of 85 %; $M_{n\ NMR}$ = 11,600 g mol^{-1}, $M_{n\ SEC}$ = 11,400 g mol^{-1}, M_w/M_n = 1.18.

2.1.2.6 Synthesis of Poly(O-Methacryloyl-trans-4-hydroxy-L-proline)$_{50}$-Poly(2-hydroxypropyl methacrylate)$_{300}$ (P$_{50}$-H$_{300}$) via RAFT Aqueous Dispersion Polymerisation

P$_{50}$ macro-CTA (0.14 g, 0.012 mmol), H monomer (0.76 g, 5.3 mmol), ACVA (1.0 mg, 0.004 mmol, CTA/ACVA molar ratio = 5.0) and water (5.1 g) were weighed into a glass vial containing a stir bar. The solution was purged with nitrogen for 30 min and sealed with a rubber septum under a positive nitrogen pressure, prior to immersion in a pre-heated oil bath at 70 °C for 6 h. The reaction was quenched by exposure to air and rapid cooling at 20 °C.

2.1.2.7 Synthesis of Poly(glycerol monomethacrylate)$_{70}$ macro-CTA (G$_{70}$ macro-CTA) via RAFT Solution Polymerisation

To a round-bottomed flask containing CPCP RAFT agent (0.96 g, 3.43 mmol), G monomer (38.44 g, 0.24 mol) and anhydrous ethanol (59.40 g, 1.28 mol) were added to afford a target degree of polymerisation (DP) of 70. To this, ACVA initiator (0.19 g, 0.69 mmol, CTA/ACVA molar ratio = 5.0) was added and the resulting pink solution was sparged with N$_2$ for 20 minutes, before the sealed flask was immersed into an oil bath set at 70 °C. After 2.5 h (conversion 88 % as judged by ^{1}H NMR) the polymerisation was quenched by immersion of the flask in an ice bath and opening it to air. The polymerisation solution was then precipitated into a ten-fold excess of DCM and washed three times in the precipitation solvent before being placed under high vacuum for three days at 40 °C. ^{1}H NMR analysis indicated a DP of 70 for this macro-CTA. DMF GPC analysis indicated M_n and M_w/M_n values of 16,500 g mol^{-1} and 1.11, respectively.

2.1.2.8 Synthesis of Poly(glycerol monomethacrylate)$_{70}$-Poly(benzyl methacrylate)$_x$ (G$_{70}$-B$_x$) via RAFT Emulsion Polymerisation

A typical protocol for the synthesis of G$_{70}$-B$_{100}$ is given as below: G$_{70}$ macro-CTA (115 mg, 10 μmol) and ACVA initiator (0.9 mg; 3.3 μmol, macro-CTA/ACVA molar ratio = 3.0) were weighed into a vial containing a magnetic stirrer bar. Thereafter, deionised water (2.6 g) and benzyl methacrylate (B monomer, 176 mg, 1 mmol, target DP = 100) were added, giving a final solid concentration of 10 % w/w. The vial was sealed and purged with N$_2$ for 30 min prior to transfer to a preheated oil bath set at 70 °C for 24 h. To prepare G$_{70}$-B$_{300}$ diblock copolymer nanoparticles, the usage of benzyl methacrylate should be increased to 3 mmol and deionized water should also be tuned to target desired solid concentrations.

2.1.2.9 Synthesis of Poly(ammonium 2-sulfatoethyl methacrylate)$_x$ macro-CTA (S$_x$ macro-CTA)

Briefly, a typical protocol for the synthesis of S_{73} macro-CTA is as follows: a 25 % w/v aqueous solution of S monomer (136.0 g, 0.15 mol; target DP = 60) was weighed into a 250 mL round-bottomed flask equipped with a magnetic stirrer. Before addition of the CPCP RAFT agent (0.70 g, 2.50 mmol) and ACVA initiator (0.14 g, 0.50 mmol; CPCP/ACVA molar ratio = 5.0), the solution pH was adjusted to pH 6 by dropwise addition of 1 M NaOH solution. The flask was sealed using a rubber septum and degassed with N_2 for 30 min and then transferred to an oil bath preheated to 70 °C. After 2 h, the RAFT polymerisation was quenched by cooling the flask in ice followed by exposure to air. The reaction mixture was then placed in a -20 °C freezer overnight. The remaining polymer was dissolved in methanol and filtered to remove any excess insoluble monomer; thereafter, the filtrate was added dropwise to excess dichloromethane with continuous stirring to precipitate the polymer. The solvent was carefully decanted, the precipitate was redissolved in water and freeze-dried overnight to obtain the S_x macro-CTA. ^{1}H NMR studies indicated 90% conversion and the CTA efficiency was calculated to be 74 %. Aqueous GPC analysis (vs. poly(ethylene oxide) standards) indicated M_n and M_w/M_n values of 14,900 g mol^{-1} and 1.12, respectively.

2.1.2.10 Synthesis of Poly(ammonium 2-sulfatoethyl methacrylate)$_x$-Poly(benzyl methacrylate)$_y$ (S_x-B_y) Diblock Copolymer Nanoparticles

The synthesis of S_{73}-B_{300} at 10 % w/w solids is representative and was conducted as follows. S_{73} macro-CTA (337 mg, 20.0 μmol) and ACVA initiator (1.9 mg; 6.7 μmol, macro-CTA/ACVA molar ratio = 3.0) were weighed into a vial containing a magnetic stirrer bar. B monomer (1057 mg, 6.0 mmol, target DP = 300) was added, followed by 12.5 g of either deionized water for aqueous emulsion polymerisation or a 2:1 v/v ethanol/water mixture for dispersion polymerisation. The vial was sealed and purged with N_2 for 30 min prior to transfer to a preheated oil bath set at 70 °C for 24 h. For diblock copolymer nanoparticles prepared by RAFT dispersion polymerisation, the ethanol co-solvent was removed by dialysis against deionised water (dialysis tubing MWCO = 5,000).

2.1.2.11 Synthesis of [0.5 Poly(ammonium 2-sulfatoethyl methacrylate)$_{73}$ + 0.5 Poly(glycerol monomethacrylate)$_{70}$]-Poly(benzyl methacrylate)$_{300}$ [0.5 S$_{73}$ + 0.5 G$_{70}$]-B$_{300}$ Diblock Copolymer Nanoparticles

S$_{73}$ macro-CTA (84 mg, 5 µmol), G$_{70}$ macro-CTA (57 mg, 5 µmol) and ACVA initiator (0.9 mg; 3.3 µmol, total macro-CTA/ACVA molar ratio = 3.0) were weighed into a vial containing a magnetic stirrer bar. Thereafter, deionised water and B monomer (529 mg, 3 mmol, target DP = 300) were added, targeting a final copolymer concentration of 10 % w/w solids. The vial was sealed and purged with N$_2$ for 30 min prior to transfer to a preheated oil bath set at 70 °C for 24 h.

2.1.2.12 Synthesis of Poly(methacrylate acid)$_{68}$ macro-CTA (M$_{68}$ macro-CTA)

The synthesis of poly(methacrylate acid) macro-CTAs has been described in detail elsewhere.[3] A typical synthesis of M$_{68}$ macro-CTA was conducted as follows. A 50 ml round-bottomed flask was charged with M monomer (7.00 g; 81.4 mmol), CPCP (0.325 g; 1.16 mmol; target DP = 70), ACVA (0.065 g, 0.23 mmol, CPCP/ACVA molar ratio = 5.0), and ethanol (11.0 g). The sealed reaction vessel was purged with nitrogen and placed in a pre-heated oil bath at 70 °C for 3 h. The resulting macro-CTA (monomer conversion = 74 %; M_n = 9 300 g mol^{-1}, M_w/M_n = 1.08) was purified by dialysis against water and freeze-dried overnight. The mean degree of polymerisation (DP) of this macro-CTA was determined to be 68 using ^{1}H NMR spectroscopy and the CTA efficiency was calculated to be 76 %.

2.1.2.13 Synthesis of Poly(methacrylic acid)$_{68}$-Poly(benzyl methacrylate)$_{300}$ (M$_{68}$-B$_{300}$) Nanoparticles by RAFT Aqueous Emulsion Polymerisation

M$_{68}$ macro-CTA (122 mg, 20 µmol) was weighed in a 17 mL vial containing a magnetic stirrer bar, followed by water (10.6 g). The pH was carefully adjusted to around 5 by 0.1 M NaOH. Thereafter, ACVA initiator (1.9 mg, 6.7 µmol, macro-CTA/initiator mole ratio = 3.0) was added and B monomer (1060 mg, 6.0 mmol) was weighed into the vial. The vial was sealed and purged with N$_2$ for 30 min prior to transfer to a preheated oil bath set at 70 °C for 24 h. ^{1}H NMR studies indicated a

final B monomer conversion of > 99 %. The resulting M_{68}-B_{300} were used without further purification.

2.1.2.14 Synthesis of [0.5 Poly(ammonium 2-sulfatoethyl methacrylate)$_{73}$ + 0.5 Poly(methacrylic acid)$_{68}$]-Poly(benzyl methacrylate)$_{300}$ ([0.5 S$_{73}$ + 0.5 M$_{68}$]-B$_{300}$) Nanoparticles by RAFT Aqueous Emulsion Polymerisation

M_{68} macro-CTA (61 mg, 10 µmol) and S_{73} macro-CTA (168 mg, 10 µmol) were weighed into a 17 mL vial containing a magnetic stirrer bar and then water (12.8 g) was added. The pH was carefully adjusted to around 5 using 0.1 M NaOH. Thereafter, ACVA initiator (1.9 mg, 6.7 µmol, macro-CTA/initiator mole ratio = 3.0) was added and B monomer (1057 mg, 6 mmol) was weighed into the vial. The vial was sealed and purged with N_2 for 30 min prior to transfer to a preheated oil bath set at 70 °C for 24 h. ^{1}H NMR studies indicated a final B monomer conversion of > 99 %. The resulting [0.5 S$_{73}$ + 0.5 M$_{68}$]-B$_{300}$ were used without further purification.

2.1.2.15 Synthesis of Poly(glycerol monomethacrylate)$_{70}$-stabilised Gold Nanoparticles (G$_{70}$-AuNPs)

The synthesis of gold nanoparticles has previously been reported elsewhere.[4] In the present study, 480 mL deionised water was charged into a 1000 mL beaker and then 5.0 mL of 10 g L^{-1} gold(III) chloride trihydrate was added and stirred for 5 minutes. Thereafter, sodium citrate aqueous solution (10 mL, 38.8 mM) was added and stirred for another 5 minutes before rapid addition of sodium borohydride aqueous solution (5.0 mL, 0.075 % w/w), containing sodium citrate tribasic dehydrate (57 mg, 38.8 mM). G_{70} macro-CTA (100 mg) was dissolved in 10 mL deionised water and added to the gold sol. Excess G_{70} macro-CTA and sodium citrate were removed by centrifugation, followed by dialysis against deionised water for 7 days, using dialysis tubing with a molecular weight cut-off of 50 kD.

For the 14 nm gold nanoparticles, 500 mL deionised water was mixed with 30.0 mL 1 % w/w sodium citrate solution in a 1000 mL beaker and heated to boiling for 5 minutes, followed by the rapid addition of 5.0 mL 10 mg mL^{-1} gold(III) chloride

trihydrate. The reaction was allowed to proceed for 15 minutes. 100 mg G_{70} macro-CTA dissolved in 10.0 mL water was then added and the G_{70} modified gold nanoparticles were purified by centrifugation.

2.1.3 Occlusion of Nanoparticles within Crystals

2.1.3.1 Precipitation of Calcium Carbonate Crystals in the Presence of Block Copolymer Nanoparticles

$CaCO_3$ crystals were precipitated onto glass slides via the ammonium diffusion method. Specifically, a glass slide (pre-treated with Piranha solution) was placed in a 1.5 mM calcium chloride solution containing copolymer nanoparticles or without any additives at pH 9.5. 10 mL of this solution was placed within a sealed desiccator containing 2.0 g of solid ammonium carbonate for 24 h. Crystallisation was triggered by the slow decomposition of ammonium carbonate, producing CO_2 and ammonia. The CO_2 provides a source of CO_3^{2-} ions, which therefore reacts with Ca^{2+} ions to form $CaCO_3$ crystals. CO_2 diffusion alone would result in a pH reduction within the reaction solution. The solubility of $CaCO_3$ is greater at low pH, thus the $CaCO_3$ crystal frmation will be prevented because supersaturation would never be reached at low pH. Fortunately, the ammonia acts as a buffer agent and maintains the pH of the reaction solution at ~ 9.5, reducing the solubility of $CaCO_3$ crystals and hence promoting their growth. After crystallisation, the glass slide was removed from the aqueous solution and thoroughly washed with deionised water and ethanol.

2.1.3.2 Precipitation of Zinc Oxide Crystals in the Presence of Copolymer Nanoparticles

Various volumes of aqueous nanoparticle dispersions (5.0 % w/w, 0 – 2 ml) were added to a two-necked flask containing 90 – 88 ml of an aqueous solution of zinc nitrate hexahydrate (0.446 g, 1.50 mmol). The initial pH was measured to be around 5 for all the above experiments prior to the reaction. This flask was connected with a condenser and transferred to a preheated oil bath set at 90 °C and the reaction mixture was magnetically stirred to achieve thermal equilibrium (typically 30 min).

ZnO formation commenced on addition of 10 ml of an aqueous solution of hexamethylenetetramine (HMTA, 0.210 g, 1.50 mmol), which thermally decomposes to form ammonia and formaldehyde at 90 ℃. After 90 min at this temperature, the reaction was quenched by cooling in an ice-water bath and the final pH was measured to be around 6. The precipitate was isolated by centrifugation and washed several times using water or ethanol, followed by drying under vacuum at 40 °C.

2.1.3.4 Synthesis of G_{70}-Au/ZnO Nanocomposite Crystals

Aqueous G_{70}-AuNP dispersions (0.5 g L^{-1}, 2.0 – 30.0 mL) were added to a two-necked flask containing 96.0 – 68.0 ml of an aqueous solution of zinc nitrate hexahydrate (0.446 g, 1.50 mmol) to give a total volume of 98.0 mL. This flask was connected to a condenser and transferred to a preheated oil bath set at 90 °C and the reaction mixture was magnetically stirred to achieve thermal equilibrium (typically 30 min). ZnO formation was commenced on *slow* addition of 2.0 mL of an aqueous solution of HMTA (0.210 g, 1.50 mmol). The reaction was quenched after 90 minutes by cooling in an ice-water bath. The precipitate was isolated by centrifugation and washed several times using water or ethanol, followed by drying under vacuum at 40 °C. For G_{70}-Au occluded within the surface layer of ZnO, G_{70}-AuNPs were added into the reaction solution 30 min later.

2.1.4 Photocatalytic Activity Test

Au/ZnO nanocomposites (10 mg) were dispersed in deionised water (18.0 mL) with the aid of an ultrasonic bath for 10 minutes. 2.0 mL of a 1.0×10^{-4} M RhB stock solution was added and continuously stirred in the dark for 30 minutes before irradiation using a UV lamp 6 cm above the solution (6 W, peak emission = 254 nm). Aliquots were extracted at various times and centrifuged prior to recording the visible absorption spectrum of the supernatant solution. The photodegradation of the RhB dye was monitored via the gradual reduction in its absorption maximum at 553 nm. Photocatalysis experiment was conducted at pH 7 under room temperature and repeated in triplicate.

2.2 Characterisation

2.2.1 ^{1}H NMR Spectroscopy

^{1}H NMR spectra were recorded using a Bruker Avance 400 spectrometer operating at 400 MHz using either D_2O, CD_3OD or CD_2Cl_2 as solvents.

2.2.2 Dynamic Light Scattering (DLS) and Aqueous Electrophoresis

DLS measurements were conducted using a Malvern Zetasizer NanoZS instrument by detecting back-scattered light at an angle of 173°. The concentration used for the DLS test may vary in this Thesis. If otherwise mentioned, it means the concentration is ~ 0.1 % w/w. Aqueous electrophoresis measurements were conducted in disposable folded capillary cells supplied by Malvern (DTS1070) using the same instrument and each measurement was repeated three times and averaged to give the mean zeta potential.

2.2.3 Gel Permeation Chromatography (GPC)

Aqueous GPC measurements were performed using an Agilent Technologies Infinity 1260 set-up equipped with two Agilent PL Aquagel-OH 30 8 μm columns running at 35 °C. Phosphate buffer eluent was used as GPC eluent at a flow rate of 1.0 mL min^{-1} (refractive index detector). Calibration was achieved using a series of near-monodisperse poly(ethylene oxide) standards ranging from 4.1 x 10^3 to 6.92 x 10^5 g mol^{-1}. The THF GPC system was equipped with two 5 μm (30 cm) Mixed-C columns; a WellChrom K-2301 refractive index detector operating at 950 ± 30 nm, a Precision detector PD 2020 light scattering detector (with scattering angles of 90º and 15º), and a BV400RT solution viscosity detector. The THF eluent containing 2 % v/v triethylamine and 0.05 % w/v butylhydroxytoluene (BHT) at a flow rate of 1.0 mL min^{-1}; A series of ten near-monodisperse poly(methyl methacrylate) standards ranging from 1.28 x 10^3 to 3.3 x 10^5 g mol^{-1} were employed as calibration standards with the above refractive index detector. The DMF GPC set-up was operated at 60 °C with the instrument comprising two Polymer Laboratories PL gel 5 μm Mixed C columns and one PL polar gel 5 μm guard column connected in series to a Varian

390-LC multi-detector suite (refractive index detector only) and a Varian 290-LC pump injection module. The GPC eluent was HPLC-grade DMF containing 10 mM LiBr and was filtered prior to use. The flow rate was 1.0 mL min^{-1} and DMSO was used as a flow-rate marker. Calibration was conducted using a series of ten near-monodisperse poly(methyl methacrylate) standards (M_n = 6.25 $\times$ 10^2 – 6.18 $\times$ 10^5 g mol^{-1}, K = 2.094 $\times$ 10^{-3}, α = 0.642). Chromatograms were analysed using Varian Cirrus GPC software.

2.2.4 Transmission Electron Microscopy (TEM)

TEM images were obtained by adsorbing a 0.15 % w/w aqueous dispersion of copolymer nanoparticles onto palladium-copper grids (Agar Scientific, UK) coated with carbon film. The grids were treated with a plasma glow discharge for about 30 seconds to create a hydrophilic surface prior to addition of the aqueous nanoparticle dispersion (5 µL). Excess solvent was removed via blotting and the grid was stained with uranyl formate for 30 seconds. Excess stain was removed via blotting and the grid was carefully dried under vacuum. Imaging was performed using a FEI Tecnai G2 Spirit instrument. To examine internal structures, the G$_{70}$-Au/ZnO nanocomposites were embedded in Araldite resin mixture and cured at 60 °C for 48-72 h. Ultrathin sections, approximately 85 nm in thickness, were cut using a Leica UC 6 ultramicrotome equipped with a Diatome diamond knife onto 200 mesh copper grids. TEM images were performed using either a FEI Tecnai G2 Spirit instrument (120 kV) or a high resolution TEM (Philips FEG-CM200) operating at an accelerating voltage of 200 kV.

2.2.5 Field Emission Scanning Electron Microscopy (FE-SEM)

The crystal morphology was investigated using a high-resolution field emission scanning electron microscope (Nova NanoSEM 450) or FEI Inspect F. Glass slides supporting these crystals were mounted onto SEM stubs using adhesive conducting pads with no further coating. The samples were fractured by placing a clean glass slide on top of the glass slide supporting the calcite crystals and pressing down and

twisting gently. A relatively low voltage (2-3 kV) was used in order to prevent sample charging.

2.2.6 Disk Centrifuge Photosedimentometry (DCP)

Particle size distributions of the S_{73}-B_{300}/ZnO nanocomposite particles and calcined ZnO particles were assessed using a disc centrifuge photosedimentometer (CPS DC24000 instrument). This technique reports a weight-average particle diameter (D_w). Dilute aqueous dispersions (0.10 ml at 0.10 % w/w) were injected into an aqueous spin fluid (15 mL) comprising an 8 - 24 % w/w sucrose gradient. The densities of the S_{73}-B_{300}/ZnO and ZnO particles were determined at 20 °C by helium pycnometry (Micrometrics AccuPyc 1330 helium pycnometer).

2.2.7 Analytical Centrifugation

LUMiSizer® instrument has similar basic principles compared with disc centrifuge photosedimentometry (DCP).[5-7] The LUMiSizer® employs STEP™-Technology (Space- and Time-resolved Extinction Profiles), which enables the measurement of the intensity of transmitted light as a function of time and position over the entire cell length at the same time. The progression of the transmission profiles contains information on the rate of sedimentation. Given the particle density, the particle size distribution of the particles can be readily obtained via this instrument. Volume-average particle size distribution of ZnO particles mineralized in the presence of 0.50 g L^{-1} S_{73}-B_{300} copolymer particles was determined via analytical centrifugation using a LUMiSizer® instrument (LUM GmbH, Berlin, Germany) at 20 °C. The measurements were carried out on 2 % w/v aqueous dispersions in polyamide cells (path length = 2 mm) using centrifugation rate of 500 rpm.

2.2.8 X-ray Photoelectron Spectroscopy (XPS)

XPS samples were prepared by adding a drop of nanocomposite aqueous dispersion onto clean indium foil and left overnight at room temperature. The powder samples

were directly pressed on a clean indium foil. The instrument used to collect the XPS data was a Kratos Axis Ultra DLD equipped with a monochromatic Al X-ray radiation at 6.0 mA and 15 kV at a typical base pressure of 10^{-8} Torr. The step size was 0.5 eV for the survey spectra (pass energy = 160 eV) and 0.05 eV for the high resolution spectra (pass energy = 20 eV). The raw data was corrected by a transmission function characteristic of the instrument, determined using software from the National Physical Laboratory. The adjusted data was then quantified using the theoretically derived Scofield relative sensitivity factors.

2.2.9 Other Measurements

Optical microscopy images were recorded using a Motic DMBA300 digital biological microscope equipped with a built-in camera and analysed using Motic Images Plus 2.0 ML software. Raman studies were conducted using a Renishaw 2000 Raman microscope operating with a 785 nm diode laser. Thermogravimetric analysis (TGA) was conducted using a Perkin-Elmer Pyris 1 TGA instrument. FT-IR spectra were recorded on KBr pellets using a Perkin Elmer spectrum 100 spectrometer at 4 cm^{-1} resolution. The elemental analysis was conducted using a Perkin Elmer 2400 Series II CHNS/O Elemental Analyser. Powder X-ray diffraction (XRD) measurements were made using a Bruker D2 Phaser Desktop X-ray diffractometer equipped with Ni-filtered Cu Kα radiation (λ = 1.542 Å) operating at an accelerating voltage and emission current of 30 kV and 10 mA, respectively. The amount of calcium chelated by the diblock copolymer was measured using a calcium-selective electrode (Ion selective combination electrode Eutech Calcium, Fisher Scientific). The calcium-selective electrode was then immersed into the polymer solutions to measure the free Ca^{2+} concentration. A calibration curve was produced prior to the measurement using a range of $CaCl_2$ standard solutions (0.0001, 0.001, 0.01, and 0.1). The samples were then quantified by means of the calibration curve (y = 25.41x + 452.3, R^2 > 0.999). The amount of polymer-bound calcium was calculated from the total amount of Ca^{2+} added and the amount of free Ca^{2+} measured. The Au content of G_{70}-Au/ZnO nanocomposite particles was determined by a Hewlett-Packard 4500 inductively-coupled plasma mass spectrometry (ICP-MS, Hewlett-Packard, Yokogawa Corporation, Japan). UV-vis spectra were recorded at

20 °C for the nanocomposite aqueous dispersion using a Perkin-Elmer Lambda 25 instrument operating between 200 and 800 nm. Specific surface areas were determined via BET surface area analysis using N_2 as an adsorbate at 77 K. The densities of the G_{70}-Au and G_{70}-Au/ZnO nanocomposites were determined by helium pycnometry at 20 °C (Micrometrics AccuPyc 1330 helium pycnometer). The number-average mean diameter of the Au nanoparticles was determined by analysing TEM images using Image j software, whereby more than 200 AuNPs were counted.

2.3 References

(1) Kristensen, T. E.; Vestli, K.; Fredriksen, K. A.; Hansen, F. K.; Hansen, T. Synthesis of Acrylic Polymer Beads for Solid-Supported Proline-Derived Organocatalysts. *Organic Letters* **2009**, *11*, 2968-2971.

(2) Jones, E. R.; Semsarilar, M.; Blanazs, A.; Armes, S. P. Efficient Synthesis of Amine-Functional Diblock Copolymer Nanoparticles via RAFT Dispersion Polymerization of Benzyl Methacrylate in Alcoholic Media. *Macromolecules* **2012**, *45*, 5091-5098.

(3) Semsarilar, M.; Jones, E. R.; Blanazs, A.; Armes, S. P. Efficient Synthesis of Sterically-Stabilized Nano-Objects via RAFT Dispersion Polymerization of Benzyl Methacrylate in Alcoholic Media. *Advanced Materials* **2012**, *24*, 3378-3382.

(4) Frens, G. Controlled nucleation for the regulation of the particle size in monodisperse gold suspensions. *Nature* **1973**, *241*, 20-22.

(5) Detloff, T.; Sobisch, T.; Lerche, D. Particle size distribution by space or time dependent extinction profiles obtained by analytical centrifugation (concentrated systems). *Powder Technology* **2007**, *174*, 50-55.

(6) Janotti, A.; Van de Walle, C. G. Fundamentals of zinc oxide as a semiconductor. *Reports on Progress in Physics* **2009**, *72*, 126501.

(7) Growney, D. J.; Mykhaylyk, O. O.; Armes, S. P. Micellization and Adsorption Behavior of a Near-Monodisperse Polystyrene-Based Diblock Copolymer in Nonpolar Media. *Langmuir* **2014**, *30*, 6047-6056.

3. Chapter Three

3. Incorporating Diblock Copolymer Nanoparticles into Calcite Crystals: Do Anionic Carboxylate Groups Alone Ensure Efficient Occlusion?

3.1 Introduction

Based on studies to date, it seems that carboxylate functionality at the nanoparticle surface promotes efficient occlusion within calcite.[1-4] However, the design rules for occlusion are not yet understood. This lack of detailed molecular level understanding is a significant barrier to optimising the occlusion efficiency for calcite and also for extending occlusion to include alternative inorganic host crystals. Ultimately, this is the key to producing new copolymer/crystal nanocomposites that exhibit a range of tailored properties. In this Chapter, we examine the 'carboxylate surface functionality' design rule in more detail.

Here, RAFT-mediated PISA is used to design two new examples of diblock copolymer nanoparticles. More specifically, either a poly(carboxybetaine methacrylate)$_{52}$ (C$_{52}$ macro-CTA) or a poly(proline methacrylate)$_{50}$ (P$_{50}$ macro-CTA) is chain-extended with 2-hydroxypropyl methacrylate (H) via RAFT aqueous dispersion polymerisation at 70 °C and 20 % w/w solids. In both cases the stabiliser block contains carboxylate groups. However, P$_{50}$ stabiliser is *anionic* above pH 9.2, whereas C$_{52}$ stabiliser possesses *zwitterionic* character. Thus the design rule hypothesis that will be tested herein is the following: *is the presence of carboxylate groups alone sufficient to promote efficient nanoparticle occlusion within calcite, or is overall anionic character also required?*

3.2 Results and Discussion

3.2.1 Synthesis of RAFT Agent (MPETTC)

A water-soluble (pH < 4.5) trithiocarbonate-based RAFT CTA (MPETTC) containing a morpholine group was prepared via a two-step synthesis, as recently described by Penfold and co-workers (see **Scheme 3.1**).[5] First, 4-cyano-4-(2-phenylethanesulfanylthiocarbonyl)sulfanylpentanoic succinimide ester (SPETTC) was obtained by conjugation of *N*-hydroxylsuccinimide with 4-cyano-4-(2-phenylethanesulfanyl-thiocarbonyl)sulfanylpentanoic acid (PETTC), as shown in **Scheme 3.1**. Thereafter, SPETTC was further reacted with 4-(2-aminoethyl)morpholine because amines react preferentially with succinimidyl esters rather than with the RAFT trithiocarbonate group. To maximise

the RAFT agent fidelity, the amine/succinimidyl ester molar ratio was maintained below unity (0.95 eq.).[6,7] Below pH 4.5, the protonated morpholine group facilitates the dissolution of MPETTC in water. This is important for the subsequent RAFT polymerisation of P and C monomers.
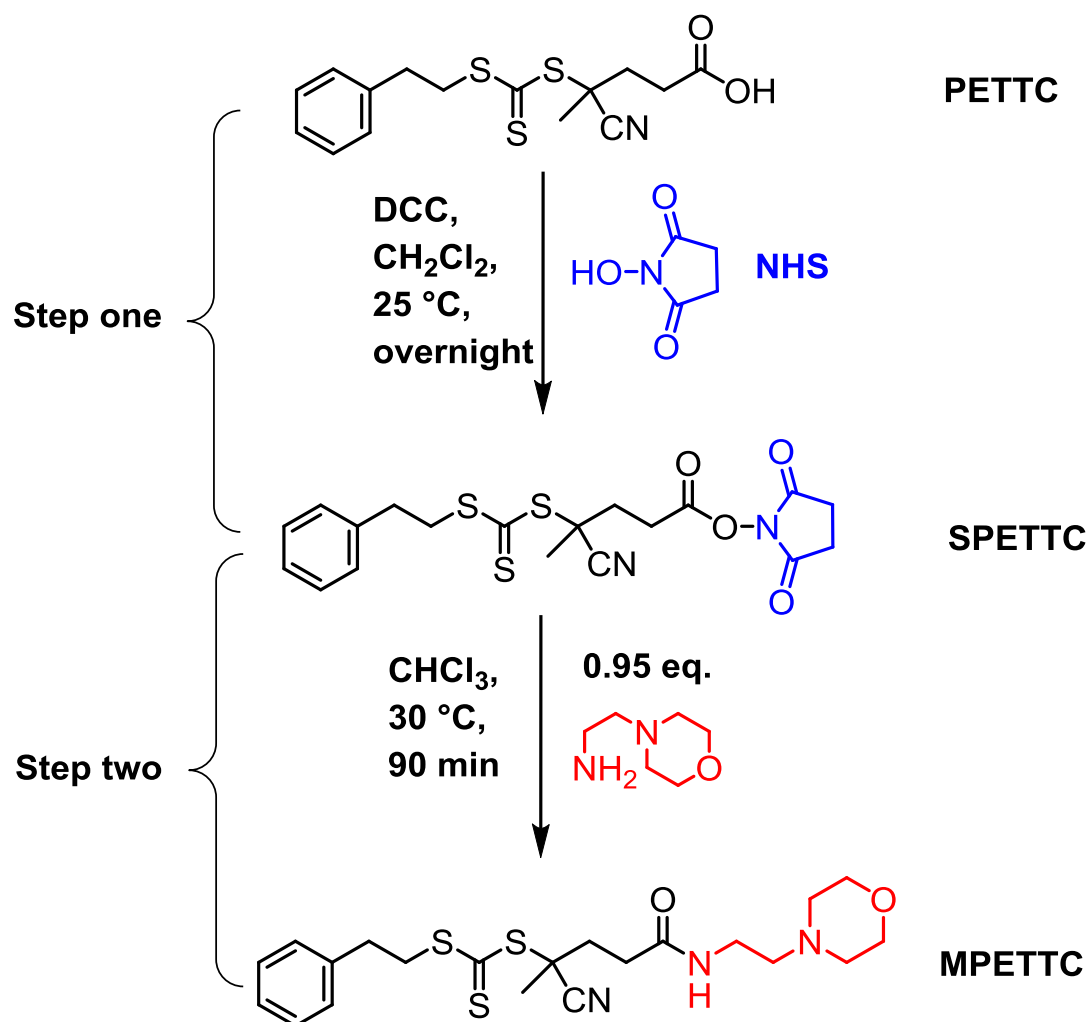
Scheme 3.1. A two-step way for synthesis of morpholine-functionalised trithiocarbonate-based RAFT chain transfer agent (MPETTC). Note: DCC = *N, N'*-dicyclohexylcarbodiimide.

3.2.2 Synthesis and Characterisation of C$_{52}$ and P$_{50}$ macro-CTAs

C monomer (see chemical structure shown in **Scheme 3.2**) was kindly donated by Dr. Saruwatari of the Osaka Organic Chemical Company, Japan. P monomer was synthesised as previously reported by Kristensen et al.[8] As shown in **Scheme 3.2**, this one-step, inexpensive method enables large-scale P monomer to be prepared

without recourse to protecting-group chemistry (detailed synthesis route can be found in the Experimental section). [8,9]
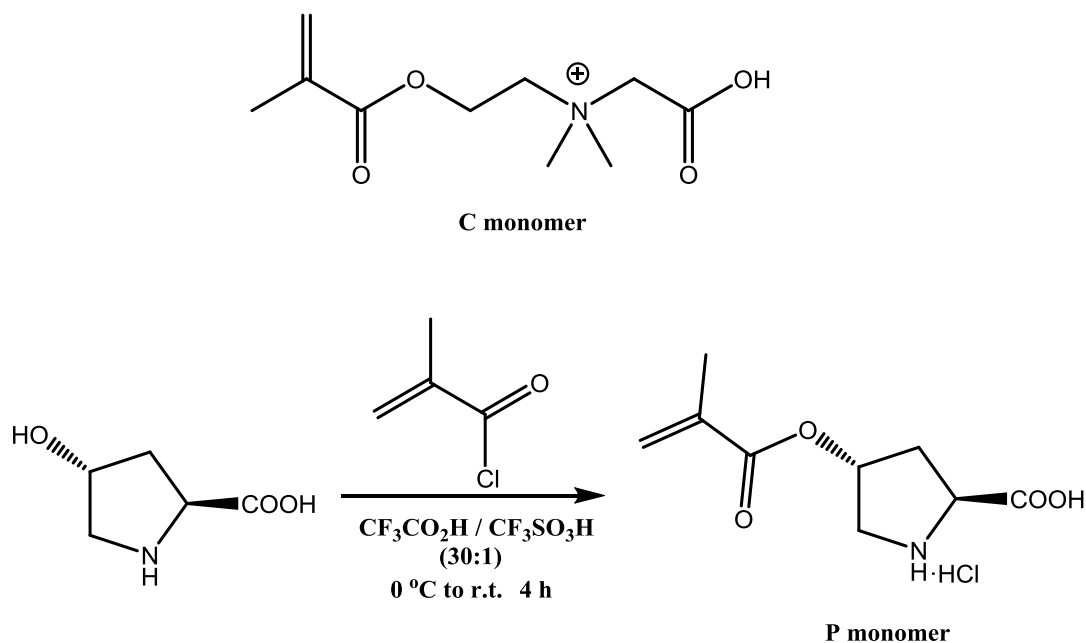
Scheme 3.2. Chemical structure of carboxybetaine methacrylate (C) and synthesis of *O*-methacryloyl-*trans*-4-hydroxy-*L*-proline (P).

Base titration of the carboxylic acid group in C monomer indicated a pK_a of ~ 2.3 (see **Figure 3.1a**). The quaternary ammonium group in C confers permanent cationic charge, so this molecule becomes zwitterionic after deprotonation of its carboxylic acid group.[10-12] In contrast, P monomer exhibits two pK_a values (pK_{a1} ~ 1.5, pK_{a2} ~ 9.0, see **Figure 3.1b**) owing to its carboxylic acid groups and secondary amine groups. On addition of base, the carboxylic acid group becomes deprotonated first, followed by deprotonation of the amine group, giving two distinct pK_a values.

C_{52} and P_{50} macro-CTAs were readily synthesised via RAFT polymerisation in aqueous solution using MPETTC and ACVA as chain transfer agent and initiator, respectively. The pK_a values of C_{52} and P_{50} are slightly higher compared to their corresponding monomers, as shown in **Figures 3.1 c** and **3.1d**.
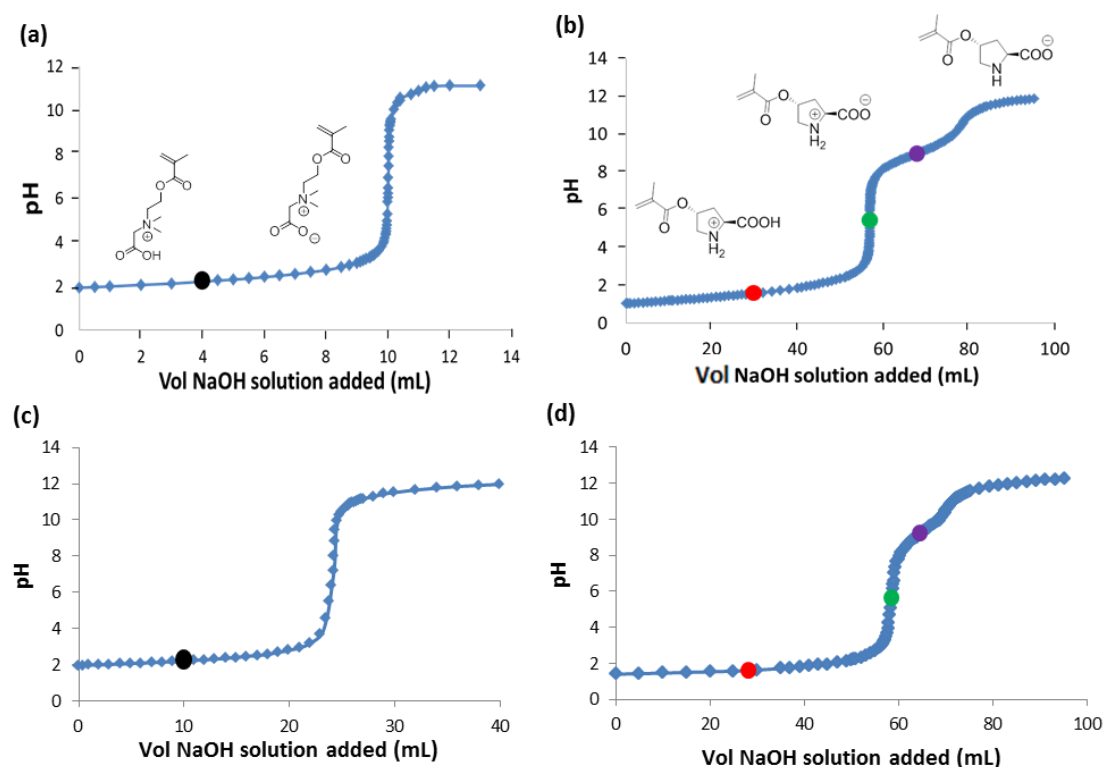
Figure 3.1. Titration curves obtained for dilute aqueous solutions of (a) C monomer; (b) P monomer; (c) C_{52}-H_{250} diblock copolymer nanoparticles; (d) P_{50}-H_{300} diblock copolymer nanoparticles. The pK_a calculated for C monomer is ~ 2.3 and pK_{a1} and pK_{a2} of P monomer are ~ 1.5 and ~ 9.0, respectively; The pK_a' value found for C_{52}-H_{250} nanoparticles is ~ 2.4 and pK_{a1}' and pK_{a2}' of P_{50}-H_{300} nanoparticles are ~ 1.6, and ~ 9.2, respectively; During titration, the solution pH was first adjusted to about pH 2.0 using 1.0 M HCl and then the solution was titrated by adding 0.01 M NaOH. Note: the crystallisation of calcium carbonate was carried out at pH 9.5.

Kinetic studies of the homopolymerisation of C confirmed that high conversions (> 90 %) could be obtained within 3 h. Moreover, there was a linear evolution of molecular weight with conversion, as expected for a well-controlled RAFT polymerisation (see **Figure 3.2**).[13] Similarly, kinetic studies of the homopolymerisation of P indicated that high conversions (> 90 %) could also be achieved within 3 h and a linear evolution of molecular weight with conversion was also obtained, as shown in **Figure 3.3b**.
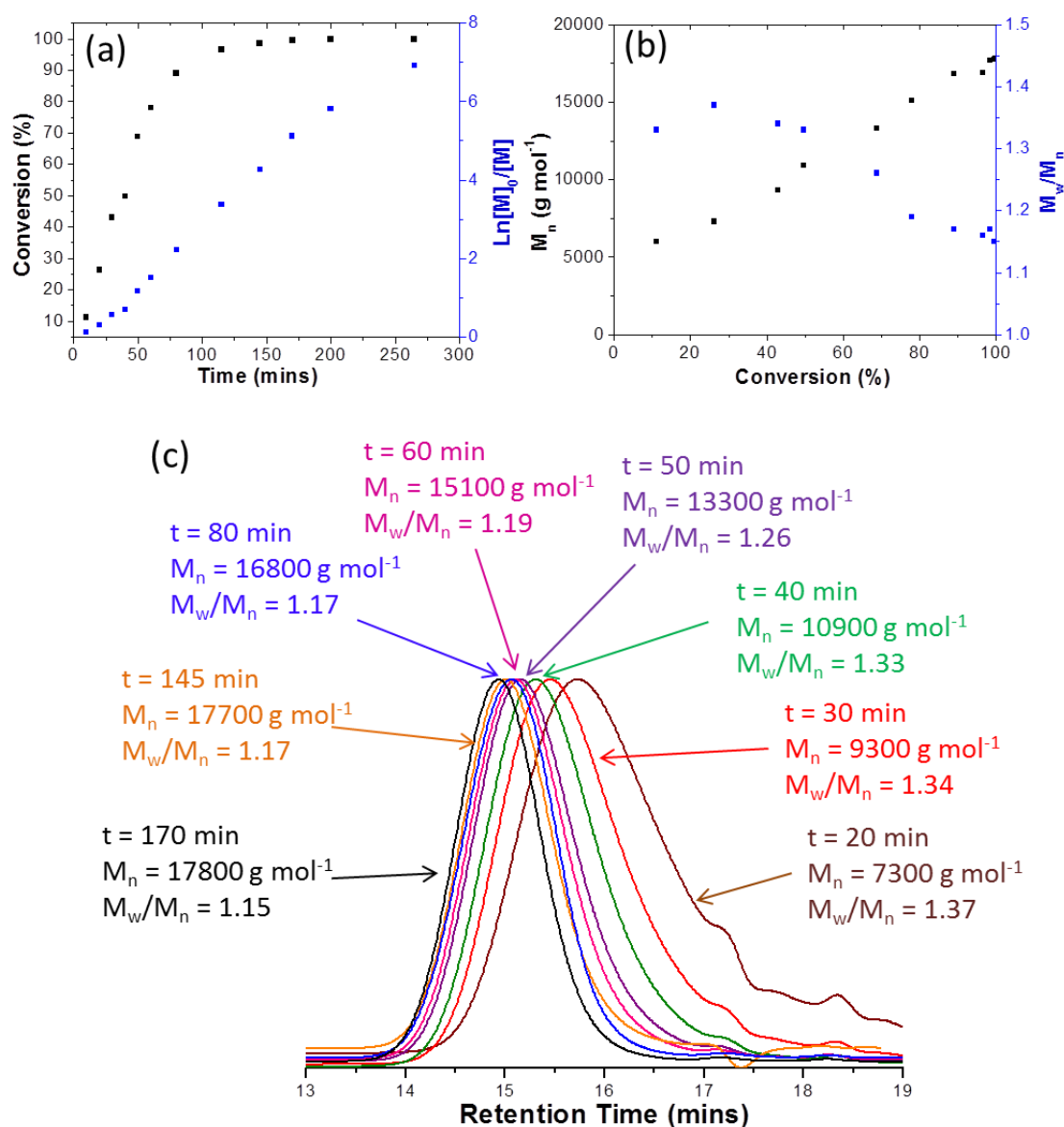
Figure 3.2. (a) Kinetics of the polymerisation of C monomer using a MPETTC chain transfer agent at 70 °C. Approximately 90 % conversion was achieved within 80 min and the semi-logarithmic plot exhibited a linear relationship. (b) Evolution of molecular weight (M_n) and M_w/M_n with conversion. (c) Gel permeation chromatograms (phosphate buffer eluent, refractive index detector) obtained for samples taken during the polymerisation of C monomer using MPETTC at 70 °C. Calibration was achieved using a series of near-monodisperse poly(ethylene oxide) standards.
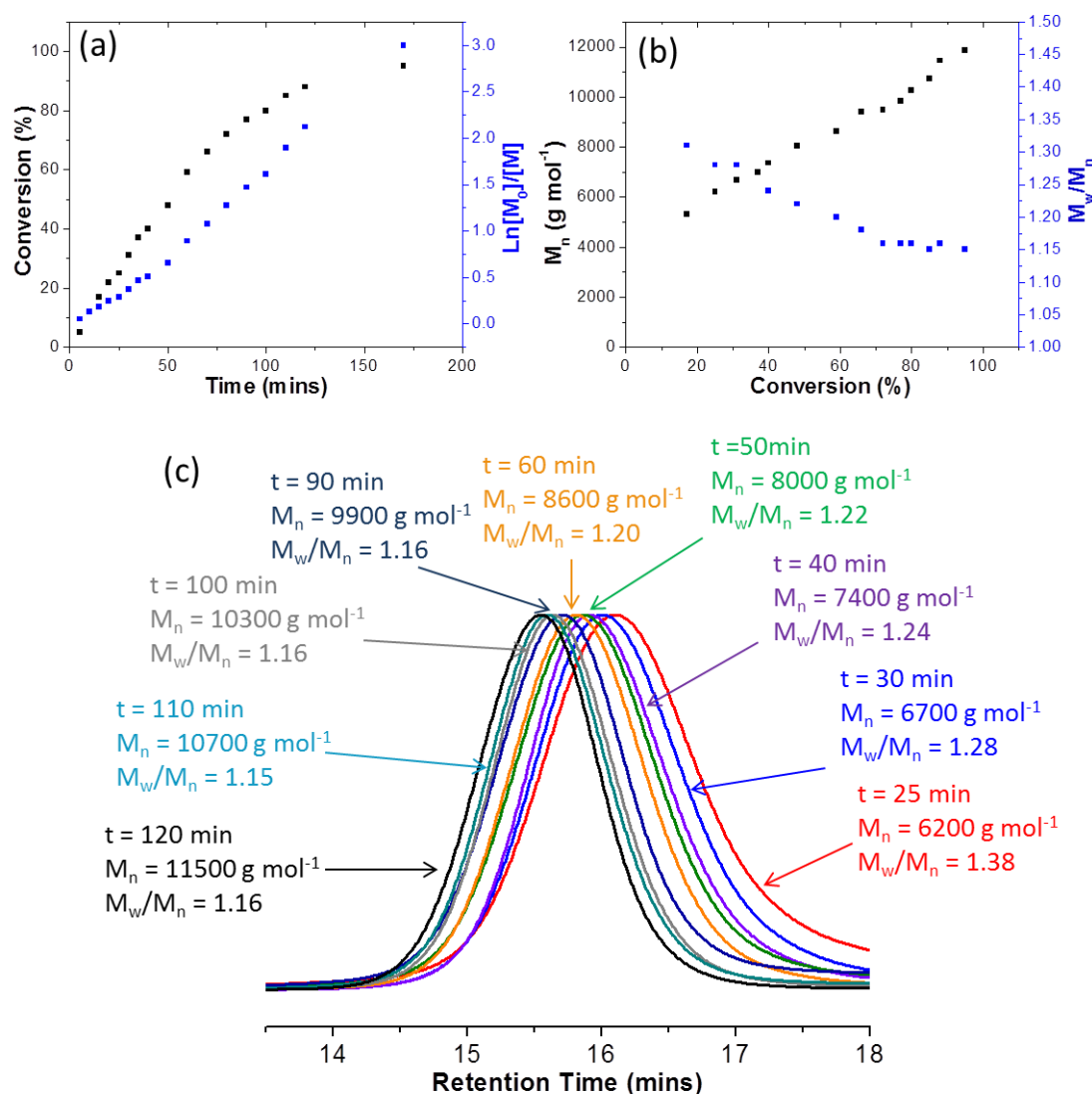
Figure 3.3. (a) Kinetics of the polymerisation of P using a MPETTC chain transfer agent at 70 °C. Approximately 90 % conversion was achieved within 3 h and the semi-logarithmic plot exhibited a linear relationship. (b) Evolution of molecular weight (M_n) and M_w/M_n with conversion. (c) Gel permeation chromatograms (phosphate buffer eluent, refractive index detector) obtained for samples taken during the polymerisation of P using MPETTC at 70 °C. Calibration was achieved using a series of near-monodisperse poly(ethylene oxide) standards.

Aqueous GPC studies indicated both C_{52} and P_{50} macro-CTAs possess relatively low molecular weight distribution ($M_w/M_n < 1.2$). It is worth noting that these two macro-CTAs have similar degrees of polymerisation. Hence the stabiliser layer thicknesses of the resulting copolymer nanoparticles should be relatively comparable. Given the lack of a suitable GPC eluent for analysis of the C-H and P-H copolymers,

the blocking efficiency of these two macro-CTAs were examined by self-blocking experiments. Briefly, addition of a further charge of the corresponding monomer i.e. C to the C_{52} macro-CTA or P to the P_{50} macro-CTA leads to chain extension. In both cases a relatively high blocking efficiency was achieved, suggesting that the majority of trithiocarbonate RAFT chain-ends remained intact (see **Figure 3.4**).

C_{52} macro-CTA: M_n = 9,500 g mol^{-1}; M_w/M_n = 1.17
Self-blocking: M_n = 28,500 g mol^{-1}; M_w/M_n = 1.30

P_{50} macro-CTA : M_n = 11,400 g mol^{-1}; M_w/M_n = 1.18
Self-blocking: M_n = 25,700 g mol^{-1}; M_w/M_n = 1.11
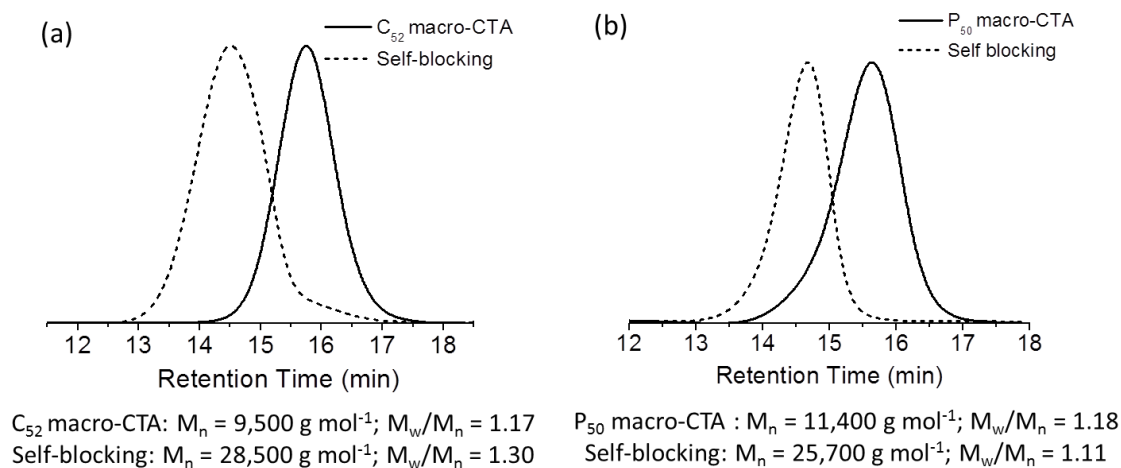
Figure 3.4. Gel permeation chromatography curves (phosphate buffer eluent, refractive index detector) obtained for chain extension of (a) C_{52} or (b) P_{50} with the corresponding C or P monomer.

3.2.3 Synthesis and Characterisation of C_{52}-H_{250} and P_{50}-H_{300} Diblock Copolymer Nanoparticles

Sterically-stabilised C_{52}-H_{250} and P_{50}-H_{300} diblock copolymer nanoparticles were readily synthesised by chain extension of each macro-CTA in turn with H using a RAFT aqueous dispersion polymerisation formulation (see **Scheme 3.3**). C_{52}-H_{250} and P_{50}-H_{300} were targeted since preliminary experiments indicated that such diblock copolymer compositions gave almost identical mean particle diameters. Indeed, as shown in **Figures 3.5a and 3.5b**, TEM analysis indicated that both types of nanoparticles possessed narrow particle size distributions with a mean diameter of 34.5 ± 3.4 nm for C_{52}-H_{250} and 33.6 ± 4.4 nm for P_{50}-H_{300}.

Aqueous electrophoresis measurements revealed that both types of nanoparticles were cationic at low pH but became anionic at high pH, with C_{52}-H_{250} and P_{50}-H_{300} exhibiting isoelectric points (IEPs) at around pH 6.6 and pH 4.1, respectively (see

Figure 3.5c). The effect of addition of $[Ca^{2+}]$ on nanoparticle zeta potential was also examined at pH 9.5 (**Figure 3.5d**).
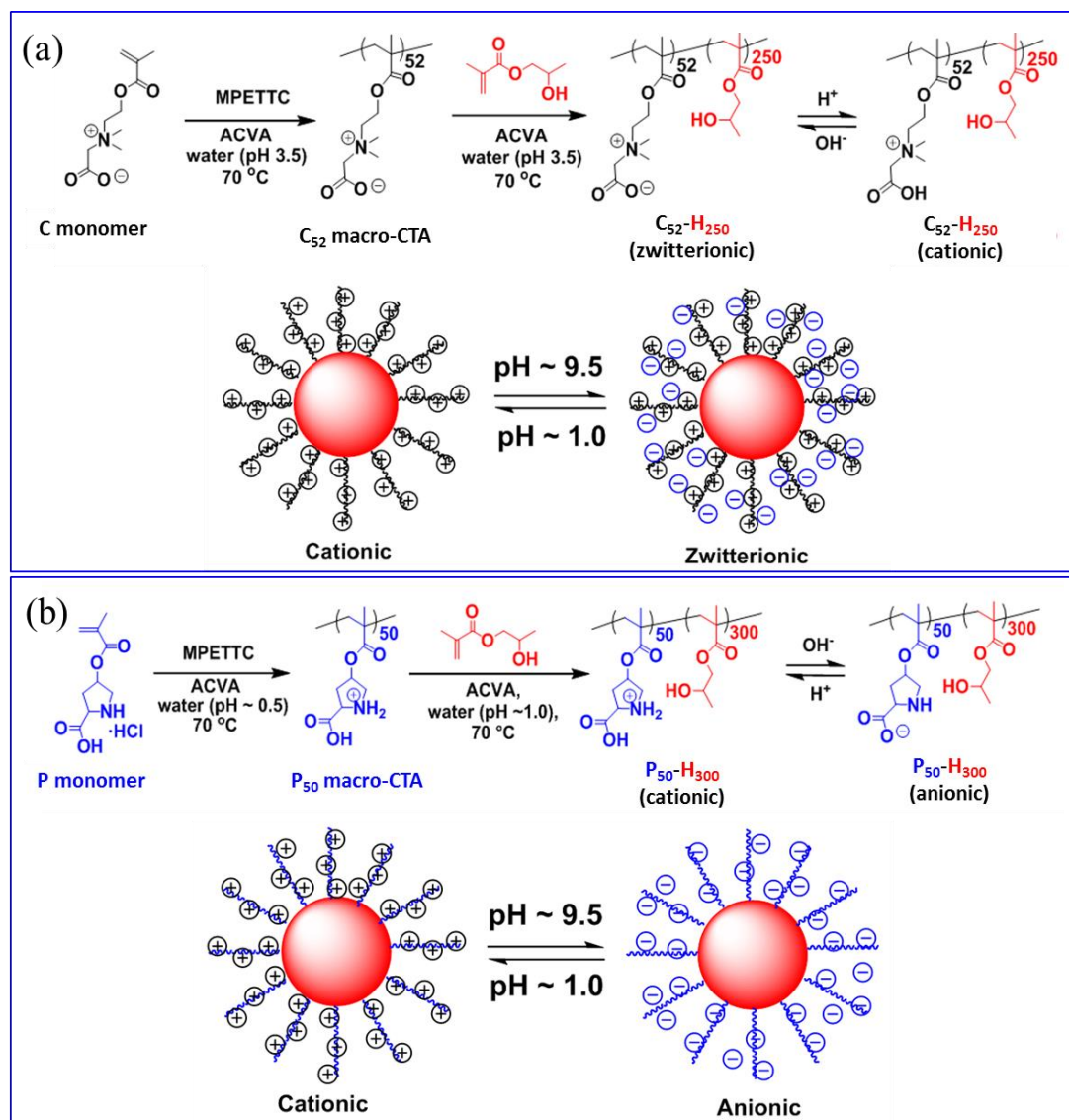
Scheme 3.3. Synthesis of (a) C_{52}-H_{250} and (b) P_{50}-H_{300} diblock copolymer nanoparticles via RAFT aqueous dispersion polymerisation of H at 70 °C. The cartoons depict the surface charge on these two types of sterically-stabilised nanoparticles at approximately pH 1.0 and pH 9.5, respectively.[14]

In both cases, the initial highly anionic character observed in the absence of any salt was significantly reduced, suggesting extensive Ca^{2+} binding to the steric stabiliser chains.[3] However the P_{50}-H_{300} nanoparticles retained a relatively high net negative zeta potential of -25 mV at $[Ca^{2+}]$ = 1.5 mM, whereas the zeta potential for the C_{52}-H_{250} was reduced to just about -3 mV under the same conditions. This difference

appears to be decisive in dictating the nanoparticle occlusion efficiency in each case (see below).
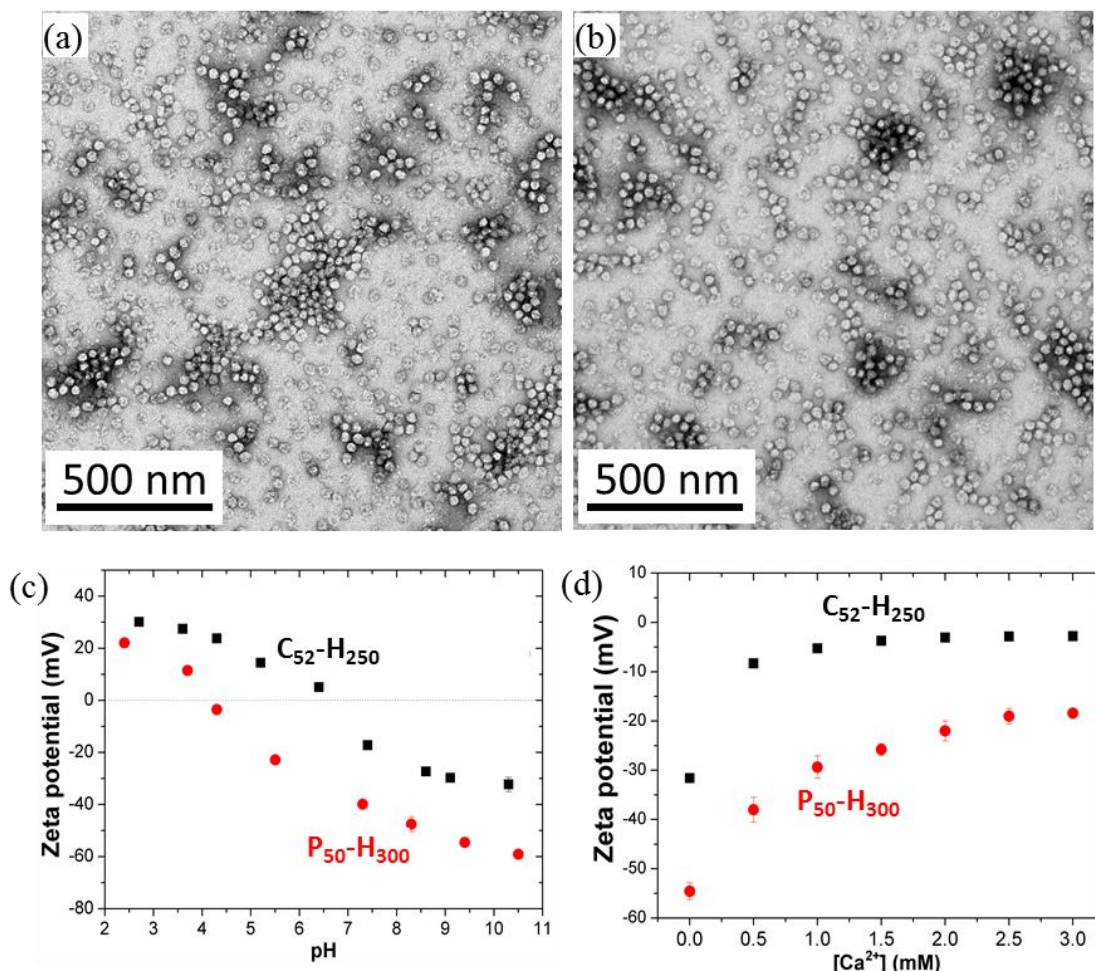
Figure 3.5. TEM images recorded for (a) C_{52}-H_{250} and (b) P_{50}-H_{300} diblock copolymer nanoparticles; (c) zeta potential versus pH and (d) zeta potential versus $[Ca^{2+}]$ obtained at pH 9.5 for C_{52}-H_{250} and P_{50}-H_{300} nanoparticles. Note: the zeta potential versus pH titration test was conducted without adding salt background and the pH was first tuned to pH 11 by NaOH.

Given that both C_{52} and P_{50} macro-CTAs have high blocking efficiency and the final conversion of HPMA monomer is very high (> 99%), thus the resulting diblock copolymer nanoparticles were used directly without further purification in the subsequent occlusion experiments. Meanwhile, dynamic light scattering studies (see **Figure 3.6**) confirmed that both types of nanoparticles exhibited essentially unchanged hydrodynamic diameters in the absence and presence of 1.5 mM $[Ca^{2+}]$, which indicated good colloidal stability under the conditions typically used for calcium carbonate formation.[2-4,15,16] Good colloidal stability is an essential

prerequisite for the occlusion studies. If the nanoparticles aggregate in the presence of [Ca^{2+}], they are unlikely to be efficiently incorporated into the host crystal.
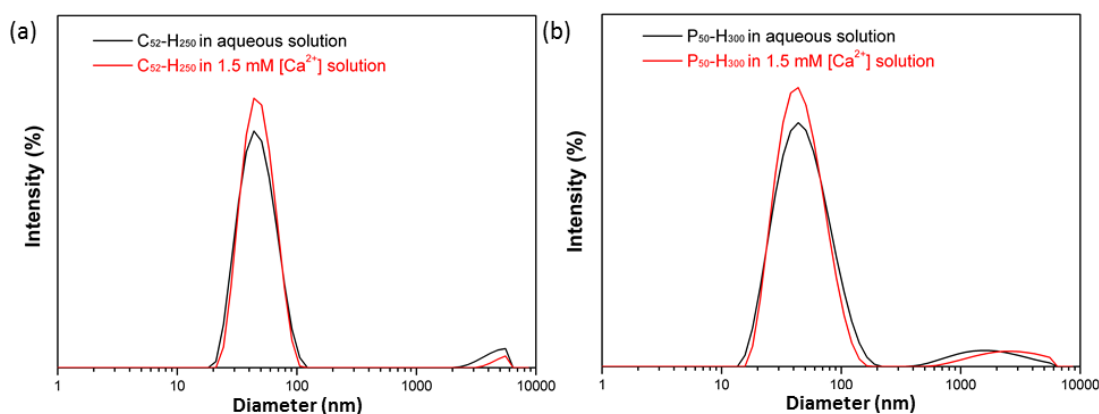
Figure 3.6. Hydrodynamic diameters recorded for (a) C_{52}-H_{250} and (b) P_{50}-H_{300} nanoparticles in aqueous solution and also in the presence of 1.5 mM [Ca^{2+}]. Dynamic lighting scattering studies were conducted using 0.1 % w/w copolymer at pH 9.5. These results indicated that both the C_{52}-H_{250} and P_{50}-H_{300} nanoparticles are colloidally stable in the presence of [Ca^{2+}] = 1.5 mM.

3.2.4 Incorporation of C_{52}-H_{250} and P_{50}-H_{300} Diblock Copolymer Nanoparticles into Calcium Carbonate Crystals

Calcium carbonate crystals were precipitated at an initial pH 9.5 by exposing an aqueous solution of 1.5 mM [Ca^{2+}] containing 0.01 % w/w C_{52}-H_{250} or P_{50}-H_{300} nanoparticles to ammonium carbonate vapour at 20 °C for 24 h.[17] As expected, experiments conducted in the absence of any nanoparticles resulted in the formation of 30 - 50 μm rhombohedral crystals, which is typically characteristic of calcite (see **Figures 3.7a and 3.7b**). The internal structure of these crystals was examined by FE-SEM after crushing the crystals. As expected, smooth cross-sections were observed, as shown in **Figures 3.7c and 3.7d**.
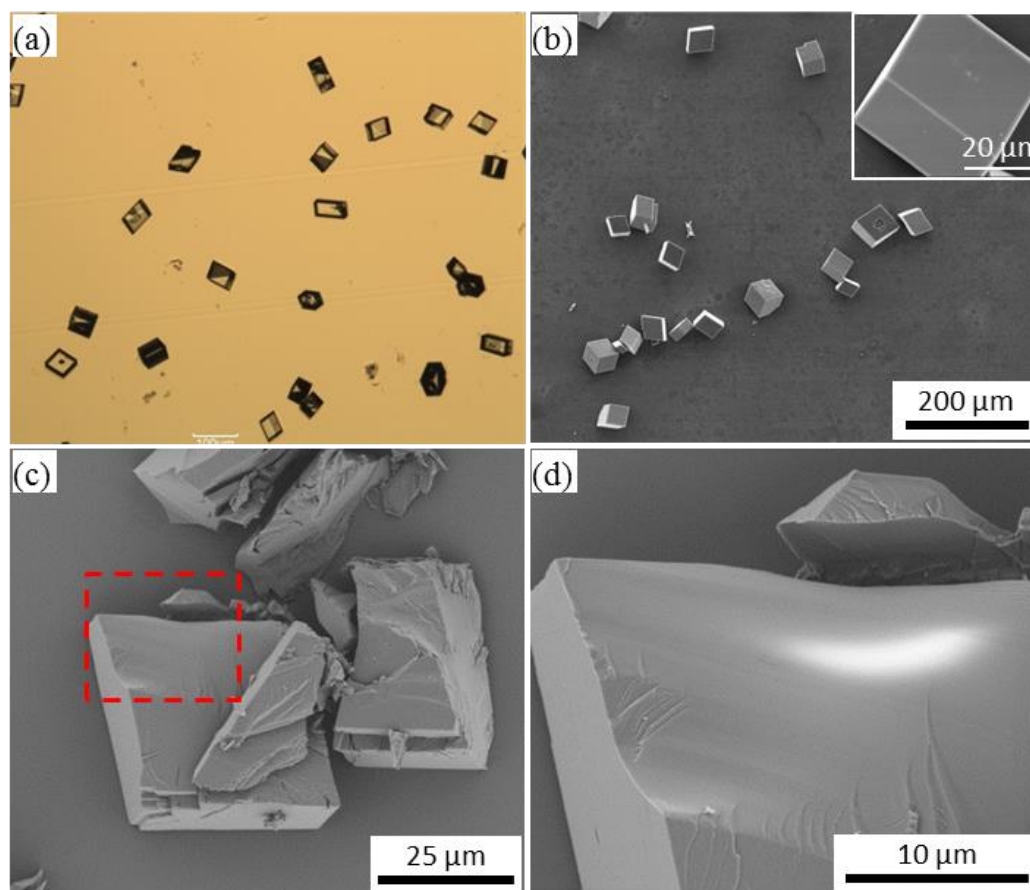
Figure 3.7. Calcium carbonate crystals prepared in the absence of any additives. (a) optical micrograph; (b) SEM image; (c) SEM image showing the crushed crystal; (d) magnified SEM image showing the dashed rectangle area indicated in (c). Note: the crystallisation was conducted at an initial pH of 9.5.

In addtion, G_{70}-B_{100} diblock copolymer nanoparticles with a mean diameter of ~20 nm (see **Figures 3.8a** and **3.8b**) were also prepared by RAFT aqueous emulsion polymerisation. The G_{70} stabiliser block is non-ionic and the calcium carbonate crystals produced in the presence of these nanoparticles exhibited a characteristic rhombohedral morphology (see **Figure 3.8c**). Observation of the internal crystal structure by SEM confirmed that there was no occlusion (see **Figures 3.8d and 3.8e**). This is not really surprising, because previous studies suggest that anionic character is usually essential for nanoparticle occlusion.[1-4,15,16] It is emphasised that the C_{52}-H_{250} and P_{50}-H_{300} nanoparticles have comparable mean diameters and coronal stabiliser thicknesses. Both types of nanoparticles possess carboxylic acid groups, which are normally considered to be a pre-requisite for efficient occlusion.[1-4,15,16]

Although the carboxylic acid groups of C_{52}-H_{250} and P_{50}-H_{300} are deprotonated above pH 9, the former nanoparticles are zwitterionic under these conditions (which correspond to those used for occlusion) while the latter are anionic. This subtle difference offers an opportunity to ask an interesting question: are anionic carboxylate groups alone sufficient to ensure efficient occlusion?
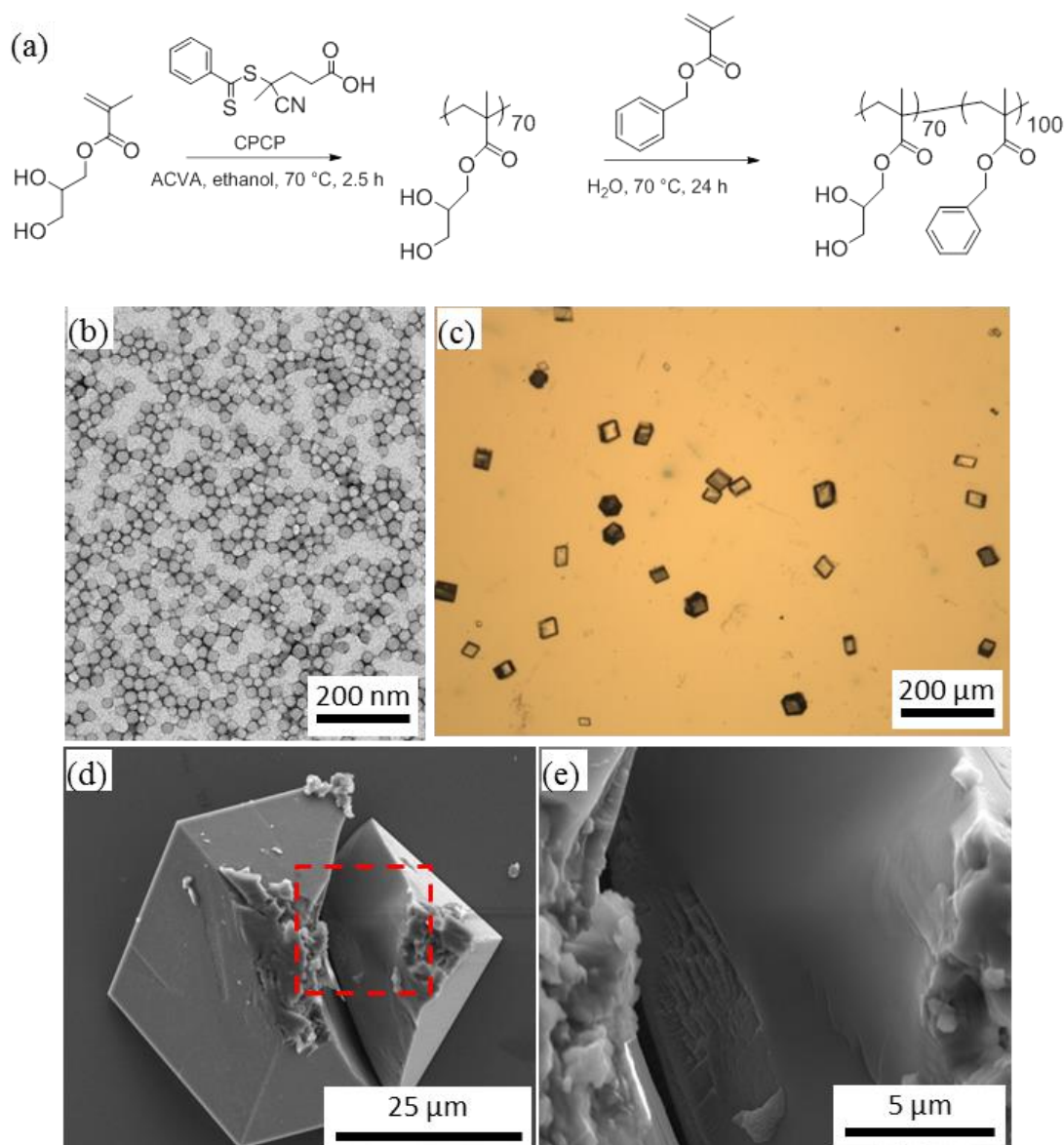
Figure 3.8. (a) Synthesis of poly(glycerol monomethacrylate)$_{70}$-poly(benzyl methacrylate)$_{100}$ (G_{70}-B_{100}) diblock copolymer nanoparticles. (b)~(e) Calcium carbonate crystals prepared in the presence of G_{70}-B_{100} diblock copolymer nanoparticles: (b) TEM of G_{70}-B_{100} nanoparticles; (c) optical micrograph of calcium carbonate precipitated in the presence of G_{70}-B_{100}; (d) representative SEM image of calcium carbonate precipitated in the presence of G_{70}-B_{100}; (e) magnified SEM image showing the area indicated in (d). Several crystals were examined by SEM and consistent results were obtained.

Similarly, calcium carbonate precipitation in the presence of the C_{52}-H_{250} nanoparticles also yielded a rhombohedral morphology, but along with a minor population of vaterite crystals (red arrows indicated in **Figures 3.9a and 3.9b**). Crystals grown in the presence of P_{50}-H_{300} nanoparticles were also rhombohedral but had smaller dimensions of 10 ~ 30 μm (see **Figures 3.9d** and **3.9e**). Meanwhile, roughened faces and truncation of the edges were also observed (see inset in **Figure 3.9e**), which is different from the crystals precipitated in the presence of C_{52}-H_{250} (see inset in **Figure 3.9b**).

The internal crystal morphology was evaluated by examining cross-sections of deliberately-fractured crystals. There was no evidence of any nanoparticle occlusion within crystals grown in the presence of C_{52}-H_{250} nanoparticles (**Figure 3.9c**). However, when P_{50}-H_{300} nanoparticles were used as an additive, FE-SEM images of the internal crystal structure confirmed that P_{50}-H_{300} nanoparticles were uniformly distributed throughout the whole crystal (**Figure 3.9f**). Further, the apparent voids/occluded particles were comparable in diameter to the P_{50}-H_{300} particles prior to occlusion. Moreover, the voids are isolated, indicating there are no nanoparticle aggregates. This observation further confirmed the copolymer nanoparticles are colloidal stable.

Raman spectroscopy studies (**Figure 3.10a**) indicated that crystals containing P_{50}-H_{300} nanoparticles possessed various spectral features that are known to be characteristic of calcite; bands at 154 cm^{-1} and 280 cm^{-1} are lattice modes, while bands at 712 cm^{-1} (υ_4) and 1086 cm^{-1} (υ_1) have been assigned to the in-plane bending and symmetric stretching of carbonate, respectively.[17,18]

Bulk crystal structures were confirmed by powder XRD studies (**Figure 3.10b**). In particular, calcium carbonate precipitated in the presence of C_{52}-H_{250} nanoparticles results in a mixture of calcite and vaterite phases. This is probably because the C_{52}-H_{250} nanoparticles can act as an 'impurity' that slightly perturbs normal calcite growth. In contrast, only calcite was detected for calcium carbonate prepared in the presence of P_{50}-H_{300} nanoparticles.
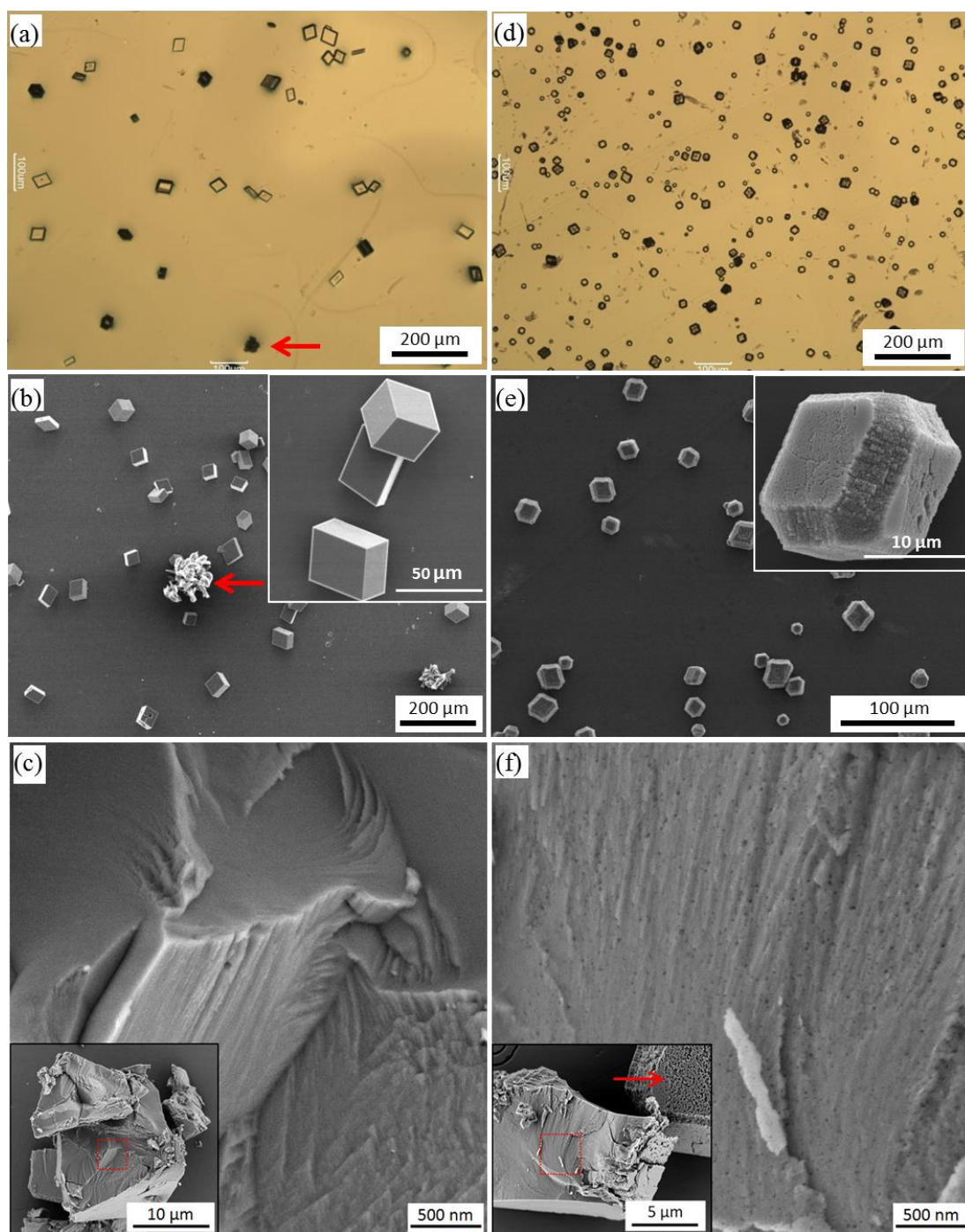
Figure 3.9. Left column: calcium carbonate crystals precipitated in the presence of 0.01 % w/w C_{52}-H_{250}: (a) optical micrograph; (b) FE-SEM image; (c) FE-SEM image showing cross-sections of calcium carbonate. Right column: calcium carbonate crystals precipitated in the presence of 0.01 % w/w P_{50}-H_{300}: (d) optical micrograph; (e) FE-SEM image; (f) FE-SEM image showing cross-sections of calcium carbonate. The insets in (b) and (e) show the surface morphologies of the crystals. The insets in (c) and (f) show low magnification images of the same crystals (Note: dashed red squares indicates the areas shown in (c) and (f)). The red arrow in (f) indicates the rough surface of the calcite. Clearly, there is no nanoparticle occlusion in (c), whereas there is extensive occlusion in (f).
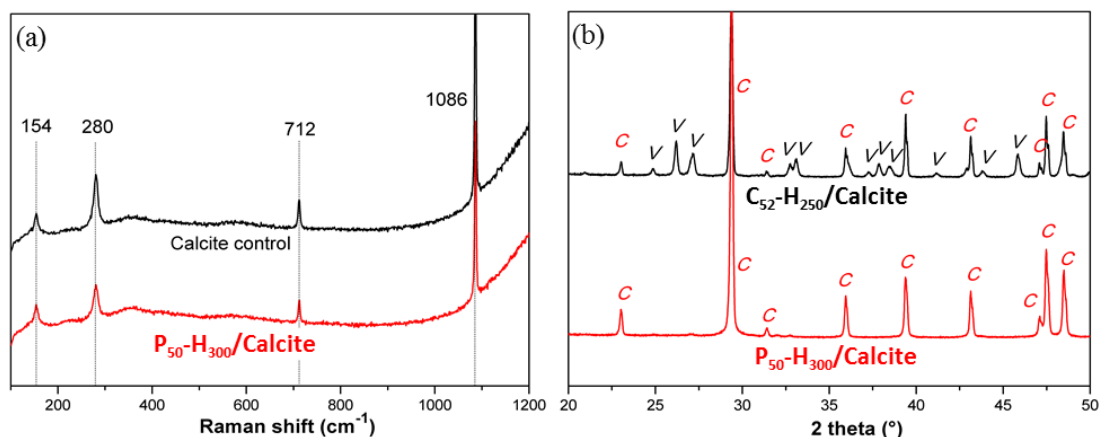
Figure 3.10. (a) Raman spectra recorded for a calcite crystal control and calcite containing occluded P_{50}-H_{300} nanoparticles; (b) XRD patterns recorded for calcite precipitated in the presence of C_{52}-H_{250} (C denotes calcite and V de-notes vaterite) and P_{50}-H_{300}.

Thermogravimetric analysis (TGA; **Figure 3.11**) studies confirmed that there was no detectable occlusion of C_{52}-H_{250} while the P_{50}-H_{300}/calcite crystals comprised 6.8 % w/w nanoparticles. It was found that heating P_{50}-H_{300} copolymer to 900 °C resulted in approximately 0.3 % w/w residue due to either residual salt and/or ash. Heating pure calcium carbonate led to its decomposition above 625 °C leaving an oxide residue (56.4 % w/w) at 900 °C (theoretical value = 56 % w/w). TGA studies indicated that P_{50}-H_{300}/calcite nanocomposite crystals contained 1.0 % w/w water by mass and exhibited a 4.0 % weight loss between 250 °C and 500 °C. This is due to copolymer pyrolysis located near the outer surfaces of the crystals. The additional 43 % weight loss observed between 500 °C and 800 °C is due to both copolymer pyrolysis and CO_2 evolution from the thermal decomposition of $CaCO_3$. As the P_{50}-H_{300} salt/ash residue is negligible (for example, if the copolymer content of the composite crystals is 50 % w/w, then the final polymer ash will be 50 x 0.3 = 0.15 % w/w), we assume that all of the 52.0 % w/w residue is CaO, which is derived from the decomposition of $CaCO_3$, corresponding to 40.5 % w/w CO_2. Thus the copolymer nanoparticle content of the original nanocomposite crystals can be calculated to be 6.8 % w/w [extent of occlusion = 4.0 % w/w + (43 % w/w - 40.2 % w/w)]. Assuming a copolymer density of 1.22 g cm^{-3}, this corresponds to 14 % v/v copolymer nanoparticle occlusion. Nanoparticle occlusion was further confirmed by

FT-IR spectroscopy by monitoring $-C=O$ stretching vibration ascribed from the copolymer P_{50}-H_{300} nanoparticles (see **Figure 3.12**).
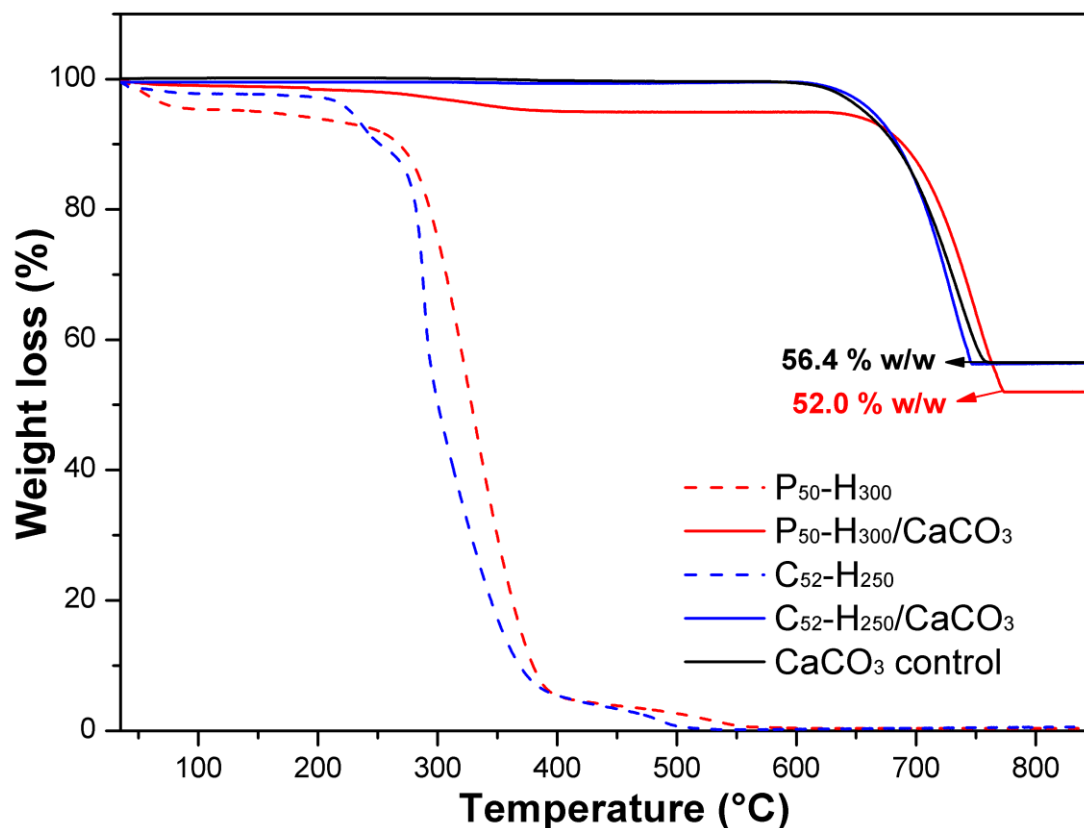
Figure 3.11. TGA curves recorded for P_{50}-H_{300} and C_{52}-H_{250} nanoparticles alone, calcite crystals grown in the presence of either C_{52}-H_{250} or P_{50}-H_{300}, and a pure calcite control.

According to the literature, anionic nanoparticles containing surface carboxylate groups could be occluded within calcite.[1-4] Furthermore, it was suggested that this motif played a key role in promoting occlusion. In the present study, both C_{52}-H_{250} and P_{50}-H_{300} nanoparticles also possess surface carboxylate groups. However, the former *zwitterionic* nanoparticles exhibit no signs of occlusion, while the overall *anionic* P_{50}-H_{300} copolymer nanoparticles are homogeneously incorporated into calcite crystals at approximately 6.8 % w/w. These observations indicate that both the presence of carboxylic acid groups *and* overall anionic character are required for successful nanoparticle occlusion.
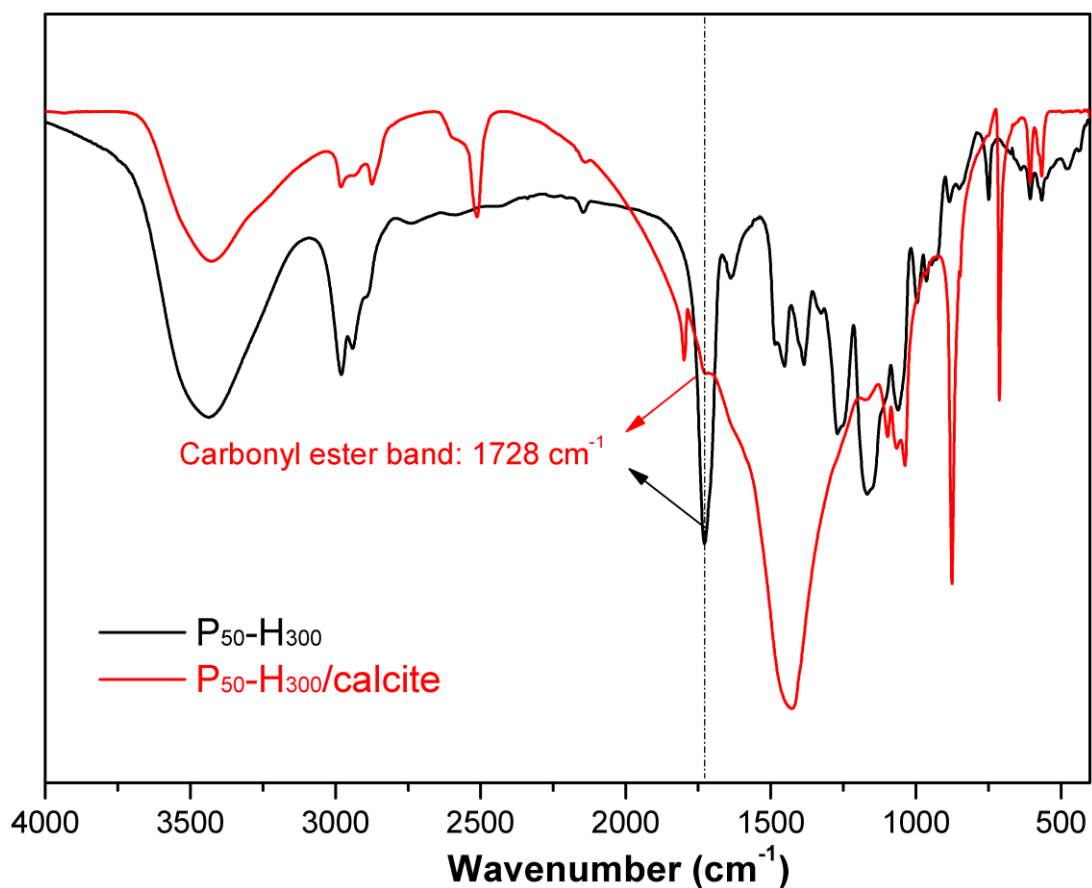
Figure 3.12. FT-IR spectra recorded for P_{50}-H_{300} nanoparticles alone and P_{50}-H_{300}/calcite nanocomposite crystals. A weak carbonyl ester band at 1728 cm^{-1} is discernible in latter spectrum, confirming successful occlusion of copolymer nanoparticles within the calcite crystals.

A reasonable explanation for these observations is as follows. Ca^{2+} ions interact strongly with the anionic carboxylate groups on both the zwitterionic C_{52} and the anionic P_{50} stabiliser chains at pH 9.5. However, the overall zeta potential is reduced to around -3 mV in the presence of 1.5 mM $[Ca^{2+}]$ in the former case (**Figure 3.5d**), which is insufficient to ensure strong electrostatic adsorption of the C_{52}-H_{250} nanoparticles onto the growing crystal surface.[19] In contrast, P_{50}-H_{300} nanoparticles retain an anionic zeta potential of -25 mV under the same conditions, which enables their strong electrostatic binding onto the growing crystal surface.[1,3,16] Thus the subtle structural differences between these two types of sterically-stabilised nanoparticles has a dramatic effect on their interactions with growing calcite crystals.

3.3 Conclusions

C_{52} and P_{50} macro-CTAs were readily synthesised by using MPETTC RAFT agent, which is water-soluble below pH 4.5. These two macro-CTAs possess relatively low polydispersities ($M_w/M_n < 1.2$), as determined by aqueous GPC analysis. C_{52}-H_{250} and P_{50}-H_{300} nanoparticles were prepared at 70 °C by chain extension via RAFT aqueous dispersion polymerisation of H at 20% w/w solids.

These two diblock copolymer nanoparticles were subsequently used as additives during the in situ crystallisation of calcium carbonate crystal. FE-SEM studies indicated that C_{52}-H_{250} nanoparticles cannot be occluded within such crystals while P_{50}-H_{300} nanoparticles are uniformly incorporated throughout the host crystal. Raman spectroscopy and XRD analysis confirmed that calcium carbonate containing P_{50}-H_{300} formed single crystals of calcite. The extent of occlusion of P_{50}-H_{300} nanoparticles within calcite was determined to be 6.8 % w/w (which corresponds to a volume fraction of 14 %).

In summary, this study demonstrates that anionic carboxylate functionality is a necessary but not sufficient condition for efficient nanoparticle occlusion within calcite. Overall *anionic* character appears to be an additional prerequisite, because essentially no occlusion is observed when *zwitterionic* polycarboxybetaine-stabilised nanoparticles are employed. This work provides a deeper understanding of the design rules for efficient nanoparticle occlusion within this particular inorganic host crystal.

3.4 References

(1) Cho, K.-R. K., Y.-Y.; Yang, P.; Cai, W.; Pan, H.; Kulak, A. N.; Lau, J. L.; Kulshreshtha, P.; Armes, S. P.; Meldrum, F. C.; De Yoreo, J. J. Direct observation of mineral-organic composite formation reveals occlusion mechanism. *Nature Communications* **2016**, *7*, 10187.

(2) Kim, Y.-Y.; Semsarilar, M.; Carloni, J. D.; Cho, K. R.; Kulak, A. N.; Polishchuk, I.; Hendley, C. T.; Smeets, P. J. M.; Fielding, L. A.; Pokroy, B.; Tang, C. C.; Estroff, L. A.; Baker, S. P.; Armes, S. P.; Meldrum, F. C. Structure and Properties of Nanocomposites Formed by the Occlusion of Block Copolymer Worms and Vesicles Within Calcite Crystals. *Advanced Functional Materials* **2016**, *26*, 1382-1392.

(3) Kim, Y.-Y.; Ganesan, K.; Yang, P.; Kulak, A. N.; Borukhin, S.; Pechook, S.; Ribeiro, L.; Kroeger, R.; Eichhorn, S. J.; Armes, S. P.; Pokroy, B.; Meldrum, F. C. An artificial biomineral formed by incorporation of copolymer micelles in calcite crystals. *Nature Materials* **2011**, *10*, 890-896.

(4) Kim, Y.-Y.; Ribeiro, L.; Maillot, F.; Ward, O.; Eichhorn, S. J.; Meldrum, F. C. Bio-Inspired Synthesis and Mechanical Properties of Calcite-Polymer Particle Composites. *Advanced Materials* **2010**, *22*, 2082-2086.

(5) Penfold, N.; Lovett, J.; Warren, N.; Verstraete, P.; Smets, J.; Armes, S. pH-Responsive non-ionic diblock copolymers: protonation of a morpholine end-group induces an order–order transition. *Polymer Chemistry* **2016**, *7*, 79-88.

(6) Anderson, G. W.; Zimmerman, J. E.; Callahan, F. M. The use of esters of N-hydroxysuccinimide in peptide synthesis. *Journal of the American Chemical Society* **1964**, *86*, 1839-1842.

(7) Bathfield, M.; D'Agosto, F.; Spitz, R.; Charreyre, M.-T.; Delair, T. Versatile precursors of functional RAFT agents. Application to the synthesis of bio-related end-functionalized polymers. *Journal of the American Chemical Society* **2006**, *128*, 2546-2547.

(8) Kristensen, T. E.; Vestli, K.; Fredriksen, K. A.; Hansen, F. K.; Hansen, T. Synthesis of Acrylic Polymer Beads for Solid-Supported Proline-Derived Organocatalysts. *Organic Letters* **2009**, *11*, 2968-2971.

(9) Kristensen, T. E.; Hansen, F. K.; Hansen, T. The Selective *O*-Acylation of Hydroxyproline as a Convenient Method for the Large-Scale Preparation of Novel Proline Polymers and Amphiphiles. *European Journal of Organic Chemistry* **2009**, *2009*, 387-395.

(10) Matsuoka, H.; Yamakawa, Y.; Ghosh, A.; Saruwatari, Y. Nanostructure and Salt Effect of Zwitterionic Carboxybetaine Brush at the Air/Water Interface. *Langmuir* **2015**, *31*, 4827-4836.

(11) Kitano, H.; Tokuwa, K.-i.; Ueno, H.; Li, L.; Saruwatari, Y. Zwitterionic polymer-grafted microspheres prepared by RAFT polymerization. *Colloid and Polymer Science* **2015**, *293*, 2931-2939.

(12) Kharlampieva, E.; Izumrudov, V. A.; Sukhishvili, S. A. Electrostatic layer-by-layer self-assembly of poly (carboxybetaine)s: role of zwitterions in film growth. *Macromolecules* **2007**, *40*, 3663-3668.

(13) Chiefari, J.; Chong, Y.; Ercole, F.; Krstina, J.; Jeffery, J.; Le, T. P.; Mayadunne, R. T.; Meijs, G. F.; Moad, C. L.; Moad, G. Living free-radical polymerization by reversible addition-fragmentation chain transfer: the RAFT process. *Macromolecules* **1998**, *31*, 5559-5562.

(14) Ning, Y.; Fielding, L. A.; Doncom, K. E. B.; Penfold, N. J. W.; Kulak, A. N.; Matsuoka, H.; Armes, S. P. Incorporating Diblock Copolymer Nanoparticles into Calcite Crystals: Do Anionic Carboxylate Groups Alone Ensure Efficient Occlusion? *ACS Macro Letters* **2016**, *5*, 311-315.

(15) Kulak, A. N.; Yang, P.; Kim, Y.-Y.; Armes, S. P.; Meldrum, F. C. Colouring crystals with inorganic nanoparticles. *Chemical Communications* **2014**, *50*, 67-69.

(16) Kulak, A. N.; Semsarilar, M.; Kim, Y.-Y.; Ihli, J.; Fielding, L. A.; Cespedes, O.; Armes, S. P.; Meldrum, F. C. One-pot synthesis of an inorganic heterostructure: uniform occlusion of magnetite nanoparticles within calcite single crystals. *Chemical Science* **2014**, *5*, 738-743.

(17) Ihli, J.; Bots, P.; Kulak, A.; Benning, L. G.; Meldrum, F. C. Elucidating Mechanisms of Diffusion-Based Calcium Carbonate Synthesis Leads to Controlled Mesocrystal Formation. *Advanced Functional Materials* **2013**, *23*, 1965-1973.

(18) Wehrmeister, U.; Soldati, A. L.; Jacob, D. E.; Haeger, T.; Hofmeister, W. Raman spectroscopy of synthetic, geological and biological vaterite: a Raman spectroscopic study. *Journal of Raman Spectroscopy* **2010**, *41*, 193-201.

(19) Metzler, R. A.; Tribello, G. A.; Parrinello, M.; Gilbert, P. U. P. A. Asprich Peptides Are Occluded in Calcite and Permanently Disorder Biomineral Crystals. *Journal of the American Chemical Society* **2010**, *132*, 11585-11591.

4. Chapter Four

4. Occlusion of Poly(ammonium 2-sulfatoethyl methacrylate)-Poly(benzyl methacrylate) Diblock Copolymer Nanoparticles within Calcite: Effect of Varying the Surface Density of Anionic Stabiliser Chains

4.1 Introduction

In Chapter 3, we demonstrated that overall anionic surface charge of the guest nanoparticles is essential for their occlusion. However, in some cases, no occlusion is observed even when this condition is satisfied. For example, Wooley and co-workers used poly(acrylic acid)-stabilised copolymer nanoparticles as additives for the *in situ* crystallisation of halite but found that such nanoparticles were solely located on the crystal surface, with little or no occlusion.[1] Qi and co-workers showed that carboxylic acid-functionalised polystyrene latexes can only be incorporated into the surface layer of calcite.[2] Similar results were observed by Hanisch et al., who utilised anionic phosphonate functionalised vesicles as additives.[3] A robust set of design rules for efficient nanoparticle occlusion remains elusive. As a result, progress in incorporating nanoparticles into inorganic crystals to date has mainly relied on empirical trial-and-error experiments.

Clearly, the surface character of the nanoparticles must play a crucial role in occlusion because this dictates the nature of the host-guest interaction. However, the influence of surface composition on the extent of occlusion is poorly understood. This is in part because precise control over the nanoparticle surface composition is somewhat problematic.[4-6] As mentioned previously, PISA-mediated by RAFT enables the facile synthesis of a wide range of sterically-stabilised diblock copolymer nanoparticles with controllable size, tunable morphology and adjustable surface functionality.[7-19] By varying the stabiliser macro-CTA, a range of non-ionic,[8,11,12,14,15,17-20] anionic,[21,22] cationic[23-25] and zwitterionic[26,27] nanoparticles can be readily prepared by chain extension with a core-forming block monomer in either polar or non-polar solvents. Moreover, Armes and co-workers demonstrated that the surface charge density can be tuned by using a binary mixture of macro-CTAs.[22,23,25] This is an attractive means of adjusting the stabiliser charge density by introducing an uncharged stabiliser macro-CTA. As far as we are aware, no other strategies that enable stabiliser charge density to be conveniently fine-tuned via PISA formulation have been reported.

In this Chapter we seek to precisely tune the surface composition of anionic diblock copolymer nanoparticles to extend our understanding of the design rules that govern

nanoparticle occlusion within a model single crystal (calcite). More specifically, we show for the first time that PISA can be used to prepare copolymer nanoparticles with differing stabiliser surface densities. This is achieved by preparing poly(ammonium 2-sulfatoethyl methacrylate)-poly(benzyl methacrylate) (S-B) nanoparticles using either RAFT dispersion polymerisation in a 2:1 v/v ethanol/water mixture or RAFT aqueous emulsion polymerisation (see **Scheme 4.1**). This approach offers an unprecedented opportunity to examine the relationship between the stabiliser surface density and the extent of nanoparticle occlusion. For the sake of brevity, a shorthand notation is utilised: 'S_x-B_y (emulsion)' denotes poly(ammonium 2-sulfatoethyl methacrylate)-poly(benzyl methacrylate) diblock copolymer prepared by RAFT emulsion polymerisation, where x and y indicate the mean DP of each block.
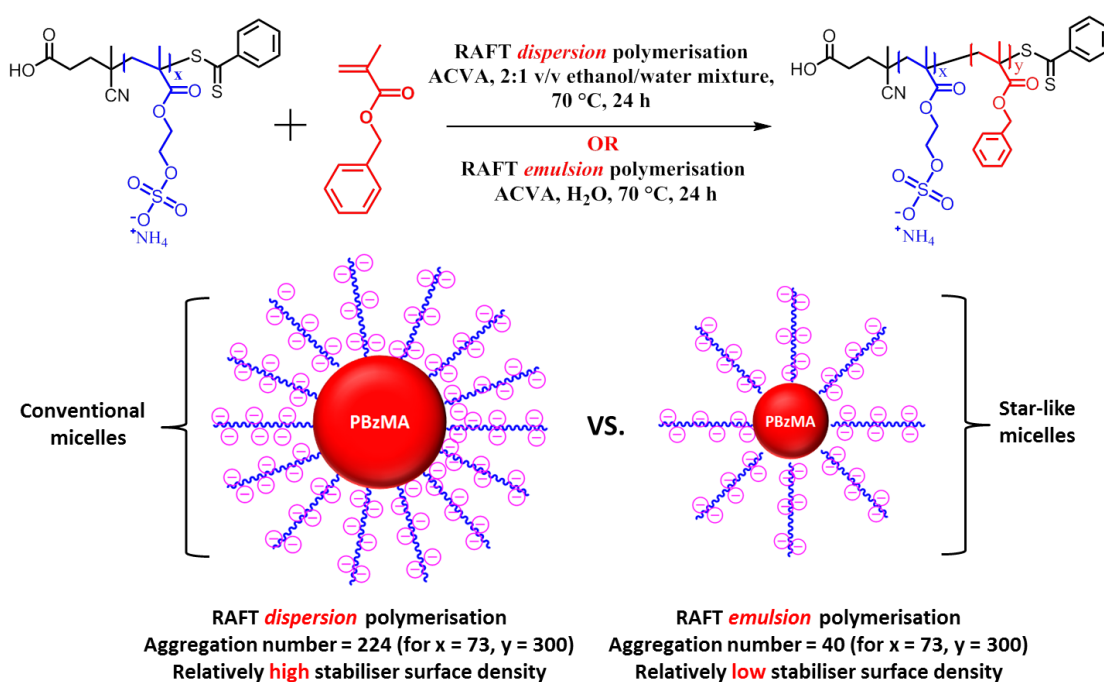
Scheme 4.1. Synthesis of poly(ammonium 2-sulfatoethyl methacrylate)-poly(benzyl methacrylate) (S-B) diblock copolymer nanoparticles at 10 % w/w solids by chain extension of a S macro-CTA via either RAFT dispersion polymerisation or RAFT aqueous emulsion polymerisation of benzyl methacrylate (B) at 70 °C for 24 h. The schematic cartoons indicate subtle differences in the mean aggregation number and stabiliser surface density when using these two PISA formulations.[28]

4.2 Results and Discussion

4.2.1 Copolymer Synthesis and Characterisation.

As far as we are aware, prior to this Thesis, there were no previous reports describing the RAFT polymerisation of ammonium 2-sulfatoethyl methacrylate. Herein two poly(ammonium 2-sulfatoethyl methacrylate) macro-CTAs with mean DPs of either 32 or 73 were prepared via RAFT aqueous solution polymerisation of ammonium 2-sulfatoethyl methacrylate monomer at 25 % w/v solids and 70 °C. **Figure 4.1a** shows the conversion vs. time curve obtained for the RAFT polymerisation of ammonium 2-sulfatoethyl methacrylate with a target DP of 60. Typically, 80 % conversion can be achieved within 2 h at this temperature. Aqueous GPC studies indicated a linear evolution in number-average molecular weight against conversion (**Figure 4.1b**), which is consistent with the expected pseudo-living character of a RAFT polymerisation.[29] Moreover, each macro-CTA had a relatively narrow molecular weight distribution ($M_w/M_n < 1.15$, see **Figures 4.2a** and **4.2b**), which in principle enables the preparation of sterically-stabilised nanoparticles with a uniform corona thickness. Unfortunately, GPC cannot be used to analyse S_x-B_y diblock copolymers because no suitable eluent was available for such amphiphilic chains. Instead, chain extension experiments were conducted using these S macro-CTAs. These studies indicated high blocking efficiencies on addition of a second charge of S monomer, which suggests a high degree of RAFT end-group functionalisation (see **Figures 4.2a** and **4.2b**). These observations are consistent with UV-visible spectroscopy analysis, which indicate degrees of RAFT end-group functionality of more than 99%, see **Figures 4.2c** and **4.2d**. CPCP has a maximum absorbance at a wavelength of 301 nm, so the end-group functionality can be calculated as follows: the absorbance at a given concentration of S macro-CTA is divided by the theoretical absorbance calculated from the Beer-Lambert calibration plot, $A = \varepsilon c l$ (**Figure 4.2d**). For example, the experimental absorbance for 5×10^{-5} M S_{73} is 0.719, while the theoretical absorbance is 0.724, thus the RAFT end-group functionality for S_{73} is given by $(0.719/0.724) \times 100\%$, or ~ 99.3%.
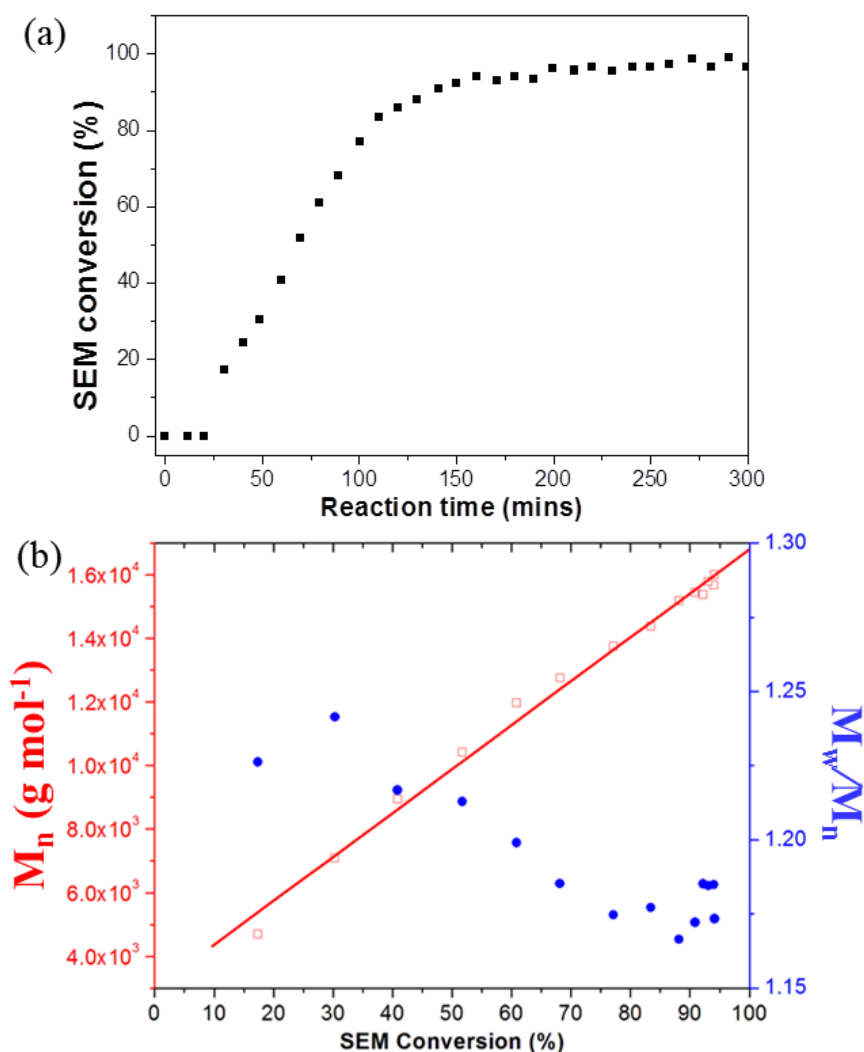
Figure 4.1. (a) Conversion *vs* time curve calculated from ^{1}H NMR spectra (D_2O) for the RAFT synthesis of S macro-CTA in water at 70 °C (target DP = 60; CTA/initiator molar ratio = 5.0). (b) Evolution of the number-average molecular weight M_n (calculated using PEO standards) and molecular weight distribution (M_w/M_n) of S macro-CTA (target DP = 60; CTA/initiator molar ratio = 5.0) with monomer conversion as judged by aqueous GPC.

As illustrated in **Scheme 4.1**, a series of anionic S-B diblock copolymer nanoparticles were prepared by either RAFT dispersion polymerisation in a 2:1 v/v ethanol/water mixture or RAFT aqueous emulsion polymerisation. The B monomer conversion was monitored by ^{1}H NMR spectroscopy, which indicated that high conversions (> 99 %) were achieved after 24 h at 70 °C in all cases. Such PISA formulations enable the particle size to be readily controlled by systematic variation

of the target DP of the core-forming block.[30-33] Furthermore, the nature of the steric stabiliser block dictates the surface chemistry.[30-33] Thus in the present Chapter choosing S macro-CTA should lead to anionic nanoparticles.
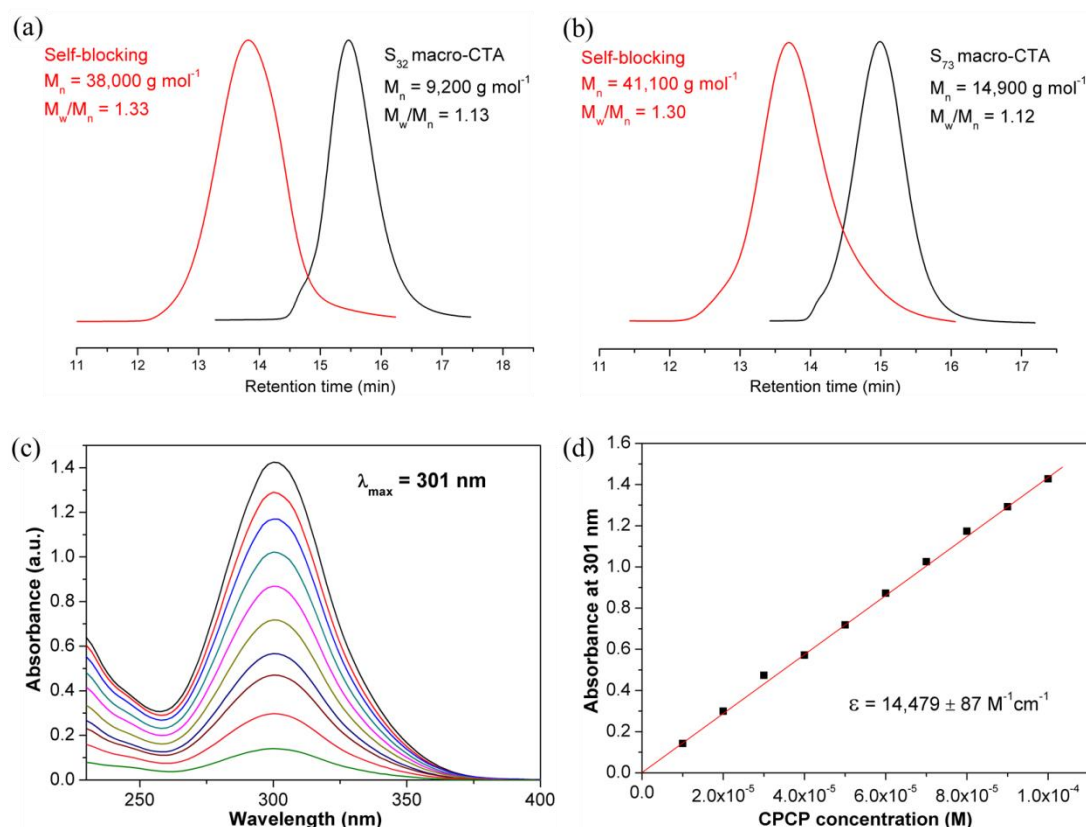
Figure 4.2. Aqueous GPC curves obtained for (a) S_{32} macro-CTA and (b) S_{73} macro-CTA and their subsequent chain extension via RAFT aqueous solution polymerisation using S monomer. This 'self-blocking' experiment was conducted in aqueous solution at 70 °C using ACVA initiator and a S macro-CTA/ACVA molar ratio of 5.0. Relatively high blocking efficiencies are obtained for these two macro-CTAs, which indicates high RAFT chain-end fidelity. (c) UV-visible spectra obtained for the CPCP chain transfer agent at concentrations ranging from 1.0×10^{-5} M to 1.0×10^{-4} M; (d) Beer-Lambert plot for this CPCP RAFT agent recorded in methanol in order to calculate the degree of end-group functionality of each S macro-CTA.

Figure 4.3 shows representative TEM images of sterically-stabilised S-B diblock copolymer nanoparticles prepared via PISA using either S_{32} or S_{73} macro-CTAs. In each case, the target DP of the core-forming B block was fixed at 300. However, the precise nature of the PISA formulation determines the final particle diameter.[21,30,33,34]

S-B nanoparticles prepared via RAFT dispersion polymerisation are significantly larger than those obtained by RAFT aqueous emulsion polymerisation. This suggests a higher mean aggregation number in the former case (see **Table 4.1**), which is presumably because the repulsive electrostatic forces operating between neighboring copolymer chains are significantly weaker in a 2:1 ethanol/water mixture ($\varepsilon_r \sim 43$ at 298 K) compared to pure water ($\varepsilon_r = 79.5$ at the same temperature).[35] Moreover, using a shorter S stabiliser block for RAFT dispersion polymerisation produces larger S-B nanoparticles (compare **Figures 4.3a** and **4.3c**). Similar results have been reported for other PISA formulations.[13,15]
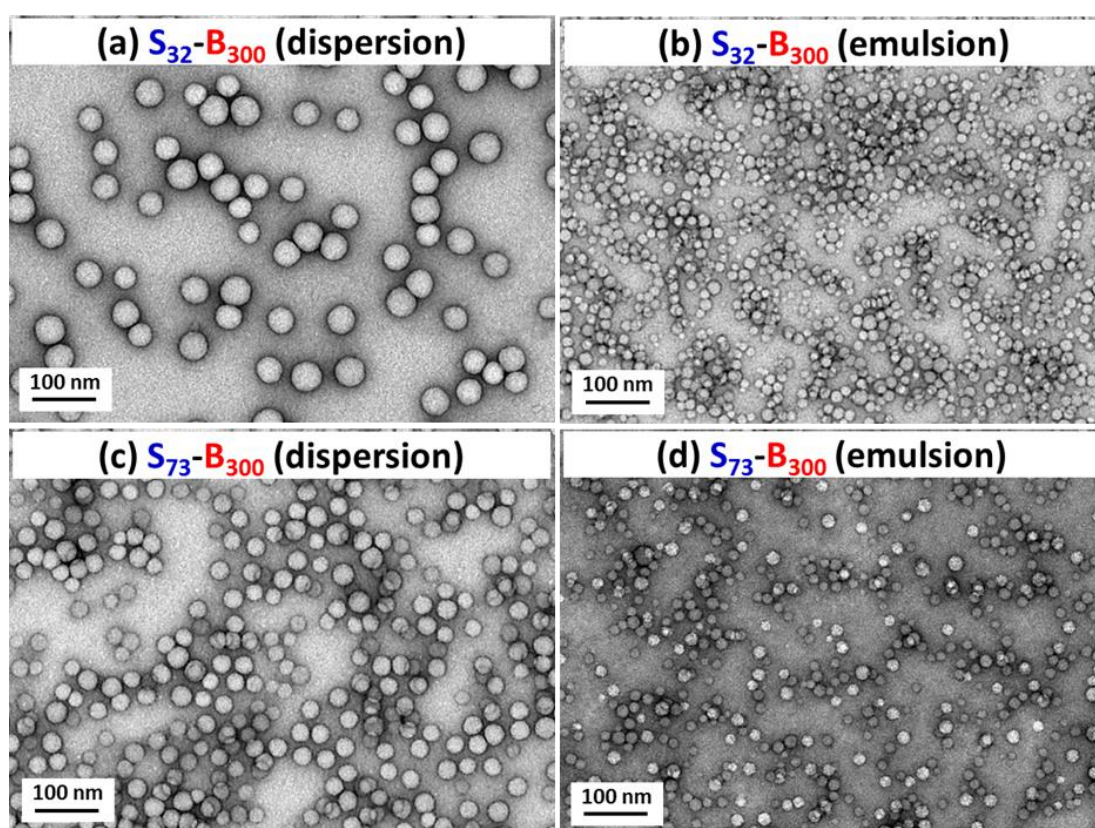
Figure 4.3. Representative TEM images obtained for various anionic diblock copolymer nanoparticles produced via RAFT-mediated PISA. (a) S_{32}-B_{300} (dispersion); (b) S_{32}-B_{300} (emulsion); (c) S_{73}-B_{300} (dispersion); (d) S_{73}-B_{300} (emulsion).

Figure 4.4 shows dynamic light scattering (DLS) and aqueous electrophoresis data for various diblock copolymer nanoparticles as a function of either pH or Ca^{2+} concentration.

Table 4.1. Summary of TEM diameters, DLS diameters, XPS elemental compositions, mean aggregation number and calculated S stabiliser surface densities obtained for various diblock copolymer nanoparticles prepared via PISA. Note: well defined S_{73}-B_{100} (emulsion) diblock copolymer nanoparticles cannot be prepared by RAFT emulsion polymerisation because the core-forming B_{100} block is relatively short.

| Sample ID | TEM diameter (nm)[a] | DLS diameter (nm) | XPS data | | | | Aggregation number (N_{agg}) | Stabilizer surface density (10^{-2} chain per nm^2) [c] |
			S2p atom %	C1s atom %	S2p/C1s atomic ratio (10^{-3})	Normalized S2p/C1s atomic ratio (%)[b]		
S_{32} homopolymer	N/A	N/A	8.2	47.6	172.3[e]	100.0	N/A	N/A
S_{32}-B_{300} (dispersion)	56 ± 5	80 (0.07)[d]	1.3	74.2	17.5	10.6	1204	10.9
S_{32}-B_{300} (emulsion)	18 ± 4	31 (0.12)	0.7	71.8	9.7	5.9	40	3.4
S_{32}-B_{500} (dispersion)	100 ± 16	129 (0.03)	1.6	73.4	21.8	13.2	4114	12.4
S_{32}-B_{500} (emulsion)	26 ± 6	36 (0.17)	0.6	72.4	8.3	5.0	72	3.2
S_{73} homopolymer	N/A	N/A	8.3	48.5	171.1[e]	100.0	N/A	N/A
S_{73}-B_{100} (dispersion)	19 ± 2	42 (0.27)	1.5	73.2	20.5	12.0	141	6.5
S_{73}-B_{300} (dispersion)	32 ± 3	52 (0.07)	1.3	72.1	18.0	10.5	224	5.4
S_{73}-B_{300} (emulsion)	18 ± 3	35 (0.10)	0.7	78.8	8.9	5.2	40	3.1
S_{73}-B_{500} (dispersion)	53 ± 12	96 (0.07)	1.4	74.9	18.7	10.9	612	6.0
S_{73}-B_{500} (emulsion)	21 ± 4	45 (0.27)	0.6	73.4	8.2	4.8	38	2.3
[0.5 S_{73}+0.5 G_{70}]-B_{300} (emulsion)	21 ± 3	45 (0.22)	0.4	72.4	5.5	3.2	64	1.9[f]
PBzMA$_{300}$	N/A	N/A	0.0	84.9	0.0	0	N/A	N/A

[a] Mean TEM diameter determined by analyzing more than 200 particles using ImageJ software.

[b] [S2p/C1s (particle)]/[S2p/C1s (stabilizer)] (%).

[c] Stabiliser surface density was calculated using equation (4.1).

[d] The number in brackets represents the DLS polydispersity.

[e] Theoretical values are 175.3 and 170.5 for S_{32} and S_{73}, respectively.

[f] There are two types of stabilizer in this case; the calculated value refers only to the PSEM$_{73}$ chains to aid comparison.

According to **Figure 4.4a**, the hydrodynamic diameter of the nanoparticles is independent of the solution pH, which is indicative of good colloidal stability. Such behavior differs qualitatively from that of poly(methacrylic acid)-stabilised diblock copolymer nanoparticles, since in the latter case the weak polyelectrolyte stabiliser chains become protonated at low pH, resulting in aggregation.[4,5] **Figure 4.4b** shows that S_x-B_y diblock copolymer nanoparticles exhibit highly anionic pH-independent zeta potentials, as expected for a strong polyelectrolyte stabiliser.[12,22,23] This pH-independent character enables aggregation to be avoided during attempted occlusion, even if crystallisation involves some variation in solution pH. It is emphasised that good colloidal stability of the nanoparticles is an essential prerequisite for successful occlusion. This point will be further discussed in the following Chapters. Comparing S_x-B_y nanoparticles prepared by dispersion polymerisation and emulsion polymerisation, the former exhibit more negative zeta potentials than the latter. The physical reason for this difference in electrophoretic behavior is examined later.
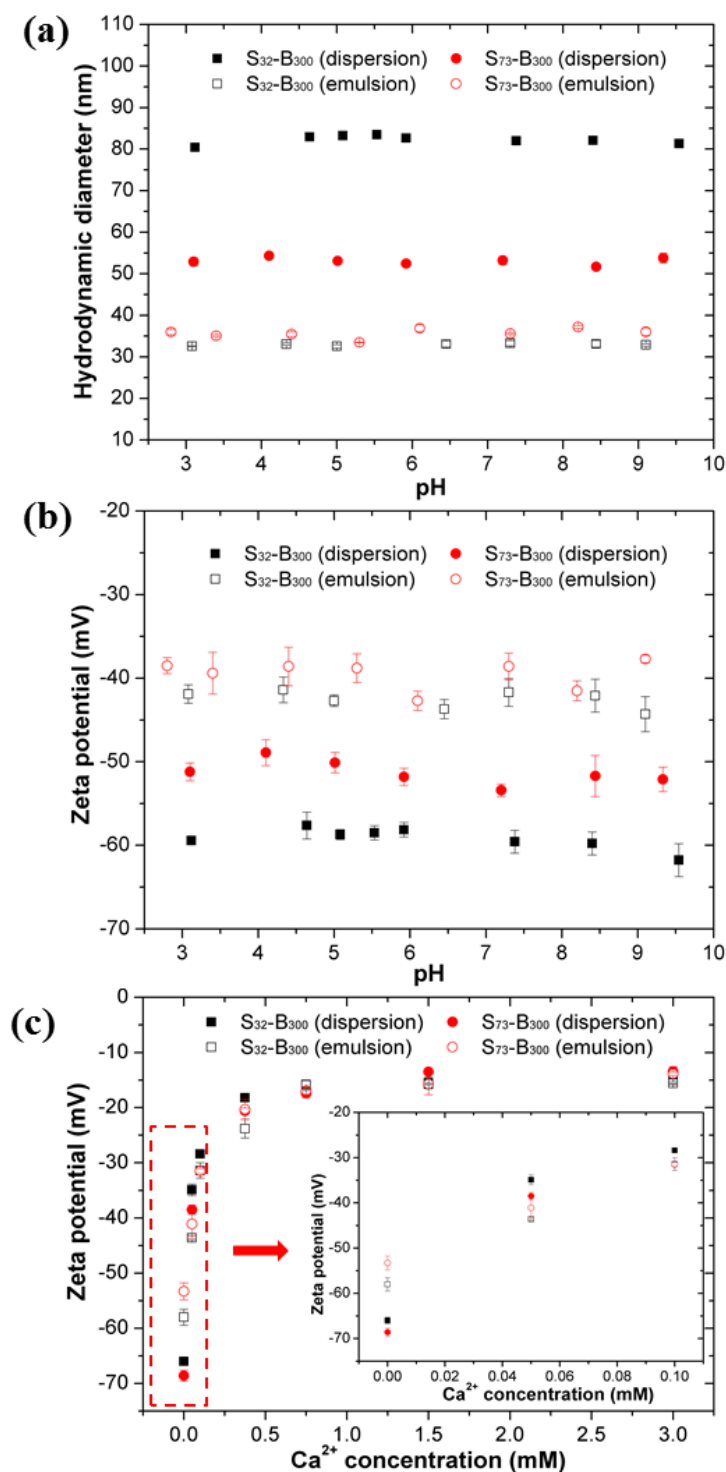
Figure 4.4. DLS and aqueous electrophoresis data obtained for spherical diblock copolymer nanoparticles conducted at a copolymer concentration of ~ 0.1 % w/w: (a) hydrodynamic diameter vs. pH; (b) zeta potential vs. pH in the presence of 1 mM NaCl as background electrolyte and (c) zeta potential vs. Ca^{2+} concentration, conducted at a copolymer nanoparticle concentration of 0.01 % w/w (which corresponds to the occlusion conditions). The inset in (c) shows the zeta potentials observed for nanoparticles at $CaCl_2$ concentrations ranging from 0 to 0.1 mM.

Although the zeta potential for the S_x-B_y diblock copolymer nanoparticles is pH-independent, this parameter is affected by the addition of $CaCl_2$, even at a relatively low concentration (0.1 mM) as shown in **Figure 4.4c**. Indeed, all nanoparticles exhibit a significant reduction in zeta potential in the presence of Ca^{2+}, although an overall zeta potential of around -15 mV is maintained at 1.5 mM $CaCl_2$ or higher. In addition, the intensity-average diameters recorded for S_{73}-B_{300} (emulsion) and S_{73}-B_{300} (dispersion) nanoparticles in the presence of 1.5 mM $CaCl_2$ are smaller than those determined in the absence of Ca^{2+} ions (see **Figure 4.5**). This is most likely the result of charge screening caused by the presence of salt, although it is worth noting that the divalent Ca^{2+} cations can bind strongly to the anionic sulfate groups on the S stabiliser chains. Importantly, the presence of 1.5 mM $CaCl_2$ does not cause any aggregation or precipitation (see **Figure 4.5**). Such S stabiliser-Ca^{2+} ion interactions are likely to be important for occlusion during *in situ* crystallisation, because they should promote nanoparticle adsorption onto the crystal surface.[4-6,36-38]
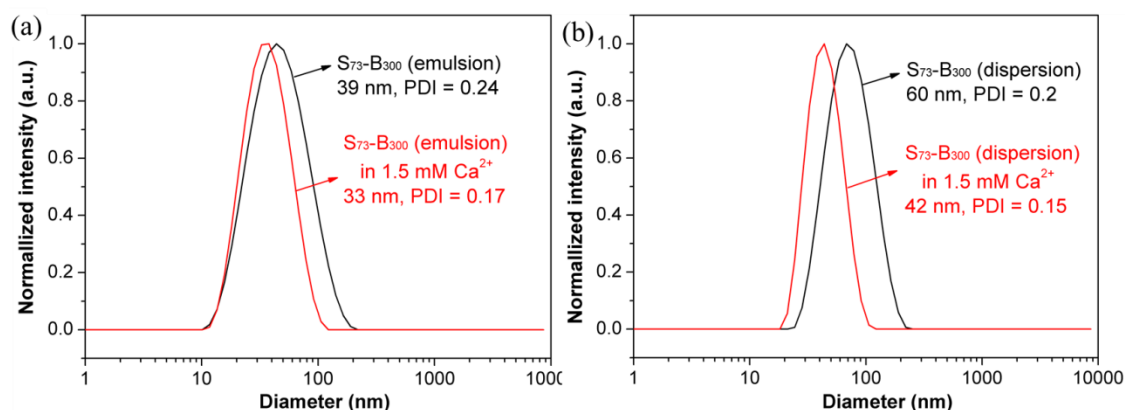
Figure 4.5. DLS diameters recorded for (a) S_{73}-B_{300} (emulsion) and (b) S_{73}-B_{300} (dispersion) copolymer nanoparticles in the absence or presence of 1.5 mM $CaCl_2$.

4.2.2 Calcium Carbonate Precipitation

Calcium carbonate crystals were precipitated at pH 8-9 by exposing an aqueous solution containing 1.5 mM $CaCl_2$ and 0.0-0.10 % w/w diblock copolymer nanoparticles to ammonium carbonate vapor at 20 °C for 24 h.[39] A mixture of calcite and vaterite was precipitated at a copolymer concentration of 0.10 % w/w (**Figure 4.6a**), which is consistent with previous reports.[5,36,37] Thus a lower copolymer

concentration of 0.01 % w/w was selected for more detailed studies. Precipitation under the above conditions yielded 30 - 50 μm rhombohedral calcite crystals in either the absence or presence of S-B diblock copolymer nanoparticles or S_{73} homopolymer, see **Figures 4.6b ~ 4.6d**.
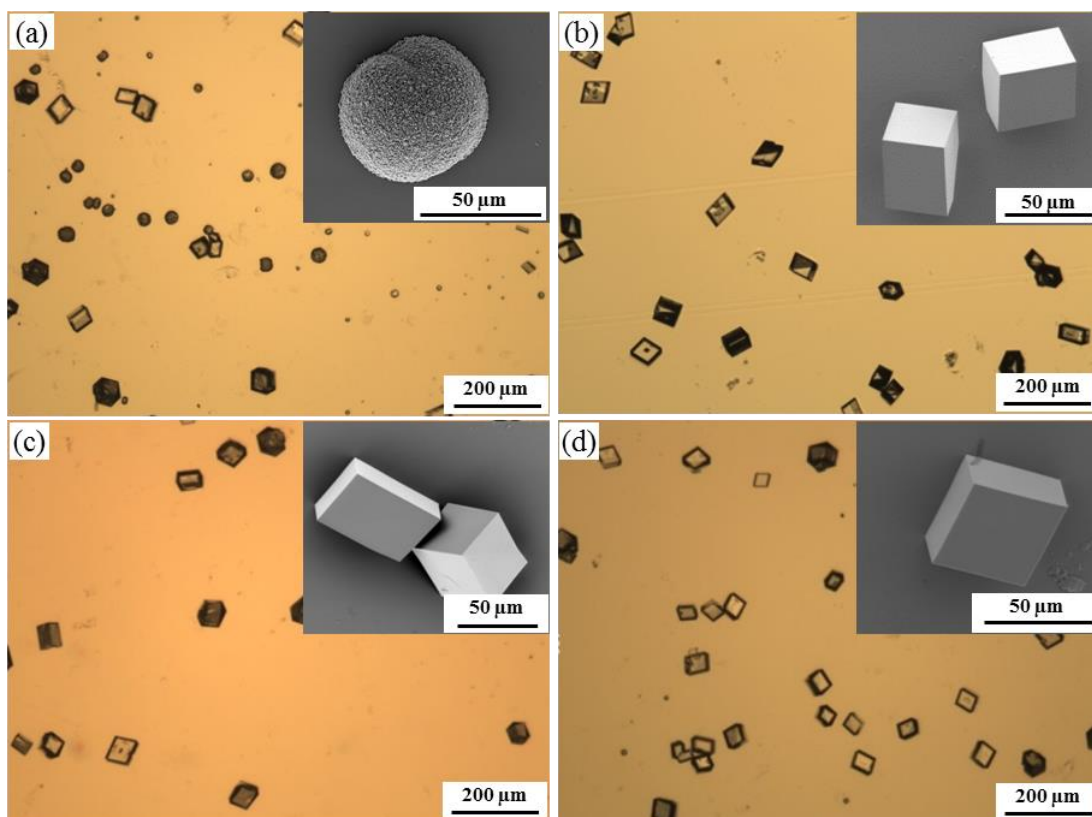
Figure 4.6. Optical micrographs recorded for calcium carbonate crytsals obtained under various conditions: (a) 0.1 % w/w S_{73}-B_{300} (emulsion) diblock copolymer nanoparticles; (b) control calcium carbonate without any additive; (c) calcium carbonate precipitated in the presence of S_{73} homopolymer (same number of moles as that used for the S_{73}-B_{300} diblock copolymer nanoparticle studies); (d) calcium carbonate precipitated in the presence of 0.01 % w/w S_{73}-B_{300} (emulsion). The insets show the corresponding FE-SEM images. N.B. **Figure 4.6a** shows a mixture of calcite and vaterite and the corresponding inset represents a vaterite crystal. Unless otherwise stated, calcium carbonate crystals were precipitated at pH 8~9 in all cases.

It is also worth noting that each of these rhombohedral calcite crystals possesses a smooth surface. This is significantly different from the crystals precipitated in the presence of P_{50}-H_{300} diblock copolymer nanoparticles, as shown in Chapter 3. The reason for these observations is still not clear, but most probably it is related to the

differing surface functionalities of these two diblock copolymer nanoparticles. As far as we are aware, the presence of carboxylic acid groups promotes a relatively rough crystal surface.[4,5,36]
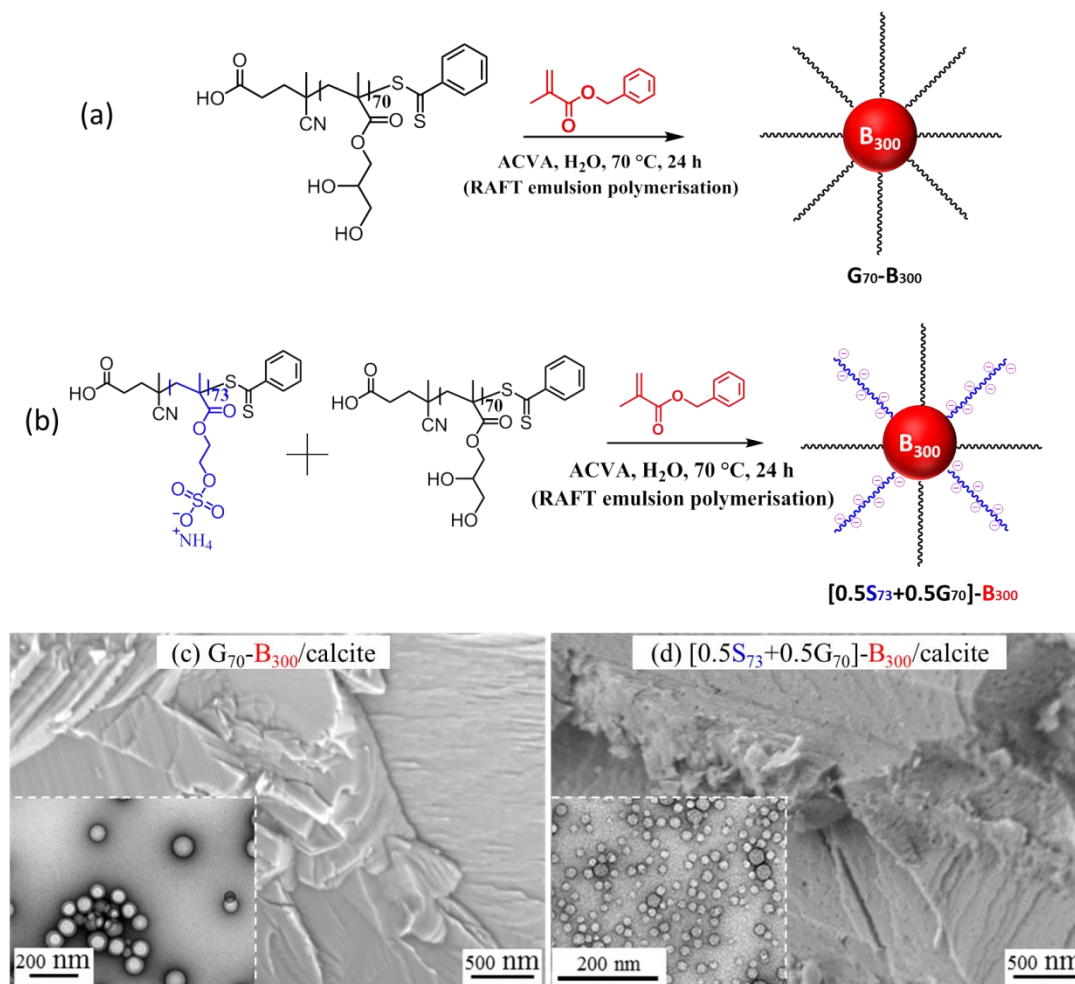
Figure 4.7. (a) Synthesis of non-ionic G_{70}-B_{300}; (b) [0.5 S_{73} + 0.5 G_{70}]-B_{300} diblock copolymer nanoparticles at 10 % w/w solids by chain extension with B monomer at 70 °C for 24 h; (c) FE-SEM image of fractured calcium carbonate crystals precipitated in the presence of 0.01 % w/w of G_{70}-B_{300} (emulsion); (d) FE-SEM image obtained for fractured calcium carbonate crystals prepared in the presence of 0.01 % w/w [0.5 S_{73} + 0.5 G_{70}]-B_{300} copolymer nanoparticles. The insets in (c) and (d) show TEM images of the corresponding diblock copolymer nanoparticles.
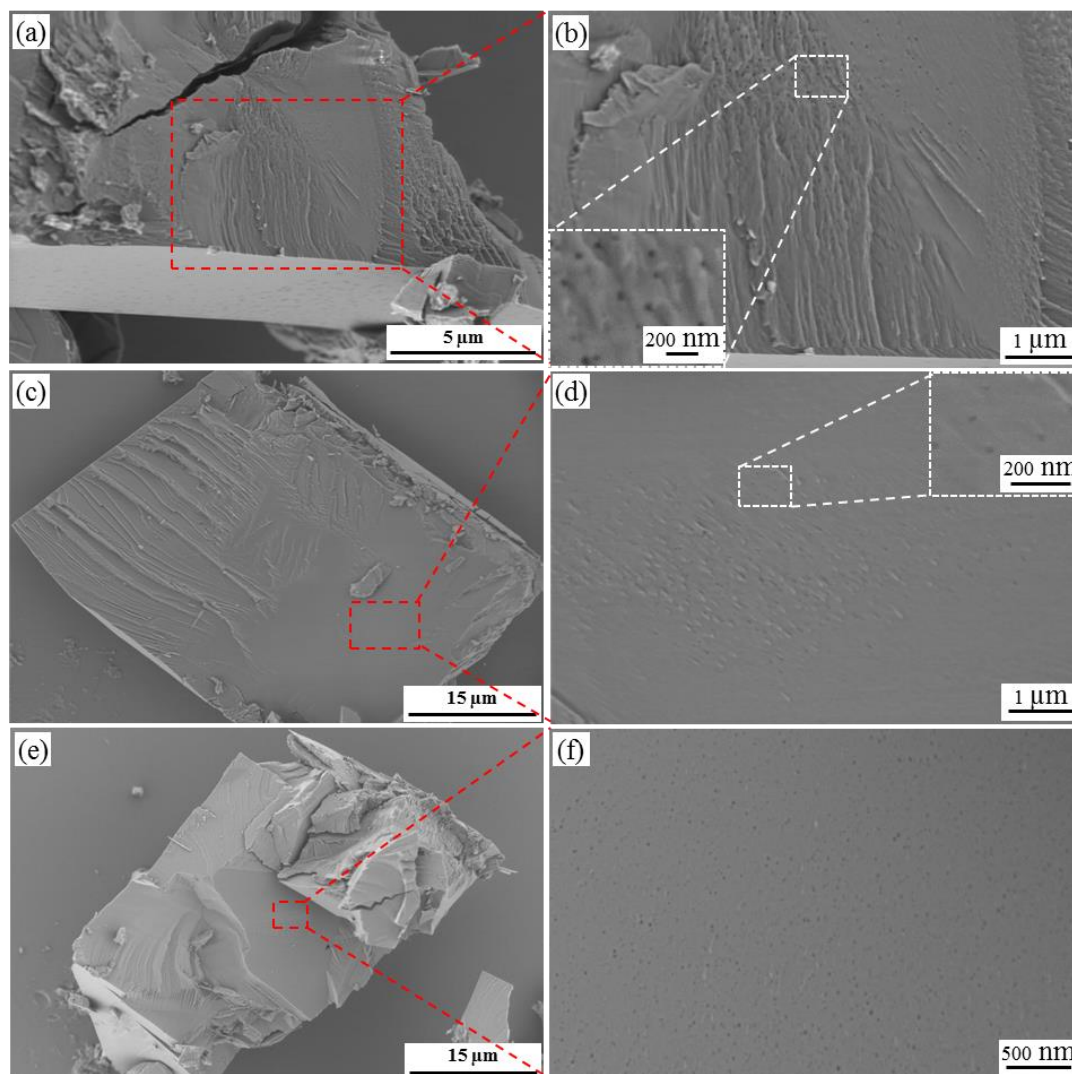
Figure 4.8. Representative FE-SEM images obtained for fractured calcium carbonate crystals prepared in the presence of (a) S_{32}-B_{300} (dispersion) nanoparticles, (c) S_{73}-B_{300} (dispersion) nanoparticles and (e) S_{32}-B_{300} (emulsion) nanoparticles at a fixed copolymer concentration of 0.01 % w/w. (b), (d) and (f) present the magnified FE-SEM images showing the corresponding areas indicated in (a), (c) and (e), respectively. The insets in (b) and (d) are magnified images corresponding to the labeled rectangular areas.

Particle occlusion within the calcite crystals was investigated by imaging fractured crystals with FE-SEM. It is worth noting that no occlusion was observed for G_{70}-B_{300} copolymer nanoparticles as expected (see **Figures 4.7a** and **4.7c**). This is because the G_{70} stabiliser is non-ionic, hence there is no favorable electrostatic interaction with the growing crystal. This observation is in good agreement with the previous

occlusion experiments, in which smaller G_{70}-B_{100} diblock copolymer nanoparticles of approximate 20 nm diameter were used as additives (see **Figure 3.8**, Chapter 3). Some degree of occlusion did occur when 50 % of the non-ionic G_{70} stabiliser chains were replaced with anionic S_{73} stabiliser for the synthesis of $[0.5\ S_{73} + 0.5\ G_{70}]$-$B_{300}$ (emulsion) nanoparticles using a binary macro-CTA mixture,[22,23,25] see **Figures 4.7b** and **4.7d**. Here the binary macro-CTA mixture means two types of macro-CTAs were used as stabilisers during the PISA syntheses. The advantage of this method is that it provides fine control over the anionic charge density, as shown in **Figure 4.7b**. Some degree of occlusion was also observed for S_{32}-B_{300} and S_{73}-B_{300} nanoparticles prepared via RAFT dispersion polymerisation, but this appears to be rather inhomogeneous (see **Figures 4.8a-4.8b** and **Figures 4.8c-4.8d**). In contrast, the S_{32}-B_{300} nanoparticles obtained using RAFT aqueous emulsion polymerisation are much more uniformly incorporated within calcite (see **Figures 4.8e** and **4.8f**). Similarly, S_{73}-B_{300} diblock copolymer nanoparticles prepared via RAFT emulsion polymerisation can also be densely incorporated into calcite, as shown in **Figure 4.9**. The calcite crystals precipitated in the presence of 0.01 % w/w S_{73}-B_{300} (emulsion) were examined in more detail. The internal structure of a fractured crystal is shown in **Figure 4.9**: these images demonstrate that the nanoparticles are both non-aggregated and uniformly occluded throughout the crystal. It is also noteworthy that all nanoparticle cavities are spherical and comparable in size to the original S_{73}-B_{300} (emulsion) nanoparticles (**Figure 4.9d**). Kim et al. previously reported that relatively soft anionic diblock copolymer spherical micelles deform and flatten during their occlusion into calcite.[5] This phenomenon was recently studied in detail by Cho et al., who used AFM and micromechanical simulations to rationalise the in situ change in copolymer morphology.[4] Presumably, the relatively high glass transition temperature of the B core-forming block prevents deformation of the S_{73}-B_{300} (emulsion) nanoparticles examined hereby.

The crystal structure can be readily assigned using Raman spectroscopy. Characteristic bands for calcite were detected at 154 and 280 cm^{-1} (lattice modes), 712 cm^{-1} (υ_4) and 1086 cm^{-1} (υ_1) for both a CaCO$_3$ control and a S_{73}-B_{300} (emulsion)/calcite nanocomposite, as shown in **Figure 4.10a**.[40,41] Although no characteristic band could be observed by Raman spectroscopy, a weak ester carbonyl band at 1729 cm^{-1} originating from S_{73}-B_{300} (emulsion) diblock copolymer

nanoparticles is discernible in the FT-IR spectrum recorded for S_{73}-B_{300} (emulsion)/calcite, which supports successful occlusion of these copolymer nanoparticles within the calcite crystals (see **Figure 4.10b**).
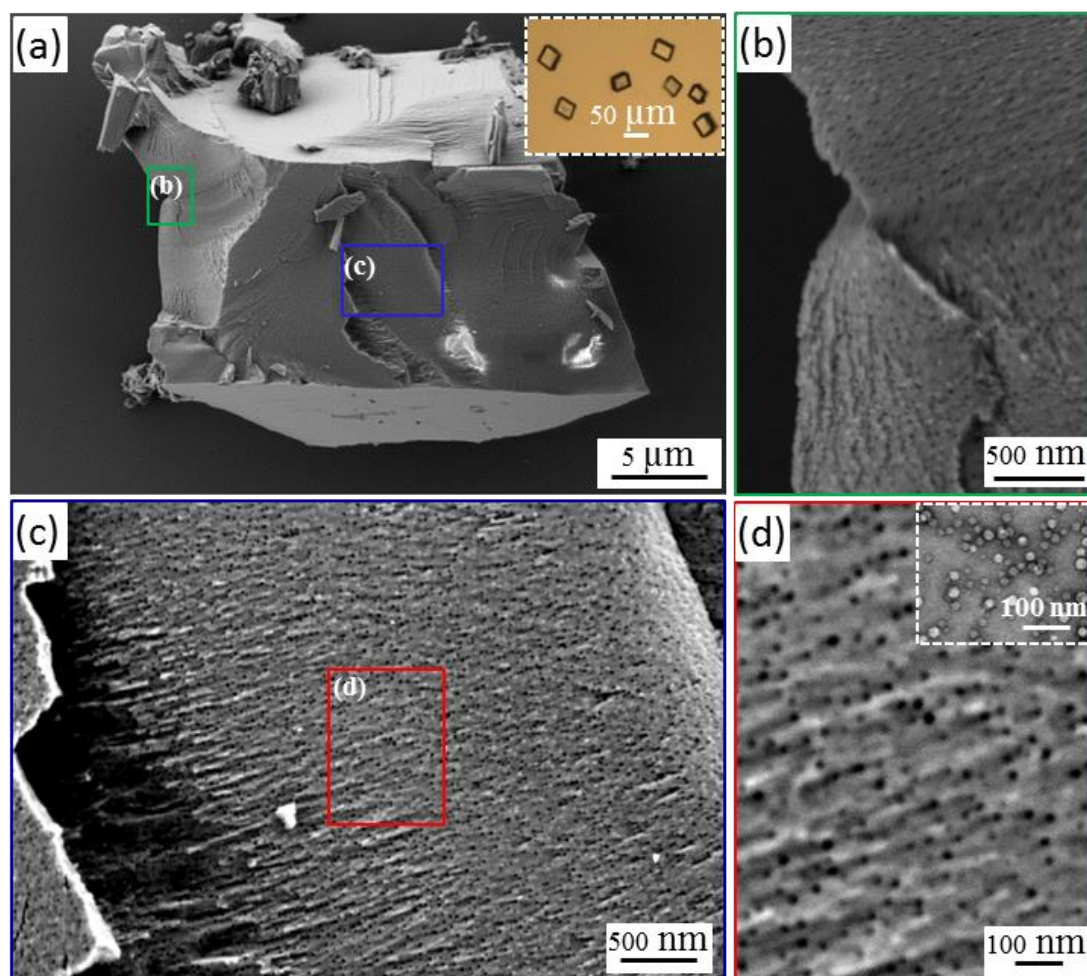
Figure 4.9. Representative FE-SEM images obtained for fractured calcium carbonate crystals prepared in the presence of (a) S_{73}-B_{300} (emulsion), showing fractured crystals at low magnification. The inset in (a) shows an optical micrograph obtained for intact rhombohedral calcite crystals prior to fracture. (b) and (c) depict magnified images of selected areas as indicated in (a), confirming that such nanoparticles are efficiently and uniformly occluded within calcium carbonate crystals. (d) Magnified image showing the rectangular area indicated in (c). The inset in (d) is a TEM image obtained for the S_{73}-B_{300} (emulsion) nanoparticles prior to their occlusion. Clearly, the dimensions of the occluded features observed in (d) are consistent with the diameter of the original nanoparticles.
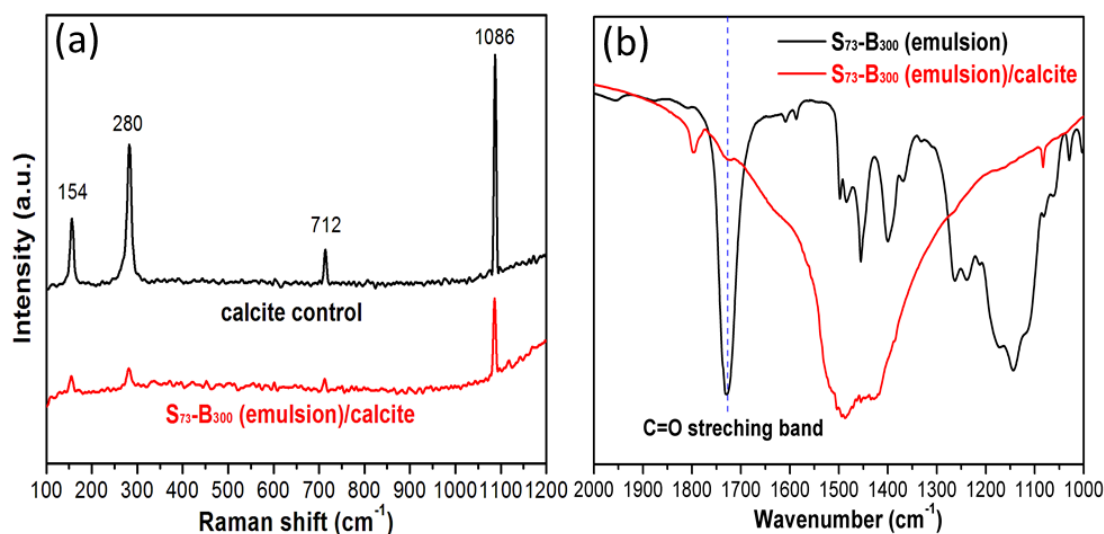
Figure 4.10. (a) Raman spectra recorded for a calcite control (black spectrum) and a S_{73}-B_{300} (emulsion)/calcite nanocomposite crystal (red spectrum). (b) FT-IR spectra recorded for S_{73}-B_{300} (emulsion) nanoparticles alone and nanocomposite crystals comprising S_{73}-B_{300} (emulsion) nanoparticles occluded within calcite.

The extent of occlusion was quantified using TGA (**Figure 4.11a**), which showed that the S_{73}-B_{300} (emulsion) diblock copolymer nanoparticles were completely pyrolysed on heating in air up to 550 °C, while pure calcite decomposed to give a CaO residue of 56.4 % w/w, which is close to its theoretical CaO content of 56.0 % w/w. Based on these data, it is calculated that the occlusion is almost negligible for S_{73}-B_{300} (dispersion) nanoparticles. For the [0.5 S_{73} + 0.5 G_{70}]-B_{300} nanoparticles, the extent of occlusion is ~ 2 % w/w. The TGA curve obtained for the S_{73}-B_{300} (emulsion)/calcite nanocomposite crystals exhibited three distinct features. First, a 3.7 % mass loss was observed up to 600 °C which is assigned to decomposition of S_{73}-B_{300} (emulsion) nanoparticles located in the outer regions of the host crystal. Second, the TGA curve was shifted to a higher temperature, suggesting enhanced thermal stability for the nanocomposite crystal. Finally, the final residue of 52.2 % w/w was significantly lower than 56 % w/w, which indicates successful occlusion. The degree of occlusion calculated for S_{73}-B_{300} (emulsion) nanoparticles is 7.5 % w/w, or approximately 16 % v/v (assuming a copolymer density of 1.18 g cm^{-3}). The occlusion of S_{73}-B_{300} (emulsion) diblock copolymer nanoparticles within calcite was also confirmed by FT-IR spectroscopy, as previous discussed in **Figure 4.10b**.
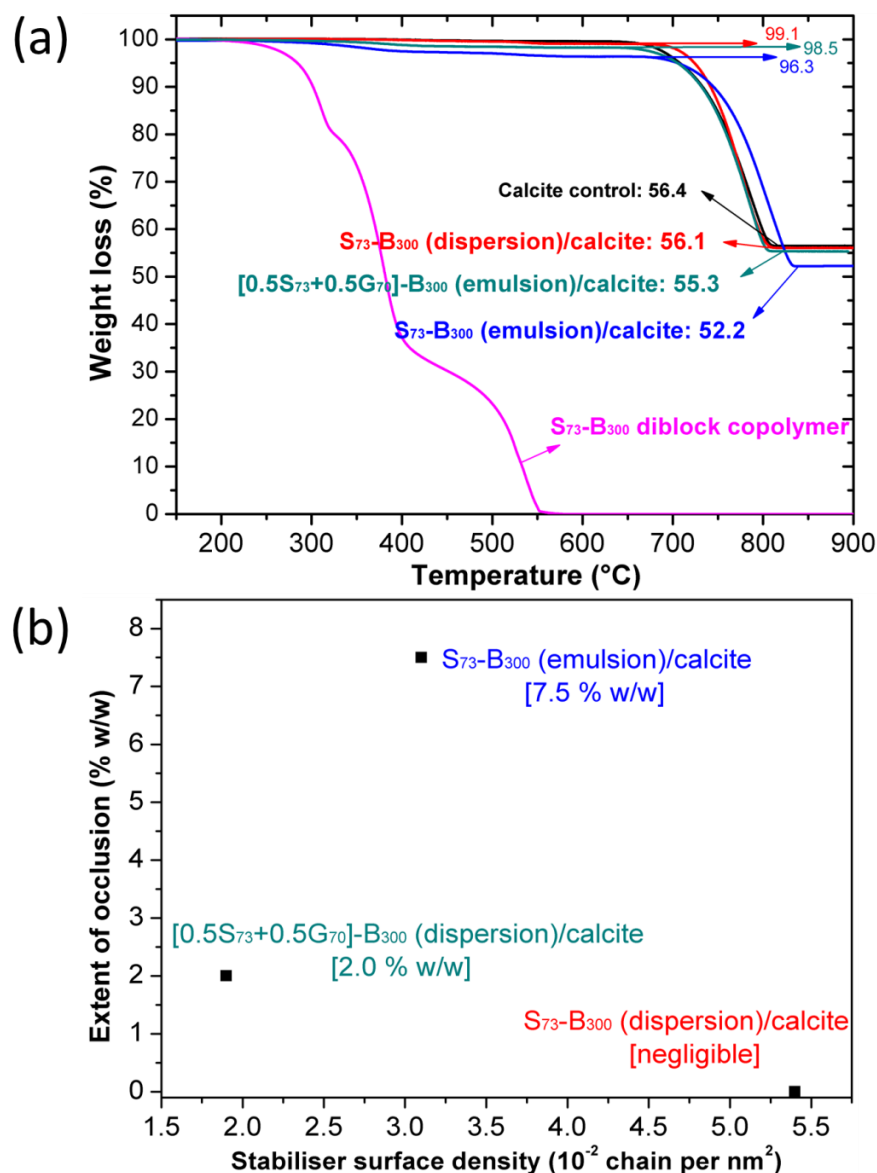
Figure 4.11. (a) TGA data obtained for S_{73}-B_{300}/calcite nanocomposite crystals and corresponding control samples. Calcite control shows the expected approximate 44% mass loss as a result of CaO formation via loss of CO_2. S_{73}-B_{300} (dispersion)/calcite nanocomposite crystals exhibit a slightly greater weight loss compared to the calcite control; this indicates a relatively low level of copolymer nanoparticle occlusion and is consistent with FE-SEM studies (see **Figure 4.8**). [0.5 S_{73}+0.5 G_{70}]-B_{300} (emulsion)/calcite nanocomposite crystals show more weight loss and S_{73}-B_{300} (emulsion)/calcite nanocomposite crystals exhibit a significantly greater weight loss. Original S_{73}-B_{300} diblock copolymer nanoparticles show complete pyrolysis of this purely organic component. (b) plots of extent of occlusion versus stabiliser surface density. **Figure 4.11b** indicates that the extent of occlusion of copolymer nanoparticles within calcite depends on the surface density of the anionic stabiliser chains. Neither a low nor a high surface density affords efficient occlusion. Instead, an *optimal* stabiliser surface density is required to achieve the *maximum* extent of occlusion.

4.2.3 Investigation of Nanoparticle Occlusion Behavior

These two sets of nanoparticles possess apparently the same surface chemistry but exhibit substantial differences with regard to their extents of occlusion within calcite crystal. Initially, this discrepancy was considered to be possibly a particle size effect. However, control experiments ruled out this explanation. More specifically, a series of S_x-B_y (dispersion) nanoparticles ranging in size from 18 nm to 100 nm diameter were prepared by varying the DP of B block at 10 % w/w solids and evaluated for occlusion into calcite under the same conditions.

Remarkably, all S_x-B_y nanoparticles prepared by RAFT dispersion polymerisation are either not occluded or only weakly occluded within calcite (see **Figure 4.12**), whereas all S_x-B_y nanoparticles prepared by RAFT emulsion polymerisation can be uniformly incorporated into calcium carbonate regardless of their particle size (see **Figure 4.9** and **Figure 4.13**).
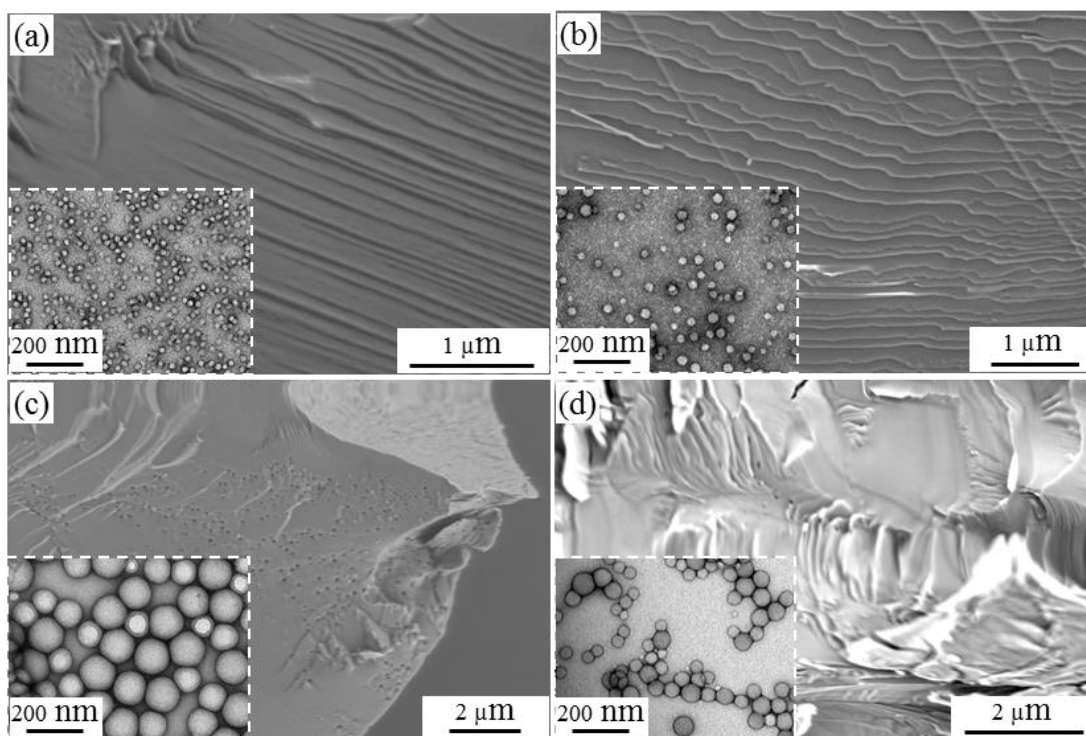
Figure 4.12. FE-SEM images obtained for fractured calcium carbonate crystals prepared in the presence of 0.01 % w/w S_x-B_y diblock copolymer nanoparticles prepared by RAFT dispersion polymerisation: (a) S_{32}-B_{100} (dispersion); (b) S_{73}-B_{100} (dispersion); (c) S_{32}-B_{500} (dispersion); (d) S_{73}-B_{500} (dispersion). Insets show TEM images of the corresponding S_x-B_y diblock copolymer nanoparticles prior to occlusion.
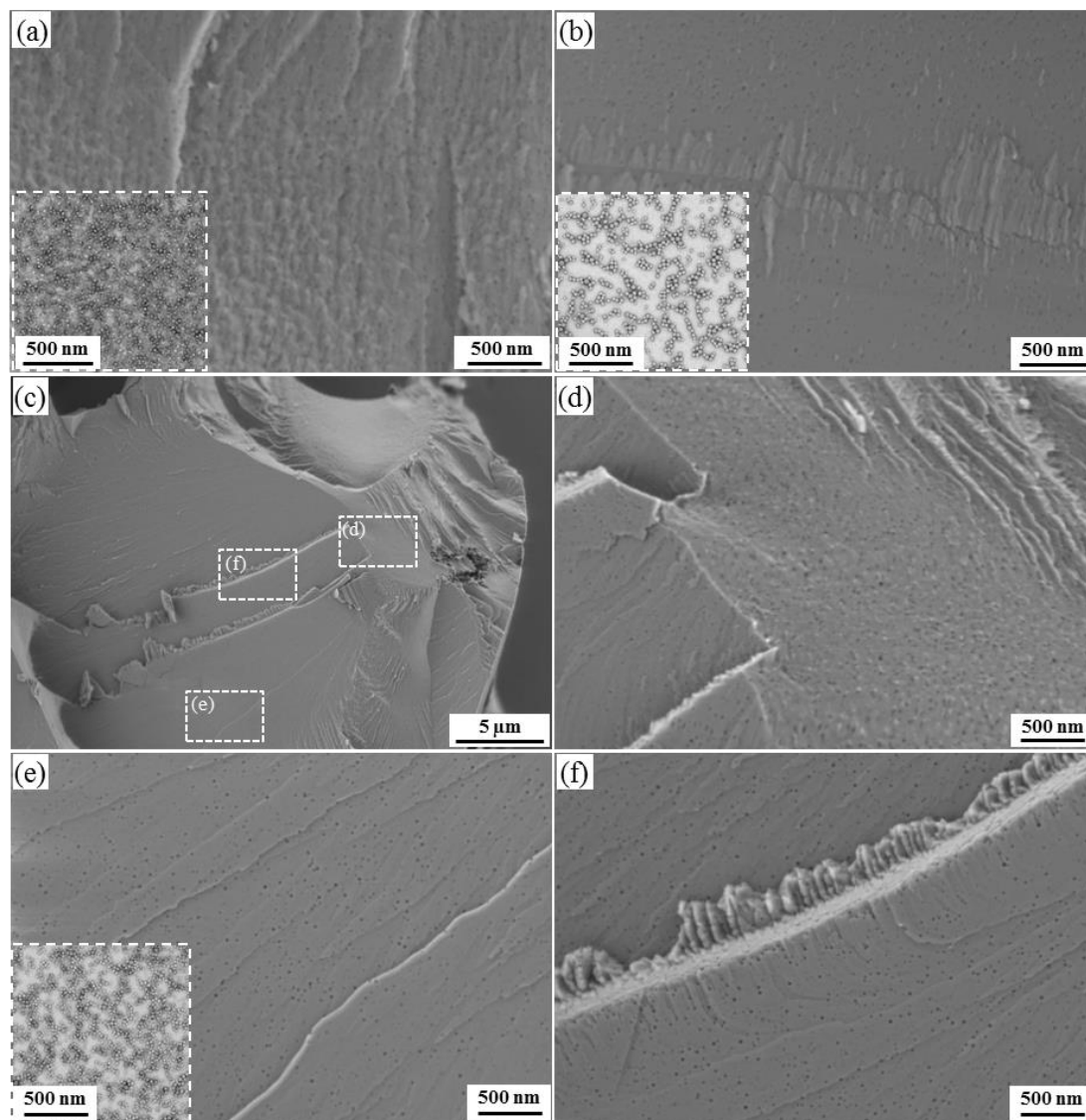
Figure 4.13. FE-SEM images obtained for fractured calcium carbonate crystals prepared in the presence of 0.01 % w/w S_x-B_y diblock copolymer nanoparticles prepared by RAFT emulsion polymerisation: (a) S_{32}-B_{100} (emulsion); (b) S_{32}-B_{500} (emulsion); (c) S_{73}-B_{500} (emulsion). (d), (e) and (f) show the magnified images as indicated in (c). Insets show TEM images of the corresponding S_x-B_y diblock copolymer nanoparticles prior to occlusion. [N.B. Well-defined S_{73}-B_{100} (emulsion) cannot be prepared as the core-forming block is too short]

Thus it seems that occlusion is not sensitive to the nanoparticle dimensions. In fact, Kim and co-workers reported that anionic carboxylated latexes of approximately 220-250 nm diameter could be occluded within calcite.[6] Recently, poly(methacrylic acid)-poly(benzyl methacrylate) worms and vesicles have been incorporated into

calcite.[36] These two types of nano-objects are obviously much larger compared to the nanoparticles used in the present work. Moreover, occlusion does not appear to be particularly sensitive to the stabiliser DP because both S_{32}-B_y and S_{73}-B_y nanoparticles prepared via RAFT aqueous emulsion polymerisation can be uniformly occluded within calcite, see **Figure 4.13**.

As discussed above, the zeta potential for nanoparticles prepared by RAFT dispersion polymerisation is significantly more negative than that for nanoparticles prepared via RAFT aqueous emulsion polymerisation (see **Figure 4.4b**). This observation led us to determine the stabiliser surface densities for these two types of nanoparticles, because we hypothesised that this parameter might explain their differing occlusion behavior. Given a high blocking efficiency, full B conversion and a relatively narrow particle size distribution, the stabiliser surface density can be obtained via the following equations:

Mass of each nanoparticle (m):

$$m = \rho V = \frac{4}{3}\pi\rho r^3$$

The number of nanoparticles (N):

$$N = \frac{m_s + m_b}{m} = \frac{3(m_s + m_b)}{4\pi\rho r^3}$$

Surface area of each particle (S_A):

$$S_A = 4\pi r^2$$

Total surface area of all particles (S_{TA}):

$$S_{TA} = S_A \times N = 4\pi r^2 N = \frac{3(m_s + m_b)}{\rho r}$$

Thus the stabiliser surface density (D_S, chain per nm^2) is given by:

$$D_S = \frac{n_{PSEM}N_A}{S_{TA}} = \frac{n_{PSEM}N_A\rho r}{3(m_s + m_b)} \times 10^{-21} \qquad (4.1)$$

Here D_s is the stabiliser surface density expressed as the number of chains per nm^2 and n_{PSEM}, N_A, ρ and r denote the number of moles of S macro-CTA (mol), Avogadro's number (mol^{-1}), the solid-state density of the dried nanoparticles (g cm^{-3}) and the mean nanoparticle radius (nm), respectively. The masses (g) of the S macro-CTA and poly(benzyl methacrylate) are given by m_s and m_b, respectively.

Using equation (4.1), the stabiliser surface densities of the diblock copolymer nanoparticles were determined from the nanoparticle dimensions and these data are summarised in **Table 4.1**. In all cases, S_x-B_y nanoparticles prepared via RAFT dispersion polymerisation have significantly higher surface stabiliser densities than the corresponding nanoparticles prepared via RAFT emulsion polymerisation. Direct experimental evidence of this finding was also provided by X-ray photoelectron spectroscopy (XPS), which is an established analytical technique for determining surface chemical compositions. XPS has excellent inter-element resolution and is highly surface-specific, with a typical sampling depth of 2-10 nm.[42] For the current study, the S stabiliser chains provide a unique source of sulfur atoms. Hence higher sulfur contents indicate higher stabiliser surface densities (see **Figure 4.14**). Both the S stabiliser and the B core-forming block contain carbon atoms, which give rise to C1s signals in XPS. All samples were run under the same conditions and the S2p/C1s atomic ratios calculated from XPS analysis of the S_x homopolymers are very close to theoretical values (see **Table 4.1**). Thus the level of surface carbon contamination is low (and assumed to be negligible). *Normalised* atomic ratios, [S2p/C1s (particle)]/[S2p/C1s (stabiliser)], were calculated to compare stabiliser surface densities for the nanoparticles, as summarised in **Table 4.1**. As expected, no sulfur signals were detected for the B_{300} control and the S_{73} control had the highest sulfur content (strongest S2p signal). More importantly, S_x-B_y nanoparticles prepared via RAFT dispersion polymerisation exhibit consistently higher normalised

[S2p/C1s (particle)]/[S2p/C1s (stabiliser)] atomic ratios (by a factor of approximately two) compared to the equivalent nanoparticles prepared via RAFT emulsion polymerisation. This indicates that the former nanoparticles have a higher stabiliser surface density than the latter.
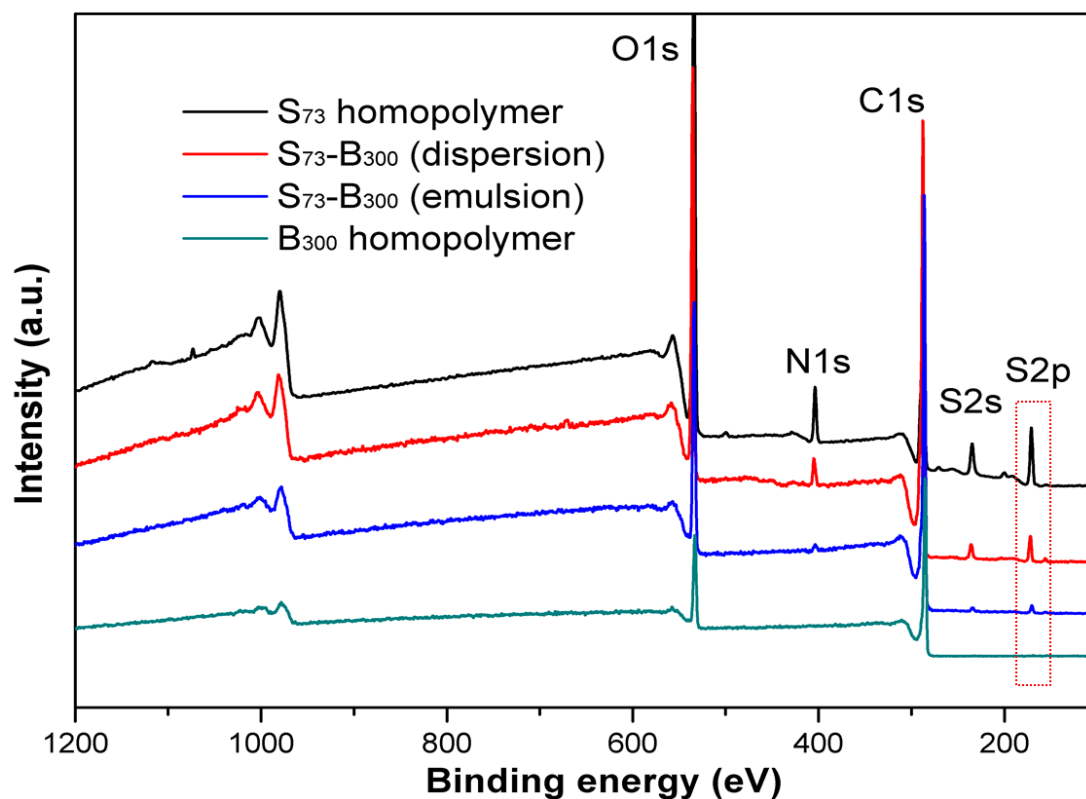
Figure 4.14. X-ray photoelectron survey spectra recorded for a S_{73} homopolymer control, S_{73}-B_{300} (dispersion), S_{73}-B_{300} (emulsion), and a B_{300} homopolymer control. The red rectangle highlights the relative S2p intensities, which are in the order: B_{300} homopolymer < S_{73}-B_{300} (emulsion) < S_{73}-B_{300} (dispersion) < S_{73} homopolymer.

This difference is consistent with the theoretical stabiliser surface densities calculated using equation (4.1) and can be ascribed to two reasons. Firstly, the relatively low dielectric constant for the 2:1 v/v ethanol/water mixture (compared to pure water) reduces electrostatic repulsion between neighboring highly anionic S stabilisers during nanoparticle formation via PISA, which results in a more densely-packed coronal layer. Secondly, the B chains are likely to be slightly more solvated (and hence more stretched, leading to more closely-packed copolymer chains in the nanoparticle cores) when grown in the 2:1 v/v ethanol/water mixture, compared to PISA syntheses conducted in pure water.[43]
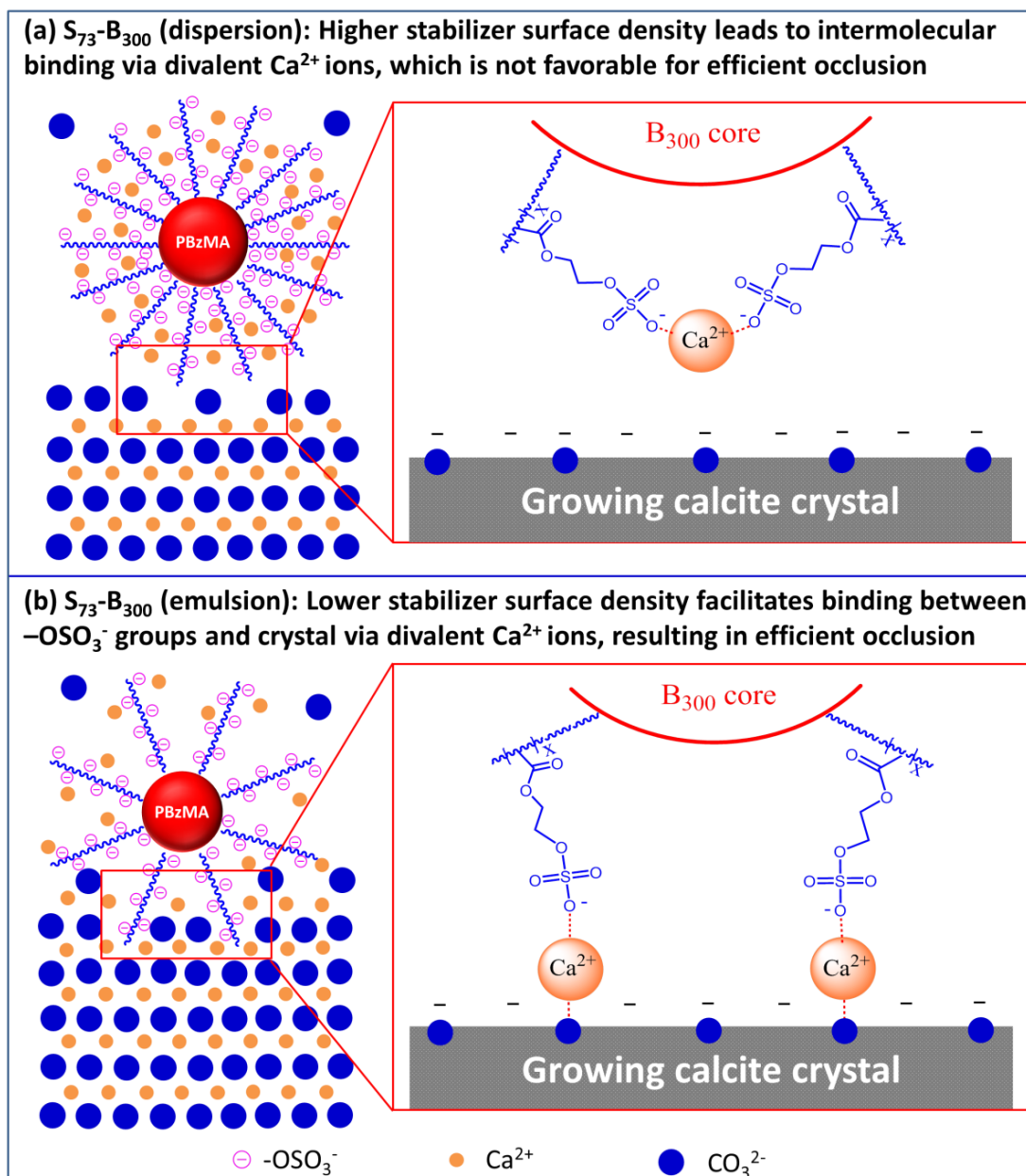
Figure 4.15. Schematic cartoon representing the proposed occlusion mechanism. (a) Crystallisation in the presence of S_x-B_y (dispersion) nanoparticles. The relatively high stabiliser surface density means that Ca^{2+} ions primarily act as ionic cross-linkers between adjacent stabiliser chains and the ensuing loss of conformational entropy reduces nanoparticle interactions with the growing crystal. (b) Crystallisation in the presence of S_x-B_y (emulsion) nanoparticles. In this case the relatively low stabiliser density reduces the degree of ionic cross-linking between stabiliser chains and enables the nanoparticles to interact more strongly with the growing crystals, hence promoting efficient occlusion.

Naively, a higher stabiliser surface density should provide stronger nanoparticle binding to the crystal surface and hence lead to higher levels of occlusion. However,

less occlusion is actually observed, which at first sight appears to be counter-intuitive. The present study shows that *effcent* occlusion actually requires an *optimum* (rather than maximum) stabiliser surface density. A tentative occlusion mechanism is as follows. Prior to precipitation of calcium carbonate, Ca^{2+} ions bind to the anionic stabiliser chains of S_x-B_y nanoparticles in aqueous solution, as indicated by their significantly lower zeta potential compared to nanoparticles in the absence of $CaCl_2$ (see **Figure 4.4c**). Under otherwise identical conditions (i.e. 1.5 mM $CaCl_2$ and 0.01 % w/w copolymer at 20 °C), the extent of Ca^{2+} ion binding to the anionic sulfate groups on the S_{73}-B_{300} (emulsion) and S_{73}-B_{300} (dispersion) nanoparticles is estimated to be 5.9 ± 1.2 mg g^{-1} and 6.1 ± 1.4 mg g^{-1} respectively, as determined using a calcium ion-selective electrode.[44] If the stabiliser chains are closely packed, the relatively high stabiliser surface density means that Ca^{2+} ions primarily act as ionic cross-linkers between *adjacent* S chains. Thus the ensuing loss of conformational entropy reduces the ability of these sterically-stabilised nanoparticles to interact with the growing crystal, see **Figure 4.15a**. However, such ionic cross-linking is much less likely to occur if the stabiliser surface density is relatively low, which allows the nanoparticles prepared via RAFT emulsion polymerisation to retain more conformational entropy. Thus a greater proportion of the stabiliser chains are able to relax, which enables these nanoparticles to bind more effectively on the growing calcite surface (see **Figure 4.15b**).

This interpretation is consistent with recent *in situ* AFM studies, which demonstrate that anionic block copolymer micelles uniquely bind at calcite step edges prior to their incorporation.[4] A further reduction in the S stabiliser surface density can be achieved by introducing non-ionic G stabiliser chains. Such $[0.5\ S_{73} + 0.5\ G_{70}]$-$B_{300}$ (emulsion) nanoparticles exhibit an extent of occlusion of just 2 % w/w. One possible explanation is that the presence of the non-ionic G stabiliser chains restricts the ability of the anionic S stabiliser chains to interact efficiently with the growing calcite crystals. Alternatively, the (diluted) S surface density is now simply too low to ensure efficient interaction between such copolymer nanoparticles and the growing calcite crystals.
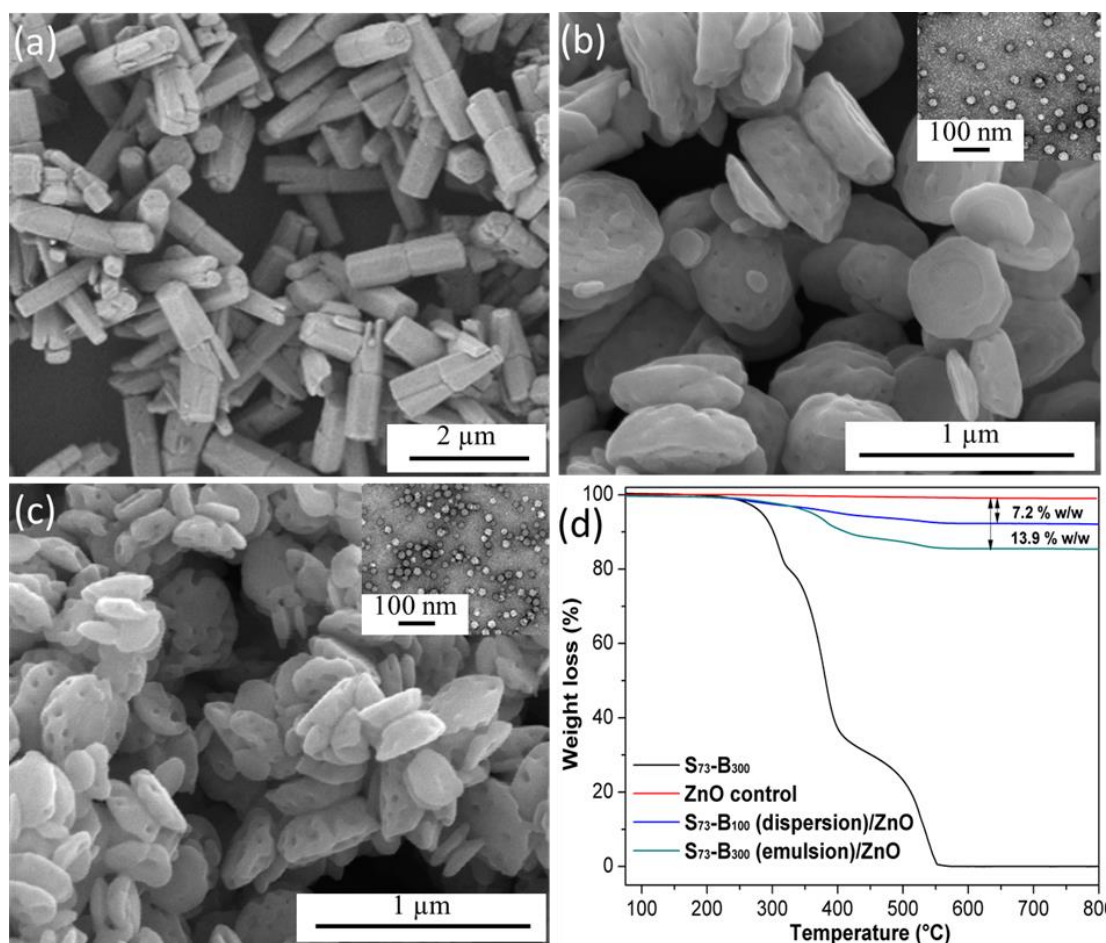
Figure 4.16. SEM images obtained for ZnO precipitated in the presence of copolymer nanoparticles. (a) ZnO control (without any additive); (b) ZnO precipitated in the presence of 0.01 % w/w S_{73}-B_{100} (dispersion) copolymer nanoparticles; (c) ZnO precipitated in the presence of 0.01 % w/w S_{73}-B_{300} (emulsion) copolymer nanoparticles; (d) TGA curves recorded for these three samples as well as for the S_{73}-B_{300} (emulsion) copolymer nanoparticles alone. The insets shown in (b) and (c) are TEM images of the corresponding S_{73}-B_{100} (dispersion) and S_{73}-B_{300} (emulsion) copolymer nanoparticles. N.B. The former nanoparticles were chosen for the ZnO occlusion experiments, because their mean diameter is comparable with that of the S_{73}-B_{300} (emulsion) copolymer nanoparticles (see **Table 4.1**).

4.2.4 Effect of Stabiliser Surface Density on the Extent of Occlusion within ZnO

To examine the effect of varying stabiliser surface density for other inorganic crystal hosts, we also performed some preliminary occlusion experiments using ZnO instead of calcite. S_{73}-B_{300} nanoparticles prepared by RAFT emulsion polymerisation exhibited a higher extent of occlusion (13.9 % w/w vs 7.2 % w/w, see **Figure 4.16**)

compared to S_{73}-B_{100} (dispersion) nanoparticles of comparable size. This is in good agreement with the calcite system and further suggests that an *optimum* stabiliser surface density is required to *maximise* the extent of occlusion. These copolymer nanoparticle/ZnO nanocomposite crystals were heated up to 900 °C in air to remove the copolymer component via pyrolysis and then gold-coated prior to scanning electron microscopy imaging.

4.3 Conclusions

In summary, a range of well-defined highly anionic diblock copolymer nanoparticles with tunable surface density have been prepared via RAFT-mediated PISA. The stabiliser surface density depends on the solvent quality for the stabiliser chains, which offers an unprecedented opportunity to examine the relationship between nanoparticle surface composition and the corresponding extent of occlusion within calcite crystals. Up to 7.5 % w/w (or ~ 16 % v/v) S_{73}-B_{300} (emulsion) nanoparticles can be incorporated within calcite ($CaCO_3$) even when using a relatively low copolymer concentration (0.01 % w/w). Surprisingly, more anionic nanoparticles prepared via RAFT dispersion polymerisation using a 2:1 v/v ethanol/water mixture are occluded much less efficiently into calcite under identical crystallisation conditions. This suggests that there is an *optimum* (rather than a maximum) surface density of anionic stabiliser chains for occlusion into this host crystal matrix. This finding indicated that higher stabiliser density does not afford higher extent of occlusion. Thus this work provides important new insights regarding the rather subtle role played by the nanoparticle surface stabiliser density in determining occlusion efficiencies within calcite.

Calcite is an interesting crystal host for the occlusion of diblock copolymer nanoparticles. However, there are only rather limited practical applications for such nanocomposite crystals. Moreover, scale-up syntheses based on the ammonium carbonate diffusion method are problematic. In view of these problems, in the next Chapter we extend the concept of nanoparticle occlusion to include alternative host crystals, e.g. ZnO.

4.4 References

(1) Pasteris, J. D.; Freeman, J. J.; Wopenka, B.; Qi, K.; Ma, Q.; Wooley, K. L. With a grain of salt: what halite has to offer to discussions on the origin of life. *Astrobiology* **2006**, *6*, 625-643.

(2) Lu, C. H.; Qi, L. M.; Cong, H. L.; Wang, X. Y.; Yang, J. H.; Yang, L. L.; Zhang, D. Y.; Ma, J. M.; Cao, W. X. Synthesis of calcite single crystals with porous surface by templating of polymer latex particles. *Chemistry of Materials* **2005**, *17*, 5218-5224.

(3) Hanisch, A.; Yang, P.; Kulak, A. N.; Fielding, L. A.; Meldrum, F. C.; Armes, S. P. Phosphonic Acid-Functionalized Diblock Copolymer Nano-Objects via Polymerization-Induced Self-Assembly: Synthesis, Characterization, and Occlusion into Calcite Crystals. *Macromolecules* **2016**, *49*, 192-204.

(4) Cho, K.-R. K., Y.-Y.; Yang, P.; Cai, W.; Pan, H.; Kulak, A. N.; Lau, J. L.; Kulshreshtha, P.; Armes, S. P.; Meldrum, F. C.; De Yoreo, J. J. Direct observation of mineral-organic composite formation reveals occlusion mechanism. *Nature Communications* **2016**, *7*, 10187.

(5) Kim, Y.-Y.; Ganesan, K.; Yang, P.; Kulak, A. N.; Borukhin, S.; Pechook, S.; Ribeiro, L.; Kroeger, R.; Eichhorn, S. J.; Armes, S. P.; Pokroy, B.; Meldrum, F. C. An artificial biomineral formed by incorporation of copolymer micelles in calcite crystals. *Nature Materials* **2011**, *10*, 890-896.

(6) Kim, Y.-Y.; Ribeiro, L.; Maillot, F.; Ward, O.; Eichhorn, S. J.; Meldrum, F. C. Bio-Inspired Synthesis and Mechanical Properties of Calcite-Polymer Particle Composites. *Advanced Materials* **2010**, *22*, 2082-2086.

(7) Zhang, L. F.; Eisenberg, A. Multiple morphologies of "crew-cut" aggregates of polystyrene-b-poly (acrylic acid) block copolymers. *Science* **1995**, *268*, 1728-1731.

(8) Li, Y.; Armes, S. P. RAFT Synthesis of Sterically Stabilized Methacrylic Nanolatexes and Vesicles by Aqueous Dispersion Polymerization. *Angewandte Chemie-International Edition* **2010**, *49*, 4042-4046.

(9) Penfold, N. J. W.; Lovett, J. R.; Warren, N. J.; Verstraete, P.; Smets, J.; Armes, S. P. pH-Responsive non-ionic diblock copolymers: protonation of a morpholine end-group induces an order-order transition. *Polymer Chemistry* **2016**, *7*, 79-88.

(10) Warren, N. J.; Armes, S. P. Polymerization-Induced Self-Assembly of Block Copolymer Nano-objects via RAFT Aqueous Dispersion Polymerization. *Journal of the American Chemical Society* **2014**, *136*, 10174-10185.

(11) Warren, N. J.; Mykhaylyk, O. O.; Mahmood, D.; Ryan, A. J.; Armes, S. P. RAFT Aqueous Dispersion Polymerization Yields Poly(ethylene glycol)-Based Diblock Copolymer Nano-Objects with Predictable Single Phase Morphologies. *Journal of the American Chemical Society* **2014**, *136*, 1023-1033.

(12) Derry, M. J.; Fielding, L. A.; Armes, S. P. Polymerization-induced self-assembly of block copolymer nanoparticles via RAFT non-aqueous dispersion polymerization. *Progress in Polymer Science* **2016**, *52*, 1-18.

(13) Derry, M. J.; Fielding, L. A.; Warren, N. J.; Mable, C. J.; Smith, A. J.; Mykhaylyk, O. O.; Armes, S. P. In situ small-angle X-ray scattering studies of sterically-stabilized diblock copolymer nanoparticles formed during polymerization-induced self-assembly in non-polar media. *Chemical Science* **2016**, *7*, 5078-5090.

(14) Fielding, L. A.; Lane, J. A.; Derry, M. J.; Mykhaylyk, O. O.; Armes, S. P. Thermo-responsive Diblock Copolymer Worm Gels in Non-polar Solvents. *Journal of the American Chemical Society* **2014**, *136*, 5790-5798.

(15) Fielding, L. A.; Derry, M. J.; Ladmiral, V.; Rosselgong, J.; Rodrigues, A. M.; Ratcliffe, L. P. D.; Sugihara, S.; Armes, S. P. RAFT dispersion polymerization in non-polar solvents: facile production of block copolymer spheres, worms and vesicles in n-alkanes. *Chemical Science* **2013**, *4*, 2081-2087.

(16) Canning, S. L.; Smith, G. N.; Armes, S. P. A Critical Appraisal of RAFT-Mediated Polymerization-Induced Self-Assembly. *Macromolecules* **2016**, *49*, 1985-2001.

(17) Blanazs, A.; Ryan, A. J.; Armes, S. P. Predictive Phase Diagrams for RAFT Aqueous Dispersion Polymerization: Effect of Block Copolymer Composition, Molecular Weight, and Copolymer Concentration. *Macromolecules* **2012**, *45*, 5099-5107.

(18) Blanazs, A.; Verber, R.; Mykhaylyk, O. O.; Ryan, A. J.; Heath, J. Z.; Douglas, C. W. I.; Armes, S. P. Sterilizable Gels from Thermoresponsive Block Copolymer Worms. *Journal of the American Chemical Society* **2012**, *134*, 9741-9748.

(19) Blanazs, A.; Madsen, J.; Battaglia, G.; Ryan, A. J.; Armes, S. P. Mechanistic Insights for Block Copolymer Morphologies: How Do Worms Form Vesicles? *Journal of the American Chemical Society* **2011**, *133*, 16581-16587.

(20) Cunningham, V. J.; Ratcliffe, L. P. D.; Blanazs, A.; Warren, N. J.; Smith, A. J.; Mykhaylyk, O. O.; Armes, S. P. Tuning the critical gelation temperature of thermo-responsive diblock copolymer worm gels. *Polymer Chemistry* **2014**, *5*, 6307-6317.

(21) Semsarilar, M.; Jones, E. R.; Blanazs, A.; Armes, S. P. Efficient Synthesis of Sterically-Stabilized Nano-Objects via RAFT Dispersion Polymerization of Benzyl Methacrylate in Alcoholic Media. *Advanced Materials* **2012**, *24*, 3378-3382.

(22) Semsarilar, M.; Ladmiral, V.; Blanazs, A.; Armes, S. P. Anionic Polyelectrolyte-Stabilized Nanoparticles via RAFT Aqueous Dispersion Polymerization. *Langmuir* **2012**, *28*, 914-922.

(23) Semsarilar, M.; Ladmiral, V.; Blanazs, A.; Armes, S. P. Cationic Polyelectrolyte-Stabilized Nanoparticles via RAFT Aqueous Dispersion Polymerization. *Langmuir* **2013**, *29*, 7416-7424.

(24) Williams, M.; Penfold, N. J. W.; Armes, S. P. Cationic and reactive primary amine-stabilised nanoparticles via RAFT aqueous dispersion polymerisation. *Polymer Chemistry* **2016**, *7*, 384-393.

(25) Williams, M.; Penfold, N. J. W.; Lovett, J. R.; Warren, N. J.; Douglas, C. W. I.; Doroshenko, N.; Verstraete, P.; Smets, J.; Armes, S. P. Bespoke cationic nano-objects via RAFT aqueous dispersion polymerisation. *Polymer Chemistry* **2016**, *7*, 3864-3873.

(26) Doncom, K. E. B.; Warren, N. J.; Armes, S. P. Polysulfobetaine-based diblock copolymer nano-objects via polymerization-induced self-assembly. *Polymer Chemistry* **2015**, *6*, 7264-7273.

(27) Sugihara, S.; Blanazs, A.; Armes, S. P.; Ryan, A. J.; Lewis, A. L. Aqueous Dispersion Polymerization: A New Paradigm for in Situ Block Copolymer Self-Assembly in Concentrated Solution. *Journal of the American Chemical Society* **2011**, *133*, 15707-15713.

(28) Ning, Y.; Fielding, L. A.; Ratcliffe, L. P.; Wang, Y.-W.; Meldrum, F. C.; Armes, S. P. Occlusion of Sulfate-based Diblock Copolymer Nanoparticles within Calcite: Effect of Varying the Surface Density of Anionic Stabilizer Chains. *Journal of the American Chemical Society* **2016**, *138*, 11734-11742.

(29) Chiefari, J.; Chong, Y.; Ercole, F.; Krstina, J.; Jeffery, J.; Le, T. P.; Mayadunne, R. T.; Meijs, G. F.; Moad, C. L.; Moad, G. Living free-radical polymerization by reversible addition-fragmentation chain transfer: the RAFT process. *Macromolecules* **1998**, *31*, 5559-5562.

(30) Zhang, X.; Rieger, J.; Charleux, B. Effect of the solvent composition on the morphology of nano-objects synthesized via RAFT polymerization of benzyl methacrylate in dispersed systems. *Polymer Chemistry* **2012**, *3*, 1502-1509.

(31) Zhang, W.; D'Agosto, F.; Boyron, O.; Rieger, J.; Charleux, B. Toward a better understanding of the parameters that lead to the formation of nonspherical polystyrene particles via RAFT-mediated one-pot aqueous emulsion polymerization. *Macromolecules* **2012**, *45*, 4075-4084.

(32) Chaduc, I.; Crepet, A.; Boyron, O.; Charleux, B.; D'Agosto, F.; Lansalot, M. Effect of the pH on the RAFT Polymerization of Acrylic Acid in Water. Application to the Synthesis of Poly(acrylic acid)-Stabilized Polystyrene Particles by RAFT Emulsion Polymerization. *Macromolecules* **2013**, *46*, 6013-6023.

(33) Cunningham, V. J.; Alswieleh, A. M.; Thompson, K. L.; Williams, M.; Leggett, G. J.; Armes, S. P.; Musa, O. M. Poly(glycerol monomethacrylate)-Poly(benzyl methacrylate) Diblock Copolymer Nanoparticles via RAFT Emulsion Polymerization: Synthesis, Characterization, and Interfacial Activity. *Macromolecules* **2014**, *47*, 5613-5623.

(34) Boisse, S.; Rieger, J.; Pembouong, G.; Beaunier, P.; Charleux, B. Influence of the Stirring Speed and CaCl2 Concentration on the Nano-Object Morphologies Obtained via RAFT-Mediated Aqueous Emulsion Polymerization in the Presence of a Water-Soluble macroRAFT Agent. *Journal of Polymer Science Part a-Polymer Chemistry* **2011**, *49*, 3346-3354.

(35) Akerlof, G. Dielectric constants of some organic solvent-water mixtures at various temperatures. *Journal of the American Chemical Society* **1932**, *54*, 4125-4139.

(36) Kim, Y.-Y.; Semsarilar, M.; Carloni, J. D.; Cho, K. R.; Kulak, A. N.; Polishchuk, I.; Hendley, C. T.; Smeets, P. J. M.; Fielding, L. A.; Pokroy, B.; Tang, C. C.; Estroff, L. A.; Baker, S. P.; Armes, S. P.; Meldrum, F. C. Structure and Properties of Nanocomposites Formed by the Occlusion of Block Copolymer Worms

and Vesicles Within Calcite Crystals. *Advanced Functional Materials* **2016**, *26*, 1382-1392.

(37) Kulak, A. N.; Semsarilar, M.; Kim, Y.-Y.; Ihli, J.; Fielding, L. A.; Cespedes, O.; Armes, S. P.; Meldrum, F. C. One-pot synthesis of an inorganic heterostructure: uniform occlusion of magnetite nanoparticles within calcite single crystals. *Chemical Science* **2014**, *5*, 738-743.

(38) Kulak, A. N.; Yang, P.; Kim, Y.-Y.; Armes, S. P.; Meldrum, F. C. Colouring crystals with inorganic nanoparticles. *Chemical Communications* **2014**, *50*, 67-69.

(39) Ihli, J.; Bots, P.; Kulak, A.; Benning, L. G.; Meldrum, F. C. Elucidating Mechanisms of Diffusion-Based Calcium Carbonate Synthesis Leads to Controlled Mesocrystal Formation. *Advanced Functional Materials* **2013**, *23*, 1965-1973.

(40) Ihli, J.; Kim, Y.-Y.; Noel, E. H.; Meldrum, F. C. The Effect of Additives on Amorphous Calcium Carbonate (ACC): Janus Behavior in Solution and the Solid State. *Advanced Functional Materials* **2013**, *23*, 1575-1585.

(41) Wehrmeister, U.; Soldati, A. L.; Jacob, D. E.; Haeger, T.; Hofmeister, W. Raman spectroscopy of synthetic, geological and biological vaterite: a Raman spectroscopic study. *Journal of Raman Spectroscopy* **2010**, *41*, 193-201.

(42) Lovett, J. R.; Fielding, L. A.; Armes, S. P.; Buxton, R. One-Pot Preparation of Conducting Polymer-Coated Silica Particles: Model Highly Absorbing Aerosols. *Advanced Functional Materials* **2014**, *24*, 1290-1299.

(43) Jones, E.; Mykhaylyk, O.; Semsarilar, M.; Boerakker, M.; Wyman, P.; Armes, S. How Do Spherical Diblock Copolymer Nanoparticles Grow during RAFT Alcoholic Dispersion Polymerization? *Macromolecules* **2015**, *49*, 172-181.

(44) Dey, R. E.; Zhong, X.; Youle, P. J.; Wang, Q. G.; Wimpenny, I.; Downes, S.; Hoyland, J. A.; Watts, D. C.; Gough, J. E.; Budd, P. M. Synthesis and Characterization of Poly (vinylphosphonic acid-co-acrylic acid) Copolymers for Application in Bone Tissue Scaffolds. *Macromolecules* **2016**, *49*, 2656-2662.

5. Chapter Five

5. Sulfate-based Anionic Diblock Copolymer Nanoparticles for Efficient Occlusion within ZnO

5.1 Introduction

It is well-known that ZnO is a semiconductor that exhibits a wide band gap, a large excitation binding energy, near-UV emission, high electron mobility, high thermal conductivity, and piezoelectricity.[1-4] Polymer-directed growth of ZnO is of particular interest. For example, Zhang et al. demonstrated that a wide range of nanostructures, including monolayer, bilayer and multilayer ZnO, can be prepared by utilising poly(*N*-vinylpyrrolidone) (PVP) as an additive.[5] Under appropriate conditions, ZnO with various morphologies can be prepared.[5] Peng et al. employed polyacrylamide (PAM) and carboxyl-functionalised polyacrylamide (PAM-COOH) as modifiers for the crystallisation of ZnO. Ring-like ZnO was produced when using the former polymer, while the latter generated a near-monodisperse disc-like ZnO.[6] Double-hydrophilic diblock copolymers are particularly useful crystal modifiers.[7-13] Ideally, one block of such copolymers serves as an anchor block, which adsorbs onto the crystal surface. The other block acts as a stabiliser, preventing agglomeration.[12]

The main focus of this Thesis lies in the modification of ZnO crystallisation using diblock copolymer nanoparticles as additives, rather than soluble polymers. Wegner and co-workers were the first to show that anionic polystyrene latexes could be occluded within ZnO.[14-16] In this seminal work, styrene was copolymerised with acrylic acid, maleic acid or ethylene glycol methacrylate phosphate using a miniemulsion formulation. The effect of surface functionalisation and latex concentration on the crystal growth, morphology, and crystallinity of the resulting ZnO composite crystals was examined, with particular attention being paid to the acrylic acid/styrene copolymer latex. However, the extent of occlusion achieved was relatively low (< 10 % by mass) even when using a copolymer latex concentration of 9 g L^{-1}.

Herein we prepare a series of novel diblock copolymer nano-objects via RAFT aqueous emulsion polymerisation of benzyl methacrylte using either a poly(methacrylic acid) macro-CTA (M_{68} macro-CTA) or a poly(ammonium 2-sulfatoethyl methacrylate) macro-CTA (S_{32} macro-CTA or S_{73} macro-CTA), or a binary mixture of M_{68} and S_{73} macro-CTAs. Such RAFT PISA formulations enable spherical nanoparticles with narrow size distributions to be obtained and the surface chemistry of the resulting nanoparticles can be precisely tailored as desired.[17-19]

Benzyl methacrylate was selected as hydrophobic core-forming monomer.[20-26] Moreover, this surfactant-free emulsion polymerisation avoids introducing unwanted impurities. This is important for the subsequent crystal occlusion studies because impurities could affect the crystallisation behaviour.[4,7] These diblock copolymer nanoparticles are examined for their occlusion into growing ZnO crystals and novel copolymer nanoparticle/ZnO nanocomposite materials can be obtained (see **Scheme 5.1**). Where occlusion is observed, the resulting nanocomposite crystals are characterised in terms of their evolution in morphology, optical properties, crystal structure, and occlusion mechanism.
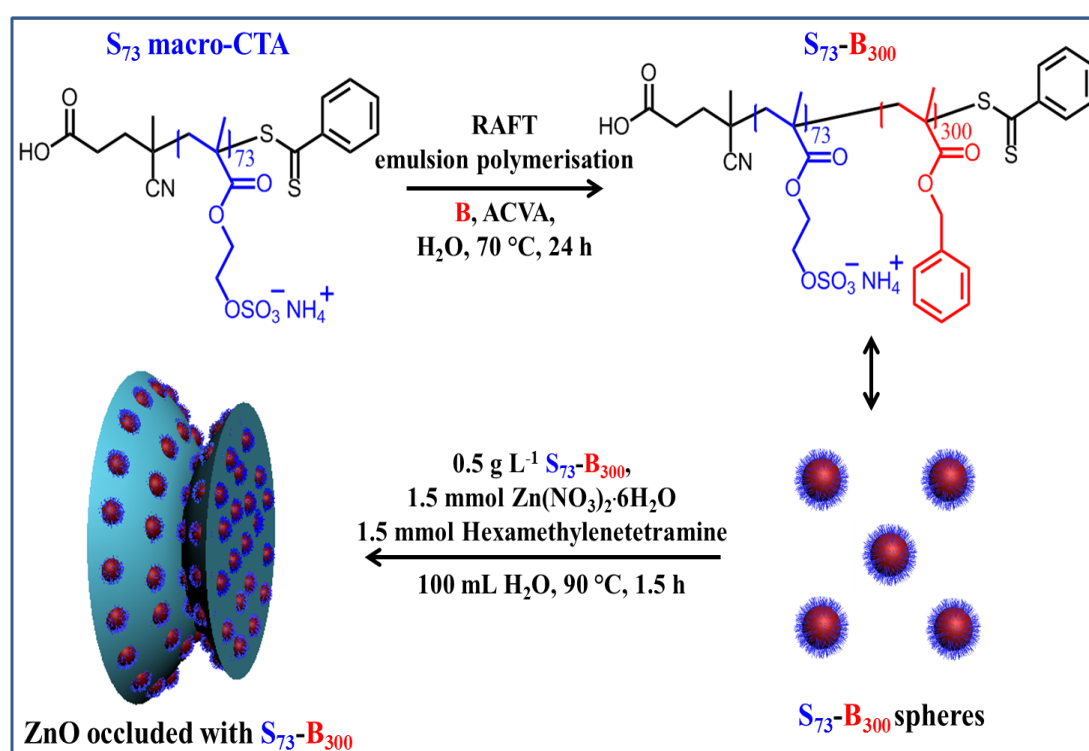
Scheme 5.1. RAFT aqueous emulsion polymerisation of benzyl methacrylate (B) using a S_{73} macro-CTA at 70 °C to produce S_{73}-B_{300} diblock copolymer nanoparticles and associated cartoon showing S_{73}-B_{300} spherical nanoparticles and their occlusion within ZnO.[27]

5.2 Results and Discussion

5.2.1 Synthesis and Characterisation of Copolymer Nanoparticles

Poly(ammonium 2-sulfatoethyl methacrylate) is an example of a strong polyelectrolyte, remaining highly anionic even at relatively low pH. Atom transfer

radical polymerisation (ATRP) has been used by Weaver et al. to polymerise ammonium 2-sulfatoethyl methacrylate in aqueous media. However, this protocol only afforded relatively polydisperse poly(ammonium 2-sulfatoethyl methacrylate) chains.[11] Nevertheless, a poly(ammonium 2-sulfatoethyl methacrylate)-based diblock copolymer prepared using a poly(ethylene glycol) macro-initiator proved to be an effective crystal habit modifier for the preparation of micron-sized barium sulfate crystals.[11]
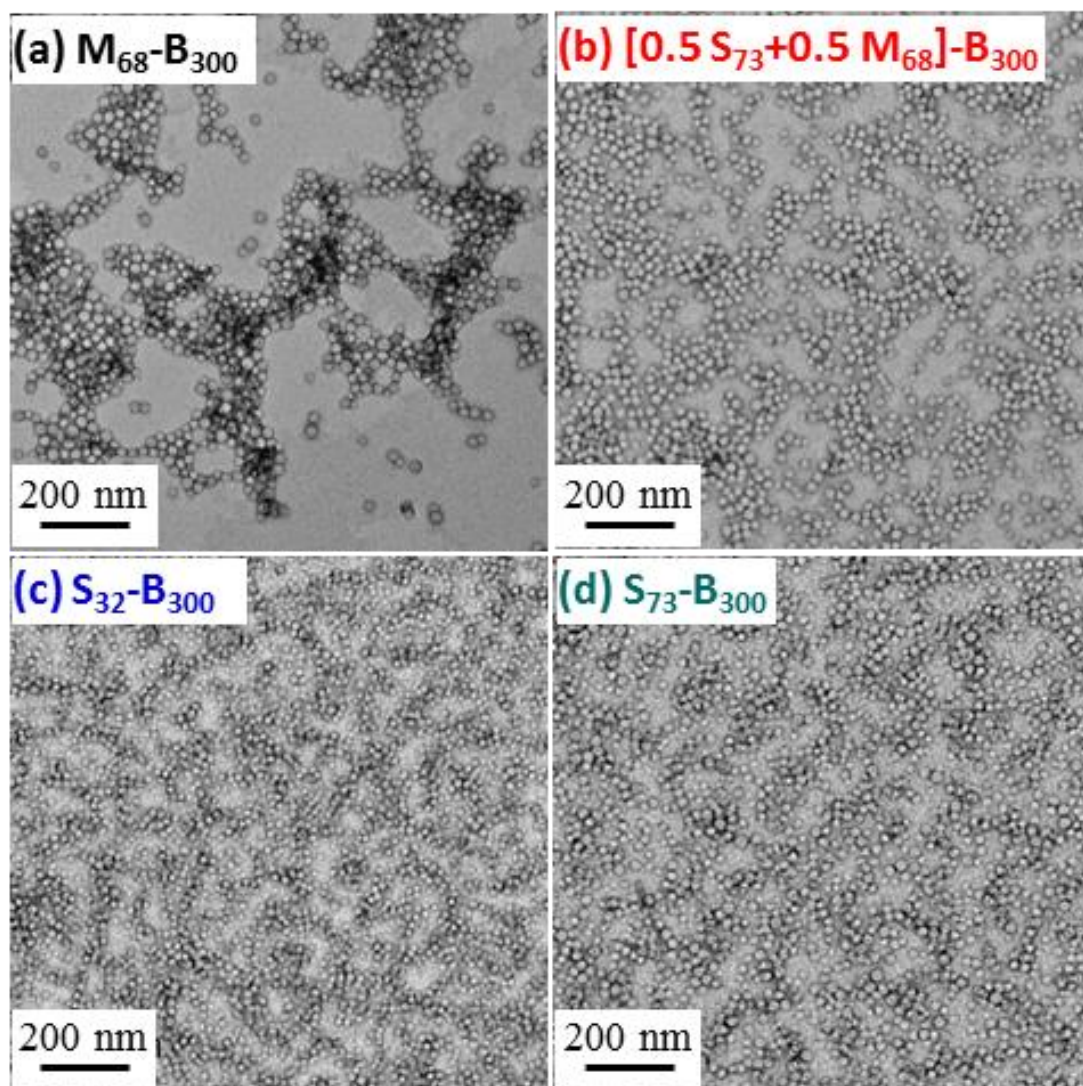
Figure 5.1. Representative TEM images obtained for: (a) M_{68}-B_{300} copolymer nanoparticles; (b) [0.50 S_{73} + 0.50 M_{68}]-B_{300} copolymer nanoparticles; (c) S_{32}-B_{300} copolymer nanoparticles; (d) S_{73}-B_{300} copolymer nanoparticles.

Four types of nano-objects with differing surface chemistries and mean DPs were prepared via RAFT aqueous emulsion polymerisation-mediated PISA. The RAFT polymerisation of S monomer was conducted in aqueous solution using a dithiobenzoate-based RAFT agent to afford two S macro-CTAs with mean DPs of either 32 or 73 in high yield within 2 h at 70 °C. S macro-CTAs were chain-extended in turn with B monomer via surfactant-free RAFT aqueous emulsion polymerisation to obtain a series of S-B diblock copolymer nanoparticles (see **Scheme 5.1**). ^{1}H NMR spectroscopy was used to monitor the B polymerisation and more than 99 % conversion was typically attained. Such high conversions meant that purification of the resulting diblock copolymer nanoparticles was deemed unnecessary, which facilitated the subsequent occlusion studies. Indeed, all the diblock copolymer nanoparticles prepared in the present Chapter are directly used without any further purification prior to occlusion experiments. TEM images shown in **Figures 5.1a-5.1d** indicate that well-defined, near-monodisperse spherical nanoparticles with a diameter of around 20 nm were obtained when using the various macro-CTAs. M_{68}-B_{300} is pH-responsive because poly(methacrylic acid) is a weak polyelectrolyte, which acquires anionic character via ionisation at around neutral pH but becomes uncharged at low pH as a result of protonation.[27] This explains why the z-average diameter of M_{68}-B_{300} is around 50 nm at relatively high pH, while a large increase in apparent particle size as a result of flocculation is observed at low pH, as shown in **Figure 5.2a.** At the same time, the zeta potential for these nanoparticles was changed from around -40 mV to around 0 mV as the solution pH is lowered from pH 10 to pH 3 (**Figure 5.2b**). In striking contrast, both the particle size and zeta potential were found to be essentially pH-independent for $[S_{73} + M_{68}]$-B_{300}, S_{32}-B_{300}, and S_{73}-B_{300}, as indicated in **Figures 5.2a** and **5.2b**. This is ascribed to the strong anionic polyelectrolyte character of the poly(ammonium 2-sulfatoethyl methacrylate) stabiliser.
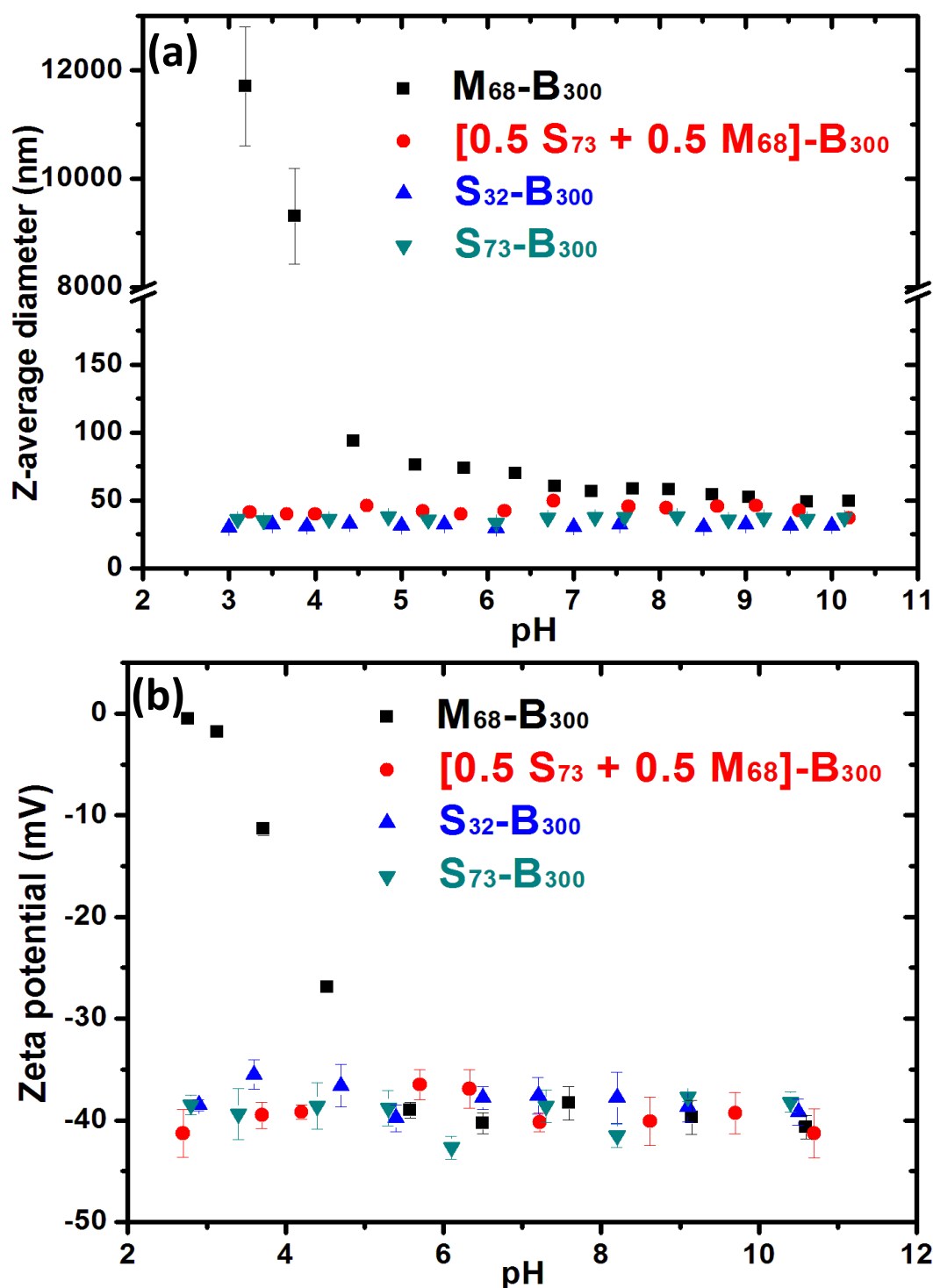
Figure 5.2. (a) Z-average diameter versus pH curves (note the apparent change in particle size for the M_{68}-B_{300} nanoparticles as a result of their flocculation at low pH) and (b) zeta potential versus pH curves recorded for the four aqueous nanoparticle dispersions corresponding to the TEM images shown in **Figure 5.1**. The zeta potential versus pH curve recorded for [0.5 S_{73} + 0.5 M_{68}]-B_{300} was unexpectedly pH-independent. This suggests that the electrophoretic mobility is dominated by the strong S_{73} polyelectrolyte stabiliser, rather than the weak M_{68} polyelectrolyte stabiliser.

5.2.2 Occlusion of Copolymer Nanoparticles within ZnO Crystals

In the absence of any anionic nanoparticles, hexagonal prismatic ZnO rods were obtained (see **Figure 5.3a**), as expected.[14] In addition, we also examined whether poly(ammonium 2-sulfatoethyl methacrylate) homopolymer (S_{73} macro-CTA) alone could act as a crystal habit modifier for ZnO. As shown in **Figure 5.3b**, ZnO generated in the presence of the S_{73} macro-CTA has a unique 'diablo' morphology, which clearly differs substantially from the native ZnO morphology. Similar observations were also made for ZnO crystals prepared in the presence of the S_{32} macro-CTA (data not shown). This suggests that the anionic poly(ammonium 2-sulfatoethyl methacrylate) chains do indeed interact with the growing ZnO crystals (it will be further discussed in the following occlusion mechanism section). Then the aforementioned four types of diblock copolymer nanoparticles were examined in turn as crystal habit modifiers for ZnO. **Figure 5.3c** shows the ZnO crystals formed in the presence of M_{68}-B_{300} diblock copolymer particles at a copolymer concentration of 0.50 g L^{-1}. Somewhat ill-defined cone-shaped ZnO clusters were obtained, but there is no evidence of particle occlusion in this case. This negative observation is perhaps surprising in the context of Wegner's data,[23] in which carboxylic acid-modified polystyrene latexes clearly played an active role during ZnO mineralisation. In our occlusion experiments, ZnO formation commenced at pH 5, which is close to the $p\text{K}_a$ of PMAA.[23] Thus the carboxylic acid groups on the stabiliser chains become partially protonated, which leads to a reduction in anionic charge density and hence weak flocculation of the M_{68}-B_{300} nanoparticles, as judged by visual inspection and DLS studies (see **Figure 5.4**). This is likely to reduce the interaction between the nanoparticles and the ZnO lattice, which may explain why occlusion is not observed under these conditions. In contrast, in the earlier study by Wegner et al.,[14] the carboxylic acid groups are *statistically* incorporated into the surface of the polystyrene latex particles, which makes them less susceptible to protonation under these conditions. The unsuccessful attempted occlusion of M_{68}-B_{300} within ZnO suggests that it is vital for the copolymer particles to maintain colloidal stability during the initial stages of the ZnO synthesis. To test this hypothesis, we also examined using an equimolar binary mixture of S_{73} and M_{68} macro-CTAs in order to target [0.5 S_{73} + 0.5 M_{68}]-B_{300} diblock copolymer nanoparticles so as to reduce their pH-dependent character. As expected, such hybrid

nanoparticles can be successfully occluded within ZnO, as evidenced by the uniformly distributed voids that are visible in the inset shown in **Figure 5.3d**.
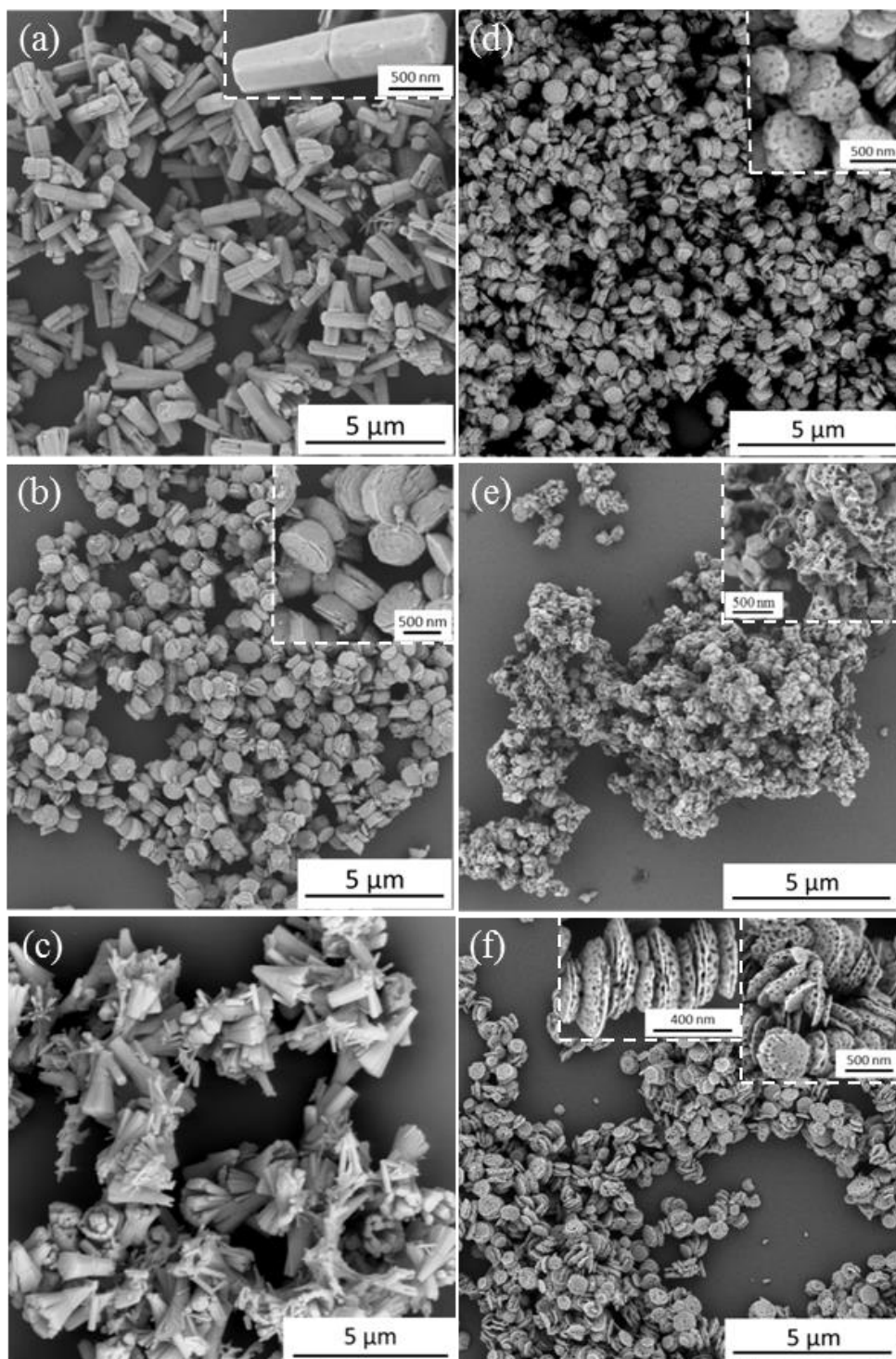
Figure 5.3. FE-SEM images of ZnO particles mineralised under various conditions after calcination at 700 °C: (a) without any additive; (b) in the presence of 0.12 g L^{-1} S$_{73}$ homopolymer (i.e. the number of moles of S$_{73}$ homopolymer is equivalent to the number of moles of S$_{73}$-B$_{300}$ nanoparticles used in (f)); (c) 0.50 g L^{-1} M$_{68}$-B$_{300}$; (d) 0.50 g L^{-1} [0.5 S$_{73}$ + 0.5 M$_{68}$]-B$_{300}$; (e) 0.50 g L^{-1} S$_{32}$-B$_{300}$; (f) 0.50 g L^{-1} S$_{73}$-B$_{300}$. The insets present the corresponding magnified images.
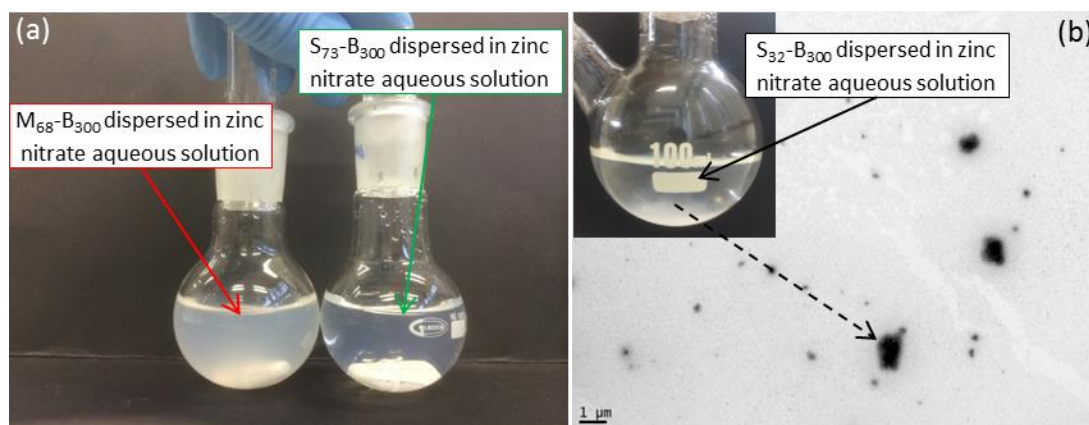
Figure 5.4. (a) Digital photograph recorded for 0.50 g L^{-1} M$_{68}$-B$_{300}$ and 0.50 g dm^{-3} S$_{73}$-B$_{300}$ dispersed in aqueous zinc nitrate solution; (b) TEM images obtained for 0.50 g L^{-1} S$_{32}$-B$_{300}$ nanoparticles dispersed in aqueous zinc nitrate solution (inset shows the corresponding digital photograph); A white precipitate was formed immediately on addition of S$_{32}$-B$_{300}$, but a stable homogeneous aqueous dispersion is maintained for long time periods (months) in the presence of S$_{73}$-B$_{300}$ nanoparticles. Note: pH is around 5 before the crystallisation of ZnO.

Clearly, the introduction of 50 % S$_{73}$ stabiliser chains plays a key role in conferring sufficient anionic character (see **Figure 5.2**) to ensure colloidal stability at pH 5 and hence allow occlusion to occur *in situ*. **Figure 5.3e** indicates that ZnO formation in the presence of S$_{32}$-B$_{300}$ produces multi-hollow porous structures after calcination. In this case the void size is significantly larger than the original S$_{32}$-B$_{300}$ nanoparticle dimensions, which is consistent with the white precipitate (see **Figure 5.4b**; [S$_{32}$-B$_{300}$] = 0.50 g L^{-1}) observed for these nanoparticles immediately after addition of zinc nitrate, i.e. prior to ZnO formation. Thus it seems that nanoparticle *aggregates* are incorporated within the ZnO crystals. In contrast, addition of S$_{73}$-B$_{300}$ nanoparticles to an aqueous solution of zinc nitrate did not lead to any precipitation (see **Figure 5.4a**). This suggests that, unlike the S$_{73}$ stabiliser, the S$_{32}$ stabiliser block is too short to maintain colloidal stability in the presence of zinc nitrate. Meanwhile, in the presence of an aqueous dispersion of 0.50 g L^{-1} S$_{73}$-B$_{300}$ nanoparticles, a strikingly different ZnO morphology was obtained, as indicated in **Figure 5.3f**. Interestingly, twinned ZnO crystals are observed, with one side smaller than the other (see **Figure 5.3f**, inset) and the aspect ratio appears to be reduced (aspect ratio equals length of the ZnO rod divides width of the ZnO rod). Moreover, S$_{73}$/ZnO retains a hexagonal basal face, whereas the hexagonal prismatic structure completely

disappears for S_{73}-B_{300}/ZnO. Although the mean length of the S_{73}-B_{300}/ZnO crystal is significantly reduced (to just 200 nm), the mean width remains more or less the same as that of the control ZnO crystals (see **Figure 5.3a** and **Figure 5.3f**). As shown in the inset of **Figure 5.3f**, voids are located within both the lateral and basal faces and the void dimensions are in good agreement with those of the original nanoparticles. However, some voids appear to be slightly elliptical rather than purely spherical, which suggests that some degree of nanoparticle distortion occurred during occlusion.

This is not unreasonable, because the reaction temperature of 90 °C employed to generate the ZnO crystals significantly exceeds the glass transition temperature of the core-forming block (~55 °C). The voids appear to be isolated, rather than inter-connected, suggesting that the nanoparticles do not become aggregated during occlusion. Indeed, the strongly anionic character of the S_{73}-B_{300} nanoparticles is expected to confer effective electrosteric stabilisation (and hence good colloidal stability) under these conditions.

5.2.3 Effect of Diblock Copolymer Nanoparticle Concentration on the Extent of Occlusion

In the light of the above observations, S_{73}-B_{300} was selected for more detailed studies. **Figure 5.5** shows the SEM images of ZnO prepared at various S_{73}-B_{300} nanoparticle concentrations ranging from 0 to 1.00 g L^{-1}. Mixed phases containing both long and short ZnO rods were observed at relatively low concentrations (0.01 g L^{-1}, **Figure 5.5b**). However, there was no evidence for occlusion under these conditions. Porous ZnO particles were obtained at a S_{73}-B_{300} concentration of 0.05 g L^{-1}, which indicates that a certain *minimum* nanoparticle concentration is required for successful (or detectable) occlusion (**Figure 5.5c**). Inspecting **Figures 5.5d** to **5.5f**, the ZnO morphology becomes more uniform as the S_{73}-B_{300} nanoparticle concentration is increased.

There is no distinct morphology change between the ZnO precipitated in the presence of S_{73}-B_{300} nanoparticles when used at 0.50 and 1.00 g L^{-1}. Particle size distributions for 0.50 g L^{-1} S_{73}-B_{300}/ZnO particles and thermal treated S_{73}-B_{300}/ZnO

determined via disc centrifuge photosedimentometry (DCP) are shown in **Figure 5.6a**.
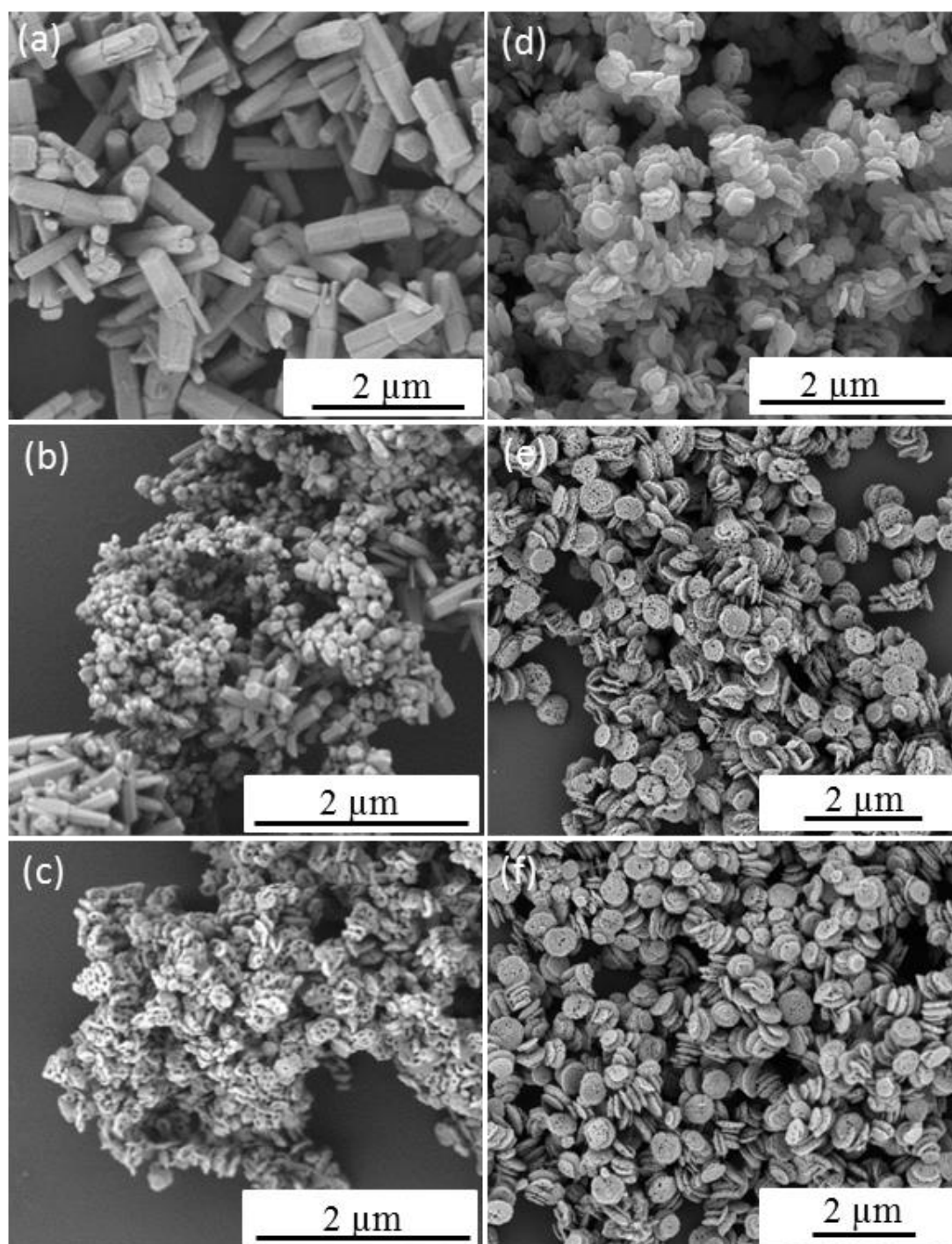
Figure 5.5. Representative FE-SEM images showing ZnO particles prepared in the presence of various concentrations of S_{73}-B_{300} copolymer nanoparticles: (a) 0.0 g L^{-1}; (b) 0.01 g L^{-1}; (c) 0.05 g L^{-1}; (d) 0.10 g L^{-1}; (e) 0.50 g L^{-1}; (f) 1.00 g L^{-1}.

Provided that the particle density is accurately known, this high resolution technique reports a weight-average diameter. Using relatively high nanoparticle concentrations (e.g. ≥ 0.50 g L^{-1}) clearly leads to the formation of ZnO particles with relatively narrow size distributions.
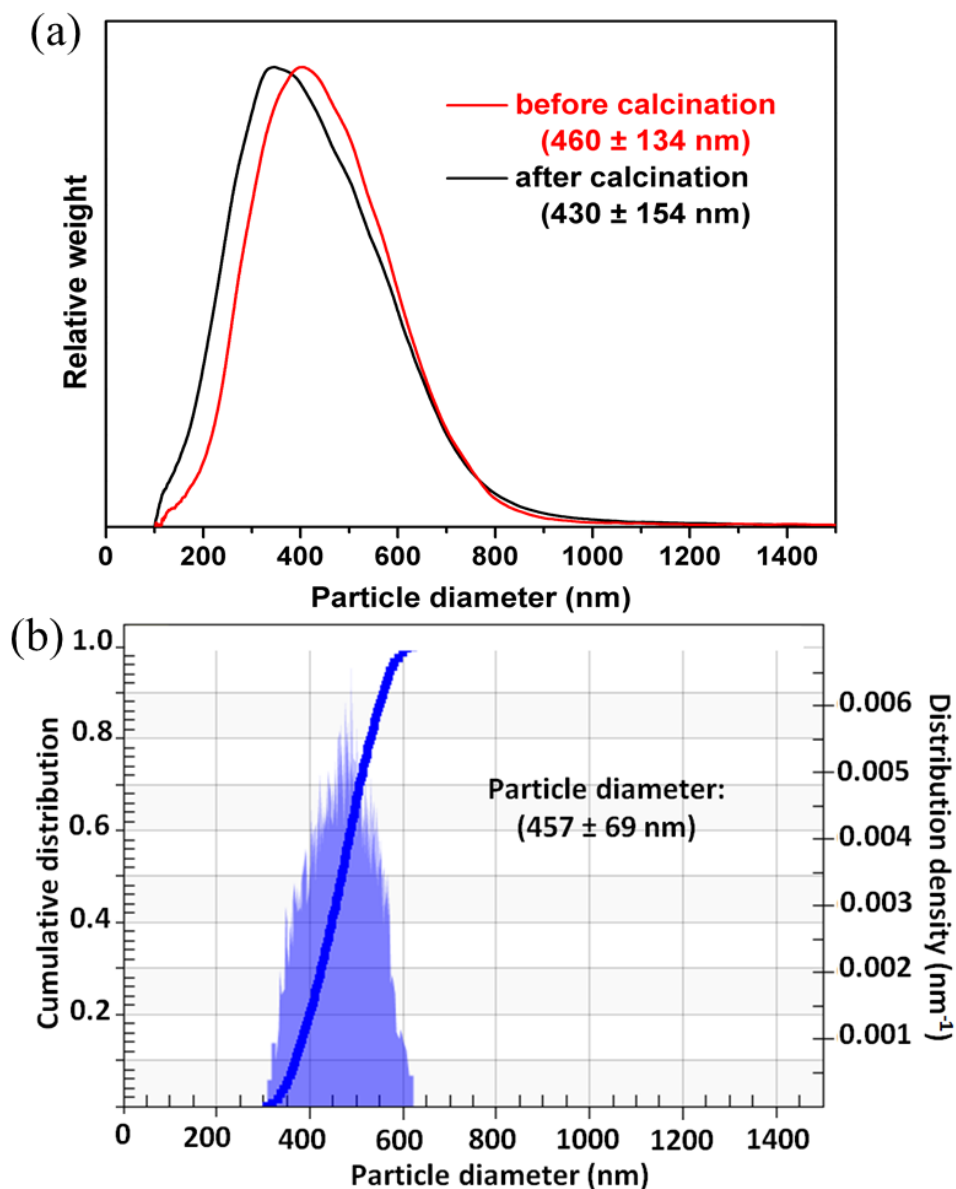
Figure 5.6. (a) Weight-average particle size distributions determined for ZnO particles prepared in the presence of 0.50 g L^{-1} S$_{73}$-B$_{300}$ copolymer nanoparticles before and after thermal treatment (calcination), as determined by disc centrifuge photosedimentometry. Particle densities were measured to be 3.17 and 5.31 g cm^{-3} for the S$_{73}$-B$_{300}$/ZnO precursor nanocomposite particles and calcined ZnO particles, respectively. (b) Volume-average particle size distribution determined for the S$_{73}$-B$_{300}$/ZnO nanocomposite before calcination, as determined by analytical centrifugation (LUMiSizer® instrument). Note: S$_{73}$-B$_{300}$/ZnO nanocomposites after calcination cannot be analised by LUMiSizer due to their low colloidal stability.

As shown in **Figure 5.6a**, the mean size of S_{73}-B_{300}/ZnO nanocomposite crystals before and after thermal treatment were approximately the same, indicating that these nanocomposites are colloidally stable. Analytical centrifugation (LUMiSizer® instrument) was also utilised to further assess the nanocomposite particle size distribution prior to calcination, which was in reasonably good agreement with the DCP data (see **Figure 5.6b**). It is noted that calcined ZnO cannot be analysed by this technique because the colloidal stability of the calcined ZnO is relatively poor. The superior colloidal stability of 0.50 g L^{-1} S_{73}-B_{300}/ZnO nanocomposites over calcined ZnO is ascribed to the S_{73}-B_{300} nanoparticles that occluded within the ZnO surface. This is supported by the observation that there are voids on the surface of the ZnO crystal surface, as shown in the insets in **Figure 5.3f**.

Thermogravimetry analysis was used to assess the S_{73}-B_{300} content within the S_{73}-B_{300}/ZnO nanocomposite particles. Complete pyrolysis of the organic component was achieved on heating to 550 °C in air (see inset, **Figure 5.7**), whereas essentially no mass loss was observed for a ZnO control sample under the same conditions. Thus any observed mass loss for the series of nanocomposites can be solely attributed to the organic nanoparticle component. The extent of nanoparticle occlusion within ZnO systematically increased when using higher S_{73}-B_{300} concentrations, with a limiting value of 23 % w/w being obtained at a nanoparticle concentration of 0.50 g L^{-1}, see **Figure 5.7**. This value is significantly higher than those reported by Wegner et al., for which the highest extent of latex occlusion was 9.5 % w/w even when using a much higher latex concentration of 9.0 g L^{-1}.[14] In the present study, if it is assumed that all of the zinc nitrate precursor is fully converted into ZnO and that all of the nanoparticles (1.0 g L^{-1}) are incorporated into the ZnO crystals, the theoretical maximum extent of occlusion is 29 % w/w. Thus the occlusion efficiency is estimated to be approximately 86 % under the conditions described herein. In principle, crystallisation should lead to the *expulsion* of impurities, rather than their occlusion.[7,28-30] Thus this relatively efficient occlusion is most likely the result of a strong electrostatic interaction between the highly anionic nanoparticles and the ZnO host crystal.
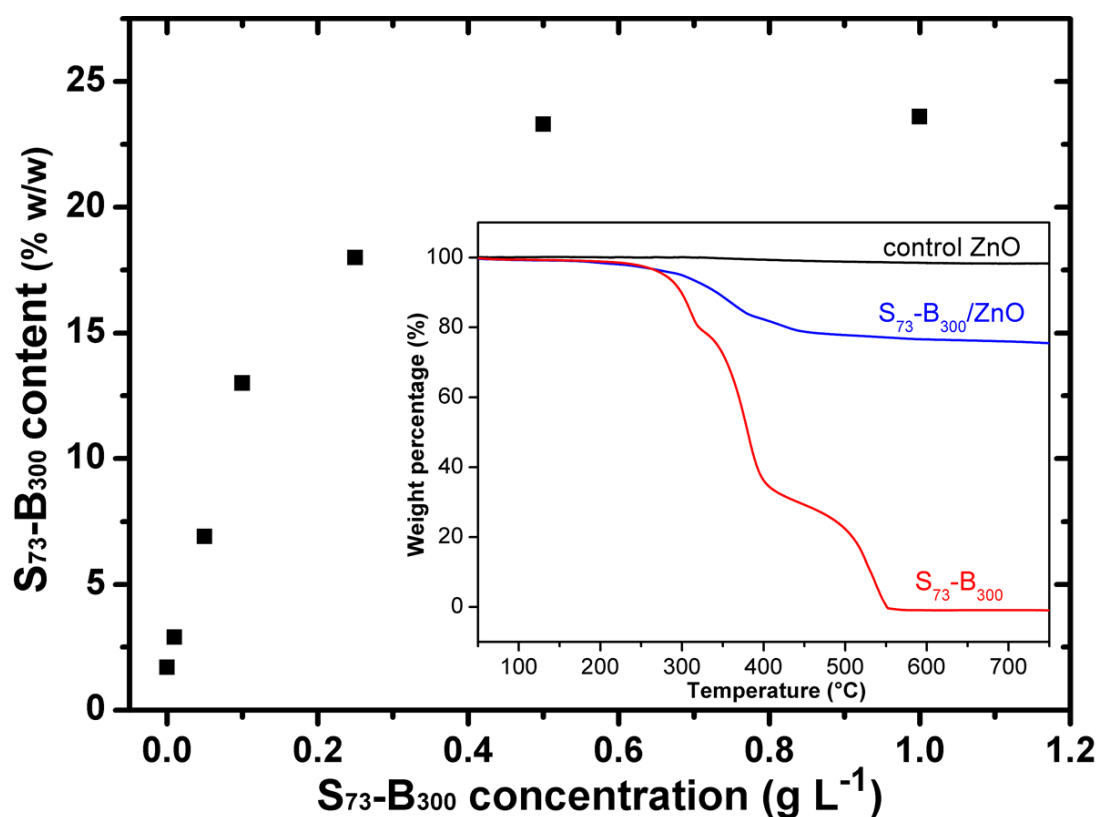
Figure 5.7. S_{73}-B_{300} mass contents within S_{73}-B_{300}/ZnO nanocomposites prepared using various S_{73}-B_{300} nanoparticle concentrations, as determined by thermogravimetry. Inset shows the weight loss curves obtained for ZnO alone, a S_{73}-B_{300}/ZnO nanocomposite prepared using 0.50 g L^{-1} S_{73}-B_{300} nanoparticles, and the precursor S_{73}-B_{300} nanoparticles.

5.2.4 Optical Properties of S_{73}-B_{300}/ZnO nanocomposite

The optical properties of the as-prepared S_{73}-B_{300}/ZnO nanocomposite particles were evaluated by FT-IR spectroscopy and UV-visible spectroscopy. According to the literature, the IR band at 437 cm^{-1} corresponds to the Raman-active E2 mode of hexagonal ZnO.[31,32] A strong absorption band was also observed at 525 cm^{-1} for the ZnO control (see **Figure 5.8a**), which may be associated with either oxygen deficiency and/or oxygen vacancy (VO) defects in ZnO.[33] However, this feature is much less intense in the spectra recorded for the four copolymer/ZnO nanocomposites. A number of bands assigned to the copolymer nanoparticles are observed in these latter samples, including an intense C=O stretch at 1727 cm^{-1} and an aromatic C-H out-of-plane bending mode at 752 cm^{-1} and 697 cm^{-1}. In each case the copolymer band intensities correlate well with the nanoparticle concentration

used to prepare these nanocomposites. Two features are apparent from the UV-visible absorption spectra (see **Figure 5.8b**). First, the absorption maximum is red-shifted at higher levels of nanoparticle occlusion, while the absorbance in the visible region is systematically reduced. This may be caused by the change in size and/or absorption states (defect energy bands) for ZnO prepared in the presence of a relatively low concentration of diblock copolymer nanoparticles.[33]
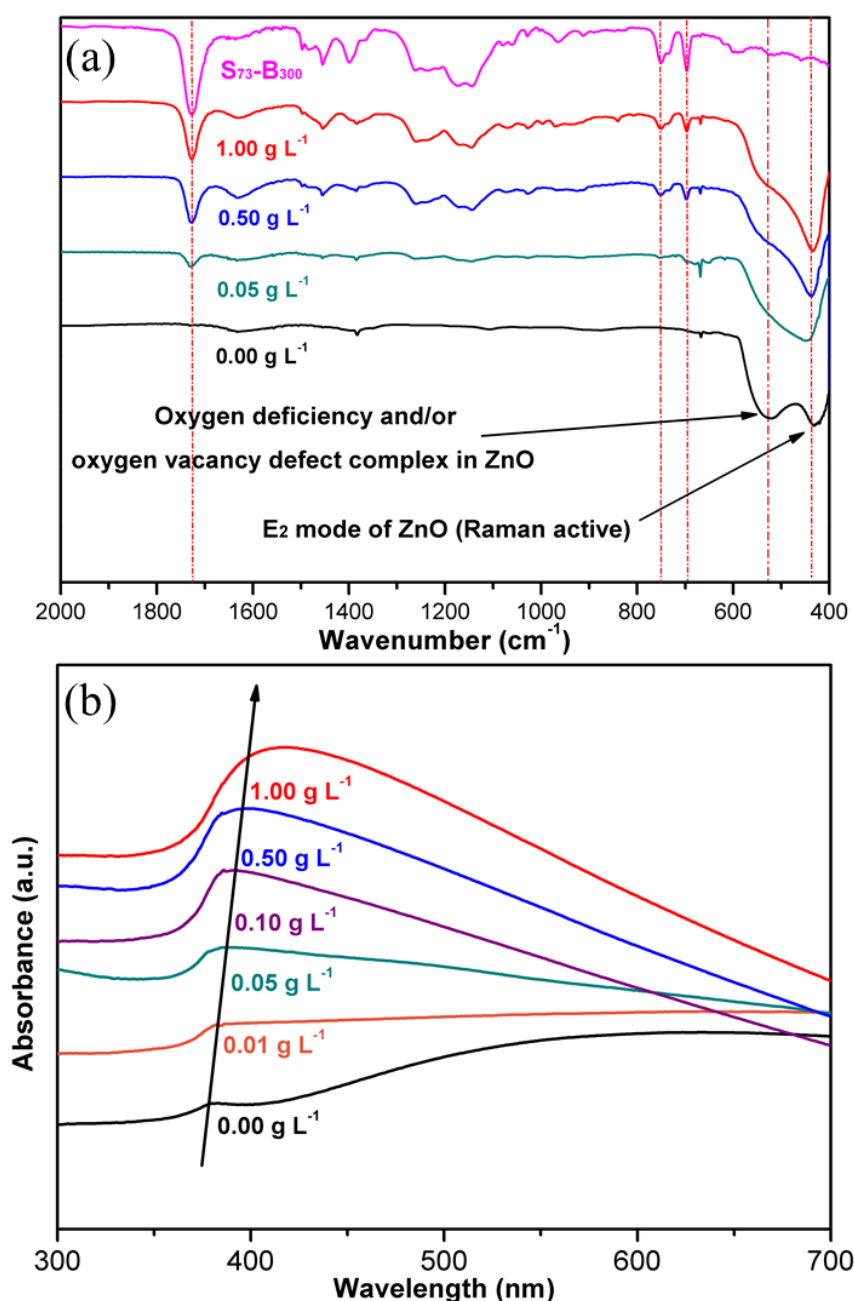
Figure 5.8. (a) FT-IR spectra recorded for ZnO nanocomposites prepared using various S_{73}-B_{300} nanoparticle concentrations and also a reference spectrum for S_{73}-B_{300} nanoparticles alone. (b) UV-visible absorption spectra recorded for ZnO particles prepared in the presence of various S_{73}-B_{300} nanoparticle concentrations after calcination.

According to the XRD data shown in **Figure 5.9**, there are no significant changes in the microcrystalline structure of this wurtzite form of ZnO, which is consistent with earlier reports.[14,34]
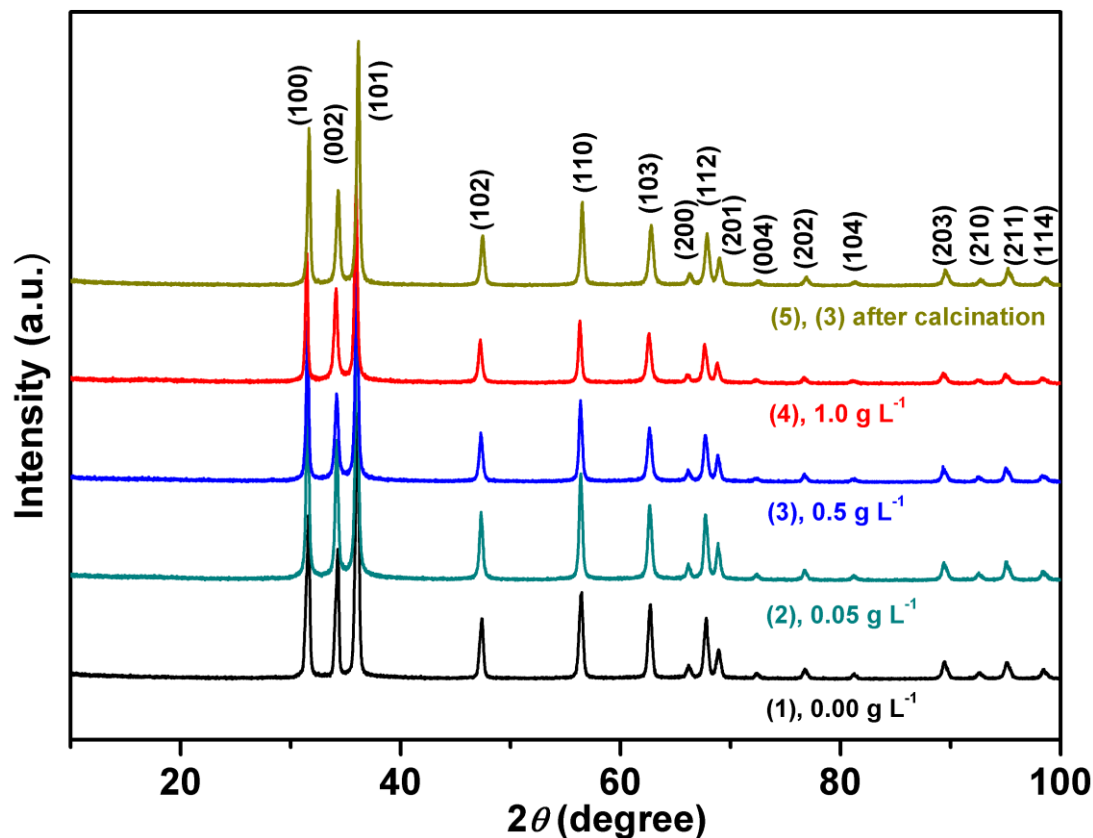
Figure 5.9. XRD patterns obtained for ZnO particle prepared in the presence of various S_{73}-B_{300} nanoparticle concentrations.

5.2.5 Occlusion Mechanism

In contrast to individual (macro)molecules, S_{73}-B_{300} nanoparticles are sufficiently large to enable their occlusion to be studied directly using electron microscopy in the present work.[35] Thus offers an opportunity to study the crystal growth mechanism. Accordingly, aliquots were extracted from the reaction solution at various time points and examined by FE-SEM. **Figure 5.10** depicts the evolution in ZnO morphology with time in the presence of 0.50 g L^{-1} S_{73}-B_{300} nanoparticles. Initially, irregular ZnO sheets are formed (see 5 min time point in **Figure 5.10a**). Thereafter, S_{73}-B_{300} nanoparticles adsorb onto these sheets, see **Figure 5.10b**. The final ZnO morphology was attained within just 15 min at 90 °C. Some impurities are observed

(see red arrows in **Figures 5.10c ~ 5.10e**), but these worm-like features disappear towards the end of the mineralisation process (see **Figure 5.10f**). Thus these impurities are most likely to be intermediate species that are not yet fully converted into ZnO.
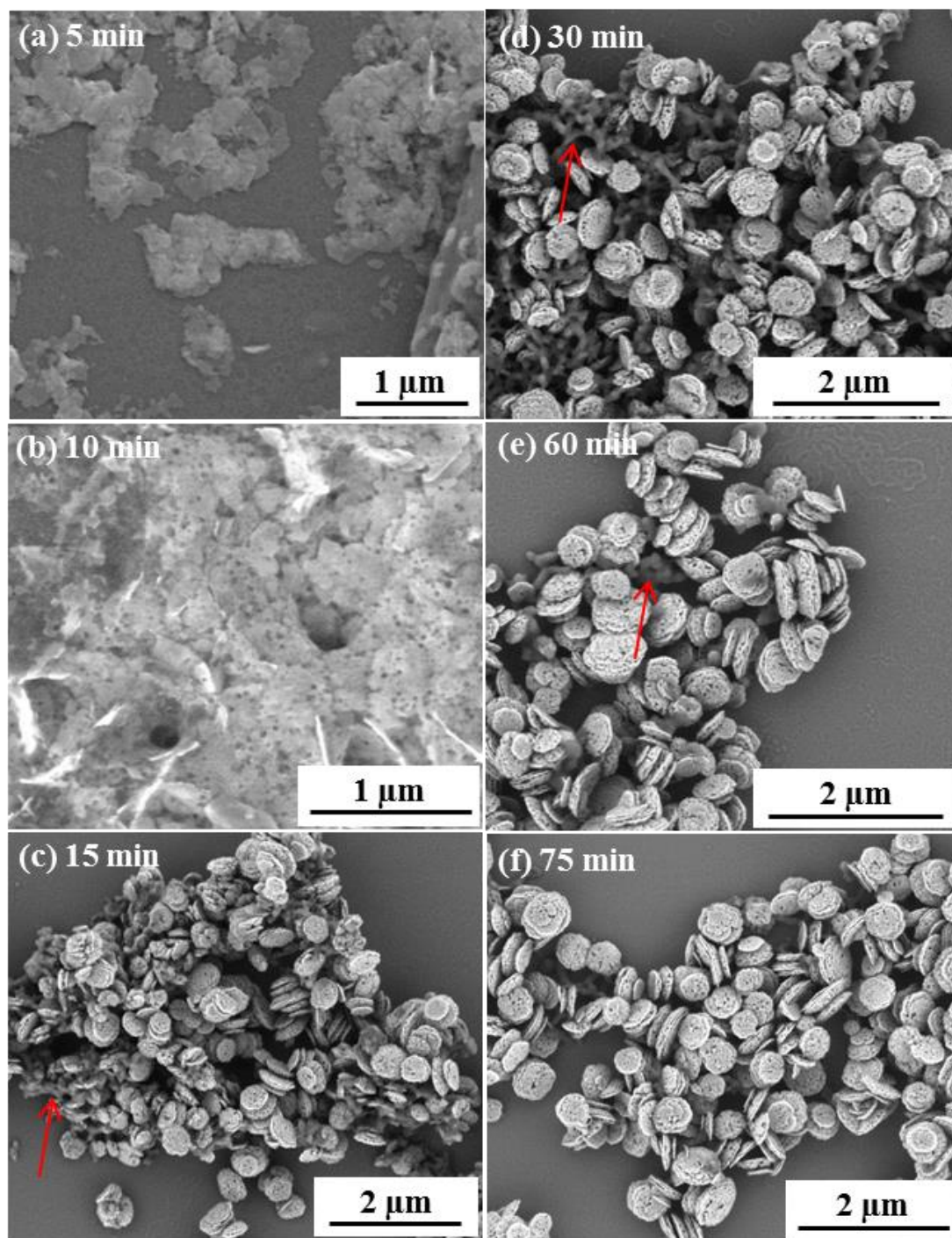
Figure 5.10. Representative FE-SEM images showing the evolution in morphology for ZnO prepared in the presence of S_{73}-B_{300} copolymer nanoparticles at various reaction times: (a) 5 min; (b) 10 min; (c) 15 min; (d) 30 min; (e) 60 min; (f) 75 min. The red arrows indicate the presence of impurities.

It is well known that ZnO contains a cationic (0001) plane rich in Zn^{2+}, an anionic (000$\bar{1}$) plane rich in O^{2-} anions, and a non-polar (01$\bar{1}$0) plane.[36-38] The long hexagonal prismatic crystal observed in the control experiment suggests that the basal face growth rate is faster than that of the lateral face. Actually, based on the literature, the relative growth velocity, V, follows the order $V_{[0001]} > V_{[10\bar{1}0]} > V_{[000\bar{1}]}$.[5] Thermal decomposition of HMTA gives ammonia and formaldehyde, with the former acting as a pH buffer.[14] In the early stages of ZnO crystallisation, anionic ZnO_2^{2-} units are preferentially absorbed onto cationic (0001) faces.[39] Meanwhile, HMTA forms a highly cationic (fully protonated) complex in aqueous solution,[40] which interacts with the (000$\bar{1}$) face. Moreover, this cationic complex also interacts with the ZnO_2^{2-} precursor species.[39,41] This leads to the formation of ZnO crystals on the (000$\bar{1}$) surface. Thus, a twin structure is gradually formed via preferential growth in two opposing directions.[39,41] We hypothesise that the highly anionic S_{73}-B_{300} nanoparticles are preferentially adsorbed onto the cationic basal face, thereby blocking the positions from which the crystal would normally tend to grow. Thus the rate of crystal growth of this face is suppressed, leading to a reduction in the aspect ratio, as well as formation of an asymmetric twin structure. Lateral growth is also suppressed during nucleation, but is apparently not affected during the subsequent crystal growth stage. This perhaps explains why the final ZnO particles have concave character, but their mean width is comparable to that observed for the ZnO control synthesis performed in the absence of any S_{73}-B_{300} nanoparticles.

5.3 Conclusions

In summary, we report the synthesis of new highly anionic diblock copolymer nanoparticles via RAFT aqueous emulsion polymerisation of benzyl methacrylate using a poly(ammonium 2-sulfatoethyl methacrylate) macro-CTA. These sulfate-based nanoparticles possess a well-defined spherical morphology and relatively narrow size distributions. Efficient nanoparticle occlusion occurs during the *in situ* synthesis of ZnO, leading to the formation of novel copolymer/ZnO nanocomposite particles. The effect of nanoparticle concentration and surface chemistry on ZnO mineralisation is examined and a tentative crystallisation mechanism is suggested based on the observed evolution of morphology. Moreover, it is also shown that the equivalent poly(methacrylic acid)-poly(benzyl methacrylate) nanoparticles are not occluded within ZnO crystals. Thus anionic character is a necessary but not sufficient condition for efficient occlusion. However, analogous nanoparticles prepared using a 1:1 binary mixture of poly(ammonium 2-sulfatoethyl methacrylate) and poly(methacrylic acid) stabiliser blocks can also be incorporated within ZnO, so significant dilution of the essential sulfate character is possible while retaining occlusion.

PISA syntheses of bespoke organic nanoparticles offer a facile and efficient means of tuning surface chemistry, which is the key to the successful preparation of novel nanocomposite crystals via *in situ* nanoparticle occlusion during mineralisation. In the next Chapter, occlusion of polymer-modified gold nanoparticles within ZnO will be exmined.

5.4 References

(1) Wang, X. D.; Ding, Y.; Summers, C. J.; Wang, Z. L. Large-scale synthesis of six-nanometer-wide ZnO nanobelts. *Journal of Physical Chemistry B* **2004**, *108*, 8773-8777.

(2) Özgür, Ü.; Alivov, Y. I.; Liu, C.; Teke, A.; Reshchikov, M. A.; Doğan, S.; Avrutin, V.; Cho, S. J.; Morkoc, H. A comprehensive review of ZnO materials and devices. *Journal of Applied Physics* **2005**, *98*, 041301.

(3) Quang Dang, V.; Kim, D.-I.; Thai Duy, L.; Kim, B.-Y.; Hwang, B.-U.; Jang, M.; Shin, K.-S.; Kim, S.-W.; Lee, N.-E. Piezoelectric coupling in a field-effect transistor with a nanohybrid channel of ZnO nanorods grown vertically on graphene. *Nanoscale* **2014**, *6*, 15144-15150.

(4) Mahmood, K.; Swain, B. S.; Amassian, A. Double-layered ZnO nanostructures for efficient perovskite solar cells. *Nanoscale* **2014**, *6*, 14674-14678.

(5) Zhang, J.; Liu, H.; Wang, Z.; Ming, N.; Li, Z.; Biris, A. S. Polyvinylpyrrolidone-Directed Crystallization of ZnO with Tunable Morphology and Bandgap. *Advanced Functional Materials* **2007**, *17*, 3897-3905.

(6) Peng, Y.; Xu, A.-W.; Deng, B.; Antonietti, M.; Cölfen, H. Polymer-controlled crystallization of zinc oxide hexagonal nanorings and disks. *The Journal of Physical Chemistry B* **2006**, *110*, 2988-2993.

(7) Kulak, A. N.; Iddon, P.; Li, Y. T.; Armes, S. P.; Cölfen, H.; Paris, O.; Wilson, R. M.; Meldrum, F. C. Continuous structural evolution of calcium carbonate particles: A unifying model of copolymer-mediated crystallization. *Journal of the American Chemical Society* **2007**, *129*, 3729-3736.

(8) Qi, L. M.; Cölfen, H.; Antonietti, M.; Li, M.; Hopwood, J. D.; Ashley, A. J.; Mann, S. Formation of BaSO4 fibres with morphological complexity in aqueous polymer solutions. *Chemistry-A European Journal* **2001**, *7*, 3526-3532.

(9) Qi, L. M.; Cölfen, H.; Antonietti, M. Control of barite morphology by double-hydrophilic block copolymers. *Chemistry of Materials* **2000**, *12*, 2392-2403.

(10) Qi, L. M.; Cölfen, H.; Antonietti, M. Crystal design of barium sulfate using double-hydrophilic block copolymers. *Angewandte Chemie-International Edition* **2000**, *39*, 604-607.

(11) Robinson, K. L.; Weaver, J. V. M.; Armes, S. P.; Marti, E. D.; Meldrum, F. C. Synthesis of controlled-structure sulfate-based copolymers via atom transfer radical polymerisation and their use as crystal habit modifiers for BaSO4. *Journal of Materials Chemistry* **2002**, *12*, 890-896.

(12) Öner, M.; Norwig, J.; Meyer, W. H.; Wegner, G. Control of ZnO crystallization by a PEO-b-PMAA diblock copolymer. *Chemistry of Materials* **1998**, *10*, 460-463.

(13) Garcia, S. P.; Semancik, S. Controlling the morphology of zinc oxide nanorods crystallized from aqueous solutions: The effect of crystal growth modifiers on aspect ratio. *Chemistry of Materials* **2007**, *19*, 4016-4022.

(14) Muñoz-Espí, R.; Qi, Y.; Lieberwirth, I.; Gómez, C. M.; Wegner, G. Surface-functionalized latex particles as controlling agents for the mineralization of zinc oxide in aqueous medium. *Chemistry-A European Journal* **2006**, *12*, 118-129.

(15) Muñoz-Espí, R.; Chandra, A.; Wegner, G. Crystal perfection in zinc oxide with occluded carboxyl-functionalized latex particles. *Crystal Growth & Design* **2007**, *7*, 1584-1589.

(16) Muñoz-Espí, R.; Jeschke, G.; Lieberwirth, I.; Gomez, C. M.; Wegner, G. ZnO-latex hybrids obtained by polymer-controlled crystallization: A spectroscopic investigation. *The Journal of Physical Chemistry B* **2007**, *111*, 697-707.

(17) Derry, M. J.; Fielding, L. A.; Armes, S. P. Polymerization-induced self-assembly of block copolymer nanoparticles via RAFT non-aqueous dispersion polymerization. *Progress in Polymer Science* **2016**, *52*, 1-18.

(18) Canning, S. L.; Smith, G. N.; Armes, S. P. A Critical Appraisal of RAFT-Mediated Polymerization-Induced Self-Assembly. *Macromolecules* **2016**, *49*, 1985-2001.

(19) Warren, N. J.; Armes, S. P. Polymerization-Induced Self-Assembly of Block Copolymer Nano-objects via RAFT Aqueous Dispersion Polymerization. *Journal of the American Chemical Society* **2014**, *136*, 10174-10185.

(20) Derry, M. J.; Fielding, L. A.; Warren, N. J.; Mable, C. J.; Smith, A. J.; Mykhaylyk, O. O.; Armes, S. P. In situ small-angle X-ray scattering studies of sterically-stabilized diblock copolymer nanoparticles formed during polymerization-induced self-assembly in non-polar media. *Chemical Science* **2016**, *7*, 5078-5090.

(21) Derry, M. J.; Fielding, L. A.; Armes, S. P. Industrially-relevant polymerization-induced self-assembly formulations in non-polar solvents: RAFT dispersion polymerization of benzyl methacrylate. *Polymer Chemistry* **2015**, *6*, 3054-3062.

(22) Cunningham, V. J.; Alswieleh, A. M.; Thompson, K. L.; Williams, M.; Leggett, G. J.; Armes, S. P.; Musa, O. M. Poly(glycerol monomethacrylate)-Poly(benzyl methacrylate) Diblock Copolymer Nanoparticles via RAFT Emulsion Polymerization: Synthesis, Characterization, and Interfacial Activity. *Macromolecules* **2014**, *47*, 5613-5623.

(23) Semsarilar, M.; Jones, E. R.; Blanazs, A.; Armes, S. P. Efficient Synthesis of Sterically-Stabilized Nano-Objects via RAFT Dispersion Polymerization of Benzyl Methacrylate in Alcoholic Media. *Advanced Materials* **2012**, *24*, 3378-3382.

(24) Jones, E. R.; Semsarilar, M.; Blanazs, A.; Armes, S. P. Efficient Synthesis of Amine-Functional Diblock Copolymer Nanoparticles via RAFT Dispersion Polymerization of Benzyl Methacrylate in Alcoholic Media. *Macromolecules* **2012**, *45*, 5091-5098.

(25) Zhang, X.; Rieger, J.; Charleux, B. Effect of the solvent composition on the morphology of nano-objects synthesized via RAFT polymerization of benzyl methacrylate in dispersed systems. *Polymer Chemistry* **2012**, *3*, 1502-1509.

(26) Kim, Y.-Y.; Semsarilar, M.; Carloni, J. D.; Cho, K. R.; Kulak, A. N.; Polishchuk, I.; Hendley, C. T.; Smeets, P. J. M.; Fielding, L. A.; Pokroy, B.; Tang, C. C.; Estroff, L. A.; Baker, S. P.; Armes, S. P.; Meldrum, F. C. Structure and Properties of Nanocomposites Formed by the Occlusion of Block Copolymer Worms and Vesicles Within Calcite Crystals. *Advanced Functional Materials* **2016**, *26*, 1382-1392.

(27) Ning, Y.; Fielding, L. A.; Andrews, T. S.; Growney, D. J.; Armes, S. P. Sulfate-based anionic diblock copolymer nanoparticles for efficient occlusion within zinc oxide. *Nanoscale* **2015**, *7*, 6691-6702.

(28) Mann, S.; Archibald, D. D.; Didymus, J. M.; Douglas, T.; Heywood, B. R.; Meldrum, F. C.; Reeves, N. J. Cystallization at inorganic-organic interfaces - biominerals and biomimetic synthesis. *Science* **1993**, *261*, 1286-1292.

(29) Meldrum, F. C. Calcium carbonate in biomineralisation and biomimetic chemistry. *International Materials Reviews* **2003**, *48*, 187-224.

(30) Kim, Y. Y.; Ganesan, K.; Yang, P. C.; Kulak, A. N.; Borukhin, S.; Pechook, S.; Ribeiro, L.; Kroger, R.; Eichhorn, S. J.; Armes, S. P.; Pokroy, B.; Meldrum, F. C. An artificial biomineral formed by incorporation of copolymer micelles in calcite crystals. *Nature Materials* **2011**, *10*, 890-896.

(31) Xiong, G.; Pal, U.; Serrano, J. G.; Ucer, K. B.; Williams, R. T. Photoluminescence and FTIR study of ZnO nanoparticles: the impurity and defect perspective. *Physica Status Solidi (c)* **2006**, *3*, 3577-3581.

(32) Trindade, T.; de Jesus, J. D. P.; O'Brien, P. Preparation of zinc oxide and zinc sulfide powders by controlled precipitation from aqueous solution. *Journal of Materials Chemistry* **1994**, *4*, 1611-1617.

(33) Ghoshal, T.; Kar, S.; Chaudhuri, S. Synthesis and optical properties of nanometer to micrometer wide hexagonal cones and columns of ZnO. *Journal of Crystal Growth* **2006**, *293*, 438-446.

(34) Xu, L.; Hu, Y.-L.; Pelligra, C.; Chen, C.-H.; Jin, L.; Huang, H.; Sithambaram, S.; Aindow, M.; Joesten, R.; Suib, S. L. ZnO with different morphologies synthesized by solvothermal methods for enhanced photocatalytic activity. *Chemistry of Materials* **2009**, *21*, 2875-2885.

(35) Kim, Y.-Y.; Ribeiro, L.; Maillot, F.; Ward, O.; Eichhorn, S. J.; Meldrum, F. C. Bio-Inspired Synthesis and Mechanical Properties of Calcite-Polymer Particle Composites. *Advanced Materials* **2010**, *22*, 2082-2086.

(36) Wang, Z. L.; Kong, X. Y.; Ding, Y.; Gao, P. X.; Hughes, W. L.; Yang, R. S.; Zhang, Y. Semiconducting and piezoelectric oxide nanostructures induced by polar surfaces. *Advanced Functional Materials* **2004**, *14*, 943-956.

(37) Zhang, H.; Yang, D.; Ji, Y. J.; Ma, X. Y.; Xu, J.; Que, D. L. Low temperature synthesis of flowerlike ZnO nanostructures by cetyltrimethylammonium bromide-assisted hydrothermal process. *Journal of Physical Chemistry B* **2004**, *108*, 3955-3958.

(38) Li, G. R.; Hu, T.; Pan, G. L.; Yan, T. Y.; Gao, X. P.; Zhu, H. Y. Morphology-function relationship of ZnO: Polar planes, oxygen vacancies, and activity. *Journal of Physical Chemistry C* **2008**, *112*, 11859-11864.

(39) Yu, Q.; Yu, C.; Yang, H.; Fu, W.; Chang, L.; Xu, J.; Wei, R.; Li, H.; Zhu, H.; Li, M.; Zou, G.; Wang, G.; Shao, C.; Liu, Y. Growth of Dumbbell-like ZnO Microcrystals under Mild Conditions and their Photoluminescence Properties. *Inorganic Chemistry* **2007**, *46*, 6204-6210.

(40) Tada, H. Decomposition reaction of hexamine by acid. *Journal of the American Chemical Society* **1960**, *82*, 255-263.

(41) Cho, S.; Jeong, H.; Park, D.-H.; Jung, S.-H.; Kim, H.-J.; Lee, K.-H. The effects of vitamin C on ZnO crystal formation. *CrystEngComm* **2010**, *12*, 968-976.

6. Chapter Six

6. Efficient Synthesis of Metal/semiconductor Nanocomposites via Spatially-controlled Occlusion of Polymer-stabilised Gold Nanoparticles within ZnO

6.1 Introduction

A wide range of metal/semiconductor hybrid nanostructures have been reported, including metal nanoparticle-decorated semiconductor particles,[1-9] metal/semiconductor core/shell (or yolk/shell) particles[10-16] and Janus particles.[16-18]

Metal nanoparticle-decorated semiconductor particles have been extensively studied.[1-7] Two common methods have been applied to decorate semiconductors with metal nanoparticles. First, metal nanoparticles can be grown on the semiconductor by in situ reduction of a soluble metal precursor.[1-7] The metal nanoparticle diameter can be tuned by controlling the reaction time and concentration of the soluble metal precursor. Unfortunately, the metal nanoparticle size distribution is usually broad. Second, both semiconductor crystals and metal nanoparticles are prepared separately.[8,9] The metal nanoparticles are assembled onto the semiconductors by cross-linking via bifunctional molecules, such as dithiol.[17,18] Given that the size of the metal nanoparticles can be finely controlled, this method enables metal nanoparticles with uniform size distribution to be adsorbed onto semiconductors.

Metal/semiconductor core/shell nanostructures have attracted a wide range of attention due to their unique properties, as well as their potential applications in the areas of photocatalysis, biotechnologies and optical devices.[10-16] The properties of core/shell hybrid nanomaterials can be adjusted by tuning the core component, shell morphology and shell thickness.[11,13-16] The core materials can be Ag, Au or Pt, while the shell can be ZnO, ZnS, TiO_2, Cu_2O, CeO, Fe_3O_4 or MnO.[19,20] The preparation of core-shell structures usually involves a wet chemistry approach, in which the semiconductor shell has been grown on metal particle cores.[10-15]

Janus particles, whose two sides or surfaces are different in terms of chemical and/or physical properties, are of considerable scientific interest.[21] Although many types of Janus particles have been reported, there are only a few examples of the preparation of metal/semiconductor Janus particles.[16-18] Typically, the pre-grown metal nanoparticles were used as seeds to mediate the formation of the semiconductor, resulting in a Janus morphology.[16-18]

It is worth noting that so far as we are aware the efficient incorporation of metal nanoparticles within growing semiconductor crystals with fine control over the spatial location of the nanoparticles has not yet been achieved. Biominerals provide many wonderful examples of the occlusion of biomacromolecules within crystals.[22-25] As mentioned in the previous Chapters, various anionic nanoparticles with appropriate surface functionality (such as carboxylic acid[26-30] or sulfonate[31]) have been incorporated into calcite, while sterically-stabilised diblock copolymer nanoparticles with carboxylic acid[32] have been occluded within ZnO crystals. Such wholly synthetic systems provide a new way to prepare organic/inorganic nanocomposites and also offer an excellent opportunity to elucidate structure-property relationships.[26,27,30] However, at best only one of the two components in such occlusion formulations can be regarded as functional. In this context, targeting noble metal nanoparticle/semiconductor hybrid nanostructures is extremely desirable, because the interaction between such plasmonic nanoparticles embedded within an optically active crystal host may lead to emergent properties that cannot be achieved for either component in isolation. However, this ambitious goal clearly requires the development of robust new occlusion protocols.

Herein we report the efficient incorporation of poly(glycerol monomethacrylate)$_{70}$-stabilised gold nanoparticles (G$_{70}$-AuNPs; where the subscript denotes the mean degree of polymerisation of the polymeric stabiliser) within ZnO single crystals generated in aqueous solution at 90 °C (see **Scheme 6.1**). The effect of varying the G$_{70}$-AuNP concentration on the morphology, extent of occlusion and internal structure of the resulting G$_{70}$-Au/ZnO nanocomposites is systematically investigated. Remarkably, tuning the reaction conditions enable three types of nanocomposite crystals to be produced: (i) G$_{70}$-AuNPs localised mainly in the central region of the ZnO rod-like crystals, (ii) uniform occlusion of G$_{70}$-AuNPs throughout the host crystal, or (iii) G$_{70}$-AuNPs occluded solely within the surface layer of ZnO crystal (denoted as G$_{70}$-Au(central)/ZnO, G$_{70}$-Au(uniform)/ZnO and G$_{70}$-Au(surface)/ZnO, respectively, see **Scheme 6.1**). The interaction between G$_{70}$-AuNPs and the ZnO crystals is examined by XPS and FT-IR spectroscopy and an occlusion mechanism is proposed. Preliminary data for the UV-induced photocatalytic decomposition of a model dye (Rhodamine B) are also presented.
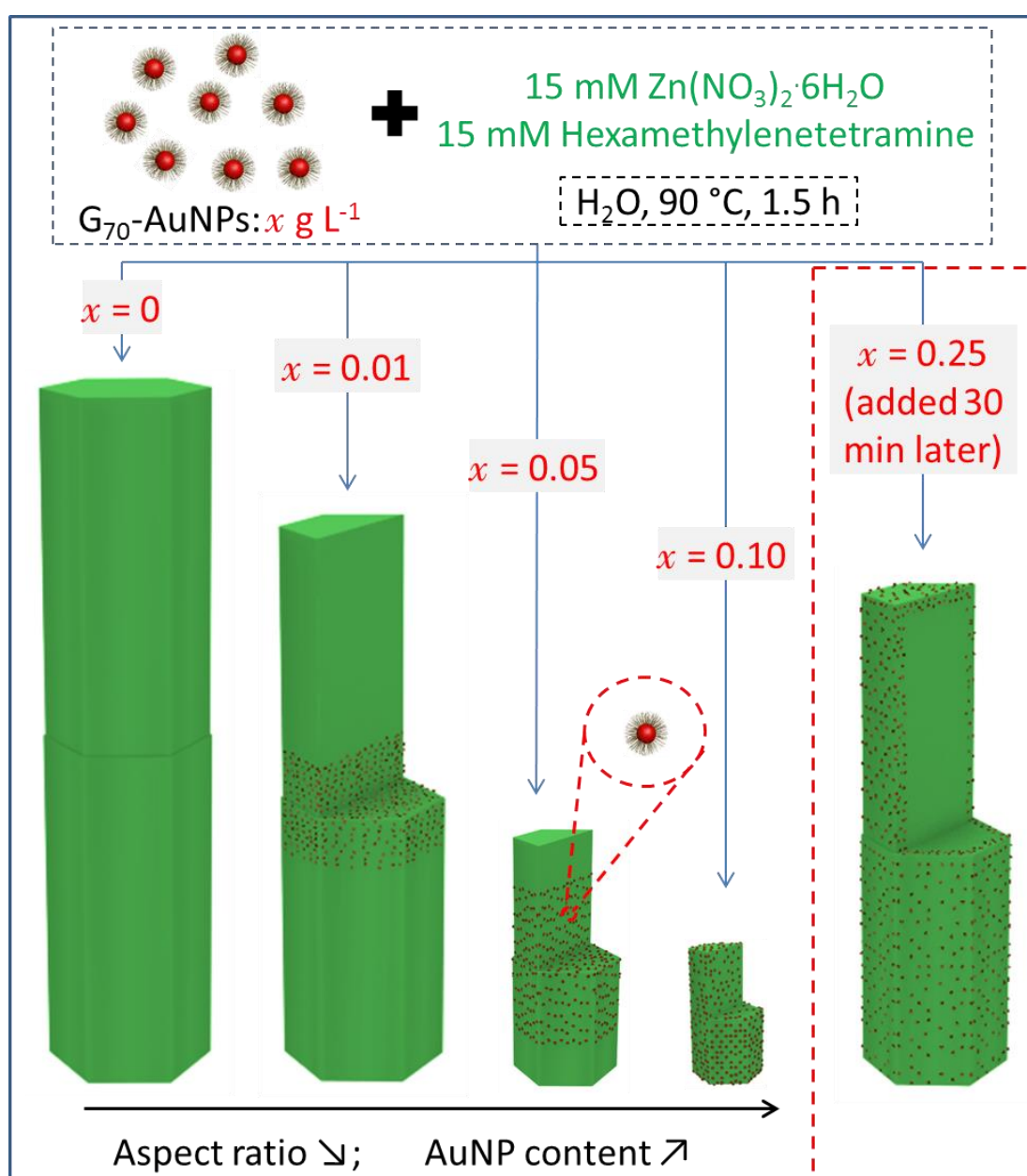
Scheme 6.1. Schematic representation of *spatially-controlled* occlusion of poly(glycerol monomethacrylate)$_{70}$-stabilised gold nanoparticles (G$_{70}$-AuNPs) within ZnO crystals. The left-hand cartoon indicates a ZnO rod-like crystal prepared in the absence of G$_{70}$-AuNPs, while the other sectioned rods indicate the AuNP distribution both within the ZnO and on its surface (with the right-hand cartoon indicating a surface-confined AuNP layer). Judicious variation of the concentration of G$_{70}$-AuNPs allows fine control over their spatial distribution within ZnO single crystals.

6.2 Results and Discussion

6.2.1 Synthesis and Characterisation of G_{70}-AuNPs

Poly(glycerol monomethacrylate)$_{70}$ (see chemical structure in **Figure 6.1a**) was synthesised via RAFT polymerisation in ethanol using 4-cyano-4-(phenylcarbonothioylthio)pentanoic acid (CPCP) and 4,4'-azobis(4-cyanovaleric acid) as RAFT chain transfer agent and initiator, respectively. G_{70} homopolymer is hydrophilic and contains a dithiobenzoate and a carboxylic acid end-group. The former group enables the facile surface modification of plasmonic gold nanoparticles. The as-prepared G_{70} possesses a narrow molecular weight distribution (M_n = 17 000 g mol^{-1}, M_w/M_n = 1.10), as confirmed by gel permeation chromatography (GPC, see **Figure 6.1b**).
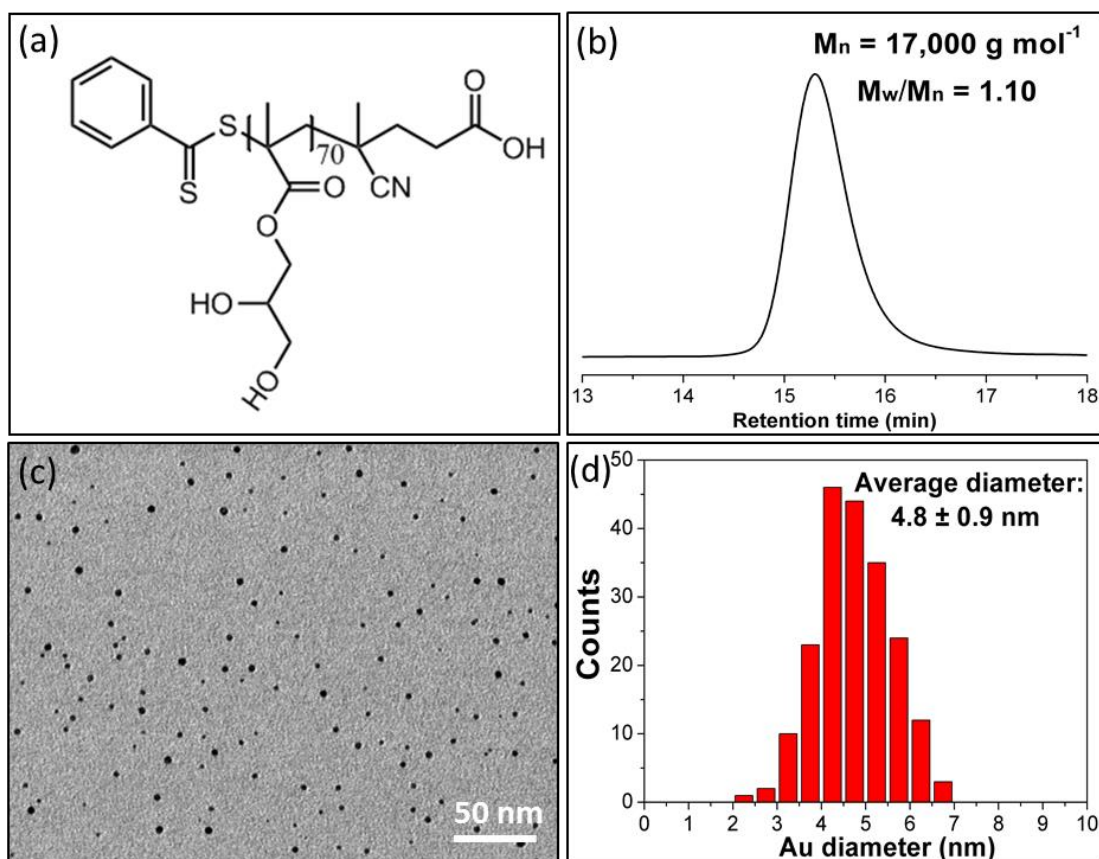
Figure 6.1. Characterisation of poly(glycerol monomethacrylate)$_{70}$ (G_{70}) and G_{70}-stabilised AuNPs. (a) Chemical structure of the G_{70} polymeric stabiliser used in this work; (b) GPC data obtained for G_{70} using a series of poly(methyl methacrylate) calibration standards; (c) representative TEM image obtained for G_{70}-AuNPs; (d) particle size distribution determined for G_{70}-AuNPs from TEM image analysis.

An aqueous dispersion of AuNPs was readily prepared as described elsewhere.[33,34] G_{70}-AuNPs were prepared via chemisorption of G_{70} chains conducted in aqueous solution; the dithiobenzoate end-group is known to bind strongly to gold via ligand change with citrate.[35] As shown in **Figures 6.1c** and **6.1d**, the as-synthesised G_{70}-AuNPs had a mean TEM diameter of 4.8 ± 0.9 nm. According to DLS studies (see **Figure 6.2**), the mean hydrodynamic diameters of the citrate-stabilised AuNPs and G_{70}-AuNPs were 6 ± 2 nm and 12 ± 3 nm, respectively. This difference indicates a G_{70} stabiliser layer thickness of ~ 3 nm, which is consistent with recent small-angle X-ray scattering studies.[36] The hydrodanymic diameter of gold nanoparticle determined by DLS is slightly bigger compared to that determined by TEM. This is because the stabiliser corona contributes to the DLS measurement.
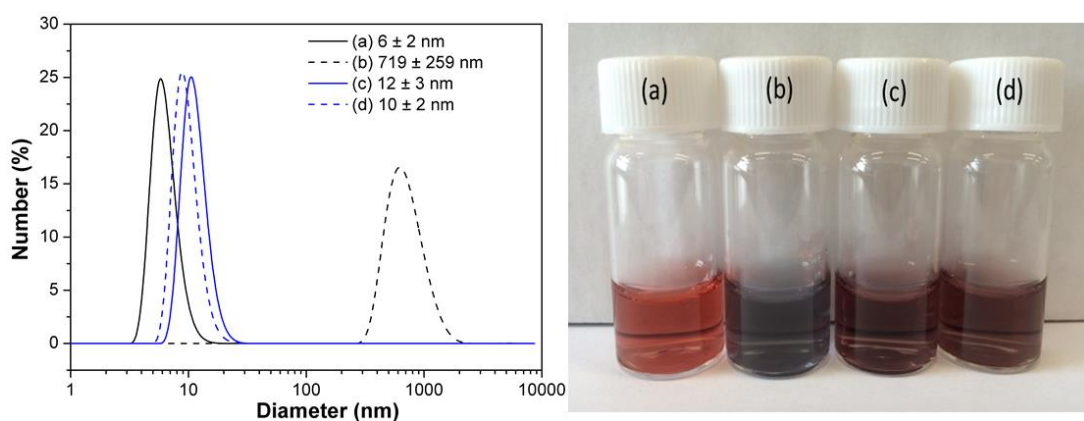
Figure 6.2. Mean hydrodynamic number-average diameter (left-band) and optical photograph (right-hand) obtained for aqueous dispersions of (a) citrate-stabilised AuNPs (gold nanoparticles prepared using sodium citrate); (b) citrate-stabilised AuNPs in the presence of 15 mM zinc ions; (c) G_{70}-AuNPs; (d) G_{70}-AuNPs in the presence of 15 mM zinc ions.

TGA was employed to determine the amount of G_{70} stabiliser of G_{70}-AuNPs. As shown in **Figure 6.3**, G_{70} homopolymer is completely pyrolysed on heating up to ~550 °C, while approximately 39 % residue is observed for G_{70}-AuNPs. It is calculated that the G_{70} stabiliser comprised approximately 40% by mass of the G_{70}-AuNPs. This composition was corroborated by carbon microanalyses, which indicated a G_{70} content of ~ 41%.
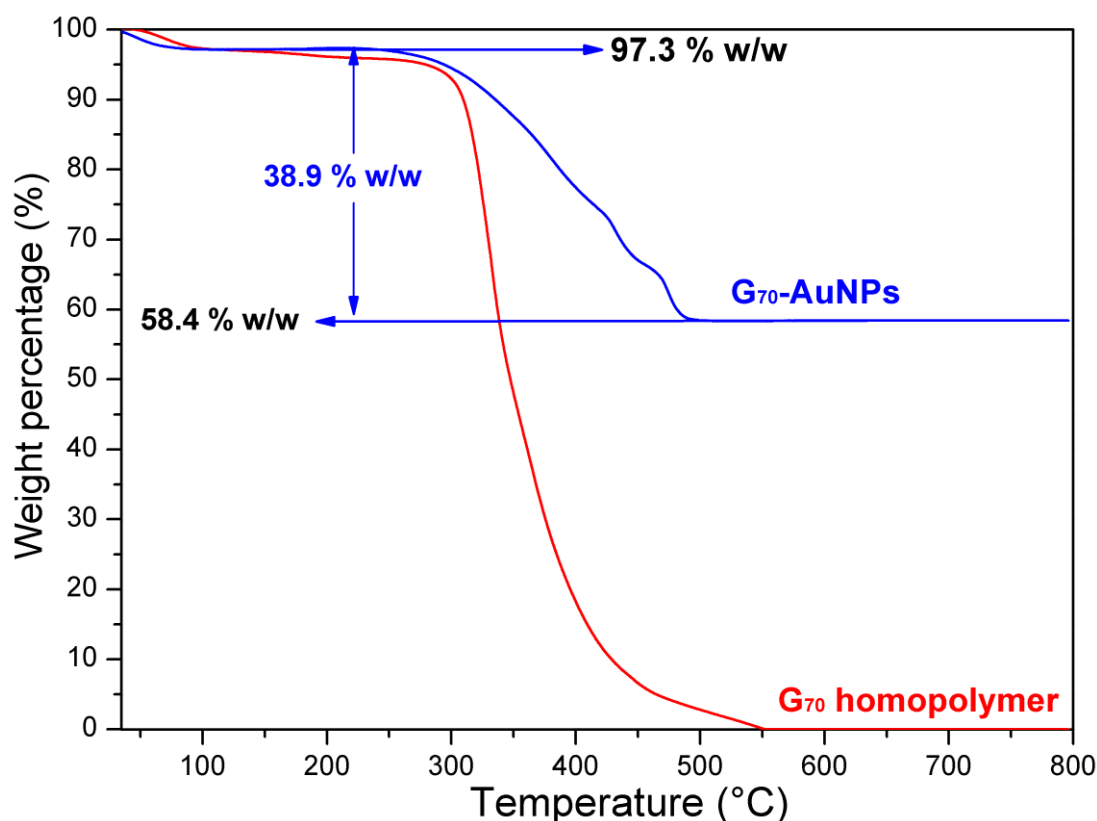
Figure 6.3. TGA of G_{70} homopolymer (red) and G_{70}-AuNPs (blue). As expected, G_{70} homopolymer is pyrolysed completely above 550 °C. Given the presence of 2.7 % w/w water in the G_{70}-AuNPs trace, the G_{70} content in G_{70}-AuNPs can be calculated to be 40.0 % w/w.

Colloidal stabilities of citrate-stabilised AuNPs and G_{70}-AuNPs in the presence of zinc ions were examined. It is worth noting that surface grafting of the G_{70} chains led to a subtle change in colour from pink to purple for the AuNP dispersion (see **Figure 6.2**). The colour of citrate-stabilised AuNPs in aqueous solution changed from pink to grey immediately after addition of zinc nitrate hexahydrate. This is due to the aggregation of the gold nanoparticles in the presence of zinc ions. This aggregation was confirmed by dynamic light scattering (DLS) measurements (see **Figure 6.2**), whereby the DLS diameter increased from 6.4 nm up to ~700 nm. In contrast, the colour remains the same regardless of the presence of zinc ions for G_{70}-AuNPs. Indeed, the mean hydrodynamic diameter of the G_{70}-AuNPs in the presence of 15 mM zinc ions was slightly reduced from 11.5 nm to 9.7 nm, which is probably the result of coronal shrinking caused by the zinc ions.
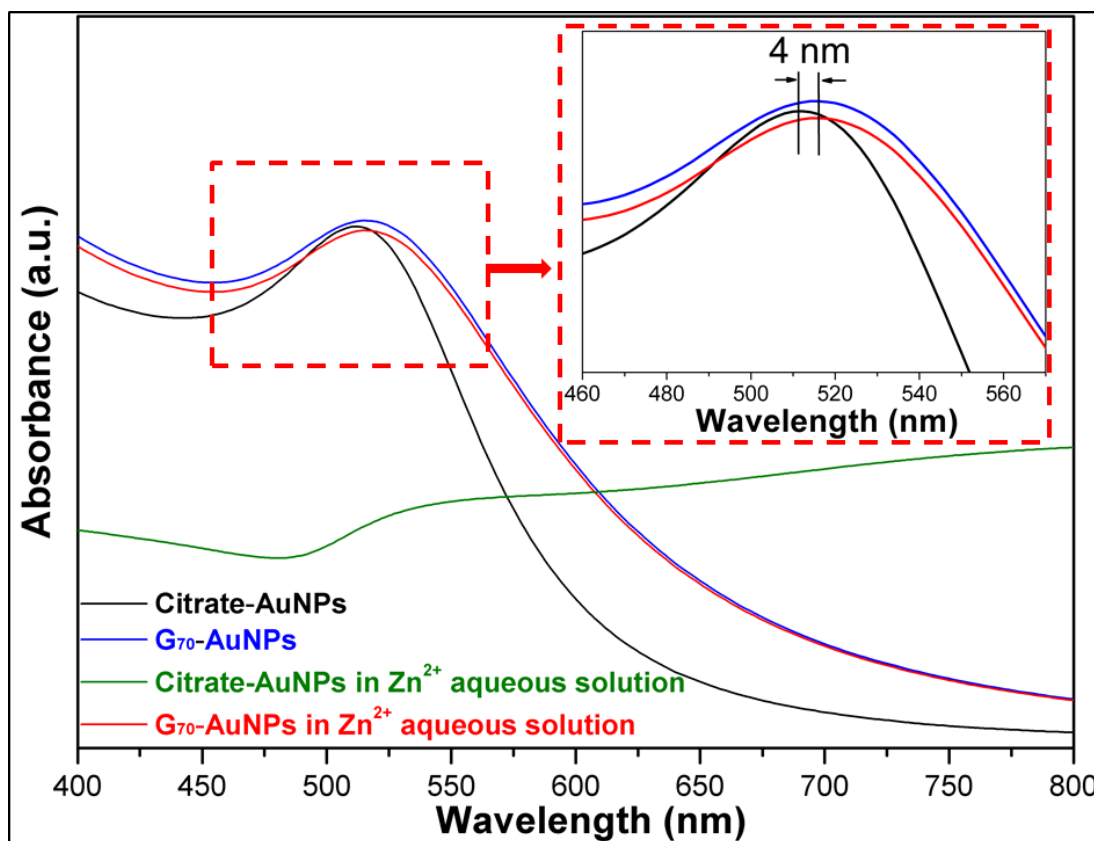
Figure 6.4. Visible absorption spectra recorded for as-synthesised citrate-AuNPs or G$_{70}$-AuNPs in either water or an aqueous solution of 15 mM Zn(NO$_3$)$_2$. The inset shows that the surface plasmon band for G$_{70}$-AuNPs is red-shifted by 4 nm compared to citrate-AuNPs. Notably, there is no further change in the presence of 15 mM zinc ions, indicating good colloidal stability for the G$_{70}$-AuNPs under these conditions.

It is well-known that the surface plasmon band of AuNPs of a given size is sensitive to surface modification.[37] Indeed, the surface plasmon band was red-shifted by 4 nm after surface-grafting the G$_{70}$ chains (see inset in **Figure 6.4**). As discussed above, the citrate-stabilised AuNPs aggregate immediately in the presence of zinc ions. This salt-induced coagulation is corroborated by the disappearance of the surface plasmon absorbance (see **Figure 6.4**) and the observation of ~ 700 nm aggregates by DLS (see **Figure 6.2**). In contrast, the surface plasmon band observed for G$_{70}$-AuNPs remains unchanged in the presence of zinc ions. Thus G$_{70}$-AuNPs retain their colloidal stability in the presence of 15 mM Zn(NO$_3$)$_2$, which is an essential prerequisite for their subsequent efficient occlusion within ZnO crystals.

6.2.2 Occlusion of G_{70}-AuNPs within ZnO Crystals

G_{70}-AuNPs (4.8 nm Au core diameter) were occluded within the host crystal by heating an aqueous solution containing $Zn(NO_3)_2 \cdot 6H_2O$ and HMTA at 90 °C for 1.5 h. In the absence of any G_{70}-AuNPs, twin-structured hexagonal prismatic ZnO rods were typically obtained, see **Figures 6.5a** and **6.5e**. When using 0.01 g L^{-1} G_{70}-AuNPs, nanoparticle occlusion was mainly confined to the central region of the ZnO rods, as indicated by the red brackets shown in **Figures 6.5b** and **6.5f**.

In addition, larger G_{70}-AuNPs were also prepared to aid visualisation of the nanoparticles within the central region of the ZnO rods by electron microscopy. Thus 14 nm AuNPs were prepared by using sodium citrate as both a stabiliser and a reducing agent. This route is slightly different from that of 4.8 nm AuNPs, which were stabilised by sodium citrate but reduced using sodium borohydride (see Experimental section). The as-prepared 14 nm AuNPs were further modified by G_{70} via ligand exchange. As shown in **Figure 6.6a**, near-monodisperse AuNPs can be readily obtained. Meanwhile, the gold nanoparticles localised in the central region of the rod-like ZnO crystals can be clearly identified, as indicated by the red arrows in **Figure 6.6b**.

Using a higher concentration of 4.8 nm G_{70}-AuNPs (0.05 g L^{-1}) led to a larger central zone (see **Figure 6.5g**, indicated using red brackets) and, when used at 0.075 g L^{-1}, essentially all the G_{70}-AuNPs are more or less uniformly distributed throughout the ZnO crystals, as indicated in **Figure 6.6c**. It is worth mentioning here that no excess G_{70}-AuNPs were observed after centrifugation of the resulting G_{70}-Au/ZnO crystals. At 0.10 g L^{-1}, the G_{70}-AuNPs are uniformly distributed throughout the whole ZnO crystal (see **Figures 6.2d** and **6.2h**) and excess non-occluded G_{70}-AuNPs in the supernatant were also observed after centrifugation of G_{70}-Au/ZnO crystals.
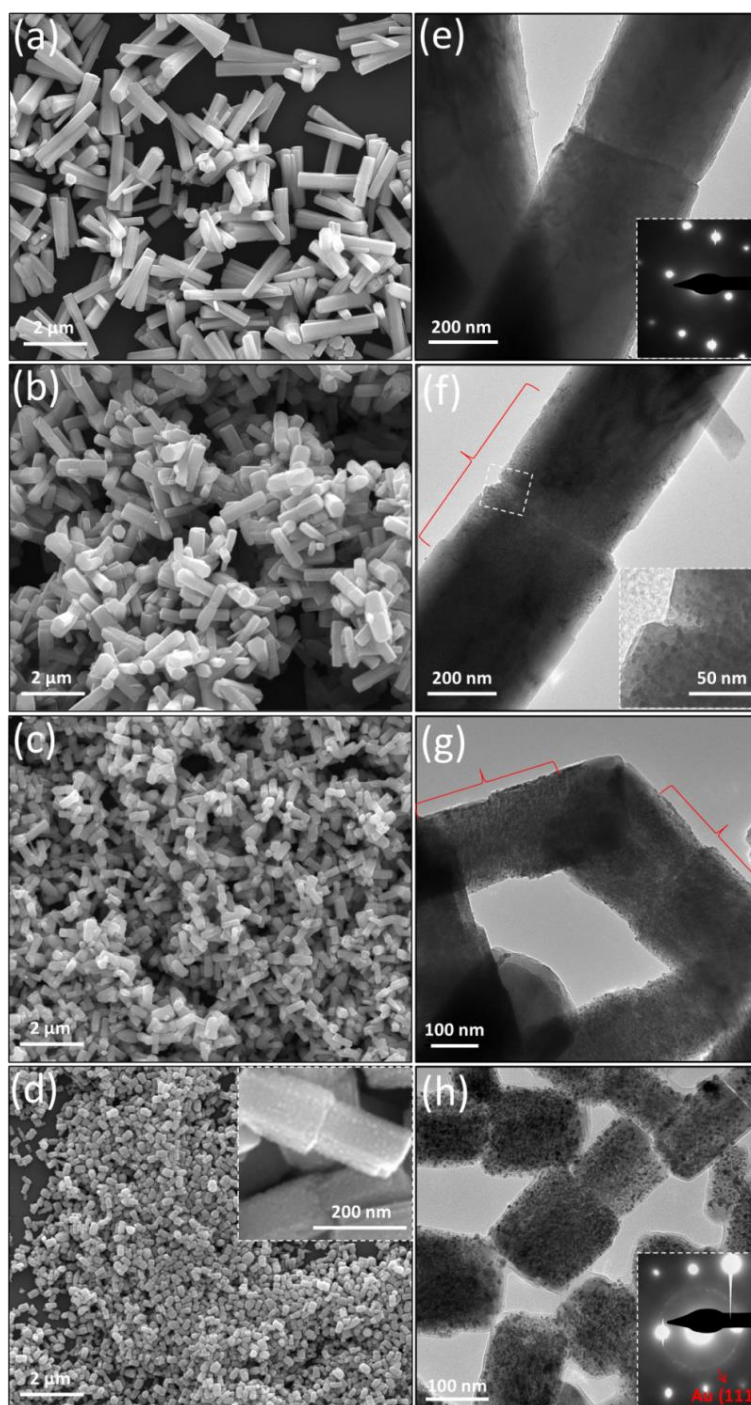
Figure 6.5. SEM images (left column) and TEM images (right column) obtained for ZnO crystals prepared in the presence of various concentrations of G_{70}-AuNPs. (a) and (e), 0 g L^{-1} G_{70}-AuNPs (pure ZnO control); (b) and (f), 0.01 g L^{-1}; (c) and (g), 0.05 g L^{-1}; (d) and (h), 0.10 g L^{-1}. The inset in (d) is a magnified SEM image, showing ZnO rods surface-decorated with gold nanoparticles (white dots). The inset shown in (f) is a magnified TEM image of the indicated region. The insets in (e) and (h) represent selected-area electron diffraction (SAED) patterns recorded for each corresponding sample. SEAD pattern shown in (e) indicates a single crystalline nature of ZnO. As well as the expected diffraction spots for ZnO, a ring of diffraction spots assigned to the Au (111) planes was also observed for G_{70}-Au/ZnO nanocomposites, see inset in (h). The red brackets shown in (f) and (g) indicate the spatial location of the AuNPs within the central region of the ZnO rods.
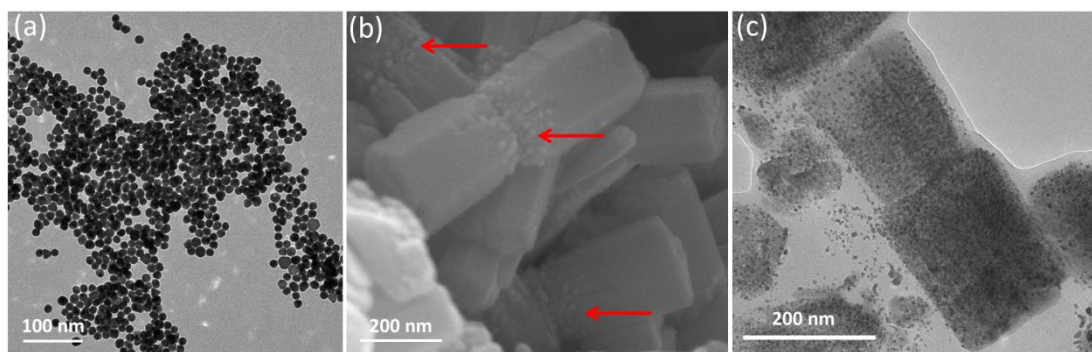
Figure 6.6. (a) TEM image recorded for 14 nm G_{70}-AuNPs. (b) SEM image recorded for G_{70}-Au/ZnO nanocomposite crystals prepared using these 14 nm AuNPs with a G_{70}-AuNP concentration of 0.10 g L^{-1}. (c) TEM image recorded for an ultramicrotomed cross-section of G_{70}-Au/ZnO nanocomposites prepared in the presence of 0.075 g L^{-1} G_{70}-AuNPs. N.B. This TEM specimen was obtained by slicing G_{70}-Au/ZnO nanocomposites embedded within epoxy resin with the aid of an ultramicrotome. Further cross-section of various samples will be presented in the following Figures.

Although the G_{70}-Au/ZnO nanocomposites retain the characteristic rod-like morphology of the ZnO control (see **Figure 6.5**), systematically lower aspect ratios were observed on increasing the G_{70}-AuNP concentration (see **Figure 6.7a**). More specifically, the mean length was dramatically reduced compared to the mean width (see **Figure 6.7b**). Aqueous electrophoresis studies (see **Figure 6.7c**) indicated zeta potentials of +4 mV and -33 mV for the ZnO control crystals and the G_{70}-AuNPs, respectively. Notably, lower zeta potentials and electrophoretic mobilities were obtained for G_{70}-Au/ZnO nanocomposites prepared at higher G_{70}-AuNPs concentrations. This suggests that there are G_{70}-AuNPs adsorbed at the surface of the ZnO crystals (see inset in **Figure 6.5d**), because the terminal carboxylic acid groups located on the G_{70} stabiliser chains lead to negative zeta potentials.[38]

The surface presence of G_{70}-AuNPs was also confirmed by XPS.[39] As expected, the Au 4d signal intensity was systematically increased when employing higher G_{70}-AuNP concentrations (see **Figure 6.7d**). Powder XRD studies confirmed that the crystalline form of ZnO was invariably wurtzite, whether prepared in the presence or absence of G_{70}-AuNPs. Moreover, the gradual increase in Au signal intensity when using a higher G_{70}-AuNP concentration indicates that greater degrees of occlusion are obtained under these conditions (**Figure 6.7e**).
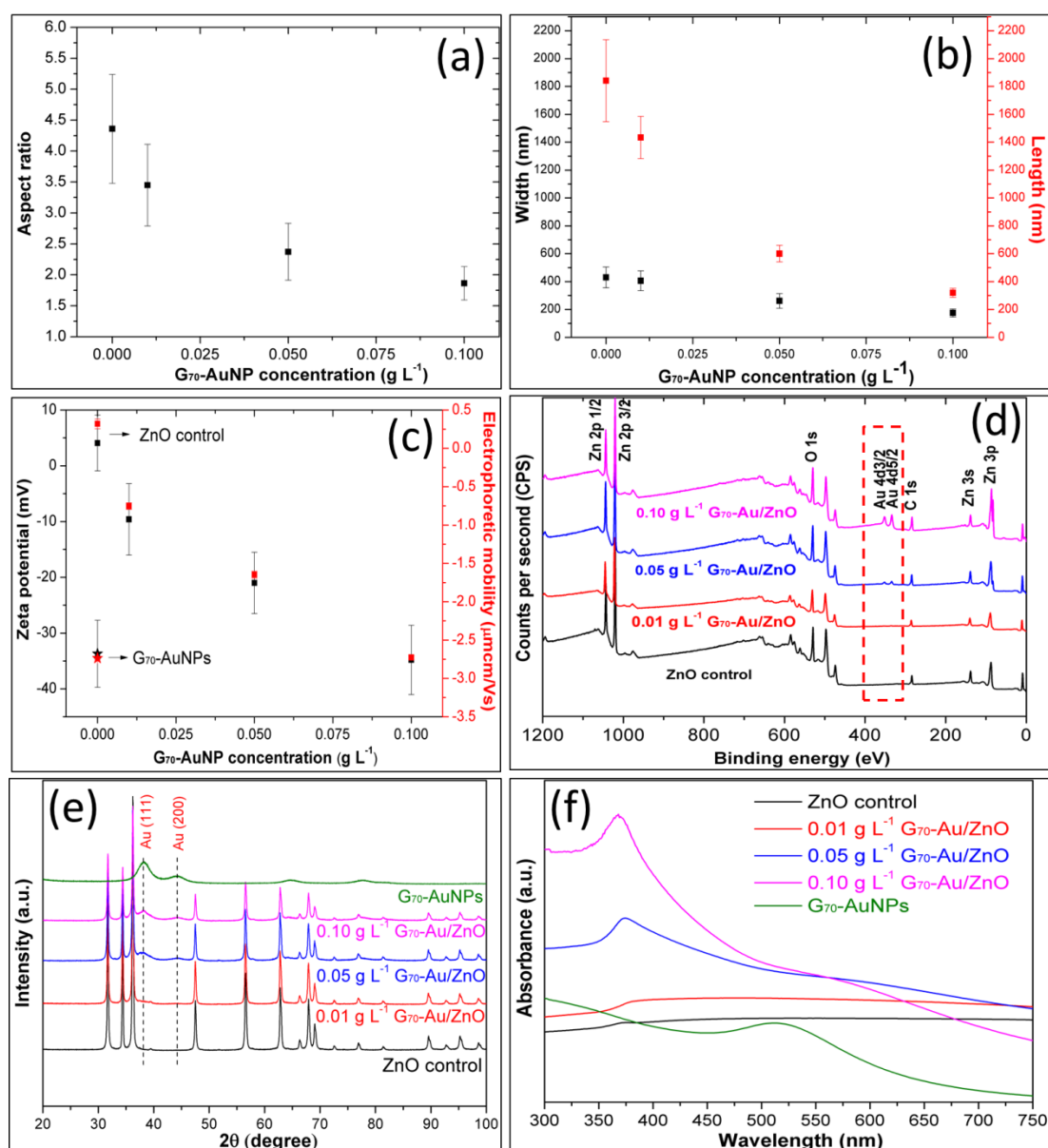
Figure 6.7. (a) Effect of varying G_{70}-AuNP concentration on G_{70}-Au/ZnO aspect ratio; (b) mean length and width of G_{70}-Au/ZnO nanocomposites versus G_{70}-AuNP concentration. Both the length and width decrease as the G_{70}-AuNP concentration increases. However, the length decreases more sharply, leading to an overall decrease of aspect ratio. (c) Zeta potential and electrophoretic mobility (conducted at pH 7) vs. G_{70}-AuNP concentration; (d) XPS spectra recorded for G_{70}-Au/ZnO nanocomposites prepared using a range of G_{70}-AuNP concentrations. The Au4d signal intensity systematically increased when using higher G_{70}-AuNP concentrations, as indicated by the red dotted lines. (e) Powder X-ray diffraction analysis for a ZnO control, G_{70}-AuNPs and ZnO precipitated in the presence of various concentrations of G_{70}-AuNPs; (f) UV-visible absorption spectra recorded for a ZnO control, G_{70}-AuNPs and ZnO precipitated in the presence of various concentrations of G_{70}-AuNPs.

UV-visible absorption spectra (**Figure 6.7f**) indicate that ZnO control crystals exhibit a relatively weak band gap absorption at ~375 nm. This spectral feature (along with generally stronger absorption in the UV region) was significantly enhanced for the series of G_{70}-Au/ZnO nanocomposites. Moreover, the AuNP surface plasmon band was red-shifted from a local maximum at 516 nm to a shoulder at around 550 nm. This is not due to aggregation, but instead reflects a change in the local environment of the AuNPs, which subtly influences their dielectric constant.[40,41] However, the latter feature remains rather weak even for relatively high levels of G_{70}-AuNP incorporation. This suggests that AuNP occlusion within ZnO leads to a subtle change in the electronic states of the two components.[42]
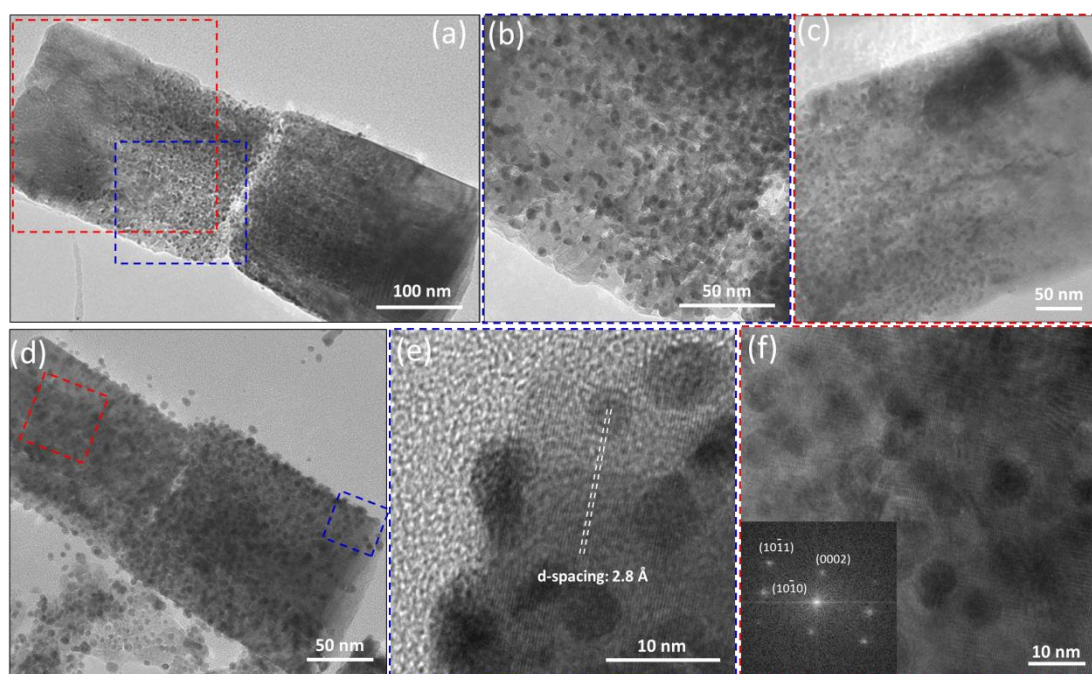
Figure 6.8. TEM images of ultramicrotomed cross-sections (parallel to the *c* axis) of G_{70}-Au/ZnO nanocomposite crystals. (a-c) 0.05 g L^{-1} G_{70}-Au(central)/ZnO, with (b) and (c) representing magnified regions, as indicated in (a); (d-f) 0.10 g L^{-1} G_{70}-Au(uniform)/ZnO, with (e) and (f) again representing magnified regions, as indicated in (d). The inset shown in (f) depicts the fast Fourier transform (FFT) obtained for this image. AuNPs are evidently occluded within the ZnO crystals and their spatial location can be controlled simply by varying the G_{70}-Au concentration; higher concentrations produce a uniform distribution, whereas lower concentrations restrict occlusion to within a central region. Moreover, AuNP occlusion does not appear to cause any distortion of the ZnO lattice, see **Figure 6.8e**.

High-resolution TEM images recorded for ultramicrotomed G_{70}-Au/ZnO nanocomposite crystals embedded in epoxy resin confirmed that the G_{70}-AuNPs were incorporated within the host matrix, rather than merely deposited on the ZnO surface (see **Figure 6.8**). By imaging the cross-section parallel to the c axis of G_{70}-Au/ZnO nanocomposite crystals (**Figures 6.8a-6.8c**), AuNPs (which appear darker than the host crystal as a result of their greater electron density) are clearly preferentially located within the centre of the ZnO rods when prepared at a G_{70}-AuNP concentration of 0.05 g L^{-1}. In contrast, doubling this concentration led to the uniform distribution of AuNPs throughout the ZnO crystal (**Figures 6.8d-6.8f**). The ZnO lattice fringes can be clearly observed, as indicated in **Figure 6.8e**. Moreover, AuNP occlusion does not disrupt the lattice continuity of ZnO and fast Fourier transform (FFT) confirmed the highly crystalline nature of the host matrix (see inset of **Figure 6.8f**). Given the presence of the G_{70} stabiliser chains at the surface of the AuNPs, It is perhaps surprising that no distinct interfacial region is observed between the AuNPs and the ZnO matrix. One likely explanation is that the surface density of the G_{70} stabiliser chains is relatively low. Indeed, the surface density of the G_{70} chains on the AuNPs is calculated to be approximately 0.54 chains nm^{-2}, which is 2-3 times lower than that reported by Liang and co-workers for certain polymer-stabilized AuNPs.[41] Moreover, Kulak et al.[38] also observed no interfacial host-guest region (and minimal disruption of the crystalline host lattice) for block copolymer-stabilised magnetite sols occluded within calcite.

Figure 6.9 shows the AuNP distribution within the cross-section of G_{70}-Au(central)/ZnO and G_{70}-Au(uniform)/ZnO rods. In each case the AuNP distribution can be compared by plotting the number of AuNPs per nm^2 against the distance from the middle of the ZnO rods. For the G_{70}-Au(uniform)/ZnO system, AuNPs are uniformly distributed throughout the whole rod, although there are somewhat fewer at the edge of the c axis. In contrast, the number of AuNPs in the central part of the rod is significantly less for G_{70}-Au(central)/ZnO ($\sim 20 \times 10^{-3}$ per nm^2) compared to G_{70}-Au(uniform)/ZnO ($\sim 35 \times 10^{-3}$ per nm^2) and graduately decreases to zero before reaching the edge of the c axis. These observations suggest that the density of the occluded G_{70}-AuNPs is graduately reduced during ZnO growth. This is reasonable because the concentration of remaining G_{70}-AuNPs decreases during their gradual incorporation into ZnO.
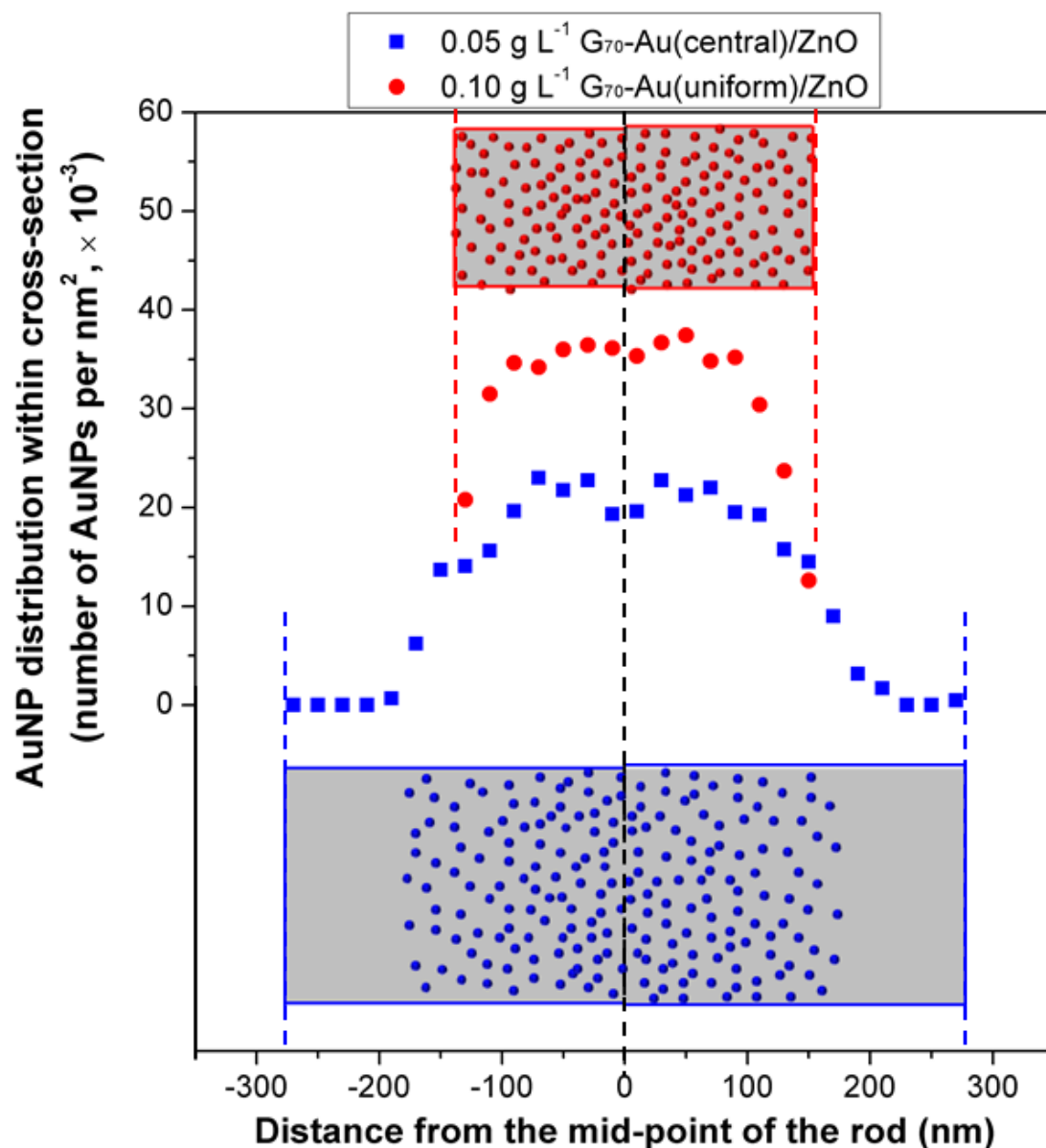
Figure 6.9. Comparison of the AuNP distribution within the cross-section of G_{70}-Au(central)/ZnO and G_{70}-Au(uniform)/ZnO rods. Note: schematic cartoons are drawn to approximate scale.

Uniform occlusion was further confirmed when imaging cross-sections perpendicular to the *c* axis of the G_{70}-Au/ZnO rods (see **Figure 6.10**). Ultramicrotomed ZnO rod-like crystals prepared in the absence of any AuNPs exhibited a hexagonal plate structure (**Figure 6.10a**). G_{70}-AuNPs were homogeneously occluded throughout these ZnO rods when using 0.10 g L^{-1} G_{70}-AuNPs (**Figure 6.10b**). Selected electron area diffraction (SEAD) patterns obtained for the ZnO control confirmed its single crystal nature, while diffraction spots

corresponding to AuNPs can be observed for G_{70}-Au/ZnO nanocomposite crystals (inset in **Figure 6.10b**). At this point, we hypothesised that ZnO crystals might also be prepared in which G_{70}-AuNPs are solely located within a surface layer. This objective was achieved via delayed addition of the G_{70}-AuNPs during ZnO formation (see **Figure 6.10**). Simply, the G_{70}-AuNPs were added 30 min later after the commencement the ZnO crystallisation. Under such conditions, ultramicrotomed cross-sections indicate that G_{70}-AuNPs are mainly confined to a ~35 nm surface layer within the ZnO crystal, as shown in **Figures 6.10c** and **6.10d.**
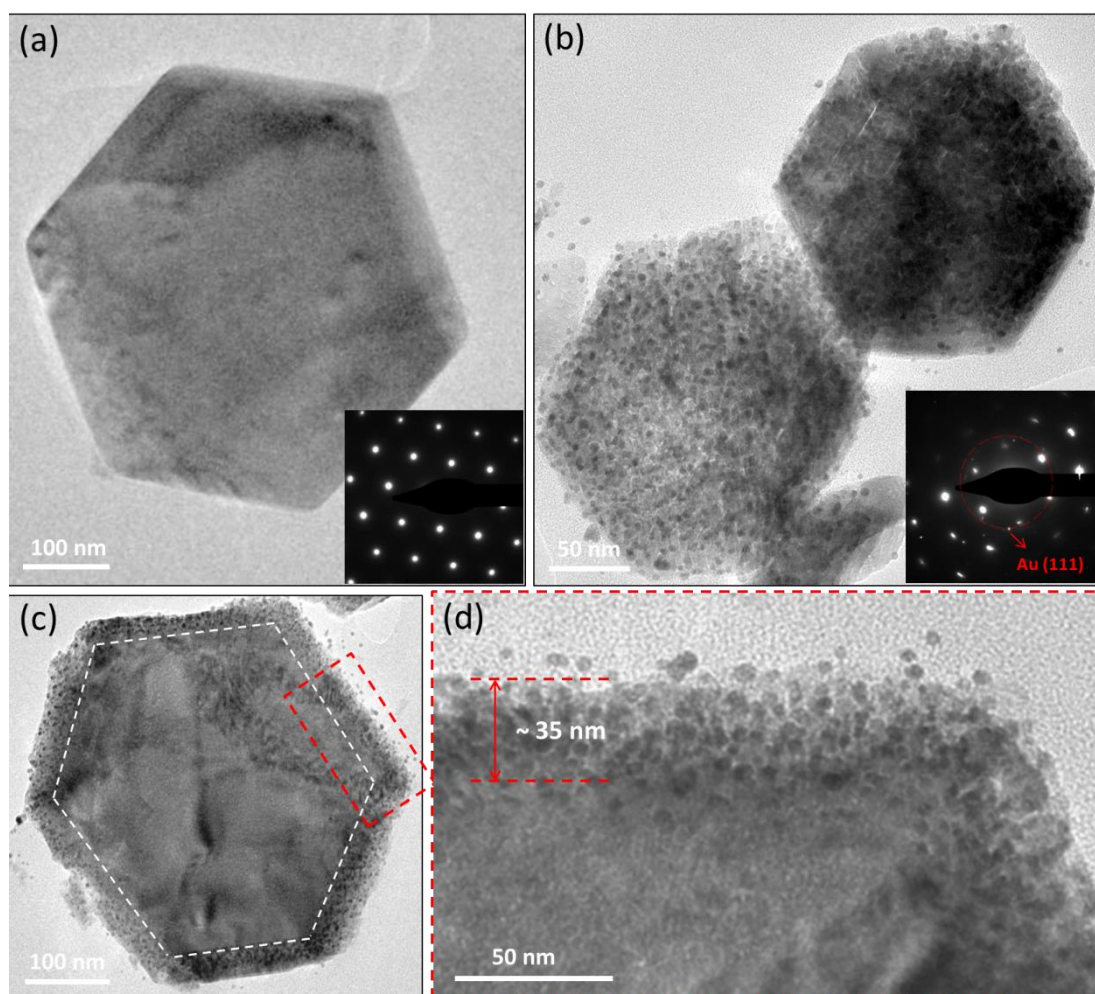
Figure 6.10. TEM images obtained for G_{70}-Au/ZnO nanocomposite crystals ultramicrotomed perpendicular to the *c* axis. (a) ZnO control; (b) 0.10 g L^{-1} G_{70}-Au(uniform)/ZnO nanocomposites with uniformly-distributed G_{70}-AuNPs; (c) G_{70}-AuNPs occluded within ZnO rod-like crystals in the form of a ~35 nm surface layer; (d) magnified image of the corresponding area indicated in (c). The insets in (a) and (b) represent the SAED patterns recorded for each corresponding sample.

Inductively-coupled plasma mass spectrometry (ICP-MS) was used to analyse the gold content of these nanocomposite crystals (see **Table 6.1**). Remarkably, ZnO crystals containing up to 11.9 % w/w gold can be prepared, which corresponds to 19.9 % w/w occluded G_{70}-AuNPs. This is approximately nine times higher compared to that recently reported for AuNPs encapsulated within a zeolitic imidazolate framework (ZIF-8).[40] Alternatively, given the solid-state densities of the ZnO control (5.45 g cm^{-3}) and the G_{70}-AuNPs (3.85 g cm^{-3}), the G_{70}-AuNP content of these nanocomposite crystals can be determined by measuring their solid-state density via helium pycnometry. These density data are summarised in **Table 6.1** and are in fairly good agreement with the ICP-MS results. FT-IR spectra (**Figure 6.11a**) also confirmed that systematically higher G_{70}-AuNP contents occluded within these ZnO crystals: the carbonyl absorption band at 1723 cm^{-1} assigned to the G_{70} stabiliser chains became progressively more intense for nanocomposite crystals prepared in the presence of higher concentrations of G_{70}-AuNPs. Meanwhile, the intensities of C-O-C, primary C-OH and secondary C-OH stretching vibrations are systematically increased when there is a higher extent of G_{70}-AuNP incorporation. These IR bands remain in the same positions, although their intensities depend on the extent of occlusion of the G_{70}-AuNPs. However, the observations made for in-plane bending vibrations of primary C-OH and secondary C-OH are qualitatively different and will be discussed in the following section.
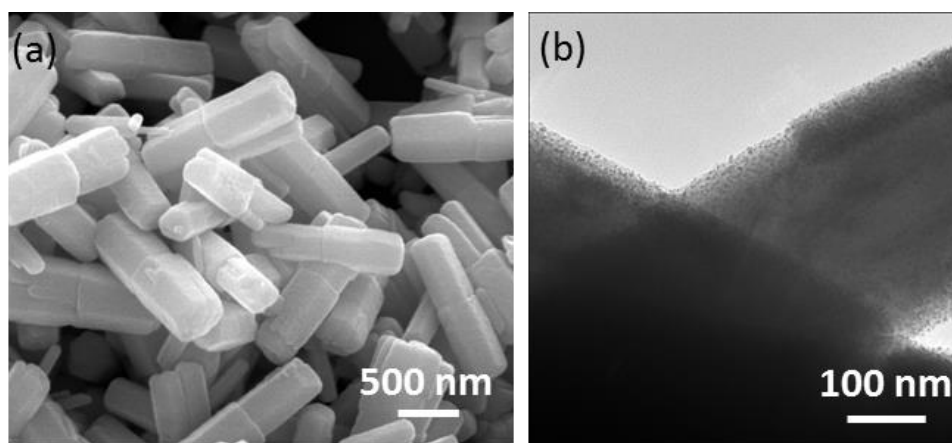
Figure 6.11. SEM image (a) and TEM image (b) of intact G_{70}-Au(surface)/ZnO nanocomposites. This sample was prepared by adding the G_{70}-AuNPs in a delayed time of 30 minutes. N.B. The cross-section perpendicular to the *c* axis can be easily prepared via ultramicrotome (see **Figure 6.10**). However, it is technically difficult to obtain a cross-section parallel to the *c* axis (with similar observations for control ZnO and 0.01 g L^{-1} G_{70}-Au/ZnO) when the G_{70}-Au/ZnO nanocomposites have a larger aspect ratio.
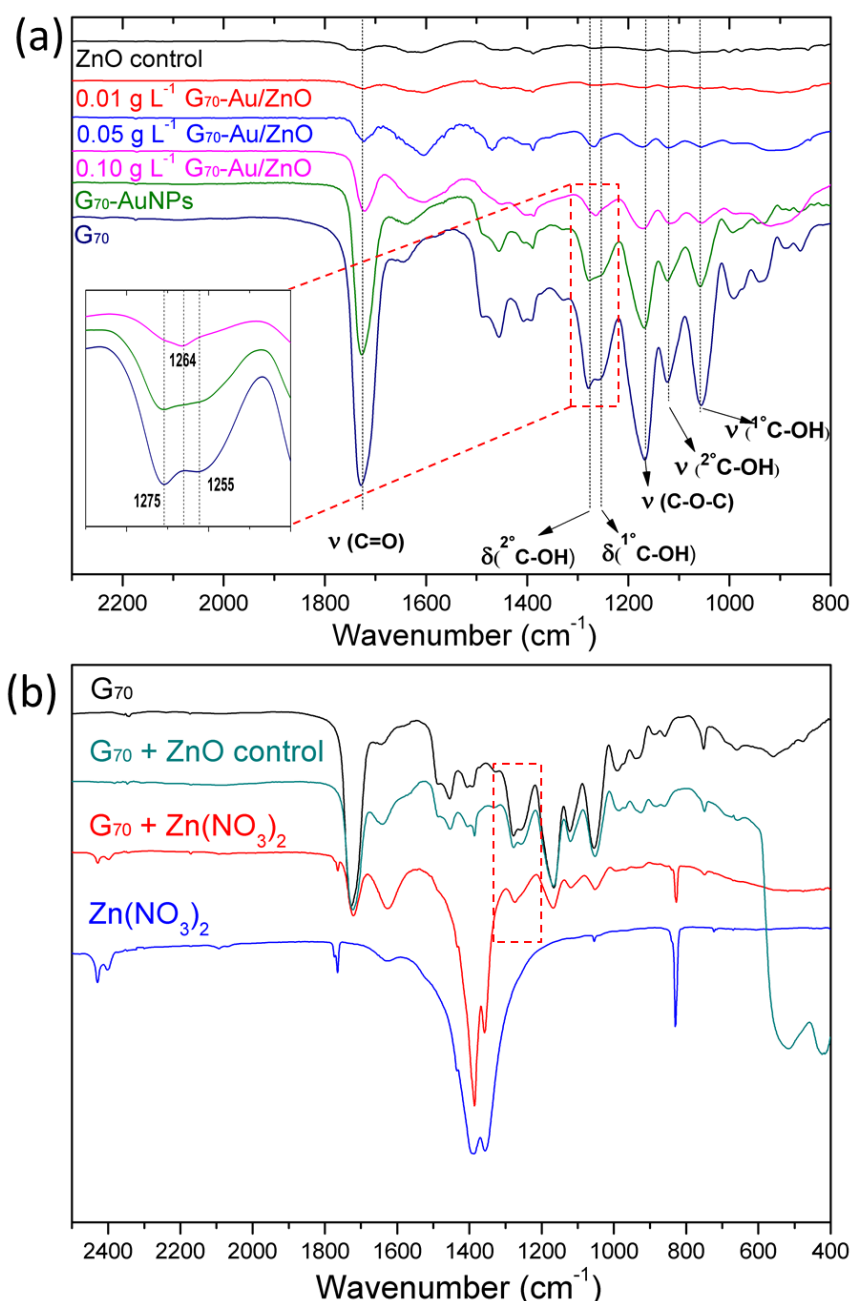
Figure 6.12. FT-IR spectra recorded for (a) three G_{70}-Au/ZnO nanocomposite crystals and three reference materials (ZnO crystals alone, G_{70} homopolymer and the G_{70}-AuNPs). The carbonyl band absorbance correlates well with the G_{70}-AuNP contents of the ZnO crystals, as determined by ICP-MS. Moreover, two C-OH in-plane bending modes merge to form a single band (see inset), suggesting that the *cis*-diol side-groups on the G_{70} chains act as coordinating ligands for Zn^{2+} cations; (b) FT-IR spectra recorded for G_{70}, G_{70} plus ZnO ad-mixture, G_{70} plus $Zn(NO_3)_2$ mixture (prepared by freeze-drying a binary aqueous solution overnight), and $Zn(NO_3)_2$ alone.

Table 6.1. Summary of Au4d/Zn2p atomic ratio (%), solid-state density, BET specific surface area, extent of occlusion of G_{70}-AuNPs within ZnO crystals, and pseudo-first-order rate constant for the UV photodegradation of a model dye (rhodamine B).

Sample	Au4d/Zn2p atomic ratio (%)	Density $(g\,cm^{-3})^a$	BET surface area $(m^2\,g^{-1})$	Extent of occlusion (% w/w)				Rate constant $(k,\,h^{-1})^b$
				ICP-MS		Helium pycnometry		
				Au	G_{70}-Au	Au	G_{70}-Au	
ZnO control	0	5.45	4.2 ± 0.2	-	-	-	-	0.18
0.01 g L^{-1} G_{70}-Au/ZnO	0.9	5.41	3.8 ± 0.3	1.3	2.2	1.1	1.9	0.27
0.05 g L^{-1} G_{70}-Au/ZnO	7.4	5.22	7.3 ± 0.2	7.0	11.6	6.4	10.7	0.63
0.10 g L^{-1} G_{70}-Au/ZnO	39.0	5.05	8.4 ± 0.1	11.9	19.9	11.5	19.1	0.84
G_{70}-Au (surface)ZnO	15.0	5.31	3.1 ± 0.4	3.4	5.7	3.9	6.4	0.42

^{a} G_{70}-AuNPs have a density of 3.85 g cm^{-3}, therefore the higher the G_{70}-Au content, the lower the density of the nanocomposite crystals.
^{b} Pseudo-first-order rate constant (k) is derived from $-\ln(C/C_o) = kt$

6.2.3 Occlusion Mechanism

Incorporation of nanoparticles into single crystals at such a high level is quite remarkable.[27] Clearly, a deeper understanding of the occlusion mechanism is desirable. In addition to non-polar $\{10\bar{1}0\}$ faces, it is well-known that hexagonal ZnO crystals possess polar (0001) and (000$\bar{1}$) planes, with the former being rich in zinc atoms, while the latter is rich in oxygen atoms.[43] In the present Au/ZnO system, ZnO crystallisation in the presence of G_{70}-AuNPs follows the twin-structure formation mechanism as discussed in Chapter 5. However, compared to the ZnO control prepared in the absence of G_{70}-AuNPs, the mean length and width of the Au/ZnO nanocomposite crystals are systematically reduced at higher G_{70}-AuNPs concentrations (see **Scheme 6.1** and **Figure 6.7b**). This is because G_{70}-AuNPs bind to the growing ZnO crystal surface, blocking the sites from which the crystal would normally tend to grow, thereby retarding its growth rate.[32] At a relatively low G_{70}-AuNP concentration (i.e. < 0.05 g L^{-1}), nanoparticle occlusion is complete before ZnO crystallisation has ceased, leading to G_{70}-AuNPs being confined within a central region. At a relatively high G_{70}-Au concentration (> 0.075 g L^{-1}), G_{70}-AuNPs

are occluded throughout the host crystal, with the ZnO growth being significantly suppressed under these conditions. Moreover, G_{70}-AuNPs can not only absorb on the polar (0001) face, but also on the six non-polar $\{10\bar{1}0\}$ faces. This explains why the delayed addition of G_{70}-AuNPs leads to near-surface occlusion.
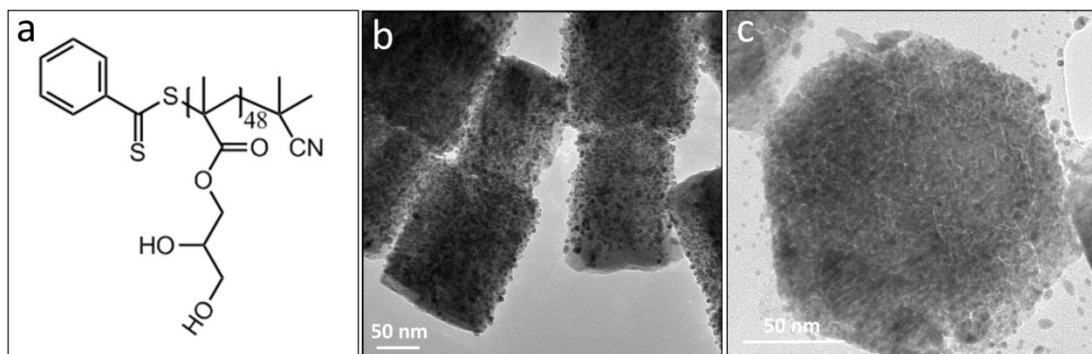
Figure 6.13. Occlusion of G_{48}-AuNPs (prepared using a poly(glycerol monomethacrylate)$_{48}$ (G_{48}) stabiliser containing no carboxylic acid end-groups within ZnO crystals. (a) Chemical structure of G_{48}; (b) TEM image of as-synthesised G_{48}-Au/ZnO nanocomposite crystal; (c) TEM image obtained for G_{48}-Au/ZnO nanocomposite crystals after ultramicrotome perpendicular to the c axis. Clearly, G_{48}-AuNPs are uniformly distributed throughout the whole ZnO crystal.

The G_{70} stabiliser chains play a key role in the interaction between the AuNPs and the host crystal. At first sight this appears rather counter-intuitive, because the non-ionic nature of the glycerol monomethacrylate repeat units might be expected to produce little or no interaction with the ZnO lattice. Indeed, previous reports suggest that an anionic surface charge density is required for efficient interaction of copolymer nanoparticles within crystals.[26-32] Although the G_{70} chains used in this study contain a carboxylate acid end-group, this anionic end-group does not appear to promote occlusion within ZnO (see **Figure 6.13**). In this control experiment, G_{48} was prepared via RAFT polymerisation in ethanol using 2-cyano-2-propyl benzodithioate (CPB) and 2,2'-azobis(isobutylnitrile) (AIBN) as RAFT chain transfer agent and initiator, respectively. This protocol produces G_{48} stabiliser chains with no carboxylic acid end-group (see **Figure 6.13a**). Apparently, uniform occlusion of G_{48}-AuNPs within ZnO can be achieved without carboxylic acid end-groups, as shown in **Figures 6.13b** and **6.13c**. Thus it is safe to conclude that such anionic end-groups do not promote occlusion.

So how do the G_{70}-AuNPs interact with ZnO? The most likely interaction between the G_{70}-AuNPs and the growing ZnO involves chelation between the Zn^{2+} cations and the *cis*-diol groups on the non-ionic G_{70} stabiliser chains.[44-46] Experimental evidence for this complexation is provided by vibrational spectroscopy studies (**Figure 6.12a**). In FT-IR spectra recorded for G_{70}-AuNPs and G_{70} homopolymer, the absorption bands at 1255 cm^{-1} and 1275 cm^{-1} are due to the in-plane bending vibrations of primary and secondary C-OH, respectively.[47] These two bands merge to form a single new band at 1264 cm^{-1} (see inset shown in **Figure 6.12a**), which supports the postulated chelation of Zn^{2+} cations by the G_{70} chains.[48] Moreover, this interaction was further confirmed by control experiments, as shown in **Figure 6.12b**. Clearly, the G_{70} plus $Zn(NO_3)_2$ spectrum is a combination of the G_{70} and $Zn(NO_3)_2$ reference spectra, except that the two in-plane bending vibrations of δ_{C-OH} are merged into a single band, as indicated by the dotted red box. This strongly suggests chelation between Zn^{2+} ions and the *cis*-diol groups on the G_{70} stabiliser chains. Notably, for the G_{70} plus ZnO control, the δ_{C-OH} in-plane bending vibrations remain as two distinct bands, confirming that no interaction occurs on simple physical mixing of these two components.

6.2.4 XPS Studies and Dye Photodecomposition Experiments

These G_{70}-Au/ZnO nanocomposite crystals were also examined by high resolution XPS, which has a typical sampling depth of 2-10 nm.[39] As shown in Figure **6.14a**, the signal intensity of two binding energy (BE) peaks corresponding to the electronic states of Au4f5/2 (87.30 eV) and Au 4f7/2 (83.60 eV) was systematically enhanced at higher AuNP contents. Importantly, each signal was shifted to a lower BE for the G_{70}-Au/ZnO nanocomposite crystals, whereas the two Zn2p signals were shifted to higher BE (see **Figure 6.14b**). These observations suggest significant charge transfer between the two components, indicate an intimate interaction between the AuNPs and the ZnO host crystal.[42]
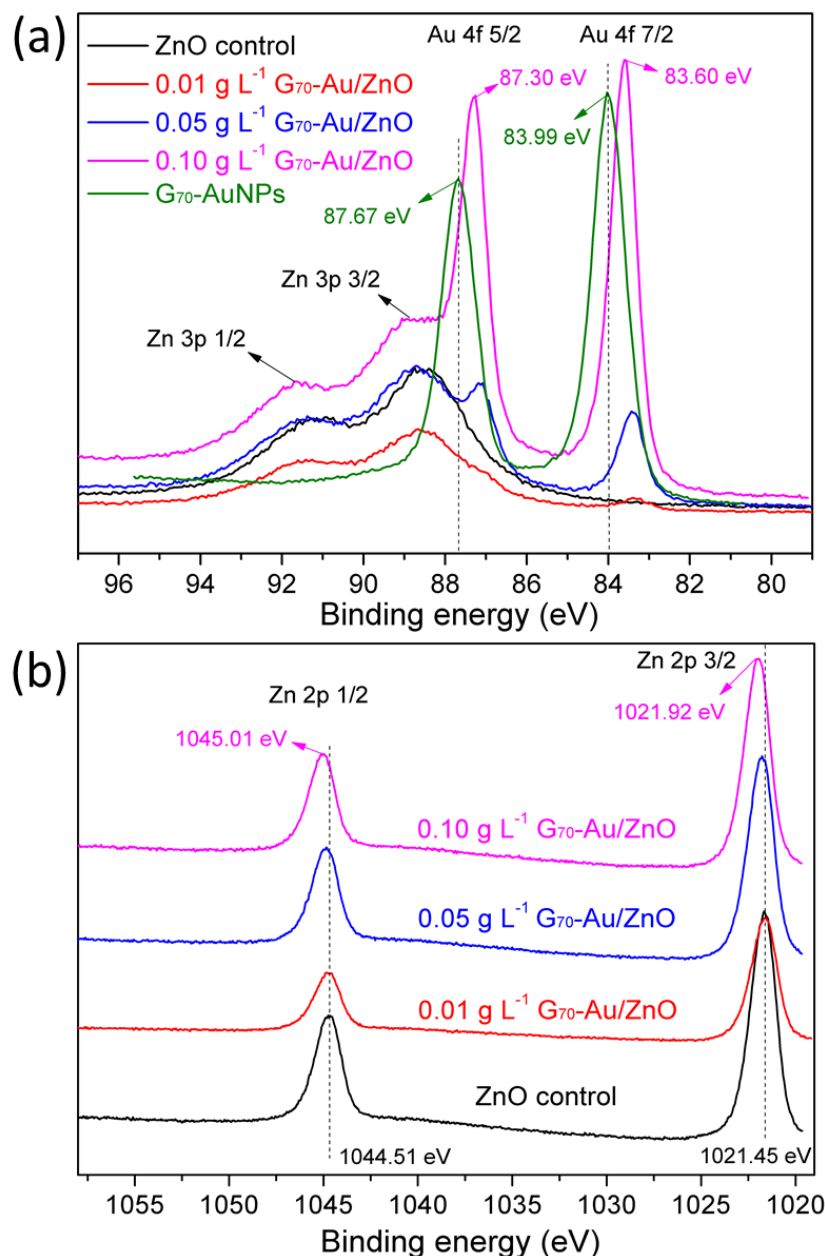
Figure 6.14. High resolution X-ray photoelectron spectra recorded for various G_{70}-Au/ZnO nanocomposite crystals and appropriate reference materials: (a) Au4f; (b) Zn2p.

It is well-known that Au/ZnO nanostructures can exhibit superior photocatalytic performance compared to ZnO alone.[20] We do not expect to achieve higher rates of photocatalysis than those reported for core-shell Au/ZnO nanoparticles or Au-decorated ZnO particles,[2,18,49] because these systems possess a significantly higher specific surface area compared to our nanocomposite crystals. Nevertheless, our new system provides a unique opportunity to examine whether uniform occlusion of gold

nanoparticles *inside* ZnO leads to enhanced photocatalytic performance relative to that observed for the near-surface occlusion of gold nanoparticles.
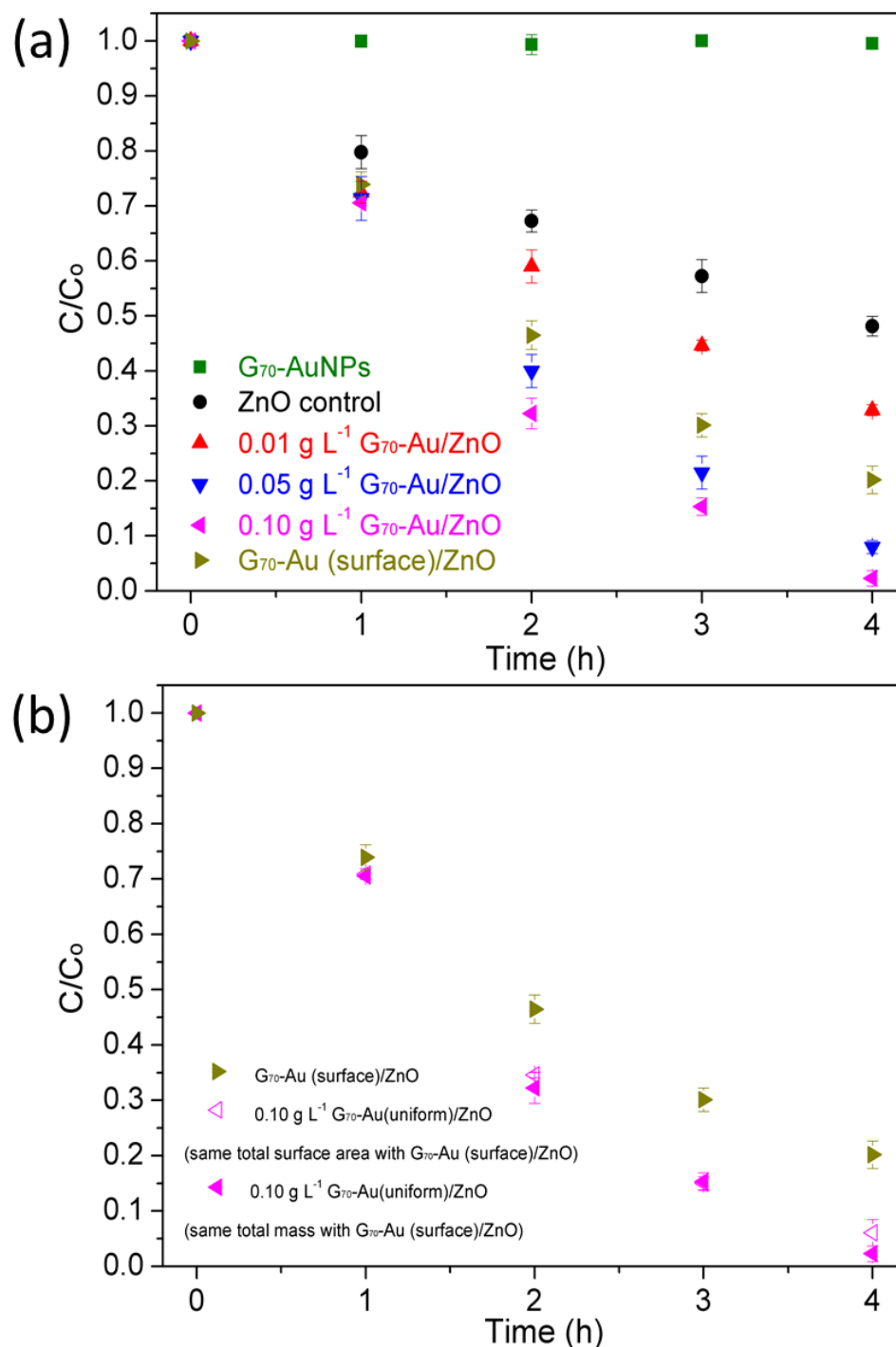
Figure 6.15. The rate of photocatalytic dye decomposition recorded for RhB in the presence of G_{70}-Au(surface)/ZnO and 0.10 g L^{-1} G_{70}-Au(uniform)/ZnO. The amount of 0.10 g L^{-1} G_{70}-Au(uniform)/ZnO crystals used in these experiments was reduced to produce approximately the same total surface area as that for the G_{70}-Au (surface)/ZnO crystals, but this had almost no discernible effect on the observed rate of dye decomposition.

Hence the rate of photodecomposition for a model dye (rhodamine B, or RhB) was studied using a UV wavelength of 254 nm (6 W, UV lamp). As expected, G_{70}-AuNPs alone produce no detectable dye decomposition, whereas the rate of photocatalysis increases monotonically with AuNP content of the G_{70}-Au/ZnO nanocomposite crystals (**Figure 6.15a** and **Table 6.1**). More importantly, the catalytic efficiency obtained for 0.10 g L^{-1} G_{70}-Au(uniform)/ZnO significantly exceeds that of G_{70}-Au(surface)/ZnO within the experimental 4 h time frame. Given that such dye decomposition involves heterogeneous catalysis, the total available surface area could potentially affect photocatalytic performance. However, a control experiment conducted at constant surface area revealed little or no change in the rate of dye decomposition (**Figure 6.15b**). Meanwhile, 0.05 g L^{-1} G_{70}-Au(central)/ZnO also exhibits a higher catalytic efficiency compared to G_{70}-Au(surface)/ZnO (8.0% vs. 20% dye remains after 4 h). As shown in **Table 6.1**, 0.05 g L^{-1} G_{70}-Au(central)/ZnO has approximately twice the Au content compared to G_{70}-Au(surface)/ZnO, but the Au4d/Zn2p surface atomic ratio for the former is around half that of the latter. This observation indicates that the photocatalytic performance mainly depends on the *bulk* Au content, rather than the *surface* Au content. In other words, the incorporated AuNPs contribute significantly to the rate of photocatalysis. This suggests that a higher extent of AuNP occlusion within ZnO provides a larger number of electron 'sinks', which facilitate charge carrier separation and extending the lifetime of the electron-hole pair,[1,2,19,20] thus in turn produces a more effective photocatalyst.

6.3 Conclusions

In summary, we report an efficient, versatile and scalable route to incorporate polymer-functionalised noble metal nanoparticles within semiconductor crystals. More specifically, both the spatial distribution and extent of occlusion of AuNPs within ZnO crystals can be controlled, which provides an unprecedented opportunity to elucidate synthesis-structure-property relationships and establish robust design rules for efficient occlusion. This study provides the first example of effective occlusion facilitated by a *non-ionic* polymer stabiliser. This represents an important paradigm shift, since all prior literature reports of occlusion into inorganic host crystals involve the use of *anionic* polymeric stabilisers. We propose an occlusion mechanism and further show that incorporation of AuNPs into ZnO crystals enhances photocatalytic performance. In principle, appropriate surface modification of various other metal nanoparticles should enable their efficient occlusion within ZnO (and perhaps other host crystals), thus providing access to a range of new functional nanocomposite materials exhibiting emergent properties.

6.4 References

(1) Liu, X.; Liu, M.-H.; Luo, Y.-C.; Mou, C.-Y.; Lin, S. D.; Cheng, H.; Chen, J.-M.; Lee, J.-F.; Lin, T.-S. Strong metal–support interactions between gold nanoparticles and ZnO nanorods in CO oxidation. *Journal of the American Chemical Society* **2012**, *134*, 10251-10258.

(2) He, W.; Kim, H.-K.; Wamer, W. G.; Melka, D.; Callahan, J. H.; Yin, J.-J. Photogenerated charge carriers and reactive oxygen species in ZnO/Au hybrid nanostructures with enhanced photocatalytic and antibacterial activity. *Journal of the American Chemical Society* **2013**, *136*, 750-757.

(3) Cozzoli, P. D.; Comparelli, R.; Fanizza, E.; Curri, M. L.; Agostiano, A.; Laub, D. Photocatalytic synthesis of silver nanoparticles stabilized by TiO_2 nanorods: A semiconductor/metal nanocomposite in homogeneous nonpolar solution. *Journal of the American Chemical Society* **2004**, *126*, 3868-3879.

(4) Zhang, Z.; Zhang, L.; Hedhili, M. N.; Zhang, H.; Wang, P. Plasmonic gold nanocrystals coupled with photonic crystal seamlessly on TiO_2 nanotube photoelectrodes for efficient visible light photoelectrochemical water splitting. *Nano Letters* **2012**, *13*, 14-20.

(5) Murdoch, M.; Waterhouse, G. I. N.; Nadeem, M. A.; Metson, J. B.; Keane, M. A.; Howe, R. F.; Llorca, J.; Idriss, H. The effect of gold loading and particle size on photocatalytic hydrogen production from ethanol over Au/TiO_2 nanoparticles. *Nature Chemistry* **2011**, *3*, 489-492.

(6) Mokari, T.; Rothenberg, E.; Popov, I.; Costi, R.; Banin, U. Selective growth of metal tips onto semiconductor quantum rods and tetrapods. *Science* **2004**, *304*, 1787-1790.

(7) Formo, E.; Lee, E.; Campbell, D.; Xia, Y. Functionalization of electrospun TiO_2 nanofibers with Pt nanoparticles and nanowires for catalytic applications. *Nano Letters* **2008**, *8*, 668-672.

(8) Unlu, I.; Soares, J. W.; Steeves, D. M.; Whitten, J. E. Photocatalytic Activity and Fluorescence of Gold/Zinc Oxide Nanoparticles Formed by Dithiol Linking. *Langmuir* **2015**, *31*, 8718-8725.

(9) Im, J.; Singh, J.; Soares, J. W.; Steeves, D. M.; Whitten, J. E. Synthesis and optical properties of dithiol-linked ZnO/gold nanoparticle composites. *The Journal of Physical Chemistry C* **2011**, *115*, 10518-10523.

(10) Sun, Z.; Yang, Z.; Zhou, J.; Yeung, M. H.; Ni, W.; Wu, H.; Wang, J. A general approach to the synthesis of gold–metal sulfide core–shell and heterostructures. *Angewandte Chemie-International Edition* **2009**, *48*, 2881-2885.

(11) Liu, N.; Prall, B. S.; Klimov, V. I. Hybrid gold/silica/nanocrystal-quantum-dot superstructures: synthesis and analysis of semiconductor-metal interactions. *Journal of the American Chemical Society* **2006**, *128*, 15362-15363.

(12) Zhang, J.; Tang, Y.; Lee, K.; Ouyang, M. Nonepitaxial growth of hybrid core-shell nanostructures with large lattice mismatches. *Science* **2010**, *327*, 1634-1638.

(13) Lee, I.; Joo, J. B.; Yin, Y.; Zaera, F. A yolk@shell nanoarchitecture for Au/TiO_2 catalysts. *Angewandte Chemie* **2011**, *123*, 10390-10393.

(14) Lee, J.-S.; Shevchenko, E. V.; Talapin, D. V. Au-PbS core-shell nanocrystals: Plasmonic absorption enhancement and electrical doping via intra-particle charge transfer. *Journal of the American Chemical Society* **2008**, *130*, 9673-9675.

(15) Zhang, L.; Blom, D. A.; Wang, H. Au-Cu$_2$O core-shell nanoparticles: a hybrid metal-semiconductor heteronanostructure with geometrically tunable optical properties. *Chemistry of Materials* **2011**, *23*, 4587-4598.

(16) Seh, Z. W.; Liu, S.; Low, M.; Zhang, S. Y.; Liu, Z.; Mlayah, A.; Han, M. Y. Janus Au-TiO$_2$ Photocatalysts with Strong Localization of Plasmonic Near-Fields for Efficient Visible-Light Hydrogen Generation. *Advanced Materials* **2012**, *24*, 2310-2314.

(17) Lee, Y.; Garcia, M. A.; Frey Huls, N. A.; Sun, S. Synthetic tuning of the catalytic properties of Au-Fe3O4 nanoparticles. *Angewandte Chemie* **2010**, *122*, 1293-1296.

(18) Li, P.; Wei, Z.; Wu, T.; Peng, Q.; Li, Y. Au− ZnO hybrid nanopyramids and their photocatalytic properties. *Journal of the American Chemical Society* **2011**, *133*, 5660-5663.

(19) Kochuveedu, S. T.; Jang, Y. H.; Kim, D. H. A study on the mechanism for the interaction of light with noble metal-metal oxide semiconductor nanostructures for various photophysical applications. *Chemical Society Reviews* **2013**, *42*, 8467-8493.

(20) Jiang, R.; Li, B.; Fang, C.; Wang, J. Metal/Semiconductor Hybrid Nanostructures for Plasmon-Enhanced Applications. *Advanced Materials* **2014**, *26*, 5274-5309.

(21) Walther, A.; Müller, A. H. Janus particles: synthesis, self-assembly, physical properties, and applications. *Chemical Reviews* **2013**, *113*, 5194-5261.

(22) Lowenstam, H. A.; Weiner, S. *On biomineralization*; Oxford University Press: New York, **1989**.

(23) Weber, E.; Pokroy, B. Intracrystalline inclusions within single crystalline hosts: from biomineralization to bio-inspired crystal growth. *CrystEngComm* **2015**, *17*, 5873-5883.

(24) Berman, A.; Addadi, L.; Kvick, A.; Leiserowitz, L.; Nelson, M.; Weiner, S. Intercalation of sea urchin protein in calcite: Study of a crystalline composite material. *Science* **1990**, *250*, 664-667.

(25) Li, H.; Xin, H. L.; Muller, D. A.; Estroff, L. A. Visualizing the 3D Internal Structure of Calcite Single Crystals Grown in Agarose Hydrogels. *Science* **2009**, *326*, 1244-1247.

(26) Kim, Y.-Y.; Ribeiro, L.; Maillot, F.; Ward, O.; Eichhorn, S. J.; Meldrum, F. C. Bio-Inspired Synthesis and Mechanical Properties of Calcite-Polymer Particle Composites. *Advanced Materials* **2010**, *22*, 2082-2086.

(27) Kim, Y.-Y.; Ganesan, K.; Yang, P.; Kulak, A. N.; Borukhin, S.; Pechook, S.; Ribeiro, L.; Kroeger, R.; Eichhorn, S. J.; Armes, S. P.; Pokroy, B.; Meldrum, F. C. An artificial biomineral formed by incorporation of copolymer micelles in calcite crystals. *Nature Materials* **2011**, *10*, 890-896.

(28) Kulak, A. N.; Yang, P.; Kim, Y.-Y.; Armes, S. P.; Meldrum, F. C. Colouring crystals with inorganic nanoparticles. *Chemical Communications* **2014**, *50*, 67-69.

(29) Cho, K.-R. K., Y.-Y.; Yang, P.; Cai, W.; Pan, H.; Kulak, A. N.; Lau, J. L.; Kulshreshtha, P.; Armes, S. P.; Meldrum, F. C.; De Yoreo, J. J. Direct observation of mineral-organic composite formation reveals occlusion mechanism. *Nature Communications* **2016**, *7*, 10187.

(30) Kim, Y.-Y.; Semsarilar, M.; Carloni, J. D.; Cho, K. R.; Kulak, A. N.; Polishchuk, I.; Hendley, C. T.; Smeets, P. J. M.; Fielding, L. A.; Pokroy, B.; Tang, C. C.; Estroff, L. A.; Baker, S. P.; Armes, S. P.; Meldrum, F. C. Structure and Properties of Nanocomposites Formed by the Occlusion of Block Copolymer Worms and Vesicles Within Calcite Crystals. *Advanced Functional Materials* **2016**, *26*, 1382-1392.

(31) Kulak, A. N.; Semsarilar, M.; Kim, Y.-Y.; Ihli, J.; Fielding, L. A.; Cespedes, O.; Armes, S. P.; Meldrum, F. C. One-pot synthesis of an inorganic heterostructure: uniform occlusion of magnetite nanoparticles within calcite single crystals. *Chemical Science* **2014**, *5*, 738-743.

(32) Muñoz-Espí, R.; Qi, Y.; Lieberwirth, I.; Gómez, C. M.; Wegner, G. Surface-functionalized latex particles as controlling agents for the mineralization of zinc oxide in aqueous medium. *Chemistry-A European Journal* **2006**, *12*, 118-129.

(33) Frens, G. Controlled nucleation for the regulation of the particle size in monodisperse gold suspensions. *Nature* **1973**, *241*, 20-22.

(34) Liang, M.; Lin, I. C.; Whittaker, M. R.; Minchin, R. F.; Monteiro, M. J.; Toth, I. Cellular Uptake of Densely Packed Polymer Coatings on Gold Nanoparticles. *ACS Nano* **2010**, *4*, 403-413.

(35) Hotchkiss, J. W.; Lowe, A. B.; Boyes, S. G. Surface modification of gold nanorods with polymers synthesized by reversible addition-fragmentation chain transfer polymerization. *Chemistry of Materials* **2007**, *19*, 6-13.

(36) Akpinar, B. F., Lee; Cunningham, Victoria; Ning, Yin; Mykhaylyk, Oleksandr; Fowler, Patrick; Armes, Steven Determining the effective density and stabilizer layer thickness of sterically-stabilized nanoparticles. *Macromolecules* **2016**, *49*, 5160−5171.

(37) Schneider, G.; Decher, G. From Functional Core/Shell Nanoparticles Prepared via Layer-by-Layer Deposition to Empty Nanospheres. *Nano Letters* **2004**, *4*, 1833-1839.

(38) Lovett, J. R.; Warren, N. J.; Ratcliffe, L. P. D.; Kocik, M. K.; Armes, S. P. pH-Responsive Non-Ionic Diblock Copolymers: Ionization of Carboxylic Acid End-Groups Induces an Order-Order Morphological Transition. *Angewandte Chemie-International Edition* **2015**, *54*, 1279-1283.

(39) Lovett, J. R.; Fielding, L. A.; Armes, S. P.; Buxton, R. One-Pot Preparation of Conducting Polymer-Coated Silica Particles: Model Highly Absorbing Aerosols. *Advanced Functional Materials* **2014**, *24*, 1290-1299.

(40) Lu, G.; Li, S.; Guo, Z.; Farha, O. K.; Hauser, B. G.; Qi, X.; Wang, Y.; Wang, X.; Han, S.; Liu, X. Imparting functionality to a metal–organic framework material by controlled nanoparticle encapsulation. *Nature Chemistry* **2012**, *4*, 310-316.

(41) Liz-Marzán, L. M.; Giersig, M.; Mulvaney, P. Synthesis of nanosized gold-silica core-shell particles. *Langmuir* **1996**, *12*, 4329-4335.

(42) Wood, A.; Giersig, M.; Mulvaney, P. Fermi level equilibration in quantum dot-metal nanojunctions. *The Journal of Physical Chemistry B* **2001**, *105*, 8810-8815.

(43) Wang, Z. L. Zinc oxide nanostructures: growth, properties and applications. *Journal of Physics: Condensed Matter* **2004**, *16*, 829-858.

(44) Kawatkar, S. P.; Kuntz, D. A.; Woods, R. J.; Rose, D. R.; Boons, G.-J. Structural basis of the inhibition of Golgi α-mannosidase II by mannostatin A and the role of the thiomethyl moiety in ligand-protein interactions. *Journal of the American Chemical Society* **2006**, *128*, 8310-8319.

(45) Gyurcsik, B.; Nagy, L. Carbohydrates as ligands: coordination equilibria and structure of the metal complexes. *Coordination Chemistry Reviews* **2000**, *203*, 81-149.

(46) Ghoshal, T.; Kar, S.; Chaudhuri, S. ZnO doughnuts: controlled synthesis, growth mechanism, and optical properties. *Crystal Growth & Design* **2007**, *7*, 136-141.

(47) Socrates, G. *Infrared and Raman characteristic group frequencies: tables and charts*; John Wiley & Sons, **2004**.

(48) Richards, N. J.; Williams, D. G. Complex formation between aqueous zinc chloride and cellulose-related D-glucopyranosides. *Carbohydrate Research* **1970**, *12*, 409-420.

(49) Chen, Y.; Zeng, D.; Zhang, K.; Lu, A.; Wang, L.; Peng, D.-L. Au–ZnO hybrid nanoflowers, nanomultipods and nanopyramids: one-pot reaction synthesis and photocatalytic properties. *Nanoscale* **2014**, *6*, 874-881.

7. Chapter Seven

7. Conclusions and Future Work

7.1 Conclusions and Future Work

In this Thesis, various diblock copolymer nanoparticles have been prepared via RAFT-mediated PISA. The occlusion of these nanoparticles within calcite or ZnO enables hybrid nanomaterials to be generated by rational design. Importantly, this Thesis provides a deeper understanding of the design rules required for efficient nanoparticle occlusion within inorganic host crystals.

Two diblock copolymer nanoparticles have been synthesised using either poly(proline methacrylate) or poly(carboxybetaine methacrylate) macro-CTAs as steric stabilisers. Both macro-CTAs contain carboxylic acid groups, but the former becomes anionic above pH 9.2, whereas the latter has zwitterionic character at this pH. The anionic poly(proline methacrylate)-stabilised particles are occluded uniformly throughout the crystals (up to 6.8 % by mass, 14.0 % by volume). In contrast, the zwitterionic poly(carboxybetaine methacrylate)-stabilised particles show no signs of occlusion into calcite crystals grown under identical conditions. Therefore, the presence of carboxylic acid groups alone does not guarantee efficient occlusion: overall anionic character is an additional prerequisite.

For the first time we demonstrate that S-B diblock copolymer nanoparticles can be prepared with either high or low S stabiliser surface densities using either RAFT dispersion polymerisation in a 2:1 v/v ethanol/water mixture or RAFT aqueous emulsion polymerisation, respectively. This difference in stabiliser surface density offers an unprecedented opportunity to investigate how this parameter affects the extent of nanoparticle occlusion. Substantial differences are observed for the extent of occlusion of these two types of anionic nanoparticles into calcite. Surprisingly, a low S stabiliser surface density leads to uniform nanoparticle occlusion within calcite at up to 7.5 % w/w (16 % v/v), whereas minimal occlusion occurs when using nanoparticles with a high S stabiliser surface density. This counter-intuitive observation suggests that an optimum anionic surface density is required for efficient occlusion. This unexpected design rule for the incorporation of nanoparticles within crystals also applies to ZnO host crystals. In future work, how to precisely control the stabiliser surface density using PISA formulations should be systematically investigated by varying the solvent composition of ethanol/water mixture.

Extending the nanoparticle occlusion protocol to other functional crystal hosts is highly desirable. S-B diblock copolymer nanoparticles prepared by RAFT aqueous emulsion polymerisation are then used as additives for the in situ formation of semiconductor ZnO crystals. Some other well-defined anionic diblock copolymer nanoparticles are also prepared by PISA-mediated RAFT aqueous emulsion polymerisation and then evaluated for occlusion in control experiments. Systematic studies indicated that both the chemical nature (i.e. whether sulfate-based or carboxylate-based) and the mean degree of polymerisation (DP) of the anionic stabiliser block play vital roles in determining the crystal morphology. S-B nanoparticles are efficiently incorporated within the ZnO crystals, leading to a substantial change in morphology from twin-structure hexagonal prismatic rod-like ZnO crystals to twin-structure "diablo" ZnO crystals. Moreover, the extent of nanoparticle occlusion within the ZnO phase can be as high as 23 % by mass. The optical properties, chemical composition and crystal structure of the resulting nanocomposite crystals are evaluated and an occlusion mechanism is proposed based on the observed evolution of the ZnO morphology in the presence of the sulfate-based anionic nanoparticles.

Diblock copolymer nanoparticles offer an excellent model for studying the effect of surface chemistry/composition on the nanoparticle occlusion within crystals. The ultimate goal is to incorporate functional nanoparticles (such as noble nanoparticles, magnetic nanoparticles etc.) into functional crystal hosts (such as semiconductors) to produce a range new functional hybrid materials with superior/emergent properties. In this context, we explored an efficient aqueous route that enabled the direct incorporation of non-ionic G_{70}-AuNPs at remarkably high levels (~20 % w/w) during the *in situ* growth of ZnO crystals under relatively mild conditions. Depending on the synthesis protocol, the localisation of G_{70}-AuNPs can be readily controlled in three ways: (i) solely located within a central region, (ii) uniformly distributed throughout the ZnO host crystal or (iii) confined to a surface layer of approximately 35 nm. The G_{70} stabiliser is essential for successful occlusion: its pendent *cis*-diol side-groups bind Zn^{2+} cations, which promote nanoparticle interaction with the growing ZnO crystal surface. The intimate interaction between the G_{70}-AuNPs and the host ZnO crystals is demonstrated by XPS studies. Finally, we demonstrate that occlusion of G_{70}-AuNPs throughout the whole ZnO crystal is

beneficial for the enhanced photocatalytic decomposition of rhodamine B, which serves as a model dye. This study provides the first example of effective occlusion facilitated by a *non-ionic* polymer stabiliser. This represents an important paradigm shift, since all prior literature reports of occlusion into inorganic host crystals involved the use of *anionic* polymeric stabilisers.

Currently, the occlusion of nanoparticles within host crystals is in its preliminary stage. Compared with traditional methods, such as mechanically mixing, annealing or alloying, uniformly distributing nanoparticles within a crystal host during its formation is of considerable scientific interest. This versatile strategy offers great potential to revolutionise the preparation of hybrid nanomaterials with a uniform distribution of guest nanoparticles within a crystal host. Given appropriate surface modification, a wide range of organic/inorganic nanoparticles can be occluded within various desired host crystals.

Topics worthy of further exploration include the following:

i), Expanding the scope of guest nanoparticles and host crystals is highly desirable. For example, Pt nanoparticles, Pd nanoparticles, Ag nanoparticles, bimetallic nanoparticles (AuAg, PtPd etc.), magnetic nanoparticles, quantum dots etc. are of great interest due to their unique properties. Similarly, TiO_2, Cu_2O, MnO_2, Fe_3O_4, $SrTiO_3$, $MnCO_3$ etc. are potential host crystals. Combination of these functional components could generate a wide range of novel nanocomposite materials.

ii), It is of great interest to investigate occlusion of nanoparticles with specific morphology (such as cubic, rod-like, porous, hollow, lamellae, anisotropic etc.) within host crystal. Such unique morphologies may well affect the crystallisation habit of the host crystals and assembly/alignment of the host nanoparticles is likely during their incorporation.

iii), To date, all occluded nanoparticles have been surface-functionalised with desired polymers in order to promote their interaction with the growing crystal surface. This means modification of the nanoparticles is essential prior to their occlusion. Can we find a general way to incorporate nanoparticles into crystals via a generic "carrier"? Recently, it has been reported that silica nanoparticles can be

loaded within diblock copolymer vesicles during the formation of the latter via PISA.[1] Moreover, anionic poly(methacrylic acid)-poly(benzyl methacrylate) vesicles can be incorporated into calcite.[2] In principle, this means that dyes, organic nanoparticles or inorganic nanoparticles could be incorporated into crystals as long as these substances can be loaded into appropriate anionic vesicles. This could be a wholly generic approach to incorporate nanoparticles into crystals.

7.2 References

(1) Mable, C. J.; Gibson, R. R.; Prévost, S.; McKenzie, B. E.; Mykhaylyk, O. O.; Armes, S. P. Loading of silica nanoparticles in block copolymer vesicles during polymerization-induced self-assembly: encapsulation efficiency and thermally-triggered release. *Journal of the American Chemical Society* **2015**, *137*, 16098-16108.

(2) Kim, Y.-Y.; Semsarilar, M.; Carloni, J. D.; Cho, K. R.; Kulak, A. N.; Polishchuk, I.; Hendley, C. T.; Smeets, P. J. M.; Fielding, L. A.; Pokroy, B.; Tang, C. C.; Estroff, L. A.; Baker, S. P.; Armes, S. P.; Meldrum, F. C. Structure and Properties of Nanocomposites Formed by the Occlusion of Block Copolymer Worms and Vesicles Within Calcite Crystals. *Advanced Functional Materials* **2016**, *26*, 1382-1392.